

Lecture Notes in Mechanical Engineering

Ketul C. Popat

S. Kanagaraj

P. S. Rama Sreekanth

V. M. Ravindra Kumar *Editors*


Advances in Mechanical Engineering and Material Science

Select Proceedings of ICAMEMS-2022

 Springer


Lecture Notes in Mechanical Engineering

Series Editors

Francisco Cavas-Martínez , Departamento de Estructuras, Construcción y Expresión Gráfica Universidad Politécnica de Cartagena, Cartagena, Murcia, Spain

Fakher Chaari, National School of Engineers, University of Sfax, Sfax, Tunisia

Francesca di Mare, Institute of Energy Technology, Ruhr-Universität Bochum, Bochum, Nordrhein-Westfalen, Germany

Francesco Gherardini , Dipartimento di Ingegneria “Enzo Ferrari”, Università di Modena e Reggio Emilia, Modena, Italy

Mohamed Haddar, National School of Engineers of Sfax (ENIS), Sfax, Tunisia

Vitalii Ivanov, Department of Manufacturing Engineering, Machines and Tools, Sumy State University, Sumy, Ukraine

Young W. Kwon, Department of Manufacturing Engineering and Aerospace Engineering, Graduate School of Engineering and Applied Science, Monterey, CA, USA

Justyna Trojanowska, Poznan University of Technology, Poznan, Poland

Lecture Notes in Mechanical Engineering (LNME) publishes the latest developments in Mechanical Engineering—quickly, informally and with high quality. Original research reported in proceedings and post-proceedings represents the core of LNME. Volumes published in LNME embrace all aspects, subfields and new challenges of mechanical engineering. Topics in the series include:

- Engineering Design
- Machinery and Machine Elements
- Mechanical Structures and Stress Analysis
- Automotive Engineering
- Engine Technology
- Aerospace Technology and Astronautics
- Nanotechnology and Microengineering
- Control, Robotics, Mechatronics
- MEMS
- Theoretical and Applied Mechanics
- Dynamical Systems, Control
- Fluid Mechanics
- Engineering Thermodynamics, Heat and Mass Transfer
- Manufacturing
- Precision Engineering, Instrumentation, Measurement
- Materials Engineering
- Tribology and Surface Technology

To submit a proposal or request further information, please contact the Springer Editor of your location:

China: Ms. Ella Zhang at ella.zhang@springer.com

India: Priya Vyas at priya.vyas@springer.com

Rest of Asia, Australia, New Zealand: Swati Meherishi at swati.meherishi@springer.com

All other countries: Dr. Leontina Di Cecco at Leontina.dicecco@springer.com

To submit a proposal for a monograph, please check our Springer Tracts in Mechanical Engineering at <https://link.springer.com/bookseries/11693> or contact Leontina.dicecco@springer.com

Indexed by SCOPUS. All books published in the series are submitted for consideration in Web of Science.

More information about this series at <https://link.springer.com/bookseries/11236>

Ketul C. Papat · S. Kanagaraj ·
P. S. Rama Sreekanth · V. M. Ravindra Kumar
Editors

Advances in Mechanical Engineering and Material Science

Select Proceedings of ICAMEMS-2022

 Springer

Editors

Ketul C. Papat
Department of Mechanical Engineering,
School of Biomedical Engineering
Colorado State University
Fort Collins, CO, USA

P. S. Rama Sreekanth
School of Mechanical Engineering (SMEC)
VIT-AP University
Amaravati, Andhra Pradesh, India

S. Kanagaraj
Department of Mechanical Engineering
Indian Institute of Technology Guwahati
Guwahati, Assam, India

V. M. Ravindra Kumar
School of Mechanical Engineering (SMEC)
VIT-AP University
Amaravati, Andhra Pradesh, India

ISSN 2195-4356

ISSN 2195-4364 (electronic)

Lecture Notes in Mechanical Engineering

ISBN 978-981-19-0675-6

ISBN 978-981-19-0676-3 (eBook)

<https://doi.org/10.1007/978-981-19-0676-3>

© The Editor(s) (if applicable) and The Author(s), under exclusive license to Springer Nature Singapore Pte Ltd. 2022

This work is subject to copyright. All rights are solely and exclusively licensed by the Publisher, whether the whole or part of the material is concerned, specifically the rights of translation, reprinting, reuse of illustrations, recitation, broadcasting, reproduction on microfilms or in any other physical way, and transmission or information storage and retrieval, electronic adaptation, computer software, or by similar or dissimilar methodology now known or hereafter developed.

The use of general descriptive names, registered names, trademarks, service marks, etc. in this publication does not imply, even in the absence of a specific statement, that such names are exempt from the relevant protective laws and regulations and therefore free for general use.

The publisher, the authors and the editors are safe to assume that the advice and information in this book are believed to be true and accurate at the date of publication. Neither the publisher nor the authors or the editors give a warranty, expressed or implied, with respect to the material contained herein or for any errors or omissions that may have been made. The publisher remains neutral with regard to jurisdictional claims in published maps and institutional affiliations.

This Springer imprint is published by the registered company Springer Nature Singapore Pte Ltd.

The registered company address is: 152 Beach Road, #21-01/04 Gateway East, Singapore 189721, Singapore

Preface

The first International Conference on Advances in Mechanical Engineering and Material Science (ICAMEMS-2022) aims to create an international conglomeration of scientists, engineers, and industrial experts. This forum serves as a platform where people can share information about diverse technological advancements, innovations, and achievements in the areas of Mechanical Engineering and Material Science. Further, it would also facilitate discussion that centers on the developments and challenges in the field of machine design, manufacturing, thermal, and fluid engineering.

The focus of this conference is to provide a technical platform that encourages scientific research and educational activities that would cater to the needs of both society and the industry. Most importantly, ICAMEMS-22 is focused on the advancement of a common man's life by utilizing the theory and practice of Mechanical Engineering and Material Science. The conference includes several keynote addresses and guest lectures by eminent speakers around the globe who would deliberate the recent trends and challenges in the field of Mechanical Engineering and Material Science.

The proceedings received full-length research manuscripts and review articles in the above-mentioned areas. All received articles went through a peer-review process by inviting reviewers who are experts in relevant areas.

Finally, the conference committee would like to thank everyone who contributed for the conference and would like to carry the ICAMEMS conference series in future also.

Fort Collins, USA
Guwahati, India
Amaravati, India
Amaravati, India

Dr. Ketul C. Popat
Dr. S. Kanagaraj
Dr. P. S. Rama Sreekanth
Dr. V. M. Ravindra Kumar

Contents

Nonlinear Frequency Response of Sandwich Beam with Frequency-Dependent Viscoelastic Core Using Reduced-Order Finite Element Method	1
Rajidi Shashidhar Reddy, Abhay Gupta, and Satyajit Panda	
Control of Jeffcott Rotor Vibrations Using Model Predictive Control	11
Abhinav Singh, R. Aashish, and Ashesh Saha	
On the Chaotic Behavior of Coupled Friction-Induced Oscillators Subjected to Base-Excitation	23
Jithin Velayudhan, M. D. Narayanan, and Ashesh Saha	
Influence of Supply Inlet Jet Angle on Ventilating Respiratory Droplets from Makeshift Isolation Enclosures	37
S. Harikrishnan and M. Manish	
Influence of PWHT on Microstructure and Mechanical Properties of Similar TRIP-TRIP and Dissimilar DP-TRIP Laser Welds for Automobile Applications	47
C. Gopi Krishna, T. Mahesh Kumar, N. Kishore Babu, P. Phani Prabhakar, and G. V. Sarath Kumar	
Optimization of Fluid Modeling and Flow Control Processes Using Machine Learning: A Brief Review	63
Surbhi Razdan and Sarth Shah	
Influence of Gyroscopic Effect and Rotary Inertia on the Vibrations of a Continuous Rotor System	87
Amit Malgol and Ashesh Saha	

Friction Stir Welding of IS:65032 Aluminum Alloy and Predicting Tensile Strength Using Ensemble Learning	103
Kaveti Upender, B. V. R. Ravi Kumar, M. S. Srinivasa Rao, and M. Venkata Ramana	
Experimental Investigation on Nozzle Flow at Different Levels of Jet State at Supersonic Mach Numbers with Sudden Expansion	115
Ridwan, J. I. Suheel, Hamza Afser Delvi, M. MashtaqAhamed Attar, Sher Afghan Khan, and Mohammed Faheem	
Multi Objective Optimization Using Artificial Neural Networks in the Cutting Parameters of Machining of Heat Treated Be-Cu Alloy	127
Manda Sreeja, K. Devaki Devi, and M. Naga Phani Shastry	
Fabrication of Highly Oriented Piezoelectric Nanofibers Using a Low Cost and Lab-Scale Electrospinning System	139
Duc-Nam Nguyen, Van-Tuan Nguyen, Ich-Hung Dam, and Van-Huong Vu	
Visual Product Assessment by Using the Eye-Tracking Equipment to Study the Effect of Product Shapes on consumer's Thinking	149
Jitender Singh and Prabir Sarkar	
Neural Network (NN) Based Qualitative Assessment of Bone Growth Over Textured Implant Surfaces	159
Rajdeep Ghosh, Souptick Chanda, and Debabrata Chakraborty	
Study and Investigation of Tribological Functions of Nano Additive with SAE 40/W20 Oil on EN 19	171
A. Vinothkumar, R. Ruban, H. Mohit, and G. R. Arpitha	
A Review on Advances in Friction Welding of Dissimilar Metals	181
Deepansh Gill and M. K. Pradhan	
Conceptual Design and Development of Automated Waste Segregator	199
Vishwas Mahesh, Manoj D. Yadav, T. C. Sinchana, S. R. Subhash, and S. Sushmitha	
Design and Analysis of Car Brake Rotor and Brake Caliper for Efficient Braking	207
J. Karthik and Manas Kumar Pal	
Effect of Impact Angles on the Frontal Structure of a Vehicle	217
Rudolf Ragis, Akshaykumar Khatane, Kesav Chandran, and P. Baskar	

Finite Element Analysis of High-Density Polyethylene (HDPE) Nanocomposite for Potential Use as Dental Implant 229
Mayank Dey, Rahul Vamsi Katabathuni, Nitesh Dhar Badgayan, and Santosh Kumar Sahu

Process Simulation of Electrical Discharge Machining: A Review 237
Diksha Jaurker and M. K. Pradhan

A Finite Element Study on the Effect of Bulk Material on the Auxetic Behavior of Additively Manufactured Three-Dimensional Reentrant Honeycomb 257
Aravind Rajan Ayagara, Chaitanya Vinayak Varma, and Rohan Gooty

Path-Planning of Robot End-Effector for Hairline Crack Sealing Using Intelligent Techniques 271
Santosh Kumar and B. Sandeep Reddy

Author Index 283

Subject Index 285

About the Editors

Dr. Ketul C. Popat is Professor in the Department of Mechanical Engineering/School of Biomedical Engineering at Colorado State University. Prior to that, he was working as Research Specialist in the Department of Physiology at University of California, San Francisco. He has authored over 100 peer-reviewed publications in journals such as *Langmuir*, *Biomaterials*, *Journal of Orthopedic Research*, and *Journal of Biomedical Materials Research* and has h-index of 42. He has also presented his work at numerous national and international-level conferences. He currently directs the Biomaterials Surface Micro/Nano-engineering Laboratory.

Dr. S. Kanagaraj is Professor in the Department of Mechanical Engineering at Indian Institute of Technology, Guwahati. He received his Ph.D. degree from Indian Institute of Technology Kharagpur in 2004. He has postdoctoral experience at University of Aveiro, Portugal, till May 2008, and since then he has been with the Department of Mechanical Engineering at the Indian Institute of Technology Guwahati. His major areas of research interests include biomaterials, carbon nanotubes-based nanocomposites, biomedical devices and implants, materials characterization, and prosthetic and orthotic devices. He published more than 100 international peer-reviewed journals and conference papers. He has sponsored research and consultancy projects of worth more than 10 crores INR.

Dr. P. S. Rama Sreekanth is currently Dean, School of Mechanical Engineering, VIT-AP University. He has obtained his Doctoral degree from IIT Guwahati in 2013. His areas of specialization include biomaterials, nanocomposites, 3D printing, and additive manufacturing. He is Active Researcher with more than 50 publications in journals of international repute and conferences. He has several patents published and granted to his credit. He has authored 12 chapters, out of which six were contributed to *Reference module in Materials Science and Engineering*, Elsevier. He worked on various research and consultancy projects of worth 5 million INR .

Dr. V. M. Ravindra Kumar is Associate Professor in the School of Mechanical Engineering at VIT-AP University, Amaravati. He obtained Master's degree and Ph.D. from Indian Institute of Technology Khragapur. He took a real-life challenging problem, "Railway Wheel Failure from Excessive Wheel Gauge Change" sponsored by Indian Railways as a part of his Ph.D. and succeeded to identify the root cause of the failure and suggested guidelines for mitigating the same. His major areas of research interests include numerical modeling of manufacturing processes, railway engineering, shape memory materials, functionally graded materials, and product design and development. He has published more than 15 international journal and conference papers. He is Active Researcher and presented his work at various national and international conferences.

Nonlinear Frequency Response of Sandwich Beam with Frequency-Dependent Viscoelastic Core Using Reduced-Order Finite Element Method



Rajidi Shashidhar Reddy , Abhay Gupta, and Satyajit Panda

Abstract In the present work, the effect of frequency-dependent viscoelastic property on the forced/parametric resonant amplitude of viscoelastic sandwich beam is investigated by deriving a reduced-order finite element model (ROM) in frequency domain. In this concern, the frequency-dependent viscoelasticity is modelled using fractional Zener model and the corresponding responses of sandwich beam are compared with that are derived using an equivalent Kelvin-Voigt model. The ROM in frequency domain is derived by implementing harmonic balance method prior to the finite element discretization and reduced-order transformation. The comparison of frequency responses evaluated using ROM and full-order model revealed that the ROM with reduction basis from modal strain energy method provides the response of frequency-dependent viscoelastic sandwich beam with reasonable accuracy. Further, the frequency-dependent viscoelastic property has shown a significant effect on the resonant amplitudes especially when compared with an equivalent Kelvin-Voigt model in wide-frequency range. Moreover, the results suggest that the nonlinear frequency response analysis of viscoelastic layered beams using Kelvin-Voigt model may be reasonably accurate when the different model parameters are considered around each modal natural frequency.

Keywords Viscoelastic sandwich beam · Reduced-order finite element model · Harmonic balance method · Kelvin-Voigt model

1 Introduction

The flexibility of beam elements leads to their large amplitude nonlinear vibrations under different kind of loads and thereby causes their fracture/fatigue failure. Hence, a substantial amount of research is conducted on the vibration control of linear and nonlinear vibrations of beam elements under various loadings [1–5]. One of the

R. Shashidhar Reddy (✉) · A. Gupta · S. Panda
Department of Mechanical Engineering, Indian Institute of Technology Guwahati, Guwahati
781039, India
e-mail: rsreddy@iitg.ac.in

© The Author(s), under exclusive license to Springer Nature Singapore Pte Ltd. 2022
K. C. Popat et al. (eds.), *Advances in Mechanical Engineering and Material Science*,
Lecture Notes in Mechanical Engineering,
https://doi.org/10.1007/978-981-19-0676-3_1

popular technique is the constrained layer damping (CLD) treatment of the structure, where the vibrational energy is dissipated through the transient deformation of viscoelastic material by constraining it between the elastic substrate/face layers. For the design of an effective damping treatment, the accurate optimization studies of geometrically complex damping treatments [6, 7] may be necessary. Hence, for this purpose, finite element (FE) method is commonly used that provides accurate nonlinear dynamics compared to other alternative methods.

To conduct nonlinear dynamic analysis especially in conjunction with optimization, the use of time integration may be inappropriate and expensive due to the requirement of response for large number of geometrical parameters and excitation frequency [2, 3]. Hence, to directly evaluate the steady-state frequency response without requiring time integration method, the harmonic balance method (HBM) is popularly used in literature [3, 8, 9]. Although it is computationally efficient compared to time integration, it needs high computational time and memory [1, 3, 8–10] mainly due to the large number of degree of freedom associated with FE discretization, Fourier expansion of HBM and especially, additional internal variables/degree of freedom to model viscoelasticity. Therefore, various reduced-order FE models (ROMs) had been developing in literature that are majorly limited to elastic structures [11–13]. Hence, the objective of the present work is to derive the reduced-order FE model in conjunction with HBM to evaluate the nonlinear steady-state frequency response of viscoelastic sandwich (VS) beam.

Most of the nonlinear dynamic studies in the literature were neglected the frequency-dependency of stiffness/damping of viscoelastic material by considering Kelvin-Voigt model [2, 14, 15]. However, the variation of nonlinear resonant frequency with the amplitude of vibration and the presence of frequency dependent damping may significantly affect the resonant amplitude of the vibration. So, the main objective is decided to investigate the effect of frequency-dependent viscoelasticity on the steady-state nonlinear response by comparing the response evaluated using fractional Zener viscoelastic model with that evaluated using an equivalent Kelvin-Voigt model.

2 Reduced-Order FE Model of Viscoelastic Sandwich Beam

Figure 1 shows the schematic diagram of a VS beam, where the thickness of substrate and viscoelastic core layer are denoted by h_s and h_v , respectively. The length and width of the beam are denoted by L and b , respectively. Since it is a plane stress problem [3] in two dimensional xz -plane, the state of stress and state of strain at any point in the xz -plane can be written as,

$$\begin{aligned} \boldsymbol{\sigma} &= \{\sigma_x \ \sigma_z \ \tau_{xz}\}^T, \boldsymbol{\varepsilon} = \{\varepsilon_x \ \varepsilon_z \ \gamma_{xz}\}^T, \boldsymbol{\varepsilon} = \boldsymbol{\varepsilon}_l + \boldsymbol{\varepsilon}_n, \\ \boldsymbol{\varepsilon}_l &= \mathbf{L} \mathbf{d}_s, \boldsymbol{\varepsilon}_n = \mathbf{L}_n(\mathbf{d}_s) \mathbf{d}_s, \mathbf{d}_s = \{u \ w\}^T \end{aligned} \quad (1)$$

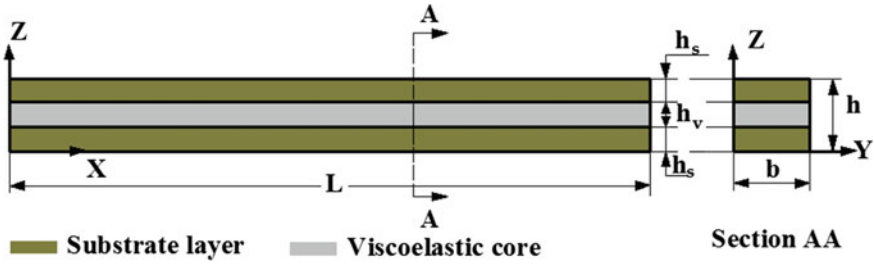


Fig. 1 Schematic diagram of a viscoelastic sandwich beam

where, $\boldsymbol{\varepsilon}_l$ and $\boldsymbol{\varepsilon}_n$ are the linear and nonlinear counterpart of Green–Lagrange strain, respectively, while \mathbf{L} and \mathbf{L}_n are the corresponding operator matrices; u and w are the displacements along x and z directions respectively. However, to derive the incremental FE model, the incremental forms of state variables ($\Delta \mathbf{d}_s, \Delta \omega$) about a reference state (${}^i \mathbf{d}_s, \omega_i$) can be given as in Eq. (2). The corresponding expressions of strain and stress vectors can be given as in Eq. (3).

$$\mathbf{d}_s = {}^i \mathbf{d}_s + \Delta \mathbf{d}_s, \omega = \omega_i + \Delta \omega \quad (2)$$

$$\begin{aligned} \boldsymbol{\varepsilon}_l &= {}^i \boldsymbol{\varepsilon}_l + \Delta \boldsymbol{\varepsilon}_l, \boldsymbol{\varepsilon}_n = {}^i \boldsymbol{\varepsilon}_n + \Delta \boldsymbol{\varepsilon}_{n1} + \Delta \boldsymbol{\varepsilon}_{n2}, \boldsymbol{\sigma} = {}^i \boldsymbol{\sigma} + \Delta \boldsymbol{\sigma}, \\ {}^i \boldsymbol{\varepsilon}_l &= \mathbf{L} {}^i \mathbf{d}_s, \Delta \boldsymbol{\varepsilon}_l = \mathbf{L} \Delta \mathbf{d}_s, {}^i \boldsymbol{\varepsilon}_n = (1/2) {}^i \mathbf{L}_n {}^i \mathbf{d}_s, \Delta \boldsymbol{\varepsilon}_{n1} = {}^i \mathbf{L}_n \Delta \mathbf{d}_s, \\ \Delta \boldsymbol{\varepsilon}_{n2} &= (1/2) \Delta \mathbf{L}_n \Delta \mathbf{d}_s, {}^i \mathbf{L}_n = \mathbf{L}_n({}^i \mathbf{d}_s), \Delta \mathbf{L}_n = \mathbf{L}_n(\Delta \mathbf{d}_s) \end{aligned} \quad (3)$$

where, pre-superscript i denotes the variable about the reference state of vibration. The incremental governing equation of VS beam subjected to transverse harmonic point load ($p_t^o \cos \omega t$)/axial compressive harmonic load ($p_a^o(1 + \lambda \cos 2\omega t)$) can be obtained by following Hamilton's principle and Eqs. (1)–(3) as,

$$\int_A \left\langle \begin{aligned} &(\delta \Delta \boldsymbol{\varepsilon}_l + \delta \Delta \boldsymbol{\varepsilon}_{n1})^T ({}^i \boldsymbol{\sigma} + \Delta \boldsymbol{\sigma}) + (\delta \Delta \boldsymbol{\varepsilon}_{n2})^T {}^i \boldsymbol{\sigma} \\ &+ (\delta \Delta \mathbf{d}_s)^T \rho ({}^i \ddot{\mathbf{d}}_s + \Delta \ddot{\mathbf{d}}_s) - (\{0 \ 1\} \delta \Delta \mathbf{d}_s|_{(x_l, z_l)})^T (p_t^o/b) \cos \omega t \\ &- (\mathbf{L}_g \delta \Delta \mathbf{d}_s)^T (p_a^o/bh_s)(1 + \lambda \cos 2\omega t) \mathbf{L}_g ({}^i \mathbf{d}_s + \Delta \mathbf{d}_s) \end{aligned} \right\rangle b dA = 0 \quad (4)$$

where, p_t^o is amplitude of transverse harmonic point load; $(x_l, z_l) = (L/4, 0)$ is the location of point load; \mathbf{L}_g is the linear operator of strain vectors associated with geometric stiffness term due to pre-stress; p_a^o and λ are the static counterpart and dynamic load parameter of axial harmonic load, respectively; ω and 2ω are the frequency of excitation of harmonic point load and axial periodic load, respectively. In Eq. (4), the last term with p_a^o vanishes for viscoelastic material mainly due to the negligible axial pre-stress induced in it.

Now, for the implementation of HBM, the response is assumed following the Fourier series with finite number (H) of harmonic terms as,

$$\mathbf{d}_s = \mathbf{d}_s^o + \sum_{m=1}^H \mathbf{d}_{sm}^c \cos(m\omega t) + \mathbf{d}_{sm}^s \sin(m\omega t) \quad (5)$$

where, \mathbf{d}_s^o , \mathbf{d}_{sm}^c and \mathbf{d}_{sm}^s are the Fourier coefficient vectors of displacement (\mathbf{d}_s) corresponding to the constant, m th cosine and m th sine terms of Fourier series, respectively. The corresponding Fourier series of stress vector in terms of strain can be given in through the constitutive relation of viscoelastic material in frequency-domain as,

$$\begin{aligned} \boldsymbol{\sigma} &= (\boldsymbol{\sigma})^o + \sum_{m=1}^{2H} (\boldsymbol{\sigma})_m^c \cos(m\omega t) + (\boldsymbol{\sigma})_m^s \sin(m\omega t), \\ (\boldsymbol{\sigma})_m^s &= \mathbf{C} \left(f_m^c (\boldsymbol{\varepsilon}_l + \boldsymbol{\varepsilon}_n)_m^s - f_m^s (\boldsymbol{\varepsilon}_l + \boldsymbol{\varepsilon}_n)_m^c \right), (\boldsymbol{\sigma})_m^c = \mathbf{C} \left(f_m^c (\boldsymbol{\varepsilon}_l + \boldsymbol{\varepsilon}_n)_m^c + f_m^s (\boldsymbol{\varepsilon}_l + \boldsymbol{\varepsilon}_n)_m^s \right) \\ (\boldsymbol{\sigma})^o &= \mathbf{C} (\boldsymbol{\varepsilon}_l + \boldsymbol{\varepsilon}_n)^o, f_m^c = E^R(m\omega)/E_o, f_m^s = E^I(m\omega)/E_o \end{aligned} \quad (6)$$

where, E_o is the relaxed elastic modulus; \mathbf{C} is the stiffness matrix in terms of E_o and Poisson ratio; E^R/E^I are the frequency-dependent storage/loss moduli of the viscoelastic material. In this work, the frequency dependent viscoelasticity is modelled using fractional Zener viscoelastic model [10]. The relation in Eq. (6) also represent the constitutive relation for an elastic material when $f_m^c = 1$, $f_m^s = 0$. However, to consider frequency-independent property for viscoelastic material, an equivalent Kelvin-Voigt model in a specified frequency range ($[\omega_1 \omega_2]$) is used, where the corresponding constitutive relation can be given in time-domain as,

$$\begin{aligned} \boldsymbol{\sigma} &= \mathbf{C} (\boldsymbol{\varepsilon} + \tau_v \dot{\boldsymbol{\varepsilon}}), \\ \tau_v &= \frac{1}{\omega_2 - \omega_1} \int_{\omega_1}^{\omega_2} \frac{\eta(\omega)}{\omega} d\omega, \eta(\omega) = E^I(\omega)/E^R(\omega) \end{aligned} \quad (7)$$

where, the relaxation time (τ_v) is evaluated by averaging the ratio of frequency-dependent loss factor ($\eta(\omega)$) and frequency (ω) in the interval $[\omega_1 \omega_2]$ [15]. The corresponding constitutive relation in frequency-domain can be obtained similar to Eq. (6) with $f_m^c = 1$ and $f_m^s = \tau_v m \omega$. To derive the FE model, the xz -plane of VS beam (Fig. 1) is discretized with nine-node isoparametric quadrilateral element. Subsequently, considering the reduce-order transformation using a reduction basis (RB) ($\boldsymbol{\Phi}$), the displacement and strain expressions at any point in a typical element can be written as,

$$\begin{aligned} {}^i \mathbf{d}_s &= \mathbf{N} \boldsymbol{\Phi}^e {}^i \mathbf{V}, \Delta \mathbf{d}_s = \mathbf{N} \boldsymbol{\Phi}^e \Delta \mathbf{V} \\ {}^i \boldsymbol{\varepsilon}_l &= \mathbf{B}_l \boldsymbol{\Phi}^e {}^i \mathbf{V}, \Delta \boldsymbol{\varepsilon}_l = \mathbf{B}_l \boldsymbol{\Phi}^e \Delta \mathbf{V}, {}^i \boldsymbol{\varepsilon}_n = (1/2) \mathbf{B}_n \boldsymbol{\Phi}_I^e {}^i \mathbf{V}_I, \Delta \boldsymbol{\varepsilon}_{n1} = \mathbf{B}_n \boldsymbol{\Phi}_I^e {}^i \mathbf{V}_I \Delta \mathbf{V} \end{aligned}$$

$$\Phi_I^e = \Phi^e \otimes \Phi^e, {}^i V_I = {}^i V \otimes I_{N_r} \quad (8)$$

where, N is the shape function matrix; N_r is the number of basis vectors in RB; B_n is a linear matrix corresponding to the operator L_n (Eq. 3) that is obtained by separating space-dependent and displacement dependent terms; Φ^e is the RB at element level; ${}^i V/\Delta V$ are the incremental forms of reduced coordinate vector. Thus, substituting Eqs. (5)–(8) in Eq. (4) and applying Galerkin method, the reduced-order FE governing equation of motion in frequency-domain can be obtained using the orthogonality of Fourier basis functions as,

$$\begin{aligned} K_t \Delta X &= R + R_\omega \Delta \omega, \\ R &= P - K_m {}^i X, R_\omega = -(\partial K_m / \partial \omega_i) {}^i X \end{aligned} \quad (9)$$

where, K_m/K_t are the effective reduced-order stiffness/tangent stiffness; R is residue vector; R_ω is the force vector per unit increment of frequency; P is external load vector. However, the corresponding full-order FE governing equation can be obtained by taking Φ^e as a unit matrix. Thus, the solution of Eq. (9) using continuation method provides the frequency response of VS beam under harmonic point load/axial compressive harmonic load. However, the RB is constructed by taking first 4 modes obtained using modal strain energy method (MSE) [16] and corresponding 10 static derivatives [17].

3 Numerical Results and Discussion

In this section, the numerical results are presented to show the effect of frequency-dependent viscoelastic property on the forced and parametric resonant response of clamped–clamped VS beam. However, initially, the validation for the accuracy of the ROM against full-order model is presented. The geometrical properties of VS beam are considered as $L = 0.4$ m, $b = 12$ mm and $h_s = 2$ mm. The substrate layers are considered to be made of Aluminum ($E = 70.3$ GPa, $\nu = 0.345$, $\rho = 2690$ kg/m³ [10]) and viscoelastic core is made of ISD 112 ($\nu = 0.499$, $\rho = 1600$ kg/m³) with its fractional Zener viscoelastic model parameters [10] as $E_o = 1.5$ MPa, $E_\infty = 69.9495$ MPa, $\alpha = 0.7915$ and $\tau = 1.4052 \times 10^{-5}$ s.

Initially, to validate the full-order FE model, the frequency response associated with forced resonance of clamped–clamped VS beam (with Kelvin-Voigt viscoelastic model) is evaluated by solving Eq. (9) using continuation method and compared in Fig. 2a with the similar results in Ref. [1]. Next, to verify the modelling of frequency-dependent properties and axial compressive harmonic load, the parametric instability region is constructed using Eq. (9) [3]. This region is compared in Fig. 2b with similar result in Ref. [18]. The good agreement shown in Fig. 2 with the similar reference results, validates the formulation of full-order FE model and solution method.

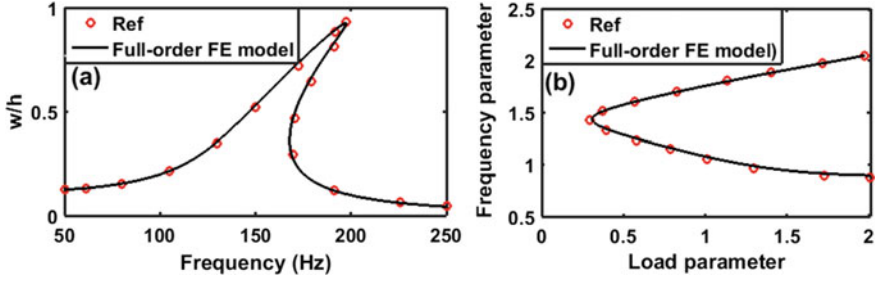


Fig. 2 Validation for the evaluation of **a** frequency response of sandwich beam with viscoelastic core modelled by Kelvin-Voigt model (Ref. [1]), **b** parametric instability region of frequency-dependent viscoelastic beam ($E_o = 425.72$ MPa, $E_\infty = 5954.6$ MPa, $\alpha = 0.2255$ and $\tau = 0.6338$ s) for a load parameter of 0.6 (Ref. [18])

Next, to validate the reduced-order FE model, the frequency response associated with parametric resonance of VS beam is evaluated by using ROM as well as full-order FE model. The corresponding responses are depicted in Fig. 3a, where also the axial load parameters are mentioned. The Fig. 3a illustrates that the frequency response evaluated using ROM reasonably agrees with that evaluated using full-order FE model. It is to be noted that RB is evaluated without considering the effect of static counterpart of axial load that significantly reduces the linear stiffness of beam. For further validation of such RB, the similar frequency response for an axial load near to the critical buckling load (331.2745 N) is evaluated and shown in Fig. 3b. It reveals that the accuracy of response is almost independent of the value of static counterpart of axial load. Thus, the present ROM and its RB with MSE method accurately evaluates the frequency response of frequency-dependent VS beam.

To investigate the effect of frequency-dependent viscoelastic property on the forced /parametric resonant response of VS beam, the corresponding frequency response is compared with the similar responses evaluated using an equivalent Kelvin-Voigt model. Considering a limited frequency range around the twice of natural frequency (100–1500 rad/s, Eq. 7), the frequency response of VS beam

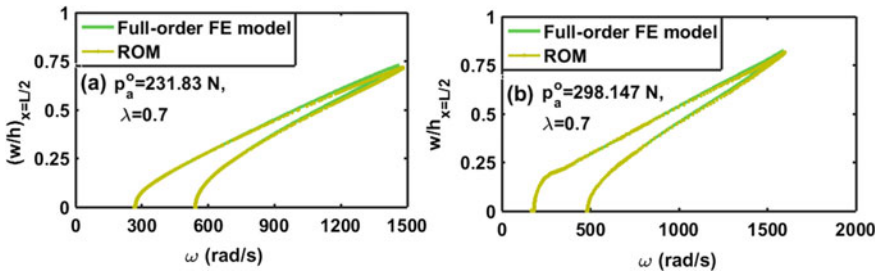


Fig. 3 Validation of reduced-order FE model for the evaluation of frequency response ($H = 7$) of VS beam ($h_v = 4$ mm) under axial compressive periodic load ($\lambda = 0.7$) with its static counterpart as **a** $p_a^o = 231.96215$ N and **b** $p_a^o = 298.14705$ N

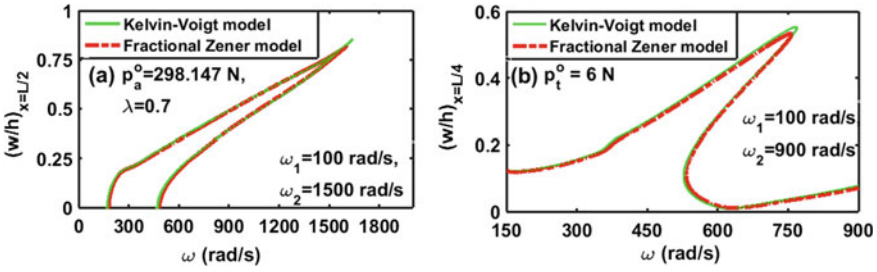
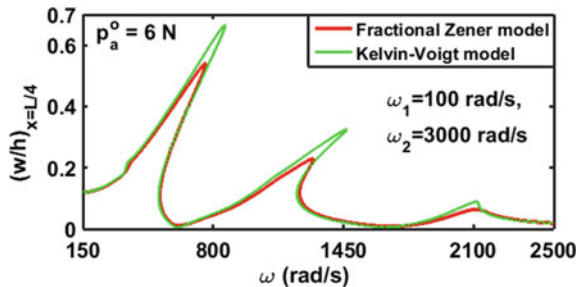


Fig. 4 Comparison of frequency response ($H = 7$) of VS beam using fractional Zener viscoelastic model and Kelvin-Voigt viscoelastic model for the **a** parametric resonance ($p_a^o = 298.23705$ N, $h_v = 4$ mm), and **b** forced resonance ($p_t^o = 6$ N, $h_v = 2$ mm)

under axial periodic load is evaluated by using Kelvin-Voigt model. The corresponding response along with the response evaluated using frequency dependent property (fractional Zener viscoelastic model) are presented in Fig. 4a. Similarly, the frequency response of VS beam under transverse harmonic point load is evaluated using Kelvin-Voigt model by considering a limited frequency range around the natural frequency (100–900 rad/s). The corresponding response along with the response evaluated using frequency dependent property are presented in Fig. 4b. Thus, from the Fig. 4 it can be observed that the effect of frequency dependent property on the forced/parametric resonant response is very less since an equivalent Kelvin-Voigt model provides nearly same response. However, to investigate the same for a wide frequency range (100–3000 rad/s), the frequency response of VS beam under harmonic transverse point load is evaluated using Kelvin-Voigt model and presented in Fig. 5 along with the response evaluated using frequency-dependent property (fractional Zener viscoelastic model). Here, Fig. 5 shows a significantly higher inaccuracy of frequency-independent property (Kelvin-Voigt model) in the representation of resonant peak amplitudes. Thus, from Figs. 4 and 5, it can be concluded that the consideration of frequency-independent property (ie. Kelvin-Voigt model) may be accurately valid when the different properties (ie. parameters of Kelvin-Voigt model parameters) are used around each modal natural frequency.

Fig. 5 Comparison of forced resonant response ($H = 7$) of VS beam in a wide frequency range using Fractional Zener viscoelastic model and Kelvin-Voigt viscoelastic model ($p_t^o = 6$ N, $h_v = 2$ mm)



4 Conclusions

In this work, the effect of frequency-dependent viscoelastic property on the forced/parametric resonant amplitude of viscoelastic sandwich beam is investigated by deriving a reduced-order finite element model (ROM) in frequency domain. The forced and parametric excitations were separately considered by applying transverse harmonic point load and axial periodic load respectively. The frequency-dependent viscoelasticity is modelled using fractional Zener model and the corresponding responses of sandwich beam are compared with that are derived using an equivalent Kelvin-Voigt model. The ROM in frequency domain is derived by implementing harmonic balance method prior to the finite element discretization and reduced-order transformation. Whereas the reduction basis is constructed using first four eigen modes through modal strain energy method and their corresponding static derivatives. The comparison of frequency responses evaluated using ROM and full-order FE model revealed that the ROM with aforesaid reduction basis evaluates the frequency response of frequency-dependent viscoelastic sandwich beam with reasonable accuracy. Further, the frequency dependent viscoelastic property has shown a significant effect on the resonant amplitudes when compared with the frequency-dependent property approximated in a wide frequency range using Kelvin-Voigt model. Thus, the results suggest that the nonlinear frequency response analysis of viscoelastic layered beams using Kelvin-Voigt model may be reasonably accurate when the different model parameters are considered around each modal natural frequency.

References

1. Jacques, N., Daya, E.M., Potier-Ferry, M.: Nonlinear vibration of viscoelastic sandwich beams by the harmonic balance and finite element methods. *J. Sound Vib.* **329**(20), 4251–4265 (2010)
2. Zhu, B., Dong, Y., Li, Y.: Nonlinear dynamics of a viscoelastic sandwich beam with parametric excitations and internal resonance. *Nonlinear Dyn.* **94**(4), 2575–2612 (2018)
3. Reddy, R.S., Panda, S., Gupta, A.: Nonlinear dynamics and active control of smart beams using shear/extensional mode piezoelectric actuators. *Int. J. Mech. Sci.* 106495 (2021)
4. Dwivedy, S.K., Sahu, K.C., Babu, S.: Parametric instability regions of three-layered soft-cored sandwich beam using higher-order theory. *J. Sound Vib.* **304**(1–2), 326–344 (2007)
5. Gupta, A., Panda, S., Reddy, R.S.: Passive control of parametric instability of layered beams using graphite particle-filled viscoelastic damping layers. *Mech. Adv. Mater. Struct.* 1–16 (2021)
6. Gupta, A., Panda, S., Reddy, R.S.: Improved damping in sandwich beams through the inclusion of dispersed graphite particles within the viscoelastic core. *Compos. Struct.* **247**, 112424 (2020)
7. Madeira, J.F.A., Araújo, A.L., Soares, C.M.M., Soares, C.A.M.: Multiobjective optimization for vibration reduction in composite plate structures using constrained layer damping. *Comput. Struct.* **232**, 105810 (2020)
8. Detroux, T., Renson, L., Masset, L., Kerschen, G.: The harmonic balance method for bifurcation analysis of large-scale nonlinear mechanical systems. *Comput. Methods Appl. Mech. Eng.* **296**, 18–38 (2015)

9. Litewka, P., Lewandowski, R.: Steady-state non-linear vibrations of plates using Zener material model with fractional derivative. *Comput. Mech.* **60**, 333–354 (2017)
10. Galucio, A.C., Deü, J.-F., Ohayon, R.: Finite element formulation of viscoelastic sandwich beams using fractional derivative operators. *Comput. Mech.* **33**(4), 282–291 (2004)
11. Rutzmoser, J.: Model order reduction for nonlinear structural dynamics. Doctoral dissertation, Technische Universität München (2018)
12. Touzé, C., Vidrascu, M., Chapelle, D.: Direct finite element computation of non-linear modal coupling coefficients for reduced-order shell models. *Comput. Mech.* **54**(2), 567–580 (2014)
13. Givois, A., Grolet, A., Thomas, O., Deü, J.-F.: On the frequency response computation of geometrically nonlinear flat structures using reduced-order finite element models. *Nonlinear Dyn.* **97**(2), 1747–1781 (2019)
14. Lv, H.-W., Li, L., Li, Y.-H.: Non-linearly parametric resonances of an axially moving viscoelastic sandwich beam with time-dependent velocity. *Appl. Math. Model.* **53**, 83–105 (2018)
15. Ray, M.C., Baz, A.: Control of nonlinear vibration of beams using active constrained layer damping. *J. Vib. Control.* **7**(4), 539–549 (2001)
16. Rouleau, L., Deü, J.-F., Legay, A.: A comparison of model reduction techniques based on modal projection for structures with frequency-dependent damping. *Mech. Syst. Signal Process.* **90**, 110–125 (2017)
17. Rutzmoser, J.B., Rixen, D.J., Tiso, P., Jain, S.: Generalization of quadratic manifolds for reduced order modeling of nonlinear structural dynamics. *Comput. Struct.* **192**, 196–209 (2017)
18. Shih, Y.-S., Yeh, Z.-F.: Dynamic stability of a viscoelastic beam with frequency-dependent modulus. *Int. J. Solids Struct.* **42**(7), 2145–2159 (2005)

Control of Jeffcott Rotor Vibrations Using Model Predictive Control



Abhinav Singh, R. Aashish, and Ashesh Saha 

Abstract In this paper, a Model Predictive Controller (MPC) is proposed to control the nonlinear vibrations of a horizontally supported Jeffcott-rotor system (JRS). MPC systems obtain the control values for the plant by solving an online optimization problem formulated using plant mathematical model and real-time measurements [7]. In the mathematical model of the Jeffcott rotor system, a nonlinear restoring force is considered. The MPC is integrated into the system via two pairs of electromagnetic poles in an active magnetic bearing (AMB). The non-linearity due to electromagnetic coupling is considered in the system model. A block diagram representing the system dynamics is constructed and MPC implementation is done in SIMULINK using MPC design toolbox. Time response and phase plane plots of both the uncontrolled and controlled systems are obtained by numerically integrating the governing differential equations using an in-built ‘ode’ solver in the software package ‘MATLAB’. The comparison of these plots shows significant reduction in steady state vibration amplitude of the controlled system.

Keywords Jeffcott rotor · Model predictive control · Active magnetic bearing

1 Introduction

Vibrations are unavoidable and undesired phenomena in rotating machines. Hence, vibration control becomes a critical task, specifically when operating in super-critical region where rotor excitation due to these vibrations may lead to rotor instability and sudden failure. The advancement in research and development of AMB is phenomenal in recent years to achieve such objectives. AMB system uses electromagnetic forces to support a rotating shaft at its center with no physical contact with stator. A typical AMB system consists of electromagnets, position sensor, power amplifier and controller. A closed loop control system is deployed which receives feedback

A. Singh · R. Aashish · A. Saha (✉)
National Institute of Technology Calicut, Calicut, Kerala 673601, India
e-mail: ashesh@nitc.ac.in

© The Author(s), under exclusive license to Springer Nature Singapore Pte Ltd. 2022
K. C. Popat et al. (eds.), *Advances in Mechanical Engineering and Material Science*,
Lecture Notes in Mechanical Engineering,
https://doi.org/10.1007/978-981-19-0676-3_2

from the position sensors. This feedback is sent to the controller generating the suitable control currents which gets amplified by the power amplifier producing the electromagnetic forces responsible to support and control the vibrations of the rotor.

The Jeffcott rotor is the simplest model consisting of a point mass attached to a massless shaft which can be used to study the flexural behavior of rotors. Despite being an oversimplification of real-world rotors, it retains some basic characteristics and allows us to gain a qualitative insight into important phenomena typical to rotordynamics [1].

The AMB combined with rotor become a highly nonlinear system which makes it difficult to design a control algorithm that provides good robustness and stability. Proportional-integral-derivative (PID) controller is a widely used control scheme for AMB as it requires small computing power to provide a good performance considering the operating point is inside the linear performance range of AMB [2–4]. Various other control methods have been proposed such as Fuzzy control [3], H ∞ [5] and Q-parametrization [6]. However, the drawback of these methods is that they cannot handle constraints which is crucial to ensure the safety of the system. With the development of computational power, it is possible to implement the MPC [7] on AMB which was limited to process industries in past [8]. MPC generates the control signals by solving an online optimization problem using mathematical model of the plant at each time, by considering its future behavior up to a certain fixed number of time steps N called as prediction Horizon. In [9], MPC was proposed to control the AMB system. Different control problems, including reference tracking and disturbance rejection, were considered in simulations and comparisons with a classical PID controller are provided in order to assess the performance of the proposed MPC [9]. The results clearly show that MPC outperforms PID controller.

In this study, vibration control of a horizontally supported nonlinear Jeffcott rotor considering the rotor weight and nonlinear restoring force is proposed. A 4-pole AMB with MPC is used to achieve the control objective. Block diagram of JRS with MPC controller integrated with MPC design Toolbox is developed in MATLAB-SIMULINK. A closed loop control system is designed and controller parameters are tuned by iterative method to obtain the best performance.

2 Nonlinear Jeffcott Rotor Model

The schematic representation of a horizontally supported JRS with 4-pole AMB is shown in Fig. 1. It consists of a rigid disc of mass ' m ' attached at the centre of a massless shaft. The eccentricity e_d between the centre of mass $C(U_e, V_e)$ and the geometric center $G(U, V)$ of the rotor is unavoidable due to different factors like manufacturing defects, disc wear, etc. The shaft rotates at constant rpm of ' ω '. The origin of the coordinate system ' O ' is at the intersection of the bearing axis with the disc.

The equations governing the motions of the JRS along the horizontal and vertical directions subjected to the magnetic forces from the AMB can be written as [10, 11]:

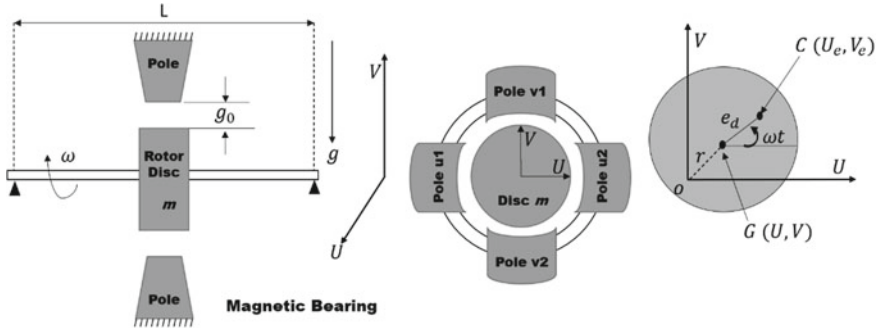


Fig. 1 Schematic diagram of a JRS with 4-pole AMB

$$m\ddot{U} + c_u\dot{U} + k_1U + k_2(U^3 + UV^2) = me_d\omega^2 \cos(\omega\tau) - F_{Mu}, \quad (1)$$

$$m\ddot{V} + c_v\dot{V} + k_1V + k_2(V^3 + VU^2) = me_d\omega^2 \sin(\omega\tau) - mg - F_{Mv}. \quad (2)$$

For further analysis, the coordinate is first shifted to the static equilibrium position $(0, V_{st})$ obtained by setting $\dot{U} = \ddot{U} = \dot{V} = \ddot{V} = 0$ in Eqs. (1) and (2). Subsequently, the dimensionless form of the governing equations is obtained using the dimensionless time $t = \sqrt{\frac{k_1}{m}}\tau$, and the dimensionless displacements $u = \frac{U}{V_{st}}$, and $v = \frac{V}{V_{st}}$ as

$$\ddot{u} + \mu_1\dot{u} + \omega_1^2u + 2\lambda vu + \lambda(u^2 + v^2)u = f\Omega^2 \cos(\Omega t) - F_{Mu}, \quad (3)$$

$$\ddot{v} + \mu_2\dot{v} + \omega_2^2v + \lambda(u^2 + 3v^2) + \lambda(u^2 + v^2)v = f\Omega^2 \sin(\Omega t) - F_{Mv}, \quad (4)$$

where $f = e_d/y_{st}$, $\mu_1 = c_u/\sqrt{k_1m}$, $\mu_2 = c_v/\sqrt{k_1m}$, $\lambda = k_2v_{st}^2/k_1$, $\omega_1^2 = 1 + \lambda$, $\omega_2^2 = 1 + 3\lambda$, $\Omega^2 = m\omega^2/k_1$. The magnetic forces F_{Mu} and F_{Mv} along u and v -directions respectively, can be written as [12]:

$$F_{Mu} = F(u, I_u) = B_o \left\{ \left(\frac{I_o + I_u}{g_o + u} \right)^2 - \left(\frac{I_o - I_u}{g_o - u} \right)^2 \right\}, \quad (5)$$

$$F_{Mv} = F(v, I_v) = B_o \left\{ \left(\frac{I_o + I_v}{g_o + v} \right)^2 - \left(\frac{I_o - I_v}{g_o - v} \right)^2 \right\}, \quad (6)$$

where B_o is the magnetic force constant, I_o is the bias current, g_o is the air gap between the disc and the magnetic poles when the disc is at the center of bearing, and I_u and I_v are control currents in u and v -directions, respectively.

3 Mathematical Formulation of MPC

In this section, the MPC algorithm applied on the nonlinear model of the AMB system [9] is briefly discussed. In MPC, the following finite horizon optimization problem is solved at every sampling instant k [9]:

$$\min_{U_0^N(k)} J_0^N(k), \quad (7)$$

subject to

$$|u_j(k+i|k)| \leq u_{j,max}, i, k \geq 0, j = 1, \dots, m, \quad (8)$$

and

$$|x_l(k+i|k)| \leq x_{l,max}, i, k \geq 0, l = 1, \dots, n, \quad (9)$$

where $J_0^N(k)$ is the objective function, $u_j(k+i|k)$, $x_l(k+i|k)$ are the control input and state vectors, respectively, at the step i of the prediction horizon N at time k . $u_{j,max}$, $x_{l,max}$ are the upper limits for the control input and state vectors, respectively [9].

When the MPC is used to regulate the state of the system from an initial value to the origin, the objective function $J_0^N(k)$ is computed as:

$$J_0^N = \sum_{i=0}^N x(k+i|k)^T Q x(k+i|k) + u(k+i|k)^T R u(k+i|k), \quad (10)$$

where Q and R are positive semi-definite and positive definite symmetric matrices, respectively, which are used to tune control objectives; Q is a state penalty matrix which determines the speed of the state performance and R is an input penalty matrix which sets the control effort [9]. The plant model in (3) and (4) is linearized about plant initial conditions using Taylor series expansion to obtain the following state-space model:

$$\dot{x} = Ax + Bu, \quad (11)$$

$$y = Cx + Du, \quad (12)$$

where A , B , C , D are the state space matrices whose values are provided in the Appendix 1 [6]. This linear model (11) and (12) is then discretized using the implicit trapezoidal rule with a sampling time $T_s = 0.1$ s to obtain the following discrete time linear model as:

$$x(k+1) = A_d x(k) + B_d u(k), \quad (13)$$

$$y(k) = C_d x(k) + D_d u(k), \quad (14)$$

where $A_d = I + T_s A$, $B_d = T_s B$, $C_d = C$, and $D_d = D$. The problem formulated above is solved by MPC in the following stepwise manner:

Initial Requirement: N , A_d , B_d , C_d , D_d , Q , R , initial state x_i .

1. For $k = 0$, assign $x(k) = x_i$
2. Solve (7) to compute $U(k)$
3. Assign $u(k) = 1\text{st element of } U(k)$
4. Apply $u(k)$ on the system (13) and (14) to obtain $x(k+1)$
5. Replace $k = k+1$
6. Repeat from step 2.

The implementation of the MPC in a MATLAB-SIMULINK is explained in the next section.

4 SIMULINK Block Diagram Modelling

The MPC design toolbox is used to design the MPC controller that is implemented on the JRS through a 4-pole AMB configuration. Closed loop control system as shown in Fig. 2 consists of a JRS plant enclosing the dynamics of magnetic bearing integrated with Jeffcott rotor. It receives input control signals from the MPC block and provides position and rate of change of position of the rotor as an output. The rotor positions are sent back as feedback to the MPC block, making it a MIMO (Multiple Input Multiple Output) plant.

The MPC block takes reference signal as input and calculates the control currents for the rotor to track the reference signals. These control currents generate suitable electromagnetic forces to control the vibrations of the rotor. The internal details of

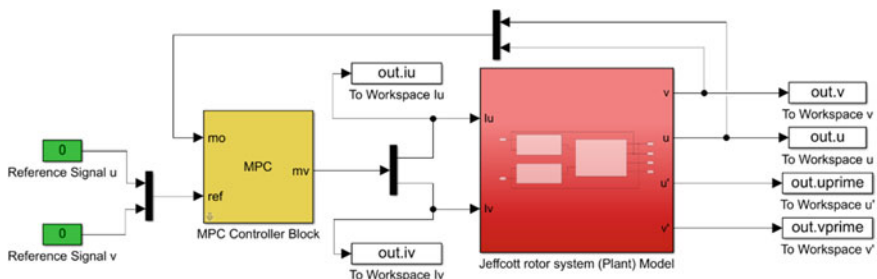


Fig. 2 SIMULINK block diagram of the entire system consisting of the MPC controller block and Jeffcott rotor system (plant) model

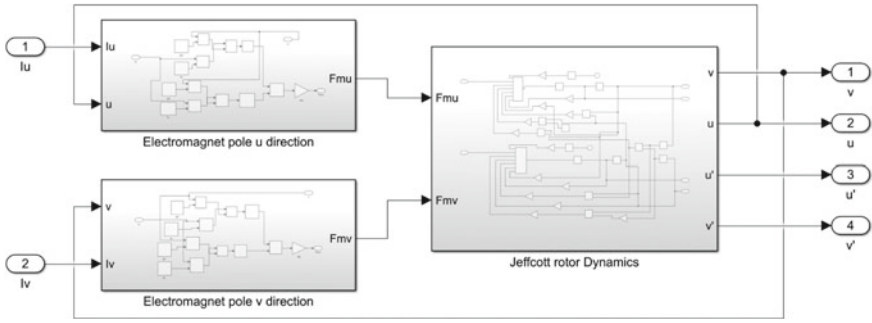


Fig. 3 SIMULINK block diagram of Jeffcott rotor system (plant) model, a subsystem of Fig. 2

JRS are shown in Fig. 3. Further details of the three subsystems in Fig. 3, i.e. the electromagnet pole in u and v -directions and Jeffcott rotor dynamics are provided in Figs. 8 and 9 in Appendix 2. The other parameter values related to Eqs. (5) and (6) are depicted Fig. 8.

5 Results and Discussion

The time-displacement responses of the uncontrolled JRS along the horizontal and vertical directions obtained by numerically simulating Eqs. (3) and (4) are shown in Fig. 4. The parameter values of the JRS used for simulation are $\lambda = 0.05$, $\Omega = 0.974$, $\mu_1 = 0.0154$, $\mu_2 = 0.0247$, $f = 0.045$ [10, 11]. The same set of parameter values are used for further analysis. The time-displacement response plots in Fig. 4

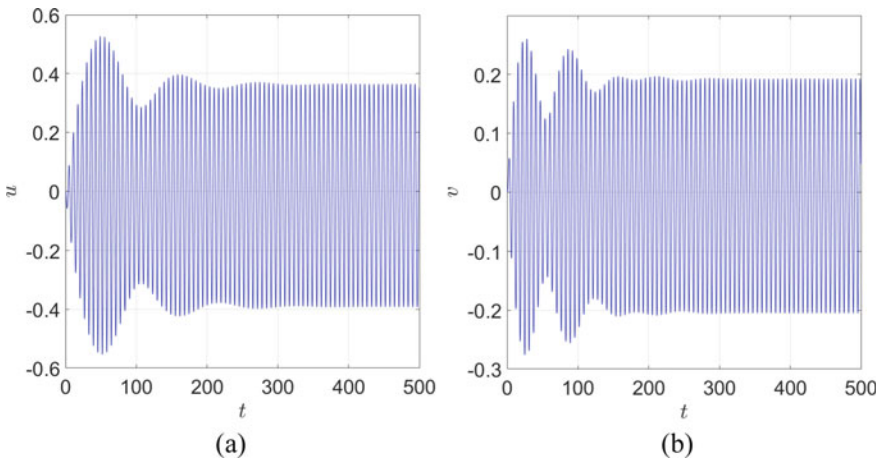


Fig. 4 Time response of **a** horizontal, **b** vertical oscillations of the rotor without MPC

reveal that the uncontrolled system has high transient state and higher settling time and it takes around 300 s to attain steady state condition. Moreover, the vibration amplitude changes drastically in the transient state. The steady-state vibration amplitude for horizontal oscillation (around 0.38) is higher than the amplitude of vertical oscillation (around 0.2). This is because of the higher value of damping considered along vertical direction in the analysis in comparison to that along horizontal direction ($\mu_2 > \mu_1$).

Now to accomplish the primary objective of controlling the vibration of the Jeffcott rotor, we simulate the plant by implementing the MPC and observe its performance in terms of the settling time and steady state vibration amplitude. To do this, the output from MPC controller is connected with input to the plant, and the response of the plant measured at output port is sent back to MPC. Reference signal is set to (0,0). Simulation time is 500 s, sampling time is set to 0.01 s with control horizon of 2 and prediction horizon of 12. The time-displacement responses of the MPC controlled system along the horizontal and vertical directions are shown in Fig. 5. It is clear from these plots that the transient state is almost eliminated and settling time is significantly reduced as compared to the uncontrolled rotor. The matrices in Eqs. (11) and (12) obtained from SIMULINK are given in Appendix 2.

The phase plane diagrams of the MPC controlled system are compared with those for the uncontrolled system in Fig. 6. The transients are removed from these figures. The efficacy of the controller is evident from these figures as the phase plane diagrams are appearing as dots in comparison to those for the uncontrolled system.

In Fig. 7, the control currents generated by the MPC controller are shown as a function of time. These are generated by the MPC controller to minimize the vibration amplitude. It is observed from Fig. 7 that MPC is optimizing the control currents in such a way that the range are almost the same in both the directions. In order to

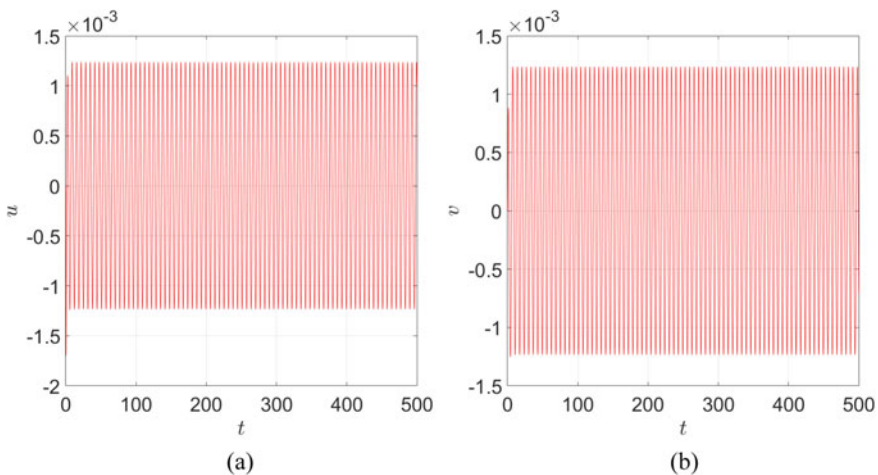


Fig. 5 Time response of **a** horizontal, **b** vertical oscillations of the rotor with MPC

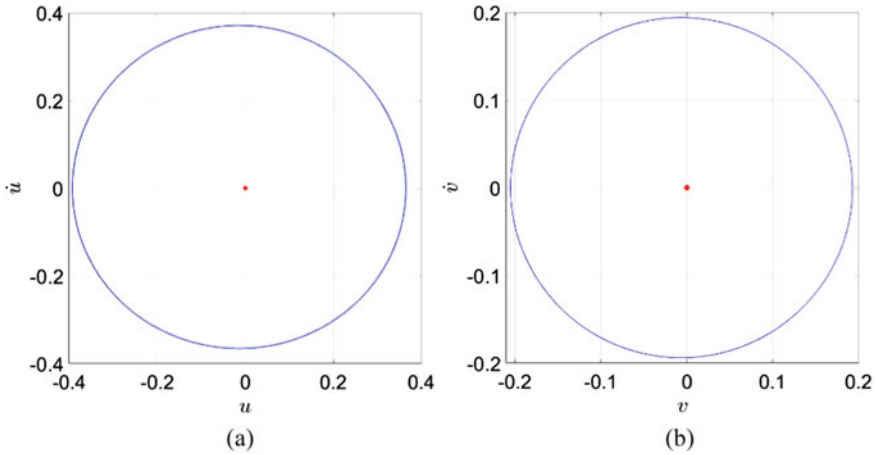


Fig. 6 Phase plane plot of **a** horizontal, **b** vertical oscillations of the rotor (Blue: without MPC, Red: with MPC)

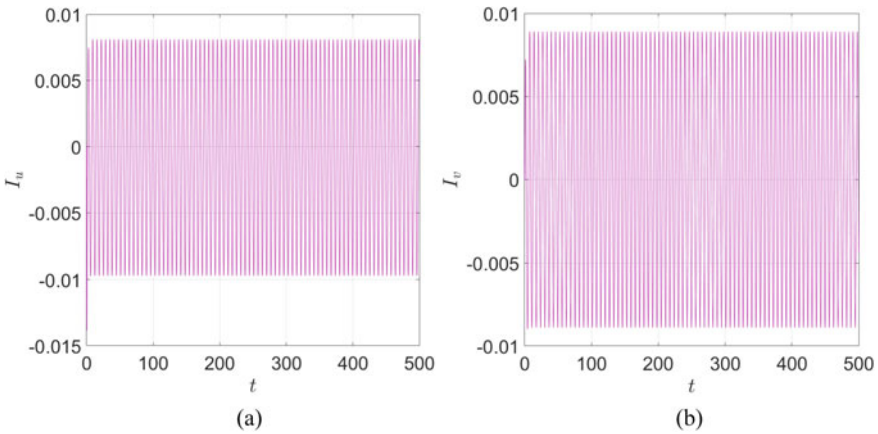


Fig. 7 Plot of control current versus time in **a** horizontal, **b** vertical directions

avoid actuator saturation, suitable constraints can be applied to MPC in the designer application.

6 Conclusion

The efficacy of a model predictive control (MPC) applied though a 4-pole active magnetic bearing (AMB) in controlling the vibrations of a horizontally supported nonlinear Jeffcott rotor system is analysed in this paper. The fundamentals of the MPC

are discussed briefly. The implementation of the MPC design toolbox in MATLAB-SIMULINK is discussed in detail wherein all the block diagrams are presented. The time displacement responses of the uncontrolled system show lower steady state vibration amplitude along vertical direction in comparison to that along the horizontal direction. This is because of our choice of higher value of damping along the vertical direction for the analysis. Comparing the results of the controlled system with those for the uncontrolled system, the MPC is found to be quite effective in controlling the vibrations of the JRS. The phase plane diagrams for the controlled system look like points in comparison to that for the uncontrolled system. It may appear from this comparison that a complete quenching of vibrations is achieved by the use of MPC.

Acknowledgements This work has been supported by DST SERB-SRG under Project File no. SRG/2019/001445 and National Institute of Technology Calicut under Faculty Research Grant.

Appendix 1

The State space matrices of the linearized plant model computed are as follows:

$$A = \begin{bmatrix} 1.5328 & 11.5919 & -8.5504e^{-05} & -0.0020 \\ 0.0071 & 1.5364 & -2.6798e^{-06} & -8.5610e^{-05} \\ 8.5504e^{-05} & 0.0020 & 1.5310 & 11.5730 \\ 2.6798e^{-06} & 8.5585e^{-05} & 0.1171 & 1.5356 \end{bmatrix},$$

$$B = \begin{bmatrix} -2.3430 & 5.3596e^{-05} \\ -0.1084 & 1.2981e^{-06} \\ -5.359e^{-05} & -2.3415 \\ -1.2981e^{-06} & -0.1084 \end{bmatrix}, C = \begin{bmatrix} 0 & 1 & 0 & 0 \\ 0 & 0 & 0 & 1 \end{bmatrix}, D = \begin{bmatrix} 0 & 0 \\ 0 & 0 \end{bmatrix}.$$

Appendix 2

The electromagnet poles shown in Fig. 8 convert the input control currents into electromagnetic forces which are applied on the Jeffcott rotor model shown in Fig. 9.

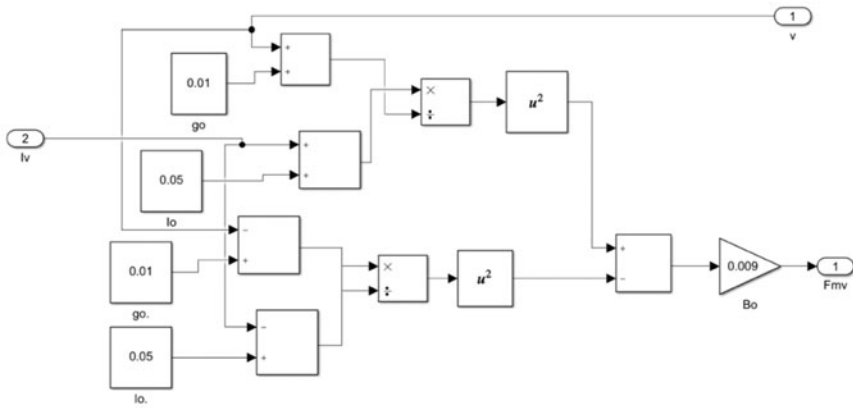
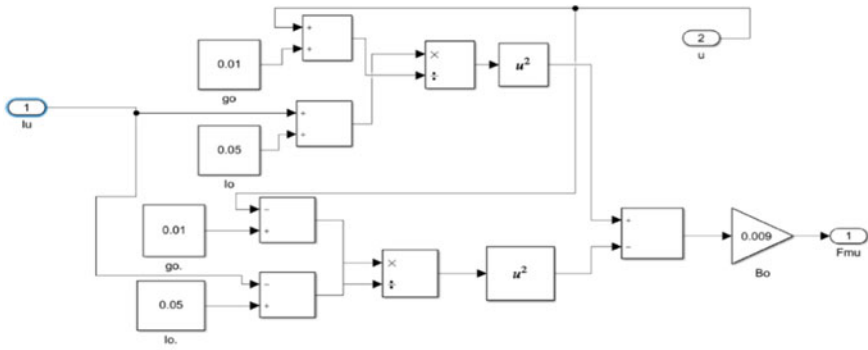


Fig. 8 SIMULINK block diagram of electromagnet pole **a** in u and **b** in v directions

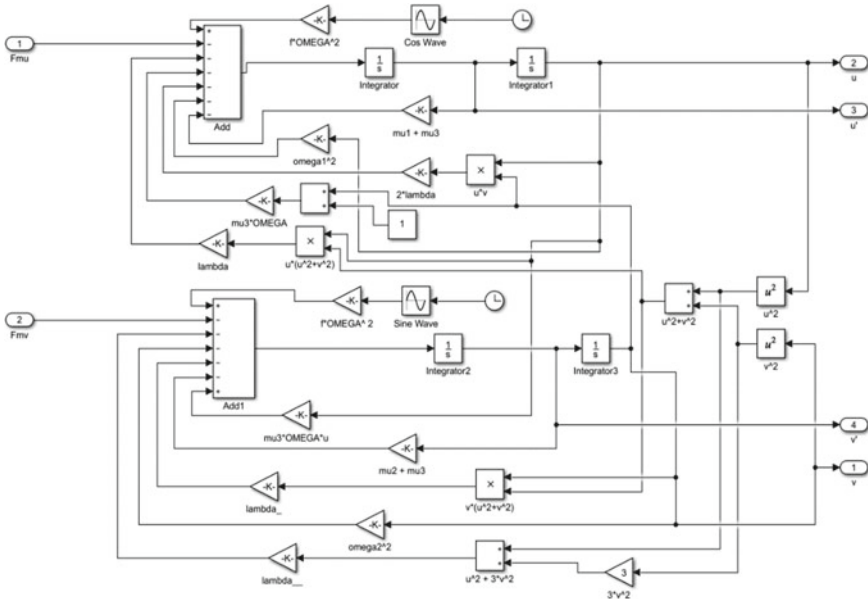


Fig. 9 SIMULINK block diagram of Jeffcott rotor dynamics

References

1. Genta, G.: Dynamics of Rotating Systems. Springer, USA (2005)
2. Xu, L., Zhang, J., Yu, T.: Design and implementation of magnetic bearing based on H_∞ theory. *Zhongguo Jixie Gongcheng/China Mech. Eng.* **17**(10), 1060–1064 (2006)
3. Chen, K., Tung, P., Tsai, M., Fan, Y.: A self tuning fuzzy PID-type controller design for unbalance compensation in active magnetic bearing. *Expert Syst. with App.* **36**, 8560–8570 (2009)
4. Yang, Y., Wang, H., Guo, L., Fan, M.: Control parameter tuning of magnetic bearing PID controller based on expansion coefficient critical proportion. *App. Mech. Mat.* **150**, 24–29 (Trans. Tech. Publications, Switzerland) (2012)
5. Peng, C., Fang, J., Xu, X.: Mismatched disturbance rejection control for voltage-controlled active magnetic bearing via state-space disturbance observer. *IEEE Trans. Power Elect.* **30**(5), 2753–2762 (2014)
6. Mohamed, A.M., Busch-Vishniac, I.: Imbalance compensation and automation balancing in magnetic bearing systems using the q-parameterization theory. *IEEE Trans. Cont. Syst. Tech.* **3**(2), 202–211 (1995)
7. Maciejowski, J.M.: Predictive Control: With Constraints. Pearson Education (2002)
8. Sivakumar, R., Mathew, S.: Design and development of model predictive controller for binary distillation column. *Int. J. Sci. Res. (IJSR)* **5**(12), 445–451 (2014)
9. Morsi, A., Ahmed, S.M., Mohamed, A.M., Abbas, H.S.: Model predictive control for an active magnetic bearing system. In: *IEEE Int. Conf. on Ind. Engg. and App.*, pp. 715–720 (2020)

10. Saeed, N.A., El-Gohary, H.A.: On the nonlinear oscillations of a horizontally supported Jeffcott rotor with a nonlinear restoring force. *Non-Lin. Dyn.* **88**(1), 293–314 (2016)
11. Saeed, N.A., Kamel, M.: Nonlinear PD-controller to suppress the nonlinear oscillations of horizontally supported Jeffcott-rotor system. *Int. J. Non-Lin. Mech.* **87**, 109–124 (2016)
12. Bleuler, H., Cole, M., Keogh, P., Larssonneur, R., Maslen, E., Nordmann, R., Okada, Y., Schweitzer, G., Traxler, A.: *Magnetic Bearings Theory, Design, and Application to Rotating Machinery*. Springer, Berlin Heidelberg (2009)

On the Chaotic Behavior of Coupled Friction-Induced Oscillators Subjected to Base-Excitation



Jithin Velayudhan , M. D. Narayanan, and Ashesh Saha

Abstract The transition of synchronization behavior in a coupled friction-induced oscillators during its route to chaos is investigated in this paper. The coupled system consists of two cantilever beams attached with tip-masses and subjected to base excitations. Each tip-mass is in nonlinear frictional contact with a rotating rigid disc. A linear spring connecting the tip-masses provides the coupling for the system. Modal analysis is employed to reduce the partial differential equation governing the motion of the system to a set of ordinary differential equations. A bifurcation study is conducted for the coupled system wherein the base excitation frequency is considered as the bifurcation parameter. A transition from periodic to chaotic behavior through a quasiperiodic route with multiperiodic windows is observed for the coupled system. In this work, we report the numerical observations of synchronous behavior between two friction-induced oscillators exhibiting such a transition. The synchronization behavior is characterized using the linear time correlation coefficient between the time displacement responses of the two systems. During the quasiperiodic route to chaos, the coupled system undergoes for a transition from synchronized periodicity to a state of desynchronized chaos. Poincaré maps are plotted to identify the periodic, quasiperiodic and chaotic behaviour of the coupled system. The qualitative nature of the oscillations is further confirmed by plotting the time responses and the phase plane diagrams for each tip-mass. Fast Fourier Transform of the time displacement response is obtained to determine the fundamental frequencies and the harmonics of the tip-mass motions.

Keywords Friction-induced oscillator · Modal analysis · Bifurcation · Quasiperiodic route · Chaos

J. Velayudhan (✉) · M. D. Narayanan · A. Saha
National Institute of Technology, Calicut, Kerala 673601, India
e-mail: jithin_p170020me@nitc.ac.in

© The Author(s), under exclusive license to Springer Nature Singapore Pte Ltd. 2022
K. C. Popat et al. (eds.), *Advances in Mechanical Engineering and Material Science*,
Lecture Notes in Mechanical Engineering,
https://doi.org/10.1007/978-981-19-0676-3_3

1 Introduction

Friction and friction-induced vibrations are serious problems in most of the machineries such as: machine tool chatter, squeal in rail wheels and brake systems, vibration in water lubricated bearings, vibration in electric equipment such as motor drive etc. These vibrations may bring down the performance of the machines, cause wear and damage to surfaces in contact, fatigue failure to the moving parts, unwanted noise etc. Studies on the friction-induced vibration and its dynamics in automobile brake system have received good attention by many researchers during the last few decades. The system considered in this paper consists of two cantilever beams coupled together subjected to base excitation. Each cantilever beam is attached with a tip mass which is in a nonlinear frictional contact with a rotating rigid disc. The objective of this work is to numerically investigate the dynamics involved in the route to chaotic behavior of the coupled beam system. This involves, determining the route and bifurcations leading to the formations of chaotic oscillations in the coupled system and to study the synchronization characteristics of the coupled oscillations along the route to chaos.

The dynamics and the physics involved in friction-induced vibration and the related ensuing phenomena are extensively reviewed by Ibrahim [1, 2]. Reference [1] is devoted to address the friction aspects and contact mechanics between the sliding surfaces and [2] provides a detailed review of research activities and important aspects in friction related classical applications in industry. Friction-induced vibrations and the resultant noise issues occurring in disc brake system of automobiles have gathered much attention of many engineers [3–6] since last many years. Dunlap et al. in [3] discussed few experimental and analytical methods to limit the occurrence of automotive disc brake noise. Automotive Noise, Vibration and Harshness (NVH engineering) is reviewed in detail by Qatu et al. in [4]. Ghazaly et al. [5] reviewed the squealing phenomenon in automotive brake system to gain knowledge on stick-slip, sprag-slip, modal coupling and hammering excitation mechanism. However, the review paper by Kinkaid et al. suggests based on their experimental findings that, squealing noise is due to the mode coupling phenomenon and the vibrations of the disc, brake calipers and the pad.

There are many established instability mechanisms to reveal the complex dynamics behind the friction-induced oscillation. This includes the drooping characteristics of the friction force [7, 8], mode coupling phenomena [9, 10], kinematic sprag-slip mechanism [11, 12] etc. Thomsen in [8] developed analytical expressions for the traditional mass-on-moving-belt model to predict the self-excited oscillations with and without the presence of external excitation force. The way in which the linear structural viscous damping affects the spectral characteristics of the instability due to the mode coupling phenomena is discussed by Hoffmann and Gaul in [9]. Kang et al. [10] proposed an analytical method to determine the instability due to the doublet mode in a thin disc with a finite contact area. The mechanism of sprag-slip in an elastic beam sliding over a rigid belt is investigated by Hoffmann and Gaul in [11]. The instability due to the spragging mechanism in a mass-on-moving-belt

model is investigated by Kang et al. [12]. A non-smooth friction-induced oscillator with excitation is modelled as a single-degree-of-freedom system consists of a mass resting on a moving belt in [13] and the rich bifurcation behavior observed is compared with experimental results. The interaction between the brake pad and the disc is studied by Shin et al. [14] by considering the brake system as a two degree-of-freedom model. Different continuous system models are also developed to study the dynamics behind the friction-induced vibration. Popp and Stelzer investigated the friction-induced vibrations in two continuous systems in [15]: one is a cantilever beam and another one is a centrally fixed plate and they reported the presence of rich bifurcational and chaotic behavior. The dynamics of an elastic system rotating around an annular disc is investigated by Ouyang et al. [16] in which the instability occurs due to the drooping friction characteristics.

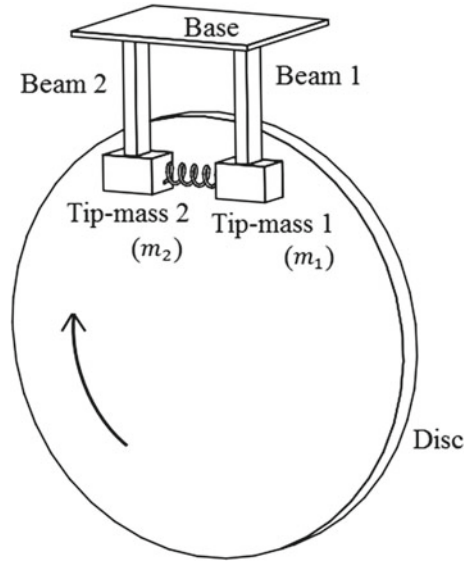
Nakae et al. [7] conducted an experimental work on a mountain bike disc brake in which the drooping characteristics of the friction force between the brake pad and the disc is found to be the reason for the vibration and the ensuing squealing phenomena. Motivated by this work, Saha et al. [17] studied such vibrations in a continuous system model consists of a cantilever beam with a tip mass which is in contact with rotating rigid disc. In our previous work [18] the continuous model considered in [17] is extended by considering two cantilever beams coupled via a linear spring subjected to base excitation. In that paper, we extensively studied the dynamics of synchronization in coupled friction-induced oscillators and reported the presence of chaotic behavior also. The present work is motivated by the chaotic behavior of coupled cantilever beams with tip-masses reported in [18]. To the best of author's knowledge, other than studies on coupled discrete friction oscillators [19, 20] no works on coupled continuous oscillators is reported in literature. The work reported in this paper examines the route and bifurcation to the formation of chaotic oscillations in coupled cantilever beams attached with end masses subjected to base excitation [18].

The mathematical modeling and the derivation of the ordinary differential equations governing the motions are explained very briefly in Sect. 2. The route and bifurcations leading to the formation of chaotic oscillation is described in Sect. 3. The dynamics of synchronization in terms of linear correlation factor between time displacement responses is reported in Sect. 4. Section 5 is devoted in detailing some conclusions drawn from the numerical analysis.

2 Mathematical Modeling

The physical system considered for the study of chaotic behavior in coupled friction-induced oscillators is shown in Fig. 1 [18]. The coupled system consists of two cantilever beams attached with end masses and both the beams are subjected to base excitation also. Each tip-mass are in frictional contact with a rotating rigid disc and this nonlinear frictional force makes the coupled beam system highly nonlinear. The coupling between the two subsystems is done via a linear spring connecting between

Fig.1 Coupled beams [18]



the tip-masses. The focus of this study is to analyze only the bending vibrations of the beams. There are some other assumptions also involved while developing the mathematical model such as both the torsional as well as the bending vibrations and the wobbling motions of the disc are neglected in this study.

Figure 2 represent the schematic diagram of the physical system considered in this paper. An excitation force Y_{si} in the form of $B_i \sin(\omega t)$, where B_i is the amplitude and

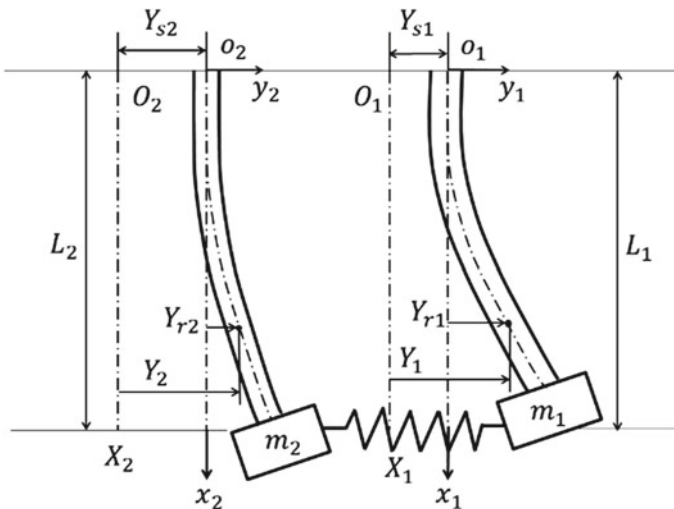


Fig.2 Schematic diagram of the system [18]

ω is the excitation frequency, is acting at the base of each beam. Here 'i' represents the i th beam with $i = 1$ or 2 . As shown in Fig. 2, the total deflection of the i th beam from the axis $O_i X_i$ can be written as,

$$Y_i(X, T) = Y_{ri}(X, T) + Y_{si}(T), \quad (1)$$

where X and T are the spatial and temporal coordinate respectively. In Eq. (1) $Y_{ri}(X, T)$ represents the relative deflection of the beam with respect to the axis $O_i x_i$ which represents the moving frame. Next, the partial differential equation representing the motion of the i th beam can be written as follows,

$$EI \frac{\partial^4 Y_i(X, T)}{\partial X^4} + \rho A \frac{\partial Y_i(X, T)}{\partial T^2} = 0, \quad (2)$$

where E , I , ρ and A are the modulus of elasticity, area moment of inertia, mass density and the cross sectional area of the cantilever beam respectively. There are four different boundary conditions associated with the i th beam which can be expressed mathematically as:

$$(i) \text{ at } X = 0, Y_{ri}(0, T) = 0, \quad (3a)$$

$$(ii) \text{ at } X = 0, \frac{\partial Y_{ri}}{\partial X} = 0, \quad (3b)$$

$$(iii) \text{ at } X = L, \frac{\partial^2 Y_{ri}}{\partial X^2} = 0, \text{ and} \quad (3c)$$

$$(iv) \text{ at } X = L, m_i \frac{\partial^2 Y_{ri}}{\partial T^2} - EI \frac{\partial^3 Y_{ri}}{\partial X^3} = F_i^* \mu(V_i) - m_i \frac{d^2 Y_{si}}{dT^2} - K \delta X. \quad (3d)$$

In Eq. (3d), m_i is the mass of the tip-mass, F_i^* is the normal load acting on the tip-mass, V_i is the relative velocity between the tip-mass and the rigid disc, and $K \delta X$ is the restoring spring force, where K is the spring constant and δX is the spring deflection. L_i is the length of the i th beam (here $L_1 = L_2$). The modal analysis is employed to reduce the partial differential equations governing the motions of the beams into set of ordinary differential equations. The non-dimensional quantities used to convert the governing equations (Eq. 2) and the boundary conditions (Eqs. 3a–3d) into dimensionless forms, are shown below,

$$x_i = \frac{X_i}{L}, y_i = \frac{Y_i}{L}, y_{ri} = \frac{Y_{ri}}{L}, y_{si} = \frac{Y_{si}}{L}, k_n = \frac{K}{m\Omega^2}, t = \Omega_n T,$$

$$\Omega_n = \sqrt{\frac{EI}{\rho AL^4}}, r_{mi} = \frac{\rho AL}{m_i}, F_{0i} = \frac{F_i^*}{m_i \Omega_n^2 L}, R_m = \frac{r_{m1}}{r_{m2}}, v_i = \frac{V_i}{\Omega_n L}, \delta x = \frac{\delta X}{L}, \Omega = \frac{\omega}{\Omega_n}.$$

where r_{mi} is the mass ratio of the i th beam and R_m is the ratio of mass ratios. The nonlinear friction contact between the tip-mass and the disc is modeled using the polynomial friction model [8] which is expressed as follows:

$$\mu(v_i) = \mu_s \text{sgn}(v_i) - \frac{3}{2}(\mu_s - \mu_m) \left(\frac{v_i}{v_m} - \frac{1}{3} \left(\frac{v_i}{v_m} \right)^3 \right). \quad (4)$$

In Eq. (4), v_i , μ_s , and v_m are the non-dimensional relative velocity between the disc and the tip-mass, the coefficient of static friction and the velocity corresponds to the minimum coefficient of kinetic friction (μ_m) respectively. According to modal analysis, the modal solution can be written as a variable separable from as:

$$y_{ri}(x, t) = \sum_{j=1}^n \phi_{ij}(x) y_{ij}(t). \quad (5)$$

As mentioned in Sect. 2, this paper conducts a numerical study on the route to chaotic behavior of the same physical system considered in the author's previous work [18]. The ordinary differential equation governing the motion of the i th beam corresponding to the k th mode of the coupled beam system shown in Fig. 1 is obtained using the modal analysis [18] is expressed mathematically as,

$$\frac{d^2 y_{rik}}{dt^2} + f_{ik}^4 y_{rik} = \frac{\phi_{ik}(1)}{r_{mi}} (F_{0i} \mu(v_r) + k_n \delta x_i) - \frac{d^2 y_{si}}{dt^2} \left(\frac{\phi_{ik}(1)}{r_{mi}} + \int_0^1 \phi_{ik}(x) dx \right), \quad (6)$$

where f_{ik} is the natural frequency of the i th beam corresponding to the k th mode. It is to be noted that only the important aspects and steps involved in the modal analysis in developing the governing equations in ordinary differential form is shown in this paper: one can refer author's previous work [18] or [17] to get a complete understanding about the procedures and steps involved in modal analysis. Another thing to be noted that all the quantities used in the numerical analysis is in the dimensionless form.

3 Results and Discussion

In what follows, the numerical analysis and results associated with the route to chaotic behavior of the coupled beam-tip mass system is discussed. It is to be noted that,

Table 1 Numerical values assigned to the parameters

r_{m1}	r_{m2}	$v_{d1} = v_{d2}$	$B_1 = B_2$	μ_s	μ_m	v_m	F_{01}	F_{02}	k_n
0.2	0.22	0.05	0.05	0.4	0.25	0.2	0.02	0.022	0.03

such models with cantilever beams attached with end-mass which is in contact with a rotating disc are developed to study the dynamics of friction-induced vibration and the ensuing phenomena in disc brake systems [17]. The focus of such studies is only to analyze the behavior of the tip-mass motion. In this paper also the dynamics of the route to chaotic behavior of such coupled masses attached at the end of two cantilever beams is analyzed. This involves the study of bifurcations and route leading to the birth of chaotic orbits in the coupled system of beams. Moreover, the dynamical changes occurring in terms of synchronous behavior between the tip-masse motions during the way to chaos is also addressed. It is known that, the strength of synchronization between two motions are considered as strong when $-1 \leq C_c \leq -0.8$ or $0.8 \leq C_c \leq 1$ and as average when $-0.8 < C_c < -0.5$ or $0.5 < C_c < 0.8$ [21]. For Any values of C_c other than the above mentioned, the motions are considered to be not synchronized. The aforementioned analyses are discussed in detail in the following subsections. Numerical values assigned for the parameters are shown in Table 1.

3.1 Bifurcation: Quasiperiodic Route to Chaos

Numerical simulation is carried out for the set of parameter values shown in Table 1, to obtain the bifurcation diagram for the coupled beam-tip mass system. The bifurcation diagrams obtained for the two tip-masses are found to be qualitatively the same possessing the same bifurcations and the route to chaos. Bifurcation diagrams of each tip-mass behavior are obtained using the dimensionless base excitation frequency (Ω) as the bifurcation parameter are shown in Figs. 3 and 5. The zero velocity crossing

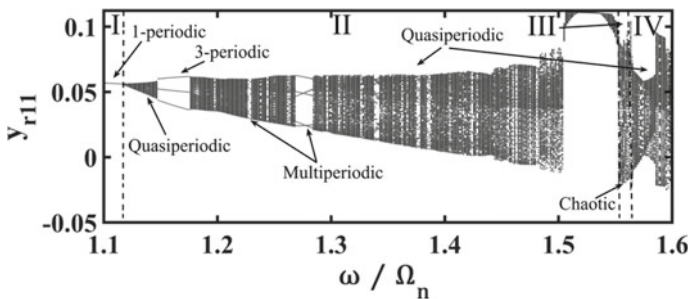


Fig. 3 Bifurcation diagram of tip-mass 1 ($r_{m1} = 0.2$). Parameters: $r_{m2} = 0.22, k_t = 0.03$, I—Period one, II—Multi and Quasiperiodic, III—Chaotic and IV—Quasiperiodic region

(from ‘+’ to ‘-’) of the tip-mass oscillation is considered here as the Poincaré section and the corresponding displacement value is taken as the Poincaré point to plot the bifurcation diagram.

The bifurcation diagrams shown in Figs. 3 and 5 corresponding to tip-mass 1 and 2 respectively have basically four different regions: (I) Single periodic, (II) Quasiperiodic with multi-periodic windows, (III) Chaotic and (IV) Quasiperiodic. The single periodic nature of tip-mass 1 in region-I is further conformed by plotting the corresponding phase plane diagram along with the Poincaré map and the frequency spectrum shown in Fig. 4 for one set of parameter values from this region. The phase plane diagram shown in Fig. 4a-I is found to be a closed loop curve with one Poincaré point on it. Presence of a single dominant frequency and its harmonics is observed in the frequency spectrum shown in Fig. 4b-I. As the bifurcation parameter value increases, a sudden abrupt transition from periodic to quasiperiodic nature is occurred at $\Omega = 1.116$. One such quasiperiodic behavior corresponding to a set of parameters at $\Omega = 1.47$ is plotted in Fig. 4-III. The closed curve structure of the Poincaré points in the phase plot shown in Fig. 4a-III and the presence of incommensurate frequency components in Fig. 4b-III further substantiate the quasiperiodic behavior of the oscillation. At $\Omega = 1.15$, a three periodic orbit is born through bifurcation and at $\Omega = 1.18$, it is again changed back to quasi-period oscillation. At $\Omega = 1.27$, the motion is converted into a five periodic oscillation which is demonstrated in the phase plane plot with five closed loops with five Poincaré points as shown in Fig. 4a-II. In the similar way presence of many multi-periodic windows in the quasiperiodic region is observed. Later, a new quasiperiodic orbit is born at $\Omega = 1.29$ and finally at $\Omega = 1.553$, the coupled system started showing chaotic behavior. The phase plane plot and the frequency spectrum corresponding to the chaotic motion are shown in Fig. 4a-IV and 4b-IV respectively. The Poincaré points are scattered in the phase plane diagram shown in Fig. 4a-IV and the presence multiple frequency components in the frequency spectrum plot in Fig. 4b-IV substantiate the chaotic nature of the motion. Both the coupled beams again regain the quasiperiodic behavior around at $\Omega = 1.56$.

Phase plane diagrams and the frequency spectrums of the second tip-mass motions corresponding to the different regions in its bifurcation diagram (Fig. 5) are shown in Fig. 6a (I-IV) and 6b (I-IV) respectively for the same set of parameter values used in Fig. 4. The time displacement responses of the tip-masses corresponding to the parameter values used in Figs. 4 and 6 are plotted in Fig. 7.

It is understood from the above analysis that, both the tip-masses follow the same route leading to the formation of chaotic behavior. It is evident from the bifurcation analysis that the chaotic orbits are born in the coupled system considered in Fig. 1 from period one orbit through a quasiperiodic route. The quasiperiodic route to chaos in the coupled system is much complex which involves multiple bifurcations such as periodic to quasiperiodic, a series of interchanging between quasiperiodic and multi-periodic nature and finally chaotic behavior from the quasiperiodic orbit.

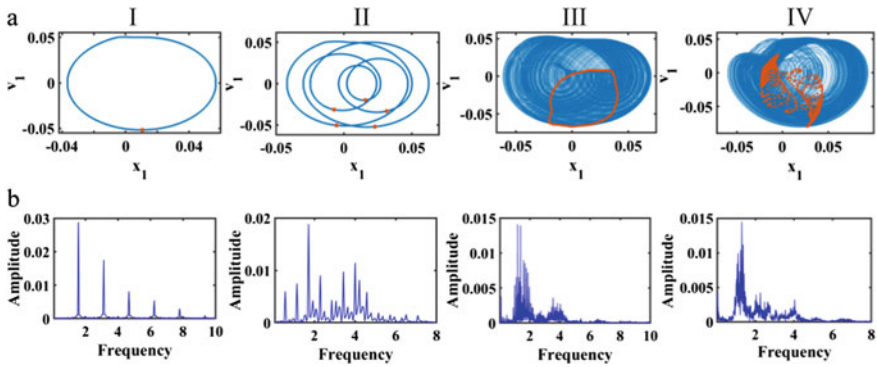


Fig. 4 **a** Phase plots and **b** Frequency spectrum plots of tip-mass 1 ($r_{m1} = 0.2$). (I) Single periodic, (II) Multi-periodic, (III) Quasiperiodic and (IV) Chaotic

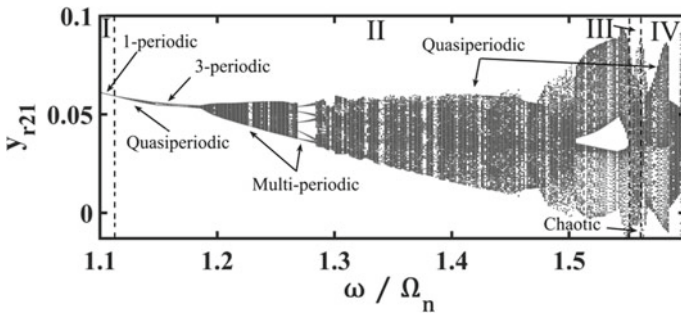


Fig. 5 Bifurcation diagram of tip-mass 2 ($r_{m2} = 0.22$). Parameters: $r_{m1} = 0.2, k_f = 0.03$, I—Period one, II—Multi and Quasiperiodic, III—Chaotic and IV—Quasiperiodic region

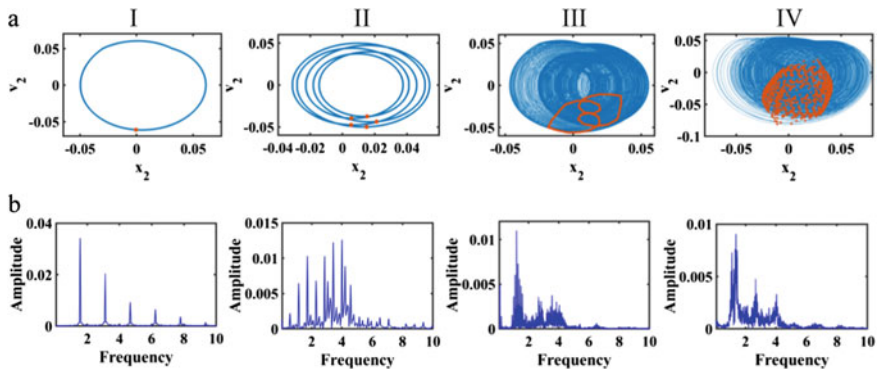


Fig. 6 **a** Phase plots and **b** Frequency spectrum plots of tip-mass 2 ($r_{m2} = 0.22$). (I) Single periodic, (II) Multi-periodic, (III) Quasiperiodic and (IV) Chaotic

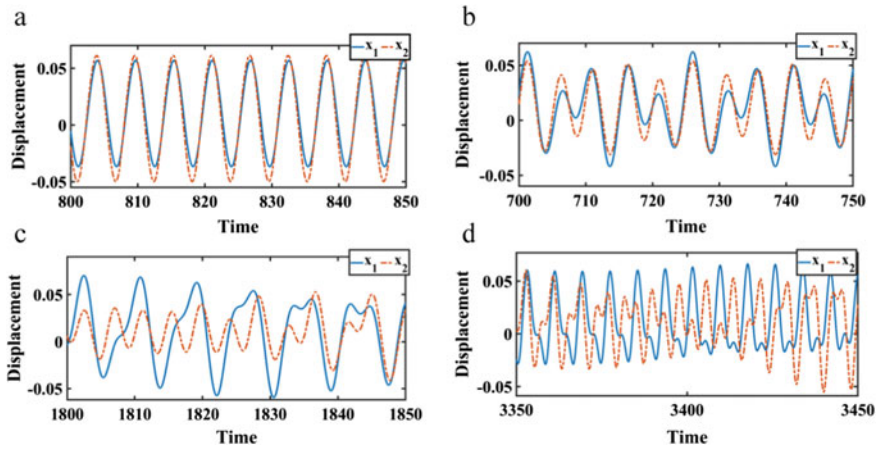


Fig. 7 Time displacement responses of tip-mass 1 and tip-mass 2 for **a** single periodic ($\Omega = 1.1$), **b** multi-periodic ($\Omega = 1.27$), **c** quasiperiodic ($\Omega = 1.47$) and **d** Chaotic ($\Omega = 1.553$) dynamics. x_1 is for tip-mass 1 (solid line) and x_2 is for tip-mass 2 (dotted line)

3.2 Characterization of Synchronization Behavior on the Route to Chaos

The dynamics of synchronization between the coupled tip-mass motions is studied all along the route from single periodic to chaotic behavior. As previously mentioned,

in this quasiperiodic route to chaos, presence of multi-periodic windows in the bifurcation diagram at many places is observed. How far the oscillations are synchronized each other in the different regions of the bifurcation diagram is determined by evaluating the time correlation factor (C_c) between the time displacement responses of the coupled tip-masses. The coupled system is numerically simulated for a particular set of parameters corresponding to different regions in the bifurcation diagram and the correlation between the tip-mass motions are evaluated. The correlation values obtained for the oscillations corresponding to the different regions are summarized in Table 2. It is understood from Table 2 that a strong correlation is observed in the single periodic as well as the multi and quasiperiodic regions implying the presence of synchronous motion of the coupled system. The correlation factor is dropped abruptly to 0.45 from a strong correlation value at $\Omega = 1.553$ where exactly the bifurcation to the chaotic region occurred. The coupled beams maintain this low correlation between their oscillations throughout in the chaotic region implying the absence of the synchronous motion.

It is to be noted that, for all the parametric combinations in the periodic, quasiperiodic and multiperiodic regions, the coupled oscillations are found to be synchronized. Moreover, a state of desynchronized chaos is observed for all the parametric values in the chaotic region. It is clear from the numerical analysis conducted that, the coupled

Table 2 Correlation factor between oscillations in different regions in the bifurcation diagram

Ω	1.1	1.15	1.2	1.228	1.261	1.27	1.32	1.542	1.553
Periodicity	1	3	Quasiperiodic	8	Quasiperiodic	5	Quasiperiodic	Quasiperiodic	Chaotic
C_c	0.97	0.83	0.94	0.95	0.94	0.91	0.89	0.87	0.45

beam system has gone through a transition from a state of periodic synchronization to a state of desynchronized chaos while undergoing a quasiperiodic route to chaos.

4 Conclusions

Numerical investigation on the route to chaotic behavior of a coupled friction-induced oscillator is conducted. The physical system under consideration consists of two coupled cantilever beam with end-masses which are in contact with a rotating disc. A base excitation is applied to each of the beams externally. The partial differential equations governing the motions of the coupled subsystem are reduced to a set of ordinary differential equations employing the modal analysis. A bifurcation analysis is performed on the behavior of the tip-masses to study the route and the bifurcations through which chaotic orbits are born in the system. The non-dimensionalized base excitation frequency is chosen as the bifurcation parameter to obtain the bifurcation diagram.

It is observed that both the tip-masses undergo for the same route and bifurcations to chaos. We observed that the chaotic orbits are born in the coupled system from the single periodic behavior through a quasiperiodic route. Initially the behavior of the couple system is found to be single periodic in nature and being bifurcated to quasiperiodic motion abruptly at one particular value of Ω . Most interestingly, within the quasiperiodic regime, presence of multi-periodic windows is observed and finally an abrupt transition from quasiperiodic to chaotic nature is occurred. Further, the dynamics of synchronization between those coupled tip-mass motions is studied by determining the linear correlation value between the time displacement responses. During the single periodic as well as the quasiperiodic region with multi-periodic windows, a strong correlation ($0.8 \leq C_c \leq 1$) implying the presence of synchronous motion between the tip-masses is observed. A weak correlation implying non-synchronous motion between the beams is observed in the chaotic region. Numerical analysis conducted shows that the coupled friction-induced oscillators has experienced a transition from periodic synchronization state to a non-synchronized chaos through a synchronized quasiperiodic as well as multiperiodic state.

References

1. Ibrahim, R.A.: Friction-induced vibration, chatter, squeal, and chaos part I. Mechanics of contact and friction. *Appl. Mech. Rev.* **47**(7), 209–226 (1994)
2. Ibrahim, R.A.: Friction-induced vibration, chatter, squeal, and chaos part II: dynamics and modeling. *Appl. Mech. Rev.* **47**(7), 227–253 (1994)
3. Dunlap, K.B., Riehle, M.A., Longhouse, R.E.: An investigative overview of automotive disc brake noise. *SAE Tech. Pap.* **108**(6), 515–522 (1999)

4. Qatu, M.S., Abdelhamid, M.K., Pang, J., Sheng, G.: Overview of automotive noise and vibration. *Int. J. Veh. Noise Vib.* **5**, 1–35 (2009)
5. Ghazaly, N.M., El-Sharkawy, M., Ahmed, I.: A review of automotive brake squeal mechanisms. *J. Mech. Des. Vib.* **1**(1), 5–9 (2013)
6. Kinkaid, N.M., O'Reilly, O.M., Papadopoulos, P.: Automotive disc brake squeal. *J. Sound Vib.* **267**(1), 105–166 (2003)
7. Nakae, T., Ryu, T., Sueoka, T.A., Nakano, Y., Inoue, T.: Squeal and chatter phenomena generated in a mountain bike disc brake. *J. Sound Vib.* **330**(10), 2138–2149 (2011)
8. Thomsen, J.J.: Using fast vibrations to quench friction-induced oscillations. *J. Sound Vib.* **228**(5), 1079–1102 (1999)
9. Hoffmann, N., Gaul, L.: Effects of damping on mode-coupling instability in friction induced oscillations. *ZAMM Zeitschrift Fur Angew. Math. Und. Mech.* **83**(8), 524–534 (2003)
10. Kang, J., Krousgrill, C.M., Sadeghi, F.: Dynamic instability of a thin circular plate with friction interface and its application to disc brake squeal. *J. Sound Vib.* **316**(1–5), 164–179 (2008)
11. Hoffmann, N., Gaul, L.: A sufficient criterion for the onset of sprag-slip oscillations. *Arch. Appl. Mech.* **73**(9), 650–660 (2004)
12. Kang, J., Krousgrill, C.M.: The onset of friction-induced vibration and spragging. *J. Sound Vib.* **329**(17), 3537–3549 (2010)
13. Hinrichs, N., Oestreich, M., Popp, K.: On the modelling of friction oscillators. *J. Sound Vib.* **216**(3), 435–459 (1998)
14. Shin, K., Brennan, M.J., Oh, J.E., Harris, C.J.: Analysis of disc brake noise using a two-degree-of-freedom model. *J. Sound Vib.* **254**(5), 837–848 (2002)
15. Popp, K., Stelzer, P.: Stick-slip vibrations and chaos. *Philos. Trans. Phys. Sci. Eng.* **332**, 89–105 (1990)
16. Ouyang, H., Mottershead, J.E., Cartmell, M.P., Friswell, M.I.: Friction-induced parametric resonances in discs: effect of a neagative friction-velocity relationship. *J. Sound Vib.* **209**(2), 251–264 (1998)
17. Saha, A., Pandey, S.S., Bhattacharya, B., Wahi, P.: Analysis and control of friction-induced oscillations in a continuous system Analysis and control of friction-induced oscillations in a continuous system. *J. Vib. Control* **18**(3), 467–480 (2011)
18. Velayudhan, J., Narayanan, M.D., Saha, A.: On the synchronization behavior of coupled friction-induced oscillators subjected to base excitation. *J. Comput. Nonlinear Dyn.* (Accepted for publication). <https://doi.org/10.1115/1.4052891>
19. Awrejcewicz, J., Sendkowski, D.: Stick-slip chaos detection in coupled oscillators with friction. *Int. J. Solids Struct.* **42**(21–22), 5669–5682 (2005)
20. Marszal, M., Saha, A., Jankowski, K., Stefański, A.: Synchronization in arrays of coupled self-induced friction oscillators. *Eur. Phys. J. Spec. Top.* **225**(13), 2669–2678 (2016)
21. Barron, M.A., Sen, M.: Synchronization of coupled self-excited elastic beams. *J. Sound Vib.* **324**, 209–220 (2009)

Influence of Supply Inlet Jet Angle on Ventilating Respiratory Droplets from Makeshift Isolation Enclosures



S. Harikrishnan  and M. Manish 

Abstract In the present-day health care systems, the setting up of makeshift isolation enclosures is unavoidably important. These are cubicles or rooms made to isolate infected patients from others. Indoor air quality is very critical in such health care facilities due to the presence of virus-laden respiratory droplets released during coughing. In the present study, numerical investigations have been carried out to understand the influence of different inlet jet angles on ventilating such respiratory droplets from a makeshift isolation enclosure. Different operating conditions such as inlet air duct location and supply jet angle have been considered. Initial numerical results have been validated against the experimental results reported in the literature. Effect of different parameters has been discussed with streamlines, velocity contours, droplet dispersion statistics etc. Changing supply inlet location as well as jet inclination is found to change the ventilation characteristics significantly. Conclusions drawn from the present study can give important guidelines for designing efficient make-shift isolation enclosures in the future.

Keywords Indoor air conditioning · Ventilation · Computational fluid dynamics · Health care · Respiratory droplets

1 Introduction

Makeshift isolation enclosures are very valuable in constrained healthcare systems to isolate infected patients. These enclosures are generally negative air pressure rooms

S. Harikrishnan

Department of Mechanical Engineering, Indian Institute of Technology Madras, Chennai, Tamil Nadu 600036, India

Department of Mechanical Engineering, Amrita School of Engineering, Amrita Vishwa Vidyapeetham, Chennai, Tamil Nadu 601103, India

M. Manish (✉)

Department of Mechanical Engineering, Rajiv Gandhi Institute of Technology, Kottayam, Kerala 686501, India

e-mail: manishxpress@rit.ac.in; manishxpress@gmail.com

which has provision of sufficient air changes per hour. Indoor air quality and thereby the proper design of ventilation systems is an important design parameter in such isolation enclosures. Poor ventilation design can be unsafe to the patients and also to the front-line health care workers as it increases the disease transmission rate due to the prolonged exposure to deadly viruses. Virus laden respiratory droplets which are produced during coughing, sneezing, talking etc. and its transmission through air is now known to be one of the major causes of infectious disease transmission [1–4]. Several researchers have noted that the deposition and dispersion of bio aerosols produced during coughing, sneezing and talking etc. has not yet been understood well [5, 6]. Coughing is also known to be one of the common symptoms in most of the respiratory diseases [7, 8].

In the current research work, a Computational Fluid Dynamics (CFD) study has been undertaken to understand the influence of inlet jet angles on ventilating the respiratory droplets produced during coughing from a makeshift isolation enclosure. Droplets dispersed during a coughing cycle has been mimicked and the effect of dispersion of droplets in such enclosures has been studied for different inlet jet angles. The effect of varying the inlet jet angle may have significant implications on the dispersion and deposition of droplets. These have been analyzed with streamlines, velocity contours, instantaneous droplet dispersion images etc.

2 Problem Statement

The dimensions of a typical makeshift isolation enclosure is shown in Fig. 1. A 2-dimensional CFD study is performed with ‘L’ and ‘H’ being the length and height of the room as shown in the Figure. Two different locations for inlet air entry namely the left wall inlet and top wall inlet are considered in the present study. Six different cases are analyzed in the present work. First 3 cases (case 1, 2 and 3) corresponds to the left wall entry and the remaining 3 cases (case 4, 5 and 6) corresponds to the top wall entry as shown in Fig. 1. Case 1 corresponds to -45° inlet jet angle whereas Case 3 corresponds to $+45^\circ$ inlet jet angle with respect to 0° horizontal (case 2)

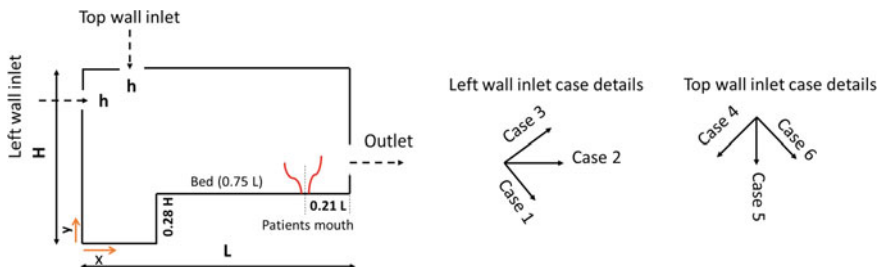


Fig. 1 Computational domain (left) used in the present study and the six cases considered for simulation in the present study (right)

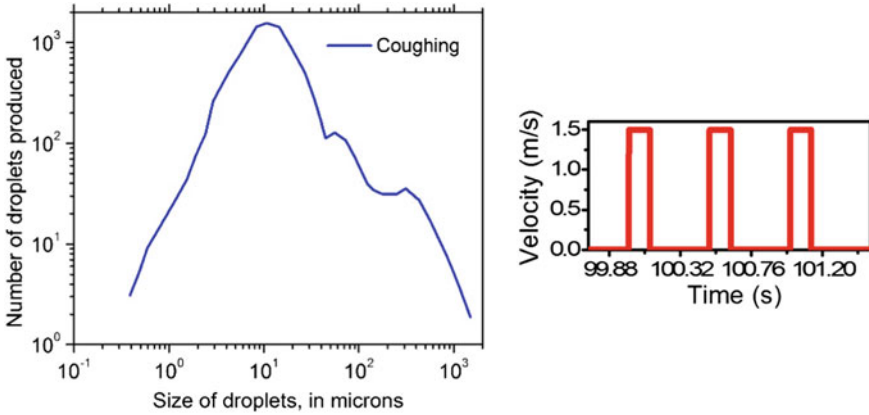
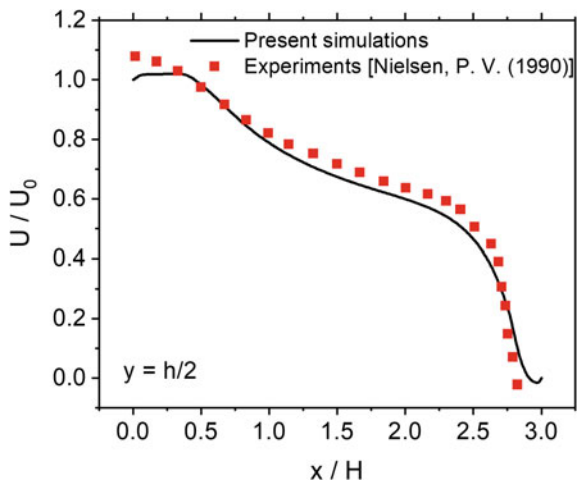


Fig. 2 Typical droplet size distribution in human cough [15]. The cyclic conditions mimicking human cough used in the present simulations are also depicted

while Case 4 and Case 6 corresponds to -45° and $+45^\circ$ inlet jet angle with respect to 0° vertical (case 5). The inlet air velocity is fixed for all the six cases and is selected considering the air changes per hour value which should be greater than or equal to 12 for a typical hospital ventilation purpose.

In the present study, the patients bed whose dimensions are same as that of a typical hospital bed which is located next to the extraction port. The exhaust window dimensions are kept same as that of a High-Efficiency Particulate Air (HEPA) filter available commonly in market. A negative pressure differential of 2.5 Pa is maintained at the extraction port which is the typical requirement of isolation rooms as per ISHRAE (Indian Society of Heating, Refrigerating and Air Conditioning Engineers) guidelines. The flow under the bed is not of any interest in the present study and hence is not simulated. A typical mean mouth opening of 3 cm is provided in the present study also as used by several researchers [9, 10] and is located at a distance of 0.21L as shown in Fig. 2. The simulated cough droplets are injected from the mouth at this location. A broad range of droplet size distribution is produced during coughing [11]. The droplet distribution generally follows a Rossin Ramler distribution with mean diameter of 10 mm, maximum of approximately 1000 mm and minimum of 0.5 mm as reported earlier by several researchers and as presented in Fig. 3. The droplets are injected in 3 pulses spread over 0.12 s each as in [12]. The cough flowrate for a typical human varies over a range of 0.1–0.9 l/s as shown in the experimental work done by [13]. However, this also depends on the age group, gender, health of the person and several other parameters. In the present study an average cough flowrate of 0.5 l/s and an average cough velocity of 1.5 m/s is assumed and is maintained same for all the six cases.

Fig. 3 Validation of the present numerical data with experimental results of Nielsen [16]



3 Numerical Methodology

In the present study, the air flow has been modelled using an Eulerian approach whereas the cough droplets are modelled using a Lagrangian approach. Water droplets are injected into the domain to mimic the cough droplets. Air flow in the makeshift isolation enclosure is unsteady, incompressible and turbulent in nature. The following Eqs. (1) and (2) are used to solve the mass and momentum conservations whereas a Lagrangian framework as described by Eq. (3) has been used to track the droplet dispersion. The details regarding (3) can be found in [10]. A standard $k-\varepsilon$ model has been used for turbulent flow simulations and an enhanced wall treatment has been employed for accurate flow prediction near the walls.

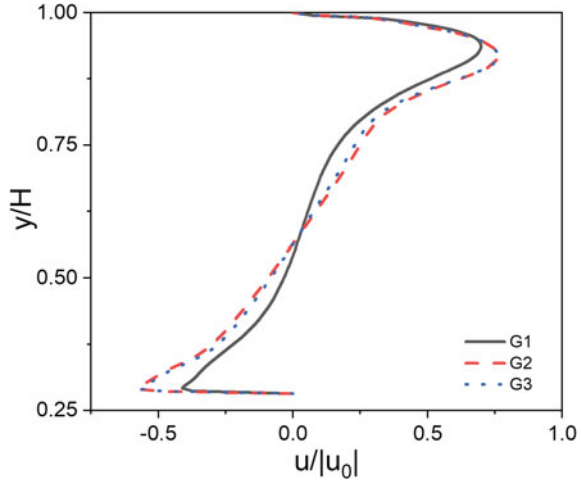
$$\frac{\partial}{\partial x_i}(\rho u_i) = 0 \quad (1)$$

$$\begin{aligned} \frac{\partial(\rho u_i)}{\partial t} + \frac{\partial}{\partial x_j}(\rho u_i u_j) = & -\frac{\partial p}{\partial x_i} + \frac{\partial}{\partial x_j} \left[\mu \left(\frac{\partial u_i}{\partial x_j} + \frac{\partial u_j}{\partial x_i} - \frac{2}{3} \delta_{ij} \frac{\partial u_k}{\partial x_k} \right) \right] \\ & + \frac{\partial}{\partial x_j} (-\rho \overline{u'_i u'_j}) \end{aligned} \quad (2)$$

$$\frac{du_p}{dt} = F_D(u - u_p) + \frac{g(\rho_p - \rho)}{\rho_p} + F \quad (3)$$

Boundary conditions are imposed at inlet, outlet, walls and injection plane. At inlet, uniform velocity inlet boundary condition has been applied while at outlet, pressure outlet boundary condition with a gauge pressure value of -2.5 Pa has been given. No slip boundary condition has been applied on walls, and on the injection surface (mouth) time varying injection condition described in previous section has

Fig. 4 Grid independence test results for three different grid sizes



been employed. Governing equations are solved by using commercial computational fluid dynamics package ANSYS Fluent 18.1. Computational Fluid Dynamics has been a widely used tool in different thermal engineering problems [14, 15]. Validity and accuracy of the present computational method has been confirmed by comparing numerical results with the experimental results reported in the literature. Numerical investigations have been carried out by considering same geometry and operating conditions reported in the experimental results of Nielson [16]. Figure 3 shows the comparison of numerical results of x-velocity profile with the experimental results at one y-location. Numerical results are found to be in good agreement with the experimental results.

Non-uniform structure mesh has been generated by using ANSYS Workbench package. Detailed grid independence study has been carried out to select the optimum grid size for computation. Three different grids have been considered in the present case are grids with 14,553 nodes (G1), 28,231 nodes (G2) and 41,971 nodes (G3). Figure 4 depicts the variation of x-velocity component along y-direction at $x = L/2$ for three different grid sizes (G1, G2 and G3). It can be inferred from Fig. 4 that the difference between the grids G2 and G3 are much less as compared to that of G1 and G2, and hence grid corresponding to G2 has been considered in the present study for all further computations.

4 Results and Discussion

The main objective of the ventilation system in makeshift hospitals is to remove air-borne droplets as early as possible to prevent the spread of diseases. Mainly two different inlet locations (left and top wall) and three different inlet supply jet angles (-45° , 0° and 45°) have been considered in the present study. To begin with, the flow

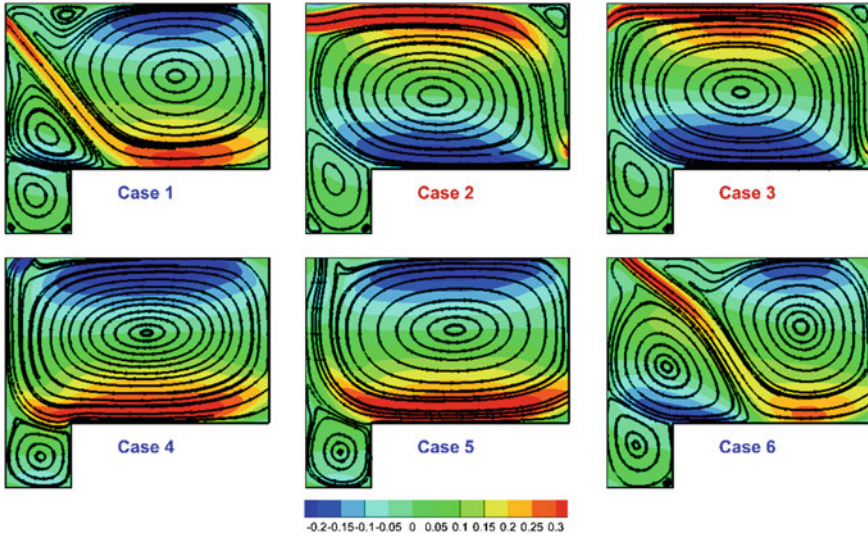
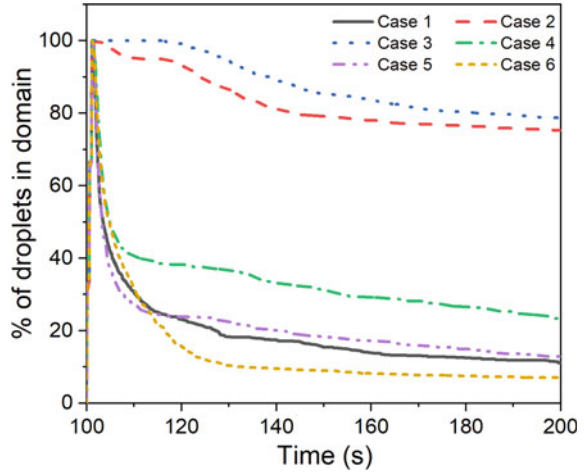


Fig. 5 Time-averaged streamlines along with non-dimensional x-velocity contours for six different inlet conditions without considering injection of droplets

characteristics of all six cases have been analyzed in detail without injecting droplets. Understanding flow features in each case can help us to understand the recirculation zones present in each case due to the inlet supply jet. Figure 5 depicts time-averaged streamlines along with x-velocity contours for different inlet operating conditions without considering the injection of droplets. The entry of higher velocity supply air into the enclosure introduces multiple smaller and larger recirculation zones in the domain. One big recirculation zone above the bed and multiple smaller recirculation zones in other parts of the domain especially near the corners have been observed. It is also interesting to note that the supply inlet conditions not only change the location of recirculation zones but also change the direction of the recirculation. The bigger recirculation zone present above the bed can decide the fate of the respiratory droplets ejected from the mouth of the patient. In other words, the clockwise direction of the larger recirculation zone can displace the droplets away from the outlet while the counter-clockwise direction can displace the droplets towards the outlet. The counter-clockwise direction of a larger recirculation zone is preferred since it can remove the respiratory droplets as early as possible from the enclosure. Except for cases 2 and 3 all other cases, counter-clockwise direction of larger recirculation zone has been observed. Interestingly, for cases 1, 4, 5, and 6 higher values of positive x-velocity have been observed near the bed which indicates that the particle ejected from the mouth of the patient move faster towards the outlet. Higher x-velocity near the source (patient's body) than that of other regions can limit the dispersion of droplets into the room, and this can remove the droplets from the room in a short period of time. For cases 2 and 3, x-velocity near the source is negative, which indicates that the droplets move away from the outlet. Also, there are good chances

Fig. 6 Percentage of trapped droplets in the domain with time for six different configurations

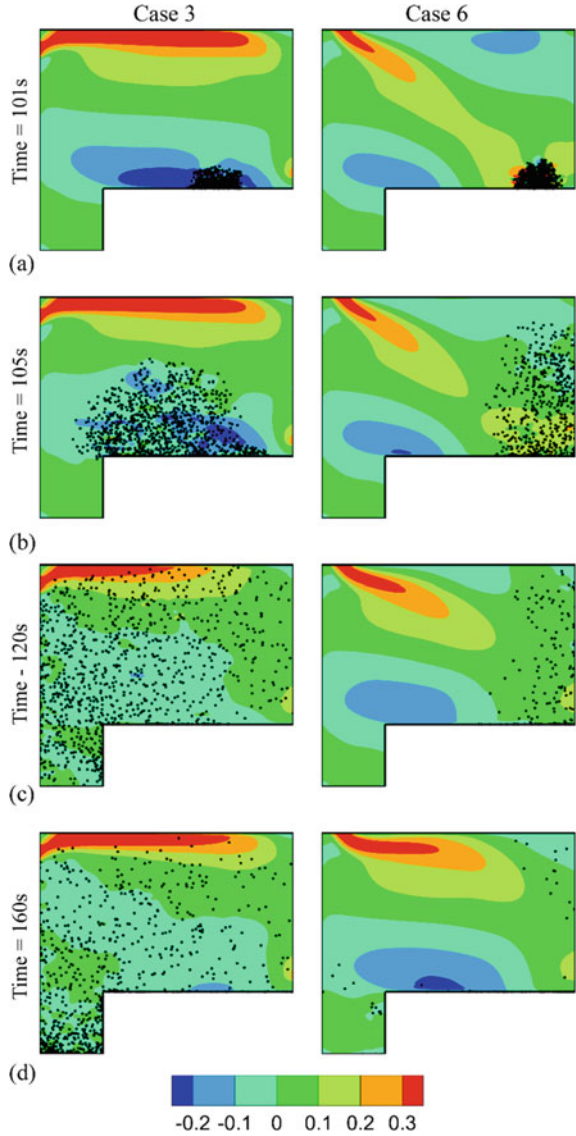


that these respiratory droplets can fall into the dead recirculation zones present in the corner of the enclosure. The falling of droplets in these dead recirculation zones stays there for a longer period of time which increases the risk of spreading the disease.

Figure 6 depicts the variation of percentage of droplets present in the domain with time. Figure 6 can be used to compare the ventilation performance quantitatively for different cases considered in the study. A total of 1200 droplets are injected into the room as pulsatile injection as mentioned in the problem statement section. It can be inferred from the figure that cases 2 and 3 require more time to flush droplets from the room as compared to other cases. This is due to the clockwise direction of larger recirculation zone developed in the domain for case 2 and 3 which displaces injected droplets away from the outlet. Case 6 is found to flush droplets efficiently as compared to all other cases considered in the present study.

Figure 7 depicts the instantaneous location of droplets for Case 3 and 6 super imposed with non-dimensional x-velocity for few representative time instants. Case 3 and 6 are two representative cases with larger recirculation zones in clockwise and counter-clockwise directions respectively. It can be inferred from the figure that for case 3 droplets are found to move away from outlet with time due to the clockwise recirculation zone present in the domain. Interestingly for case 6 the droplets are found to move towards outlet vent with time due to counter clockwise direction of larger recirculation zone. Hence, droplets are taken away from the room as early as possible for case 6. On the other hand, for case 3, movement of droplets away from the outlet vent leads to trapping of droplets on corner of the room. Accumulation of virus laden droplets in corner of the room stays there for longer time and it increase the risk of spreading the disease.

Fig. 7 Instantaneous location of droplets for Case 3 and 6 super imposed with non-dimensional x-velocity for few representative time instants



5 Conclusions

Two-dimensional numerical investigations have been carried out to study the effect of inlet location and jet angle on ventilating respiratory droplets from a make-shift isolation enclosure. Two different inlet locations viz. left and a top wall, and three different jet angles (-45° , 0° , and 45°) have been considered in the present study. Computations have been carried out by using the commercial CFD package ANSYS Fluent with the


Eulerian–Lagrangian approach. Numerical results are validated against the experimental results reported in the literature. The coughing process has been mimicked by injecting droplets in the form of pulses into the room. Several recirculation zones are produced due to the airflow, which decides the movement of droplets. The study concludes that the position of the supply duct, the negative pressure differential combined with the strength of the recirculation zone determine whether the droplets stay in the room or are flushed outside and these factors should also be taken care of while designing such rooms to contain the spread of the infection.

References

1. Greenhalgh, T., Jimenez, J.L., Prather, K.A., Tufekci, Z., Fisman, D., Schooley, R.: Ten scientific reasons in support of airborne transmission of sars-cov-2. *Lancet* **397**(10285), 1603–1605 (2021)
2. Liu, K., Allahyari, M., Salinas, J.S., Zgheib, N., Balachandar, S.: Peering inside a cough or sneeze to explain enhanced airborne transmission under dry weather. *Sci. Rep.* **11**(1), 1–9 (2021)
3. Vijayaraghavan, S., Puthenveetil, N.: Aerosol box for protection during airway manipulation in covid-19 patients. *Indian J. Anaesth.* **64**(Suppl 2), S148 (2020)
4. Puthenveetil, N., Rahman, S., Vijayaraghavan, S., Suresh, S., Kadapamannil, D., Paul, J.: Comparison of aerosol box intubation with C-MAC video laryngoscope and direct laryngoscopy—a randomised controlled trial. *Indian J. Anaesth.* **65**(2), 133 (2021)
5. Yan, J., Grantham, M., Pantelic, J., de Mesquita, P.J.B., Albert, B., Liu, F., Ehrman, S., Milton, D.K., Consortium, E.: Infectious virus in exhaled breath of symptomatic seasonal influenza cases from a college community. *Proc. Natl. Acad. Sci. U.S.A.* **115**(5), 1081–1086 (2018)
6. Li, Y., Huang, X., Yu, I.T.S., Wong, T.W., Qian, H.: Role of air distribution in SARS transmission during the largest nosocomial outbreak in Hong Kong. *Indoor Air* **15**(2), 83–95 (2005)
7. Hsu, J.Y., Stone, R.A., Logan-Sinclair, R.B., Worsdell, M., Busst, C.M., Chung, K.F.: Coughing frequency in patients with persistent cough: assessment using a 24-hour ambulatory recorder. *Eur. Respir. J.* **7**(7), 1246–1253 (1994)
8. Smyrnios, N.A., Irwin, R.S., Curley, F.J.: Chronic cough with a history of excessive sputum production: the spectrum and frequency of causes, key components of the diagnostic evaluation, and outcome of specific therapy. *Chest* **108**(4), 991–997 (1995)
9. VanSciver, M., Miller, S., Hertzberg, J.: Particle image velocimetry of human cough. *Aerosol Sci. Technol.* **45**(3), 415–422 (2011)
10. Wang, C.: Ventilation performance in operating rooms: a numerical assessment. Doctoral dissertation, KTH Royal Institute of Technology (2019)
11. Memarzadeh F (2012) Improved strategy to control aerosol transmitted infections in a hospital suite. In: Proceedings of IAQ Conference 2012
12. Dbouk, T., Drikakis, D.: On respiratory droplets and face masks. *Phys. Fluids* **32**(6), 063303 (2020)
13. Yang, S., Lee, G.W., Chen, C.M., Wu, C.C., Yu, K.P.: The size and concentration of droplets generated by coughing in human subjects. *J. Aerosol Med.* **20**(4), 484–494 (2007)
14. Harikrishnan, S., Manish, M.: Characteristics of respiratory droplets in ventilated makeshift isolation enclosures. In: 20th Annual Conference on Liquid Atomization and Spray Systems (ILASS) Asia ILASS-ASIA 2020, Jiangsu University, Zhenjiang, China, Oct 23rd-26th, 2020
15. Harikrishnan, S., Tiwari, S.: Unsteady characteristics of periodically fully developed flow in biconvex module of wavy channel. *Recent Patents Mech. Eng.* **4**, 326–331 (2018)
16. Nielsen, P.: Specification of a Two-Dimensional Test Case. 1990. (IEA). No. 8 in Gul Serie, Institut for Bygningsteknik, Aalborg Universitet

Influence of PWHT on Microstructure and Mechanical Properties of Similar TRIP-TRIP and Dissimilar DP-TRIP Laser Welds for Automobile Applications



C. Gopi Krishna , T. Mahesh Kumar, N. Kishore Babu, P. Phani Prabhakar, and G. V. Sarath Kumar

Abstract The need for lower fuel consumption along with improved safety of passengers has encouraged the auto industry to use Advanced High Strength Steels (AHSS). Fabrication of such applications involves welding, which leads to the alteration of microstructure and mechanical properties. The aim of the present work is to study and understand the effect of laser welding on similar Transformation Induced Plasticity (TRIP-TRIP) and dissimilar Dual Phase (DP)-Transformation Induced Plasticity (TRIP) welds. This weld fabrication using low heat input techniques results in fully martensitic structure in the weld and Heat Affected Zone (HAZ) rendering brittleness of the weldment. The effect of isothermal post-weld heat treatment (PWHT) on the properties of weld joints was also studied. The optical microscopy has revealed the martensite in the Fusion Zone (FZ), while the HAZ consisted of a mixture of ferrite and martensite. The variation in microstructure in the transverse direction to the weld has led to variation in microhardness. The results of the tensile test indicated the weld to be stronger and the failure location was far from the weld centre. The Ultimate Tensile Strength (UTS) and ductility of the tensile samples were less compared to the base metals. Post weld heat treatment resulted in a small decrease in fusion zone hardness. Because of the lower ductility of the weldments, cracks were observed in the fusion zone during the Erichsen cup test.

Keywords Laser welding · DP steel · TRIP steel · Tailor welded blanks · Formability

C. Gopi Krishna (✉) · T. Mahesh Kumar · N. Kishore Babu
National Institute of Technology, Warangal, India
e-mail: cgkrishna@student.nitw.ac.in

P. Phani Prabhakar
ARCI, Hyderabad, India

G. V. Sarath Kumar
Ashok Leyland, Chennai, India

1 Introduction

With the steady rise in fuel consumption, the fuel resources get depleted, leading to heavy demand for fuel-efficient vehicles. Also, the awareness among the people regarding the new environment norms to minimize carbon dioxide emissions has motivated the auto industry to develop lightweight vehicles with good strength and energy absorption in a crash event. The need to reduce the weight without compromising vehicle safety has steered the auto industry to utilize new materials with high strength to weight ratio for auto body fabrication. Though many materials compete to accomplish the requirements of the automobile industry, Advanced High Strength Steels (AHSS) have been the clear winner [1, 2]. Because the AHSS are lighter materials with high strength, they reduce vehicle weight and increase fuel consumption, while the safety of the passenger is also guaranteed due to high stiffness and ductility of the same [3]. Dual Phase (DP) steels and Transformation Induced Plasticity (TRIP) steels are the well-known grades of AHSS being used in the automobile body. The DP and TRIP steels are produced by an intercritical annealing in the ferrite plus austenite ($\alpha + \gamma$) region of the Fe-Fe₃C phase diagram. In the intercritical annealing for DP steels, with a sufficient holding time, the austenite formed in the ferrite matrix gets enriched with carbon and later to be transformed into high carbon martensite during subsequent cooling. Thus a typical DP steel microstructure is composed of ferrite islands surrounded by martensite. The ferrite phase induces ductility, while the martensite phase is the reason for strength. Several grades of DP steels with varying strengths from 500 to 1000 MPa can be produced by varying intercritical annealing temperature and time. Whereas for TRIP steels, the cooling is not continuous. The steel is held isothermally in the bainitic region and addition of Aluminium (Al) and Silicon (Si) suppress the formation of cementite. The phases present in typical TRIP steel microstructure are ferrite, retained austenite and bainite. High strength coupled with good ductility and high work hardening rate are the unique combination of properties in good agreement with the property requirements of auto industry. On the other hand, TRIP steels have a higher ductility due the TRIP effect, where transformation of retained austenite to martensite occurs under the influence of plastic strain [4].

Tailor Welded Blanks (TWB's), in which two dissimilar metal sheets are joined using an appropriate welding procedure, is a well-known way of incorporating AHSS into an automobile part. The sheets may be of different thicknesses, compositions, coatings, and properties. The use of TWB allows the placement of the right material in the correct location. They also have other notable benefits, such as cost reduction, dimensional accuracy, scrap reduction, etc. [5]. For the assembly of car bodies and other components, the auto industry has been adopting various welding techniques. Though Resistance Spot Welding (RSW) was widely used in the manufacture of auto-body, laser welding is gaining its reputation due to its advantages such as flexibility, ease of automation, less heat input, etc. [6, 7].

Several researchers have studied the effect of laser welding on the microstructure and mechanical properties of AHSS. It was reported that softening in the heat affected

zone (HAZ) adversely affects the formability of tailor-welded blanks due to high strain concentration in the softened region, leading to premature failure of the blanks. HAZ softening was linked to the tempering of the martensite phase in DP steel. Nayak et al. [8] have reported the effect of martensite content and tempering on softening behaviour of DP steels with varying chemistry. Similar studies were done by Farabi et al. [9, 10] on DP 600 and reported failure in the softened zone. A very hard and strong fusion zone was formed as a result of laser welding and it reduced the formability characteristics. Reduction in formability due to the laser welding process has also been reported for DP980 and DP800 steels. Sreenivasan et al. have studied and evaluated the formability characteristics of DP 980 steel laser welds [11] and found that the presence of softening zone has reduced the formability of welded joints irrespective of welding parameters. Several authors have prepared dissimilar DP steel laser welds and reported that nonuniform properties across the weldment resulting in formability issues and premature failure during the mechanical testing. In the study of laser welded DP 780 and DP 980 dissimilar joints, Dong et al. has observed a failure in DP 780 side [12]. The ductility of welded joints decreased when compared with base metals. This has been confirmed by Gong et al. while investigating the welding behaviour of dissimilar DP 780 and DP 1180 steels [13]. Rajashekar et al. [14] investigated the welding behavior of Nd: YAG laser welded TRIP 780 and DP 980 steels and concluded that strength difference exists between the weld zone and other zones due to the formation of softening zone (SZ). Other authors have also confirmed the presence of this softening zone [8, 15–18] in laser welded joints of AHSS. Wang et al. investigated the effect of heat input on this SZ and concluded that SZ width increased with an increase in heat input [19, 20]. The microstructures obtained in the fusion zone of laser welded AHSS materials were predominantly martensitic due to the formation of austenite during the welding process and the cooling rates involved in the process. The microstructure and properties of laser welded joints are primarily dependent on welding parameters and the type of laser used [17, 18, 21]. Gallagher et al. [22] used an Nd:YAG laser to weld HSLA300, DP600, M900 and M1310 steels at various speeds and found that weld tensile strength appeared to be dependent upon steel grade, weld penetration, and weld width. Xu et al. [23] compared different laser welding processes and found that the width of heat affected zone, as well as fusion zone, was varying with each process. Due to the high power density in fiber laser welding, narrow zones were observed. In contrast, diode laser resulted in a larger fusion zone as well as HAZ. The hard martensite present in the fusion zone has been reported to be reducing the formability of these steels. The formability of weld can be enhanced by reducing the hardness of the fusion zone using the post weld tempering process. It has been reported that the tempering temperature showed a marked effect on weldment properties than any other process parameters during the heat treatment [24].

In the current study, laser welds of DP and TRIP steels have been prepared in butt joint configuration to study their microstructural and mechanical properties. A post-weld heat treatment (PWHT) at 250 °C for 2 h was also carried out on the prepared welds. The effect of PWHT on the properties of weldments was investigated and reported.

2 Experimental

The DP 780 and TRIP 780 steel sheets with 1.2 mm thickness in cold-rolled condition were used in the current study. The sheets were cut into rectangular plates of 90 mm length and 45 mm width. The cut sheets were cleaned with acetone to clean the edges and surfaces. The chemical composition of DP 780 and TRIP 780 steels were mentioned in Table 1. Similar TRIP-TRIP and dissimilar DP-TRIP butt joints were prepared using a German-made (ROFIN) DC-035 CO₂ type laser welding machine. Trail tests, with the main aim to obtain full penetration and sound welded joints were carried out to select the optimal laser welding parameters. These trail parameters were listed in Table 2. Based on the trial tests, laser power of 3 KW and a welding speed of 4 m/min has resulted in defect free and sound welds. Hence those parameters were selected for further investigation. Helium gas shielding at a flow rate of 15 l/min was used during welding.

The as-welded samples were tempered to study the effect of PWHT on the properties of welds. The samples were heated in a muffle furnace at rate of 10 °C/min until 250 °C and held at that temperature for 2 h and subsequently cooled to room temperature by air cooling. The metallographic specimens from the welded samples were cut in a direction transverse to the weld. The cut specimens were mounted, mechanically ground, polished with a series of SiC polishing papers with an increasing grit size number from 400 till 2000. Then the specimens were polished on a disc with cloth by using a diamond paste of 9, 3 and 1 μm. The samples were etched in 2% Nital solution (98 ml ethanol, 2 ml of HNO₃) to reveal the microstructure. The microstructure of etched specimens was observed using an optical microscope.

Microhardness measurements were made on the transverse weld cross-sections using a Vickers hardness testing machine (Shimadzu HVM-G20ST) at 200 g load and a dwell time of 15 s. To study the effect of welding on tensile properties, sub

Table 1 Chemical composition

	C	Mn	Si	S	P	N	Al	Fe
DP 780	0.2	4.00	1.00	0.100	0.100	0.01	0.07	Remaining
TRIP 780	0.19	1.78	1.5	0.17	0.008	0.003	0.036	Remaining

Table 2 List of laser parameters used for trail tests

S. No	Laser power (KW)	Speed (m/min)	Heat input (J/mm)
1	2.5	4	37.5
2	2.5	5	30
3	2.5	6	25
4	3	4	45
5	3	5	36

The parameters indicated in bold letters

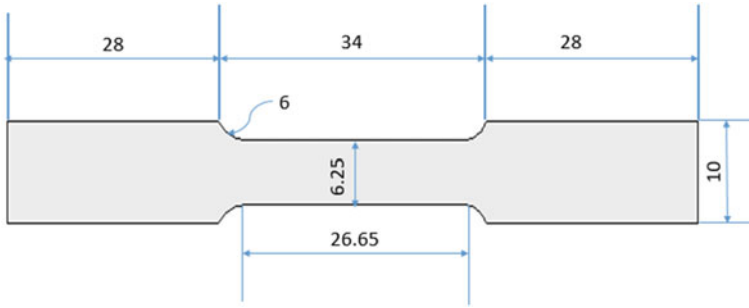


Fig. 1 Dimensions of tensile specimen used in the present study (All dimensions are in mm)

sized tensile samples perpendicular to welding direction were prepared as per the ASTM E8 standard. The sample dimensions were as shown in Fig. 1. Tensile tests were carried out on base metal as well as welds using a universal testing machine (UTM) at a displacement rate of 1 mm/min. Ultimate tensile strength (UTS), yield strength (YS) and percentage elongation were calculated from the tensile data. Prior to the test, the specimens were polished until 600 grit sized SiC paper to remove any stress concentration points. The square (90 × 90 mm) blanks in as-weld condition and PWHTed condition were stretch formed using an Erichsen cupping machine to evaluate the formability. The tests were conducted with the root side of the weld facing the hemispherical punch and continued until the appearance of crack. For all the tests, the weld was at the centre of the blank.

3 Results and Discussion

The base metal microstructure of DP780 steel consists of ferrite and martensite, as shown in Fig. 2a. The volume fraction of each phase is calculated using image

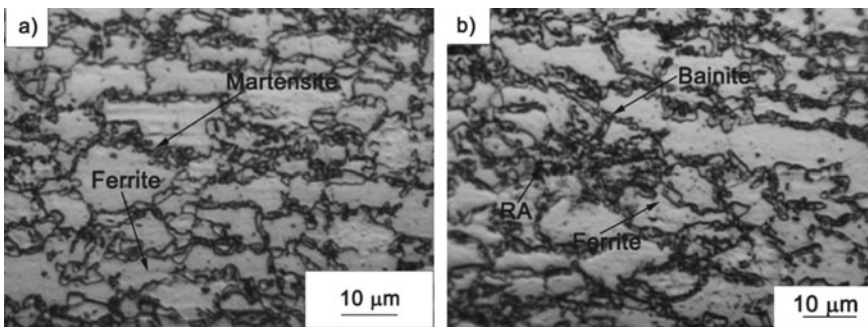


Fig. 2 Microstructure of **a** DP steel, **b** TRIP steel

analysis software and the values are found to be 25 and 75% for martensite and ferrite phases, respectively. TRIP 780 steel showed ferrite islands with retained austenite and bainite at grain boundaries is as shown in Fig. 2b. In the TRIP steel, The volume fraction of the ferrite phase was 72%, while the remaining 28% is of retained austenite and bainite.

3.1 Weld Macrostructure

Figure 3 shows the cross-sectional macroscopic view of the DP-TRIP and TRIP-TRIP weld joints. Sound welds are obtained in this study and the weldments did not show any weld defects such as porosity and under cut. The upper part of the weld bead is found to be wider with a narrower bottom. The width of the weld at the top is found to be approximately two times that at the bottom of the weld.

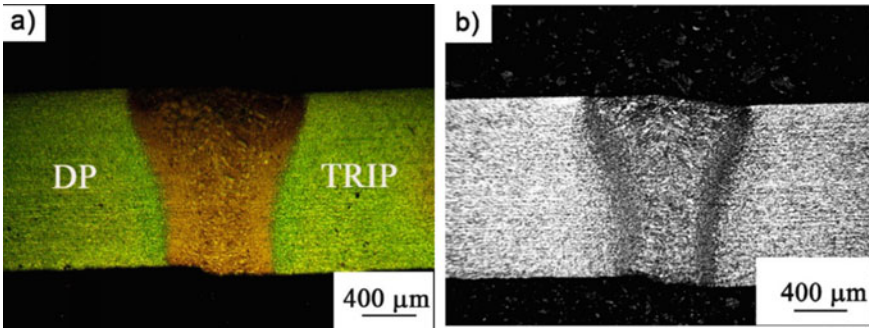


Fig. 3 Macroscopic view of a DP-TRIP joint and b TRIP-TRIP joint

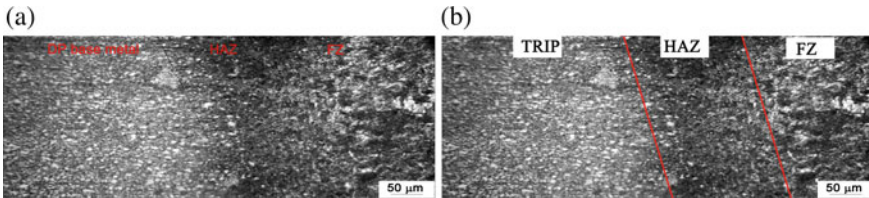


Fig. 4 Microstructures in DP-TRIP welds a showing FZ, HAZ and DP Base metal b FZ, HAZ and TRIP Base metal

3.2 Fusion Zone and Heat Affected Zone

Figure 4a, b shows optical micrographs of the DP-TRIP dissimilar weld cross-section on DP and TRIP sides, respectively. The cross-sectional images showed different zones of the weldment viz, FZ, HAZ and BM. Figure 5 shows the optical micrographs of the TRIP-TRIP weld cross-section and also showed FZ, HAZ and BM. Figure 6a, b shows optical micrographs of the DP-TRIP dissimilar weld cross-section in PWHTed condition on DP and TRIP sides, respectively. Figure 7 shows the optical micrographs of the TRIP-TRIP weld cross-section in PWHTed condition. In both the weldments, after PWHT, the cross-sectional images showed different zones similar to that in the as-welded condition. In all the conditions, significant microstructural changes are observed in the HAZ compared to the base metal. The microstructures of the fusion

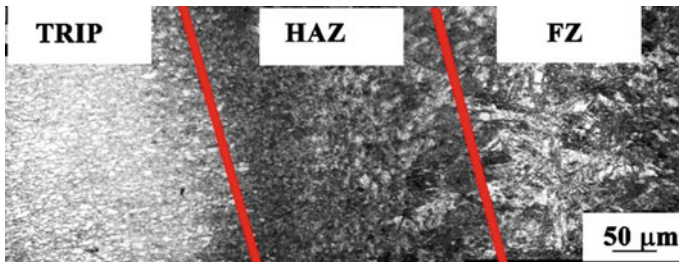


Fig. 5 Microstructures in TRIP-TRIP welds showing FZ, HAZ and TRIP base metal

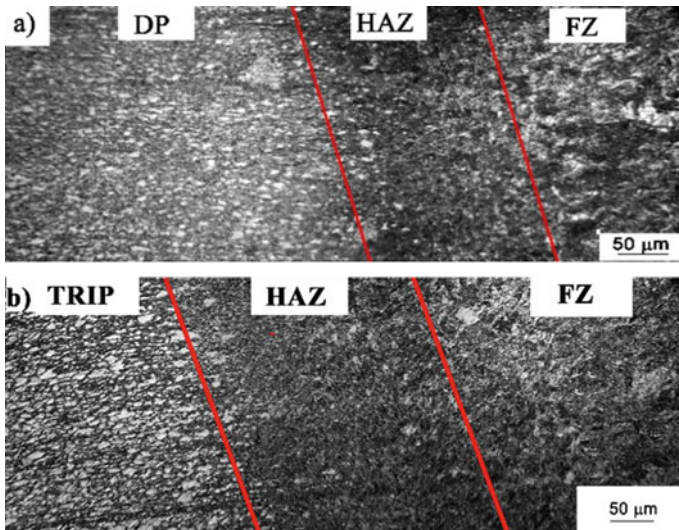


Fig. 6 Microstructures in DP-TRIP welds **a** showing FZ, HAZ and DP Base metal and **b** showing TRIP BM, HAZ and FZ in PWHT condition

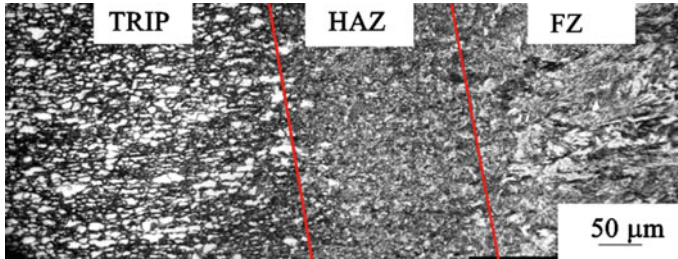


Fig. 7 Microstructures in TRIP-TRIP welds showing FZ, HAZ and TRIP base metal in PWHT condition

zone for DP-TRIP and TRIP-TRIP welds in as-welded and PWHTed condition are shown in Fig. 8. Similar to Gong et al. [13] martensite structure has been observed in the fusion zone of all the weldments in as-welded and PWHTed conditions. This can be attributed to the thermal cycle during welding. In a typical weld thermal cycle, the metal in the melt pool melts during heating and subsequently cooled rapidly to room temperature. The cooling rates in the laser welding process, higher than the critical cooling rate required for martensite formation which results in martensite formation in the fusion zone.

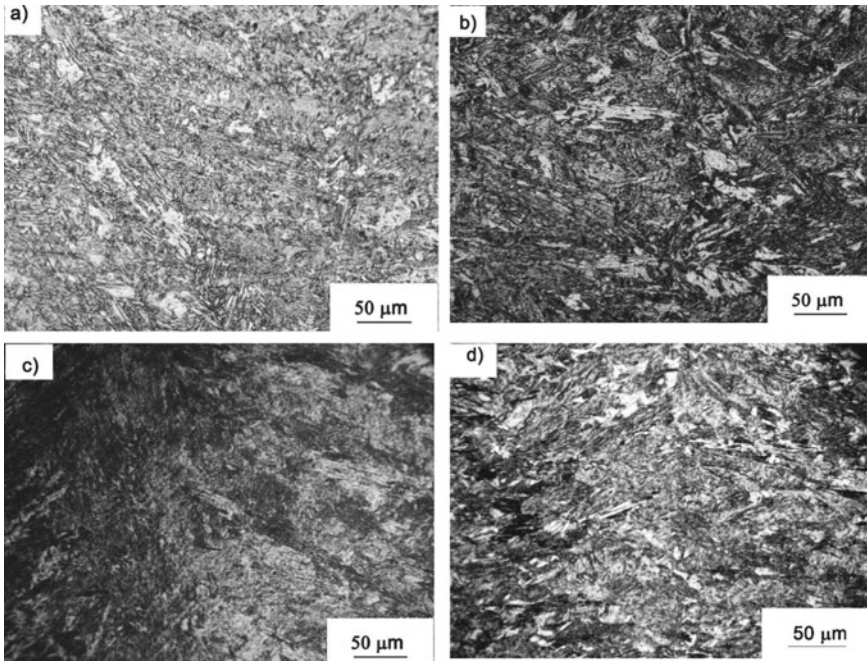


Fig. 8 Microstructure of fusion in **a** DP-TRIP as weld, **b** TRIP-TRIP as weld, **c** DP-TRIP in PWHT and **d** TRIP-TRIP PWHT conditions

Figure 9a, b shows the transverse hardness profiles of the DP-TRIP dissimilar weldment and TRIP-TRIP weldment, respectively in as-welded condition. Figure 9c, d shows the transverse hardness profiles of the DP-TRIP dissimilar weldment and TRIP-TRIP weldment, respectively, in PWHTed condition. In DP-TRIP weldment, a sequential increase in hardness from base metal to fusion zone through the HAZ is observed. The variation in hardness can be attributed to variation in the microstructure. In the fusion zone, the presence of martensite resulted in a high hardness compared to the other regions of the weldment. The peak temperature attained during the weld thermal cycles in the HAZ depends on the distance from the fusion boundary. The HAZ region, near to the fusion zone, that experiences temperatures above A_3 and below the A_4 line in the Fe-Fe₃C phase diagram develops a fully austenite structure compared to the HAZ regions that experience peak temperatures below A_3 . HAZ regions with peak temperatures between A_3 and A_1 also develop varying amounts of austenite depending on the peak temperature. This results in varying amounts of martensite in the microstructure across the HAZ. The regions close to the fusion boundary develop a higher volume fraction of martensite. This variation in the percentage of martensite from the fusion zone to BM through HAZ resulted in a decrease in hardness. In TRIP-TRIP weldments, a similar hardness profile with a sequential increase in hardness from BM to fusion zone is observed. This is also due to the change in the percentage of martensite from the fusion zone to BM through HAZ. The hardness profiles in the PWHTed condition are similar to the as-welded condition for both DP-TRIP and TRIP-TRIP weldments. The fusion zone hardness is reduced with PWHT for TRIP-TRIP as well as DP-TRIP weldments. In the as-welded condition, the average hardness in the fusion zone of DP-TRIP weld is 464 HV, which is approximately two times higher than that of DP and TRIP base metals. In PWHTed condition, the value gets reduced to 425 HV. Whereas the hardness of the fusion zone in the as-welded condition of TRIP-TRIP weldment is 450 HV, which is also approximately twice that of TRIP base metal and in the PWHTed condition the value is 410 HV. This reduction in hardness of the fusion zone after PWHT can be attributed to the tempering of martensite present. The average fusion zone hardness values of all the weldments and BM in as-welded a PWHTed condition are shown in Table 3.

Figure 10a, b shows the stress versus strain plots of TRIP-TRIP and DP-TRIP weldments, respectively. Table 4 consolidates the results obtained from the tensile test. From the careful observation of the stress–strain curves, it is evident that ductility has reduced post welding. The UTS of TRIP base metal is 780 MPa, whereas DP has a UTS of 760 MPa. TRIP-TRIP weldments showed slightly lower elongation in comparison to the base metal. A slight reduction (0.4%) in elongation is observed after the PWHT of the TRIP-TRIP weldments. The TRIP-TRIP weld joint after PWHT has shown a yield point phenomenon, whereas the remaining weldments haven't shown any such effect. A continuous yielding was observed in DP-TRIP welds in both the as-welded and PWHTed conditions, TRIP-TRIP weld in the as-welded condition. The appearance of the yield point phenomenon was probably due to the interstitial diffusion of carbon during PWHT of the weld. The PWHT temperature was sufficient for the carbon atoms from austenite to undergo a long-range diffusion

Fig. 9 Microhardness profiles of **a** DP-TRIP, **b** TRIP-TRIP in as-welded condition, **c** DP-TRIP and **d** TRIP-TRIP in PWHT condition

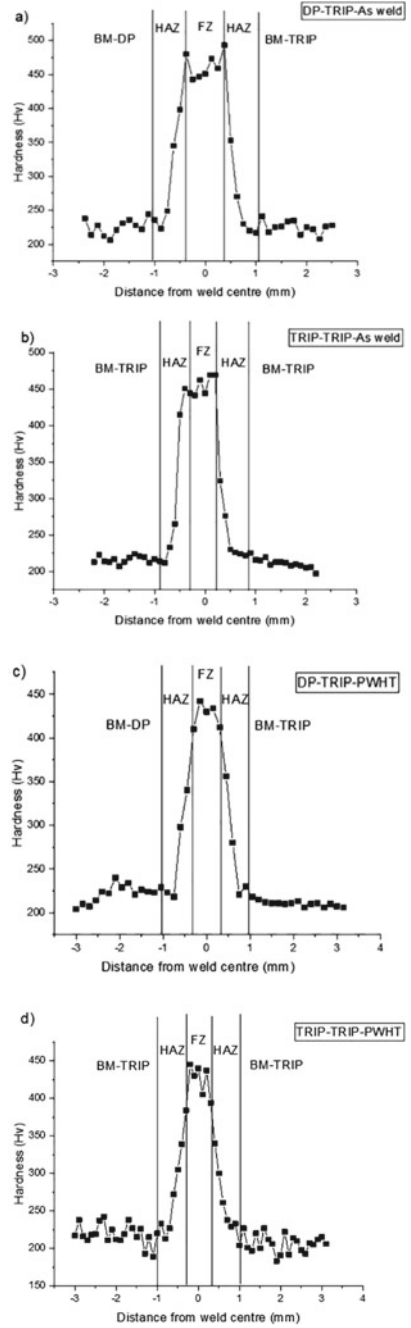


Table 3 Hardness test results

S.No	Name	Location	Hardness (HV) Avg
1	DP-TRIP-as welded	FZ	464
2	TRIP-TRIP-as welded	FZ	450
3	DP-TRIP-PWHT	FZ	425
4	TRIP-TRIP-PWHT	FZ	410
5	DP-as welded	BM	223
6	TRIP-as welded	BM	217
7	DP-PWHT	BM	221
8	TRIP-PWHT	BM	212

Fig. 10 Stress versus strain plots for **a** TRIP-TRIP and **b** DP-TRIP weldments

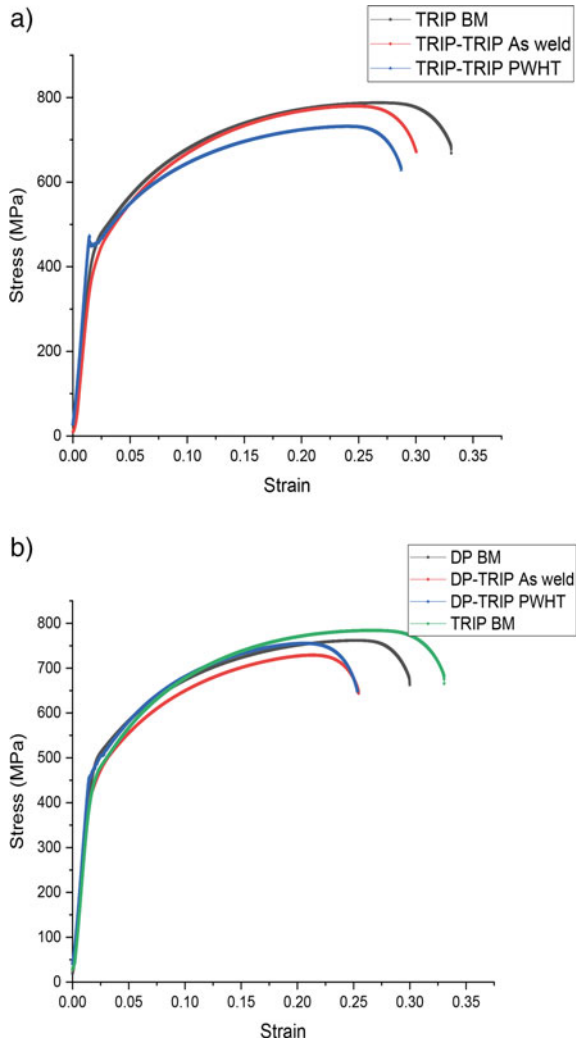


Table 4 Results of tensile test

S.No	Name of joint	YS (MPa)	UTS (MPa)	Elongation (%)	Failure location
1	DP base metal	479 ± 5	760 ± 10	29.2 ± 0.8	–
2	TRIP base metal	420 ± 9	784 ± 2	33.0 ± 0	–
3	DP-TRIP as-welded	455 ± 4	720 ± 20	26.9 ± 1	BM
4	TRIP-TRIP as-welded	410 ± 10	770 ± 10	28.9 ± 1	BM
5	DP-TRIP PWHTed	450 ± 8	750 ± 4	26.7 ± 1	BM
6	TRIP-TRIP PWHTed	460 ± 10	724 ± 4	27 ± 2	BM

and pin the dislocation. The YS of TRIP-TRIP welds after PWHT was increased due to the yield point phenomenon. On the other hand, the DP-TRIP welds showed UTS values lower than that of both the base metals. Elongation of these welds was found to be higher than DP steel and lesser than TRIP steel. The UTS of DP-TRIP weld after PWHT was increased by 30 MPa while not much change was observed in YS. Figure 10a, b shows the tensile specimens before and after the test respectively. As shown in Fig. 11b, all specimens tested were failed in BM, far from FZ.

Figure 12a, b show the Erichsen cup test samples of DP-TRIP and TRIP-TRIP weldments before the test and Fig. 12c, d shows the weldments after the test. Both the weld joints developed a crack in the fusion zone. In the Erichsen test, the presence of a crack in the fusion zone indicates the low or no effect of softening on formability. Though the fusion zone has high strength, poor plasticity has led to crack formation in it. Once the crack has initiated, the test was stopped and height of the cup was measured and the value is considered as an index for formability. The height of

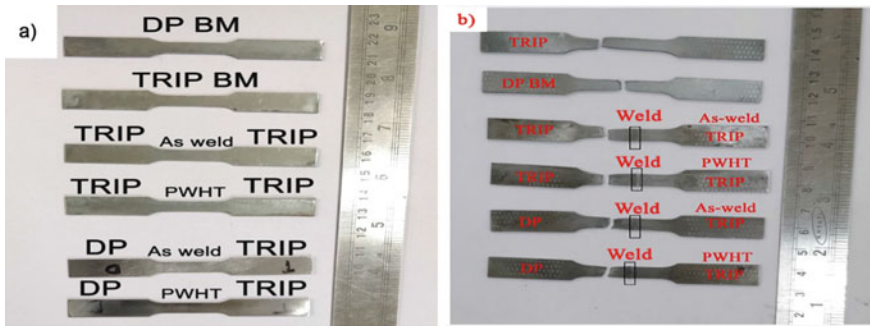


Fig. 11 Tensile specimens **a** before the test and **b** after the test

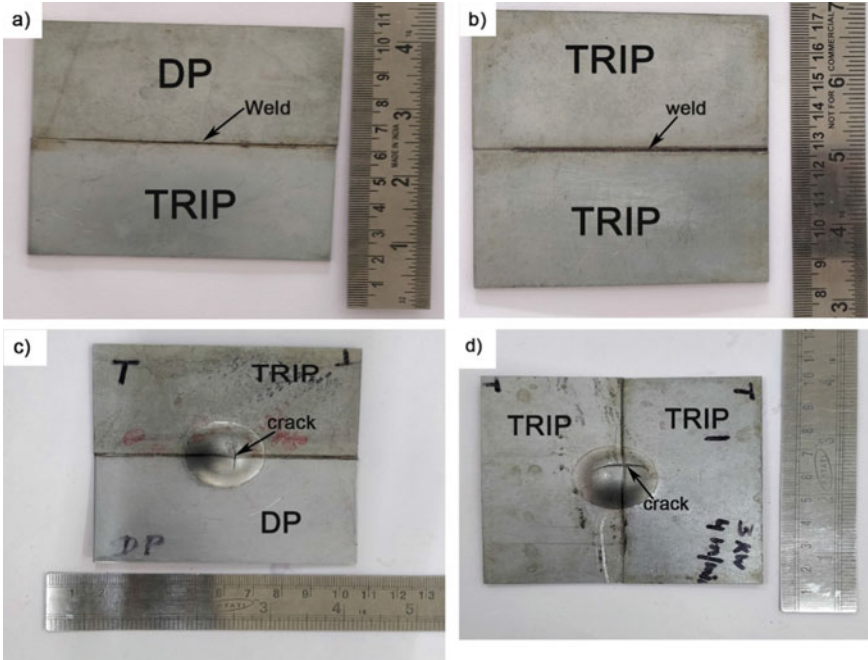


Fig. 12 Erichsen cupping test samples of **a** DP-TRIP, **b** TRIP-TRIP before the test, **c** DP-TRIP, and **d** TRIP-TRIP after the test

cups measured were 7.29 and 6.73 for TRIP-TRIP PWHTed weldment and DP-TRIP PWHTed weldment respectively. Thus it can be concluded that the TRIP-TRIP weldments had better formability than DP-TRIP weldments.

4 Conclusions

Similar TRIP-TRIP weldments and dissimilar DP-TRIP weldments were prepared in butt joint configuration using laser beam welding. A PWHT at 250 °C for 2 h was carried out on the weldments. The effect of laser welding and PWHT on the microstructure and mechanical properties of the weldments was investigated and the following conclusions were drawn.

1. Defect-free weldments without cracks, porosity, inclusions, etc. were prepared.
2. Different zones viz., FZ, HAZ, BM were observed in all the weldments in as-welded and PWHTed conditions. Martensite was observed in the FZ of all the weldments.
3. Hardness profiles revealed a sequential increase in hardness from BM to FZ through HAZ irrespective of weldment. With PWHT, a small decrease in FZ hardness was observed for both DP-TRIP and TRIP-TRIP weldments.

4. All the tensile specimens fractured in the BM, far from FZ, irrespective of the weldment in as-welded and PWHTed conditions.
5. Yield point phenomenon was observed for TRIP-TRIP weldment after PWHT, while the remaining weldments exhibited a continuous yielding behavior.
6. All the tensile test specimens exhibited a significant amount of elongation which is a clear indication of ductile failure.
7. The Erichsen cup test has concluded that TRIP-TRIP weldments had high formability than DP-TRIP weldments.

References

1. Schmitt, J.H., Jung, T.: New developments of advanced high-strength steels for automotive applications. *Comptes Rendus Physique* **19**(8), 641–656 (Elsevier Masson SAS, Dec. 01) (2018). <https://doi.org/10.1016/j.crhy.2018.11.004>
2. Khedkar, P., Motagi, R., Mahajan, P., Makwana, G.: A review on advance high strength steels. *Int. J. Curr. Eng. Technol.* **6**, 240–243 (2016)
3. Demeri, M.Y.: *Advanced High-strength Steels: Science, Technology, and Applications* (2013)
4. Fonstein, N.: *Advanced High Strength Sheet Steels* (2015)
5. Shome, M., Tumuluru, M.: *Introduction to Welding and Joining of Advanced High-Strength Steels (AHSS)*. Elsevier Ltd, (2015)
6. Mangudkar, U.V., Hiremath, R.B.: Formability analysis and its parameters—a review paper. *Int. J. Eng. Res. Appl.* **3**(6), 300–303 (2013)
7. Nayak, S.S., Biro, E., Zhou, Y.: Laser welding of advanced high-strength steels (AHSS). In: *Welding and Joining of Advanced High Strength Steels (AHSS)* (2015)
8. Baltazar Hernandez, V.H., Nayak, S.S., Zhou, Y.: Tempering of martensite in dual-phase steels and its effects on softening behavior. *Metall. Mater. Trans. A Phys. Metall. Mater. Sci.* **42**(10), 3115–3129 (2011). <https://doi.org/10.1007/s11661-011-0739-3>
9. Farabi, N., Chen, D.L., Zhou, Y.: Microstructure and mechanical properties of laser welded dissimilar DP600/DP980 dual-phase steel joints. *J. Alloys Compd.* **509**, 982–989 (2011). <https://doi.org/10.1016/j.jallcom.2010.08.158>
10. Farabi, N., Chen, D.L., Li, J., Zhou, Y., Dong, S.J.: Microstructure and mechanical properties of laser welded DP600 steel joints. *Mater. Sci. Eng. A* **527**(4–5), 1215–1222 (2010). <https://doi.org/10.1016/j.msea.2009.09.051>
11. Sreenivasan, N., Xia, M., Lawson, S., Zhou, Y.: Effect of laser welding on formability of DP980 steel. *J. Eng. Mater. Technol.* **130**(4), 041004 (2008). <https://doi.org/10.1115/1.2969246>
12. Dong, D., et al.: Microstructure and deformation behavior of laserwelded dissimilar dual phase steel joints. *Sci. Technol. Weld. Join.* **21**(2), 75–82 (2016). <https://doi.org/10.1179/1362171815Y.0000000067>
13. Gong, H., Wang, S., Knysh, P., Korkolis, Y.P.: Experimental investigation of the mechanical response of laser-welded dissimilar blanks from advanced- and ultra-high-strength steels. *Mater. Des.* **90**, 1115–1123 (2016). <https://doi.org/10.1016/j.matdes.2015.11.057>
14. Sharma, R.S., Molian, P.: Yb:YAG laser welding of TRIP780 steel with dual phase and mild steels for use in tailor welded blanks. *Mater. Des.* **30**(10), 4146–4155 (2009). <https://doi.org/10.1016/j.matdes.2009.04.033>
15. Xia, M., Biro, E., Tian, Z., Zhou, Y.N.: Effects of heat input and martensite on HAZ softening in laser welding of dual phase steels. *ISIJ Int.* **48**(6), 809–814 (2008). <https://doi.org/10.2355/isjinternational.48.809>
16. Wang, J., Yang, L., Sun, M., Liu, T., Li, H.: A study of the softening mechanisms of laser-welded DP1000 steel butt joints. *Mater. Des.* **97**, 118–125 (2016). <https://doi.org/10.1016/j.matdes.2016.02.071>

17. Nayak, S.S., Biro, E.: Laser welding of advanced high-strength steels (AHSS). In: *Welding and Joining of Advanced High Strength Steels (AHSS)*. Elsevier, pp. 71–92 (2015)
18. Kuril, A.A., Janaki Ram, G.D., Bakshi, S.R.: Microstructure and mechanical properties of keyhole plasma arc welded dual phase steel DP600. *J. Mater. Process. Technol.* **270**, 28–36 (2019) (October 2018). <https://doi.org/10.1016/j.jmatprotec.2019.02.018>
19. Wang, J., Yang, L., Sun, M., Liu, T., Li, H.: Effect of energy input on the microstructure and properties of butt joints in DP1000 steel laser welding. *Mater. Des.* **90** (2016). <https://doi.org/10.1016/j.matdes.2015.11.006>
20. Huan, P.C., et al.: Effect of martensite content on failure behavior of laser welded dual-phase steel joints during deformation. *J. Mater. Eng. Perform.* **28**(3), 1801–1809 (2019). <https://doi.org/10.1007/s11665-019-03941-3>
21. Wan, Z., Guo, W., Jia, Q., Xu, L., Peng, P.: Hardness evolution and high temperature mechanical properties of laser welded DP980 steel joints. *High Temp. Mater. Process.* **37**(6) (2018). <https://doi.org/10.1515/htmp-2017-0007>
22. L. H. L. assembly Gallagher, M., Yan, B., Nadkarni, G., Polon, M., Aefferer, H.: Laser assembly welding of advanced high strength steels. In: *Adv Laser Appl Conf Expo. 2005*, vol. 3, pp. 49–62 (2005)
23. Xu, W., et al.: Microstructure and fatigue performance of single and multiple linear fiber laser welded DP980 dual-phase steel. *Mater. Sci. Eng. A* **553**, 51–58 (2012). <https://doi.org/10.1016/j.msea.2012.05.091>
24. Rashid, M.S., Rao, V.N.: Tempering characteristics of a vanadium containing dual phase steel. *Met. Trans A* **13**(N 10), 1679–1686 (1982). <https://doi.org/10.1007/bf02647823>

Optimization of Fluid Modeling and Flow Control Processes Using Machine Learning: A Brief Review



Surbhi Razdan and Sarth Shah

Abstract Understanding and solving fluid-related problems pose a significant demand for computationally inexpensive flow simulations, which the conventional fluid mechanics approach fails to satisfy. Thus, researchers choose to incorporate fluid mechanics with Machine Learning (ML) as a possible solution. This technology provides several tools and algorithms that help with prediction-based decision making, building optimized control theories, experience-based learning, and many more, all of which depend upon available data. Since its inception, the field of fluid mechanics has generated a lot in terms of experimental and simulation data. Hence, we can apply Machine Learning to extract meaningful information from fluid flow databases. Complex domains of fluid mechanics such as turbulence modeling, active flow control, and optimization all seek to gain from such a multidisciplinary approach. However, these domains from the world of fluids pose new problems for the data science world. These newly found complexities encourage engineers to create more robust learning models than conventional ones. Thus, a blend of fluid mechanics and machine learning creates a powerful and vastly complex field of study that will help completely revolutionize current research and industrial applications. This paper covers research from the earliest to some of the most recent ML algorithms and provides a brief overview of ways these algorithms complement the field of fluid mechanics. Three case studies—turbulence closure modeling using ML, flow control and manipulation using ML, and aerodynamic shape optimization, are used to explain this. To help better understand these applications, the underlying fundamentals of supervised, semi-supervised, and unsupervised learning models and some of the most widely used algorithms are also under consideration in the paper. The paper, thus, covers in great depth both the fields of fluids and ML

Keywords Turbulence modeling · Flow control · Machine learning

S. Razdan (✉) · S. Shah
School of Mechanical Engineering, Dr. Vishwanath Karad MIT World Peace University, Pune,
Maharashtra 411038, India
e-mail: surbhi.razdan@mitwpu.edu.in

© The Author(s), under exclusive license to Springer Nature Singapore Pte Ltd. 2022
K. C. Popat et al. (eds.), *Advances in Mechanical Engineering and Material Science*,
Lecture Notes in Mechanical Engineering,
https://doi.org/10.1007/978-981-19-0676-3_6

1 Introduction

Certain disciplines of fluid mechanics, such as turbulence modelling, accurate fluid flow simulations, active flow control, and so on, have posed computational hurdles resulting from the complexity of the flow from their beginnings that have yet to be entirely overcome. These complexities are a result of high dimensional, non-linear characteristics of the flow, observed at varying spatiotemporal scales. The entirety of the nineteenth century witnessed the development of newer and efficient mathematical and experimental models to tackle and understand complications related to fluids. Research in the first half of the century kicked off with the development of control mechanisms such as, rotating cylindrical sails for ships, wires on wing profiles, etc. [1]. The latter part of the century saw the development of even more efficient flow manipulation devices (e.g. wings/spoilers, splitter plates, vortex generators, etc.) [1], some of which continue being used on modern cars for aerodynamic advantage, even till date. By the end of the nineteenth century, relatively better computational systems had given rise to Direct Numerical Simulations (DNS); a method that formed the bedrock of understanding fluids, that is still in use today. Kim et al. [2] studied skin friction drag by resolving different turbulence scales using Direct Numerical Simulations. Active turbulence control [3] or vorticity flux control [4] for drag minimization were also performed using DNS. Some recent studies include, simulation of fully developed incompressible flow through a pipe on 630 million grid nodes using DNS [5], DNS of unsteady flow in channel with uneven walls [6], and comparison of turbulent flow through smooth square duct and through ribbed square duct using DNS [7].

Thus, fluid mechanics has generated vast quantities of data in terms of empirical flow observations, experimental results, and flow field simulations up to this point [8]. Availability of data and, advances in high performance computing capabilities have fueled the development of large-scale databases (e.g. NOAA Database [9]), time efficient simulations through parallel computations, advanced data processing algorithms, and softwares that allow data transfer and work integration with other softwares [8, 10]. Indeed, start of the twentieth century was the beginning of a new era of fluid mechanics. Fluid mechanics of today is not only governed by the first principles, but is also data driven [8]. These newfound advances have, thus, created a growing interest among researchers and scientists to pair fluid mechanics with the field of machine learning. However, the blend of these two fields is not entirely an accomplishment of the twentieth century. Some profound research works were conducted towards the end of the nineteenth century that used Proper Orthogonal Decomposition (POD) [11], neural networks [12] and, suboptimal control strategies [13] to generate feedback control models in order to minimize drag by actively controlling turbulence [1].

At present, a wealth of different, robust Machine Learning algorithms are available, each offering its own benefits depending on the mode of learning, architecture and implementation strategy. Apart from this, the commercial successes of ML in the fields of image recognition, control and reduced order modeling [14] have intrigued

researchers to test these algorithms for fluids as well. ML provides sufficiently generalizable and flexible tools that can be formulated to suit complex requirements of fluid modelling such as high dimensionality of turbulence, nonlinearity of flow control and, multi-objective, multi-parameter aerodynamic shape optimization, etc. [8]. However, the fruitfulness of ML is high so long as the implementation of these algorithms is within the bounds of their limitations [15]; not all algorithms are suitable for all fluid flow problems and at the same time, a user must be aware of the proper implementation of a specific algorithm [8, 15]. Thus, fluid mechanics and machine learning, both fields stand to benefit from such a multidisciplinary approach. This paper provides a thorough review of the aforementioned blend of fluid mechanics and machine learning. The review first covers the fundamentals of machine learning followed by applications of ML in three of the most significant studies in fluid mechanics—turbulence closure modeling, active flow control and flow manipulation, and lastly, aerodynamic shape optimization.

2 Basics of Machine Learning

Human intelligence is defined as the fundamental method of obtaining knowledge by observing/learning a task. Machine learning, thus suggests, the use of some method to impart intelligence to a computer. In doing so, a machine is able to simulate human-like learning behavior that arises from obtaining new skills/knowledge based on past experiences, and existing knowledge to further improve the learning capabilities [16]. The evaluation of this subject is also performed in a human-like behavior. The computer is given a task, and its performance is assessed by determining how much it improved at completing the same job by using previous knowledge and experiences. This, in turn, imparts knowledge to the machine, allowing it to predict/forecast outcomes for situations that are similar but not identical to the one learned. As a result, it is a type of AI that digitises the fundamental process of ‘human learning’ [17].

Alike humans, a machine fails to learn a model in a single go and cannot make reliable enough predictions right away. It is looped through the process of learning, which eventually results in a good agreement between observed values and predicted values. Machine learning can hence, be formulated as an optimization tool that automates the process of iteratively solving multi-objective, multi-parameter problems of underlying physical formulae [1]. The extended version of ‘Machine learning as an optimization tool’ might seem both an over-exaggerated statement and an undeniable fact—The ideology of applying Machine Learning to a problem, as a whole can be thought of as an optimization task. Not only would we be optimizing the task of mapping inputs to outputs [8, 18], but also the use of our time, available computing hardware, implementation of sophisticated learning algorithms, and the monetary expenses that would have been, had we had to perform experiments to prove similar concepts.

Machine learning is not just a realization of the modern computer era, but has been an effort of researchers since the inception of the computer era [19]. However,

the inspiration of this field began not with computers, but at the roots of the issue—how we as humans learn to store, sort, and recall information as and when needed. In fact, the first machine learning algorithm, the perceptron [20] was heavily based on understanding the capabilities of the brain for perceptual recognition, generalization, recall, and thinking. The perceptron learning machine was mainly built for carrying out regression and classification tasks [20]. Soon enough, Dr. O.G. Selfridge in 1959, touched upon the topics of supervised and unsupervised learning models through his contribution—Pandemonium, a learning machine capable of recognizing patterns under human supervision [21]. In years 1960 and 1967, A.L. Samuel explored and touched upon training machine learning algorithms to play games [22] such as checkers [23]. Even after some remarkable strides in the field of Artificial Intelligence (AI), ML was criticized for not being as good as expected. However, there was a renewed interest in AI, soon after the advancement of reinforcement learning [24] and multi-layered neural networks [25], due to an algorithm—back propagation algorithm [26], that allowed fine tuning of parameters of the aforementioned multi-layered neural net (NN). Another big step in the field of neural networks, was the realization that NNs are universal function approximators [27], meaning, a sufficiently large NN could approximate any function given that its weights and biases are adjusted precisely [27]. As a result, by the early 1990s, ML and NNs were already being used in flow related problems: Particle image velocimetry [28, 29], reconstruction of turbulent flow fields using NNs and principal component analysis [30], reconstruct near wall turbulent flow using POD [31], etc. In recent years, ML has a wide set of applications in a variety of different fields such as, (a) Robotics: Use of machine learning in multi-agent systems (MAS) [32], learning motor primitives for single-stroke and rhythmic tasks by mimicking human presenter with reward driven self-improvement [33], actor-critic imaging for improvised robot learning [34]; (b) Games: Atari games [35], Go [36], Dota 2 [37], StarCraft 2 [38]; (c) Language Processing: convolutional neural network architecture for predictions in language processing domain [39], Algorithmic Actor-Critic Sequence Prediction for language processing applications [40], and many more.

Thus, in the past couple years, Machine Learning has outgrown the efforts of a few computer engineers trying to figure out the capabilities of computers in learning how to play games, to a broad study of statistical-computational theories that, when applied to learning processes give rise to newer learning algorithms that extend beyond the field of games, and into the field of speech recognition, computational mechanics, computer vision, data mining to extract patterns, and many more. Thus, ML has truly spun off the industry by opening up possibilities of integrating such learning architectures with other disciplines of engineering [41]. Machine learning is mainly classified in three major types—supervised learning, semi-supervised learning and, unsupervised learning, each of which branches into different types of algorithms (see Fig. 1). The types of learning are mentioned in the subsequent topics, but for the sake of brevity, all algorithms under each type are not mentioned.

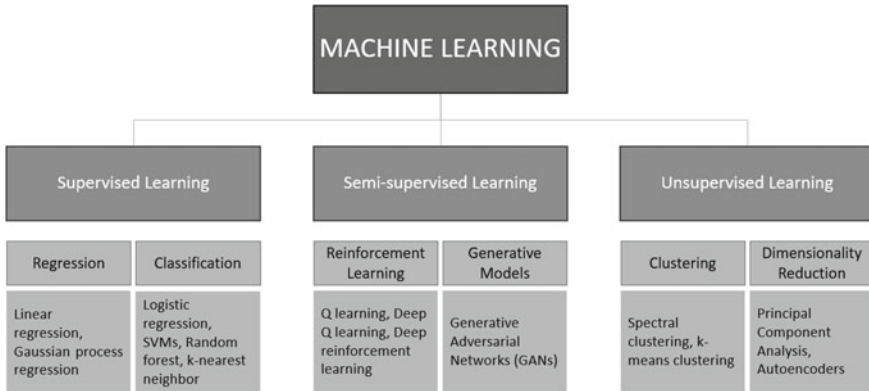


Fig. 1 General hierarchical structure of Machine Learning and its various different algorithms

2.1 Supervised Learning

The characteristic feature of supervised learning is, training data that is available in a labelled or annotated form. The name suggests the presence of a ‘supervision’ that is established in the form of instructions about that labels associated with the training examples for efficient learning. Typically these labels can be classes, numerical values (e.g. prices), etc. depending on the type of problem. Supervised learning algorithms make use of these training data to generate models and predict outputs for other unlabeled data [42].

As mentioned, depending upon the problem category (regression or classification), there exist a variety of different algorithms that can be implemented—Linear regression, Gaussian process, K-nearest neighbor, Support vector machines, Random forests, etc. The choice of the algorithm is governed entirely by the properties of the problem such as, category of problem, available data, size of dataset, number of features, etc. For the sake of brevity, only a few algorithms are mentioned for all three types of learning processes (supervised, semi-supervised and unsupervised). For additional information, readers are referred to the mentioned references.

Linear Regression. Linear regression, more or less, suggests the idea of interpolation [43]. While machine learning suffers at the hands of extrapolation, linear regression could also be used as an extrapolation tool, provided the number of samples in the training dataset is so large, that any new input has a high probability of either being in the training dataset or in close proximity of another sample point. As for its working principle, linear regression is the process of fitting a line through a collection of data points. This line has an intercept and a slope. Thus, in order to find the best fit, the slope and intercept values need to be optimized. A general, more commonly employed optimization criterion is that of least-squares, which suggests that the sum of all squared differences between the actual data points (label) and the predicted values (corresponding point on the line) should be as low as possible. The

mathematical representation of the least squares statement is what is called the cost function or loss function [44].

Studies involving regression have a wide set of applications, from predicting housing prices to studying patterns in rainfall data.

K-nearest neighbor. Data can be of various kinds, and a lot of times either two or more classes can be observed in the labels. One of the most fundamental algorithms of ML to tackle this issue is the classification algorithm. Classification is the supervised process of a learning machine trying to determine which class (or group) the newly entered input belongs to. While, there are different methods to implement classification, the one under consideration is the K-nearest algorithm. The goal of the algorithm is to find the k observations from training data with distances closest to the input x and average their responses [44]. A cost function can be used to determine the goodness of the classification and the goal is to minimize the value of the cost function. A general cost function for a classification problem outputs the probability of misclassification.

K-nearest neighbor method has also been used in fluid mechanics to detect exotic wakes [45]. Other applications of classification and k-nearest algorithm include: Data mining application on weather prediction [46], deriving downscaled information regarding precipitation and temperature from prediction models of weather data [47].

Neural Networks. Neural networks are the most widely used algorithm of ML. This is due to the inherent property of neural networks to approximate any linear/non-linear function, provided that the network is sufficiently large and deep enough [27, 48]. A single unit of neural network, called the neuron is exactly analogous to the neuron in a human brain. These neurons stacked on top of one another is a single layer, and multiple layers stacked in parallel builds the neural network. It is common for all neural networks to have an input layer, an output layer, and depending upon the complexity of the problem, one or many layers in between, also called as hidden layers. Among the most common types of neural networks is the feed forward neural network. Feed forward neural networks have the aforementioned structure and, propagate information by the activation (also called firing) and deactivation of neurons of one layer. The firing of a neuron is governed by a non-linear activation function that takes in an input, either from an input layer or the weighted output from a previous neuron layer, and computes a new output. Thus, all the neurons of a layer, activating and deactivating irrespective of one another is what carries forward information received at the input layer.

Differences in the structure of the NNs and the activation functions give rise to different working principles and hence, a variety of applications that NNs can tackle. A few powerful classes of networks are: convolutional neural networks (CNNs), best known for image and pattern recognition [49, 50], Recurrent neural networks (RNNs), best known for time dependent data (e.g. videos) [51, 52], and Long short-term memory (LSTM) algorithms, best known for utilizing cell states and gating mechanisms [8, 53, 54].

2.2 *Semi-supervised Learning*

Semi-supervised learning reflects a more bio-inspired and human-like learning approach used to train machines. This human-like approach is established through the presence of both labelled and unlabeled data. This is a rather unique and unconventional approach of learning as opposed to pure unsupervised or pure supervised learning. The type of labelled data available is purely dependent on the type of semi-supervised algorithm implemented. While some algorithms make use of traditional labelled data (like in classification problems), some algorithms make use of ‘rewards’ to inform the machine of the presence of labels. The goal of semi-supervised architecture is to understand the effect of such a unique combination of training data [55]. Depending on the type of problem and the desired output, a variety of different semi-supervised learning algorithms can be implemented—Generative Adversarial Networks (GANs), Q learning, Deep Q learning, Reinforcement Learning (RL), Deep Reinforcement Learning (DRL), etc.

Generative Adversarial Networks (GANs). Generative adversarial networks have been a part of extensive research since 2014 [56] and have been implemented in various applications ever since: image super resolution [57], object detection [58], video generation [59], etc. [60]. The working principle of GANs is rather unique, since the learning is competitive between two networks—the generative network (generates new data) and the discriminative network (classifies data either as generated or original). The goal of the generative network is to generate new samples based on the learned probability distribution of the training data. Hence, the generative network learns to generate data as detailed as possible, in order to maximize the probability of making the generated data pass as original. On the other hand, the discriminative network learns to tell apart even the most accurately generated data from the original data, and in doing so, maximizes the probability of classifying the data accurately. In an adversarial learning environment, such as the one under consideration, the competitiveness between the networks, only ends up improving them simultaneously. This is a characteristic feature of GANs that make it a go-to learning algorithm for a wide set of applications [56, 61].

Q Learning. Q learning falls under the category of reinforcement learning and is a classic example of reward based learning. The labels that supervise Q learning, are these sparsely placed rewards that determine the “goodness” of the algorithm’s performance. Q learning comprises of two fundamental entities—the agent and the environment. The agent observes the environment to determine its state at time ‘ t ’, denoted by s_t . The observed state helps the agent determine an action at the same time step (a_t), that will lead to a reward (r_t). Another terminology, called trajectory, denoted by τ , is introduced to club together all states and actions of agent from time ($t = 0$ to T). The goal of the learning algorithm is to maximize the reward over the entire trajectory. However, this involves some inefficiencies, because such a formulation involves temporally distant rewards as well. In order to reduce the effect of these temporally distant rewards, and only have the immediate rewards taken into consideration, another term, called discount factor, denoted by γ , is introduced

which value ranges between 0 and 1. The discount factor is responsible for making the values of temporally distant rewards almost insignificant, whilst keeping few of the immediate rewards almost unaffected. Therefore, the final goal of the agent can now be stated as, following a process that maximizes the discounted reward over an entire trajectory, meaning, maximizes the discounted cumulative reward [62]. This so-called ‘process’, that is essentially a mapping between optimal actions and states is called the policy ($a = \pi(s)$), and the goodness of following a policy is given by a value function. Thus, if an optimal value function is learned, the agent can then use that information to determine the policy, which in turn dictates the optimal actions that need to be taken in each state, in order to maximize the reward. One such value function used in Q learning is the Q function which is expressed through a Q table. The Q table stores the values of optimal Q functions for all possible combinations of state-action pairs, allowing the agent to choose the best action by using the Q table as a simple look-up table.

Q learning has quite a few downsides and limitations as well, that researchers are trying to improve, by building up on the basic algorithm using newer, more efficient algorithms: Nash Q learning [63], Double Q learning [64].

Deep Reinforcement Learning (DRL). While the above method of generating Q tables is a good enough method, scaling the tables to accommodate state-action pairs for a multi-iterative, large scale problem is quite a tedious task; not only computationally expensive, but also time inefficient. The fact that neural networks are universal non-linear function approximators [27, 48], provides a rather unique solution to tackle the issue of scaling to big data—a deep enough neural network can be trained to approximate the value functions. This notion of using deep neural networks in reinforcement learning gave rise to Deep reinforcement Learning (DRL) [62]. A significant study on using DRL with Q learning was performed, in order to reduce Q learning algorithm’s tendency to overestimate the value function [65]. After succeeding in using DRL to play Atari games [35], Volodymyr et al. set out to create an universal intelligence algorithm using DRL to be able to learn a variety of challenging tasks [66]. DRL has made its way in control methodologies and robotics as well [67, 68].

2.3 *Unsupervised Learning*

Finally, neither desired outputs nor rewards from the environment are supplied in the third and final form of learning, known as unsupervised learning. Unsupervised algorithms are used to analyze data that is essentially noisy. The use of machine learning to unstructured noisy data results in the discovery of patterns, reduced order models, and efficient data separation. These findings are then utilized to make decisions, make forecasts, and communicate data [69].

Principal Component Analysis (PCA). Principle component analysis is a fundamental dimensionality reduction algorithm that goes by many different names

depending on the field of application. A few such applications include PCA in signal processing, called Karhunen–Loeve Transform, PCA in computational engineering applications, called Proper Orthogonal Decomposition (POD) or Singular Value Decomposition (SVD), etc. However, irrespective of the field of application, all the algorithms operate in a similar sense of reducing high dimensional data to an orthonormal basis vector set. These basis vectors are also defined as best-fit lines for the data where a best-fit line is defined as, a line across which the data is seen to have the most variance, and the least averaged squared distances from data points. Reduced Order Modelling (ROM) is essentially a PCA of data, but instead of choosing all principal components (eigenvectors), only the first few components that capture majority of the features, are used, thus reducing the dimensions of data. One of the oldest applications of PCA was in 1987, to develop a characterization process for human faces [70]. PCA has also been used in the field of environmental and atmospheric sciences. One such example involves applying the non-linear PCA algorithm to hydrodynamic circulation and other such conditions in coastal areas [71]. Even in the field of robotics, PCA algorithms have been implemented to learn humanoid motion features [72].

Autoencoders. In situations when the available input data is high dimensional, building models and simulating the output is very computationally expensive. To tackle this issue, a considerable amount of effort and research has gone into building reduced order models of these high dimensional data. One such method is PCA which finds the eigenfeatures of data, thereby reducing the dimensions of the data to only a select number of eigenfeatures. Another such working model is the autoencoder. The autoencoder in working, is essentially no different than a PCA algorithm. These autoencoders consist of two networks, an encoder and a decoder. The role of the encoder is to find a set of key features that can be used as the orthonormal basis to project the data onto. The role of the decoder is the exact opposite as that of the encoder. The decoder takes as its input, the reduced order data and tries to map it back to its original high dimensionality form. The efficiency of the autoencoder lies in the goodness of the mapping between input and output with least distortion [73]. A significant downside of scaling generative learning algorithms to capture rich data distributions is the probability of imprecision as the learning progresses. An efficient solution prescribed for this issue is the use of autoencoders. Modified autoencoder algorithms such as, adversarial autoencoders [74] and Importance Weighted Autoencoders [75] have been proven to give the best results.

k-means clustering. The “unsupervised version” of classification is called clustering. Clustering algorithms perform the exact same task as classification algorithms, only without any supervision or labeled data. While a variety of clustering algorithms are available to choose from, k-means clustering is known to be the fastest to converge, thus making it preferable for different applications. The algorithm starts off by taking the value of k as an user input. K signifies the number of clusters that the algorithm will be looking for. After initiating k random cluster centroids, the distance (generally euclidean) between each data point and the k centroids is calculated. Points closest to any of the centroids is marked as belonging to that cluster. Likewise, k such clusters

are formed depending on all points closest to a centroid than any other centroid. In the next step, the algorithm averages all the points of a cluster to calculate the centre of gravity of that respective cluster, which will be the new centroid. K such new centroids are calculated, following which, new clusters are formed due to changed distances between data points and cluster centroids. These two processes are iterated till convergence, meaning, the centroids stop moving and data points stop migrating between clusters [76]. Ever since the advent of k -means, modifications have been proposed to improve convergence to a more desirable local minima [77], and reduce computational load to further increase the speed of reaching convergence condition [78]. The field of fluid mechanics and computational fluid dynamics have a few unique examples of using k -means clustering such as, integrating k -means clustering algorithm and CFD simulations for maintaining a local control over the temperature using an HVAC system [79], clustering for efficient discretization of a fluid mixing layer [80].

3 Case Study: Turbulence Closure Modeling Using Machine Learning

3.1 Reynolds Averaged Turbulence Modeling Using Deep Neural Networks with Embedded Invariance [81]

Reynolds Averaged Navier Stokes (RANS) turbulence models have been in existence since years now. However these models suffer from inaccuracies that arise from a certain assumptions, truncations and discretization schemes, etc. Thus, there is a significant need to improve these models. This study, focused on solving the issue by using deep neural networks to learn the Reynolds stress anisotropy tensor from flow simulation data. The network, trained via stochastic gradient algorithm, consists of 8 hidden layers with 30 nodes in each layer. The novelty of this architecture however, arises from the multiplicative layer which embeds Galilean invariance into the neural network, thus allowing the network to predict the full anisotropy tensor, as opposed to predicting only the anisotropy eigenvalues. This novel architecture, called the Tensor Basis Neural Network (TBNN) (see Fig. 3), essentially embeds rotational invariance, thus nullifying the effect of the observer's orientation on flow physics. Simulation data of 9 flows generated using RANS, LES and DNS were used, out of which, 6 flows were used for training, 1 for validation and 2 for testing. The salient features about the test cases were that, one test case had a wavy geometry duct, a geometry that exhibited flow separation and was not included in the training set, while the second test case had a duct with corners. The TBNN predictions were proven to be significantly more accurate than both linear eddy viscosity RANS model and the non-linear eddy viscosity model. Not only was the model successful in resolving corner vortices in the second test case, but also showed fairly accurate flow separation in the wavy geometry test case, a geometry that was never encountered before. This strongly suggested

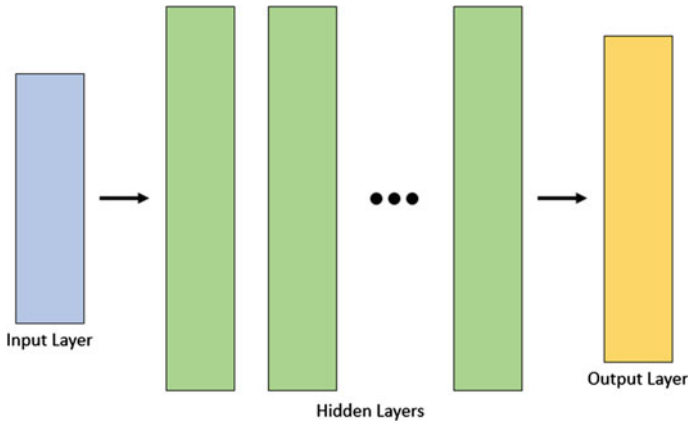


Fig. 2 Architecture of a general Deep Neural Network where the arrows show the direction of information propagation

that the network had shown remarkable extrapolation performance by learning the underlying fluid physics efficiently. The study was concluded by showing that the TBNN model had overcome all the shortcomings of the baseline LEV RANS model (Fig. 2).

3.2 *Bayesian Uncertainty Analysis with Applications to Turbulence Modeling [82]*

This paper focused on applying Bayesian inference techniques in order to calibrate complex mathematical models (governing equations of fluid flows—Navier stokes) to predict certain pre-decided quantities of interest (QoI). These quantities of interest are defined as predictions of a set of output quantities that are essential for making informed decisions about the system. In the approach proposed by the authors, a model of incompressible, turbulent flow over a flat plate under various pressure gradient conditions was considered. 3 stochastic models with the same physics and the same uncertainties in the experimental data were used. The only differentiating factor about these models was the probabilistic representation of the physics. The relations unfolded from the RANS equations gave rise to 7 individual model calibration parameters. It was noted that specific values of the parameters gave rise to different canonical flow physics (free shear flows, zero-pressure-gradient boundary layer, etc.) and thus, was concluded, that a single turbulence model most certainly will fail to generalize for different types of flows. Such a behavior is observed because certain parameters are associated with features like, near-wall behavior, intermediate distances from the wall, and outer parts of the boundary layer, and hence, the ability of the model to predict the quantity of interest depends on the values of

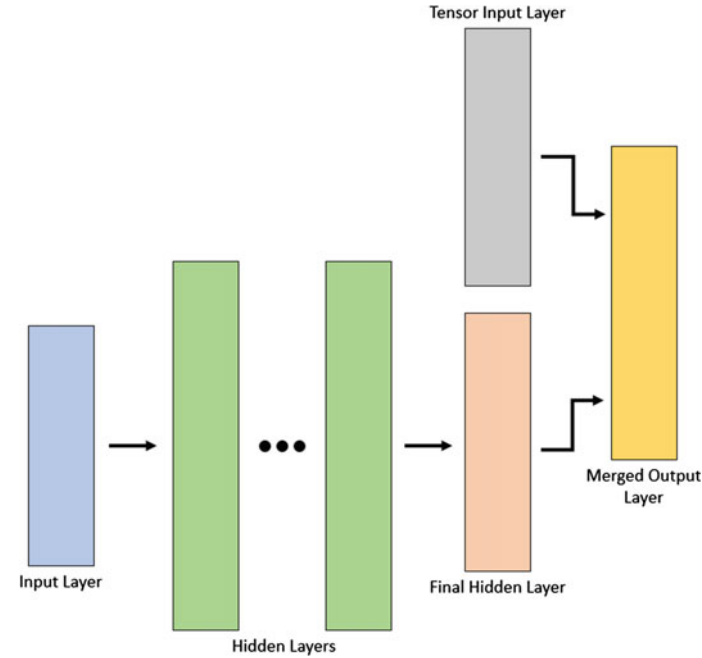


Fig. 3 Novel TBNN architecture containing a multiplicative layer to embed Galilean invariance in the network. Arrows show the direction of information propagation. Image reconstructed based on [81]

these 7 parameters. Such a Bayesian inference method was applied to the Spalart Allmaras turbulence model. The aforementioned parameters were calibrated for the three classes after the model learned patterns in the experimental data of incompressible flow over flat plate. Thus, essentially, all three classes were formulated to predict the QoI. The study was concluded by taking note of the effect of model class evaluation procedure on the uncertainty of QoI, since all three models were similar otherwise.

3.3 Predictive RANS Simulations via Bayesian Model-Scenario Averaging [83]

Turbulence modelling has forever been known to be the most significant source of error in most RANS simulations. One way to deal with this error is to estimate the error and calibrate the output accordingly. However, not a lot of error estimators currently exist to tackle the issue. A build-up on the study conducted by Cheung et al. 2011 is presented in this paper. Instead of considering model inadequacy as the deviation of actual process from its predicted simulation output, as is common practice,

the authors suggested modeling the probabilistic inadequacy in the empirical model itself, thus, providing a generalizable framework for incorporating the inadequacy in turbulence closure problems. While the problem was that of flat plate boundary layer flow at varying pressure gradient conditions; unlike Cheung et al. 2011, experimental data was achieved from k - ϵ , k - ω , Spalart-Allmaras, Baldwin-Lomax and stress- ω turbulence closure models. After performing Bayesian inference on each of the turbulence model for 14 different scenarios, a strong dependence between closure coefficients and scenarios was observed. These results were a concrete enough proof that, there is no single best choice of turbulence model or closure coefficients, instead, Bayesian Model-Scenario Averaging (BMSA) method is to be used. The study was concluded by experimenting with another method to further improve results, which was, developing a smart scenario sensor which improved the predictor capabilities for all 14 scenarios.

3.4 Sub-grid Modelling for Two-Dimensional Turbulence Using Neural Networks [84]

In this study, the authors experimented with sub-grid modeling of data-driven Kraichnan turbulence using artificial neural networks involving both a-priori and a-posteriori assessments of decaying 2D turbulence. The major motivation behind conducting this study was the hope that a-priori model selection and a-posteriori deployment formulate a machine learning problem in order to unfold valuable information about the underlying flow physics. The deployed artificial neural network takes in as input, snapshots from DNS simulations. These snapshots are used for eddy-viscosity computations, based on which, the ANN predicts a temporally and spatially dynamic closure term which can be substituted in the vorticity equation either as a source or a sink of vorticity in much refined scales. Thus, the statistical approach proposed in this framework was proven to be successful in injecting a dynamic kinetic energy dissipation term in the 2D decaying turbulence models.

3.5 Using Statistical Learning to Close Two-Fluid Multiphase Flow Equations for a Simple Bubbly System [85]

In this study, direct numerical simulations using Neural Networks (NNs) were performed on bubbly multiphase flow physics to close the relatively simple model. The flow under consideration was assumed to be consisting of many nearly spherical bubbles rising in a unidirectional and recurring fashion with negligible fluctuations in the viscous term. Further it was assumed, that the initial vertical velocity and the average bubble density remain homogeneous in two of the three directions but fluctuates and varies in the remaining third direction. Thus, the formulation of the problem

was that of a flow in a rectangular box with effects of gravity visible, purely along the negative y -axis. The goal of the study was to essentially have a neural network learn a simulated flow, understand the underlying physics of the flow and use this “knowledge” to make valid closure predictions for similar flows but with different scenarios and conditions. Hence, the unidirectional evolution of bubbles for one initial condition was simulated using DNS followed by the generation of a database. In this database, information regarding the velocity profile and bubble distribution were stored throughout the evolution. The information from this database is used to generate the closure predictions. The model is then used to predict the evolution of bubbles with other different initial conditions. Overall, what was observed is that, the equations with the neural network closure were able to reproduce data similar to the DNS database thus proving the efficiency of such a system (in spite of the relative simplicity of the problem).

4 Case Study: Active Flow Control and Flow Manipulation Using Machine Learning

4.1 Efficient Collective Swimming by Harnessing Vortices Through Deep Reinforcement Learning [86]

Schooling is a concept generally employed by fish. The concept exhibits a ‘smartness’ in the swimming behavior, that is seen in the way fish navigate through complex, vortex rich flow fields in the wake of the fish in the front. While the actual mechanism used by fish is still unknown, Siddhartha et al. 2018, were able to simulate this intelligent schooling mechanism using deep reinforcement learning (DRL). The authors also showed significant improvements in propulsive efficiency and energy savings, that are achievable if the fish follows a certain specific path in the wake of the leader. High-fidelity fluid flow simulations were performed to replicate the vortex shedding behind the leader, while essential unsteadiness and two-way interactions between the vortical flow and the fish were captured to generate an ‘intelligent’ swimming policy using DRL. In order to train the DRL algorithm, two rewards were used, one that penalized the follower for swaying laterally away from the path of the leader, while the other simply equal to the follower’s swimming efficiency. It was observed, that followers started placing themselves, not in-line, but at off-center positions with a leader. In such off-center position(s), the follower(s) learned timely deformations of their bodies to efficiently harvest energy from the oncoming vortices. Thus, the study was able to prove the advantages of fish swimming in formations (schooling). Moreover, the possibility of using such bio-inspired energy harvesting techniques for navigating autonomous robot swarms, were shown to have promising implications.

4.2 Control of a Quadrotor with Reinforcement Learning [87]

In this paper, the authors explored using reinforcement learning to develop a control method for the actuators of a quadrotor. The goal of this study was to be able to train a neural net to map states of the agent (the quadrotor), to actuator commands, thus making the quadrotor capable of actively manipulating flow and stabilizing itself in air. In order to tackle this complex issue, the authors introduced a novel learning architecture called, deterministic on-policy method. This architecture made use of 4 total layers in the network, which mapped the input, an eighteen dimensional state vector, to the output, a four dimensional action vector (an action for each of the 4 available rotors) through two hidden layers consisting of 64 neurons each. The cost evaluation included different failure criteria such as the quadrotor touching the ground, angular velocity, linear velocity, etc. The evaluation of the policy was performed both experimentally and through simulations by placing the quadrotor in random states and recording the failure. While the simulations involved way point tracking and recovery tests, the experiments involved rather harsh test cases such as throwing the quadrotor upside-down at speeds up to 5 m/s, etc. In spite of such harsh initialization scenarios, the computation time of the policy was observed to be of the order of 7 μ s per time step. Thus, the study was concluded over the remarkable performance achieved by DRL in active flow manipulation.

4.3 Reinforcement Learning for Active Flow Control in Experiments [88]

This study is first of its kind, as it demonstrated the feasibility of applying reinforcement learning in experimental flow problems, capable of actively learning control strategies without a-priori knowledge of the flow. The experimental setup consisted of a main cylinder and two more cylinders placed parallel to the main cylinder, and downstream of the turbulent flow past the main cylinder. The two cylinders were such, that their rotational speeds and directions could be varied to achieve the goal of minimizing drag or maximizing power gain efficiency. The effect of diameter ratio (d/D) and gap ratio (g/D) were also taken into consideration. For the training purposes, another novel DRL algorithm, called Twin Delayed Deep Deterministic policy gradient algorithm was implemented. The architecture of the algorithm consisted of 2 hidden layers, with 256 neurons in each layer, all connected in a feedforward neural net. By designing appropriate rewards and applying effective noise reduction techniques, it was demonstrated that the learning agent achieves hydrodynamic performance stability in only four episodes. The result of rotating the control cylinders in equal and opposite directions close to their maximum speeds was the exact same achieved through computer simulations, thus proving the effectiveness of the experimental method. The study was concluded by proving that the

drag force across the main cylinder was indeed reduced by actively controlling the wake in an experimental setup.

4.4 Mixing Layer Manipulation Experiment From Open-Loop Forcing to Closed-Loop Machine Learning Control [89]

This study focuses on machine learning control in an experimental setup as well. The experiment under consideration is of a turbulent mixing layer performed in a sufficiently large, low speed wind tunnel. The flow is passed over a splitter plate. Along the span of the trailing edge of the plate, there were 96 circular nozzles with a diameter of 2 mm each. Each of them being separately controlled by a micro-valve actuator, flow manipulation for obtaining and studying characteristic mixing layer properties using control strategies was made possible. The overall goal to be achieved via local manipulation of mixing layer, was to maximize turbulent kinetic energy at a desired location downstream of the flow. Hot wire probes were placed downstream of the flow for sensing. The study proposed three different control strategies, namely—extremum-seeking adaptive control, Proper Orthogonal Decomposition (POD) analysis, and lastly, a bio-inspired, model free genetic algorithm called Machine Learning Control (MLC). Thus, the experiment was conducted with all three control strategies and the results were summarized. The extremum seeking control was shown to arrive at a local maximum with ease. However, determining whether a global maxima had been reached was not possible due to experimental complexities. Thus, there was no guarantee of an optimal solution by using extremum seeking control. The POD feedback approach was able to extract dominant mixing characteristics to feed back the optimal actuation frequency to itself. Finally, MLC was able to build up on the POD approach by making use of several sensors outputting velocity signals thus, automating the process of thresholding actuation. Thus, MLC strategy was proven to be the best in practice.

4.5 Closed-Loop Separation Control Using Machine Learning [90]

Another application of the novel Machine Learning Control (MLC), a model-free genetic learning framework, was studied in this paper. The goal of this study was to reduce and manipulate the recirculation zone caused due to flow over a backward-facing step (BFS) boundary. The experimental setup included a gravity driven flow over the BFS in a fluid channel at Reynolds number of 1350. The actuator in the setup was a slotted jet providing upstream actuation at 45° to the wall. Depending on this setup, the control law was optimized for the objective function of the problem

in 12 generations, by measuring recirculation area in real-time and linking that to the actuation value. With an 80% reduction in the recirculation area, the control law was also proven to be generalizable for other operative conditions and the study was concluded.

5 Case Study: Aerodynamic Shape Optimization Using Machine Learning

5.1 Multidisciplinary Shape Optimization in Aerodynamics and Electromagnetics Using Genetic Algorithms [91]

This study was based on improving the traditional design shape optimization problem that works on minimizing only a single objective function from a single discipline. The authors thus, take into consideration a multi-objective, multidisciplinary approach of optimizing a 2D airfoil shape for minimizing drag coefficient and electromagnetic backscatter using genetic algorithms. Hence, the two objective functions of the optimization were—reducing the drag coefficient whilst keeping the lift coefficient above a certain value, and the second objective function is equivalent to the integral of the transverse magnetic radar cross section (RCS) over a given sector. A CFD solver models the flow using finite volume discretization of the 2D inviscid Euler equations whereas, a fictitious domain method of computational electromagnetics (CEM) was used to analyze the 2D Helmholtz equation. The genetic algorithm used was based on Nondominated Sorting Genetic Algorithm (NSGA). By using 2 Bezier curves to parameterize the airfoil shape, a total of 15 design variables were formulated, which included 9 control points on the airfoil and 1 variable for the angle of attack of the airfoil. By assuming the wave to be incident at 10° , the backscatter was measured in a sector between 180° and 200° . While computation of solution took multiple iterations, an optimized solution for the airfoil shape was achieved by utilizing efficient parallel computing techniques.

5.2 Machine Learning for Adjoint Vector in Aerodynamic Shape Optimization [92]

Adjoint method is the most commonly employed practice in aerodynamic design optimization. However, from a computational standpoint, the cost of calculating the adjoint vector and the cost of computing the flow is approximately equal. In order to make the process time efficient and run faster, the authors studied incorporating machine learning with adjoint vector modeling. Deep neural network (DNN) was employed to generate a nonlinear mapping between the adjoint vector and the local flow variables. The architecture of the DNN was as follows—a total of 5 hidden layers

were constructed with 100, 100, 80, 50, and 30 neurons respectively. The output layer consisted of four neurons, each corresponding to one of the 4 quantities of the adjoint vector. The process was carried out at a Mach number of 0.75 and an angle of attack of 2.5° . Thus, by training on data of different combinations of incoming transonic states, drag reduction of NACA0012 airfoil was optimized. Moreover, it was found that the result generated by DNN-based adjoint method (DAM) was in accordance with the results obtained from the traditional adjoint method thus, proving the validity of DAM.

5.3 Aerodynamic Shape Optimization Using a Novel Optimizer Based on Machine Learning Techniques [93]

In this study, the authors proposed and tested the application of a different optimization technique paired with computational fluid dynamics (CFD) simulations, to a typical aerodynamic shape optimization problem of missile control surfaces. The novel optimizer made use of two most widely used machine learning techniques, reinforcement learning and transfer learning, to improve optimization performance and efficiency. Deep deterministic policy gradient (DDPG), a cutting-edge reinforcement learning approach, was utilised to extract the optimization experience from DATCOM, a fast aerodynamic prediction software. Then, by transferring learning, the experience was employed for CFD-based aerodynamic optimization. The problem of aerodynamic shape optimization of missile fins was used to evaluate the performance of the proposed optimizer. DDPG algorithm was then verified by comparing the obtained results against three traditional evolutionary algorithms—NCGA, NSGA-II, and MOPSO. Based on the results, it was concluded that, the new optimizer had improved in terms of search speed, the lift to drag ratio (L/D) of the missile was up by 18.67% than baseline, and 62.5% CFD calls were saved. Overall, TL-DDPG was shown to outperform evolutionary algorithms in terms of both search performance and optimised outcomes, thanks to the use of DATCOM's optimization expertise as priori knowledge, which is particularly useful for computationally expensive aerodynamic optimization problems.

6 Conclusions

Fluid mechanics is a complex, high-dimensional, nonlinear field of computational engineering. Even for some of the most frequent fluid-related issues, traditional techniques fail to give well-resolved solutions. While not perfect, machine learning provides the ideal tools for resolving fluid-related problems. This review paper is aimed to:

- Give a quick rundown of some of the most impressive uses of these strong machine learning techniques in fluid mechanics.
- Provide a review of machine learning basics, from its birth through some of the early algorithms to contemporary learning modes and principles.
- Applications of ML in three of the most significant fields of fluid mechanics, turbulence closure modelling, active flow control and flow manipulation, and aerodynamic shape optimization.
- And finally, some limitations of ML that despite current technological and computational advances, we are still a long way from finding a solution for fluid-related problems that is resolved at all spatiotemporal scales exhibited by natural flows.

As a conclusion, we would like to say that the purpose of this study is to excite and motivate readers by highlighting recent advances in the area, as well as to encourage academicians to continue working on innovative interfaces between the two domains. Having said that, we too are currently working on one such application—aerodynamic shape optimization of an airfoil using genetic algorithm (a semi-supervised learning algorithm).

References

1. Muller, S., Milano, M., Koumoutsakos, P.: Application of machine learning algorithms to flow modeling and optimization. In: Annual Research Briefs 1999. Center for Turbulence Research, Stanford University, pp. 169–178 (1999)
2. Kim, J., Moin, P., Moser, R.: Turbulence statistics in fully developed channel flow at low Reynolds number. *J. Fluid Mech.* **177**, 133–166 (1987)
3. Choi, H., Moin, P., Kim, K.: Active turbulence control for drag reduction in wall-bounded flows. *J. Fluid Mech.* **262**, 75–110 (1994)
4. Koumoutsakos, P.: Vorticity flux control for a turbulent channel flow. *Phys. Fluids* **11**(2), 248–250 (1999)
5. Wu, X., Moin, P.: A direct numerical simulation study on the mean velocity characteristics in turbulent pipe flow. *J. Fluid Mech.* **608**, 81–112 (2008)
6. Bhaganagar, K.: Direct numerical simulation of unsteady flow in channel with rough walls. *Phys. Fluids* **20**(10), 101508 (2008)
7. Mahmoodi-Jezeh, S., Wang, B.: Direct numerical simulation of turbulent flow through a ribbed square duct. *J. Fluid Mech.* **900**, A18 (2020)
8. Brunton, S.L., Noack, B.R., Koumoutsakos, P.: Machine learning for fluid mechanics. *Annu. Rev. Fluid Mech.* **52**, 477–508 (2020)
9. NOAA Database homepage. <https://www.ncdc.noaa.gov/data-access>
10. Perlman, E., Burns, R., Li, Y., Meneveau, C.: Data exploration of turbulence simulations using a database cluster. In: SC'07: Proceedings of the 2007 ACM/IEEE Conference on Supercomputing, pp. 1–11. Association for Computing Machinery, Reno, Nevada (2007)
11. Lumley, J., Blossey, P.: Control of turbulence. *Annu. Rev. Fluid Mech.* **30**, 311–327 (1998)
12. Lee, C., Kim, J., Babcock, D., Goodman, R.: Application of neural networks to turbulence control for drag reduction. *Phys. Fluids* **9**(6), 1740–1747 (1997)
13. Lee, C., Kim, J., Choi, H.: Suboptimal control of turbulent channel flow for drag reduction. *J. Fluid Mech.* **358**, 245–258 (1998)
14. Brunton, S.L., Hemati, M.S., Taira, K.: Special issue on machine learning and data-driven methods in fluid dynamics. *Theoret. Comput. Fluid Dyn.* **34**, 333–337 (2020)

15. Brenner, M., Eldredge, J., Freund, J.: Perspective on machine learning for advancing fluid mechanics. *Phys. Rev. Fluids* **4**(10), 100501 (2019)
16. Wang H., Cuiqin, M., Zhou L.: A brief review of machine learning and its application. In: 2009 International Conference on Information Engineering and Computer Science, pp. 1–4. IEEE, Wuhan, China (2009)
17. Ray, S.: A quick review of machine learning algorithms. In: 2019 International Conference on Machine Learning, Big Data, Cloud and Parallel Computing (COMITcon), pp. 35–39. IEEE, Faridabad, India (2019)
18. Cherkassky, V., Mulier, F.M.: *Learning from data: Concepts, Theory, and Methods*, 2nd edn. Wiley-IEEE Press, Hoboken, NJ (2007)
19. Carbonell J.G., Michalski R.S., Mitchell T.M.: An overview of machine learning. In: Michalski R.S., Carbonell J.G., Mitchell T.M. (eds) *Machine Learning. Symbolic Computation*. Springer, Berlin, Heidelberg (1983)
20. Rosenblatt, F.: The perceptron: a probabilistic model for information storage and organization in the brain. *Psychol. Rev.* **65**(6), 386–408 (1958)
21. Selfridge, O.G.: Pandemonium: a paradigm for learning. In: Blake, D., Uttley, A. (Eds.) *Proceedings of the Symposium on Mechanization of Thought Processes*, pp. 511–529. HMSO, London (1959)
22. Samuel, A.L.: Programming computers to play games. *Adv. Comput.* **1**, 165–192 (1960)
23. Samuel, A.L.: Some studies in machine learning using the game of checkers. II-recent progress. *IBM J. Res. Dev.* **11**(6), 601–617 (1967)
24. Sutton, R.S.: Learning to predict by the methods of temporal differences. *Mach. Learn.* **3**, 9–44 (1988)
25. Crick, F.: The recent excitement about neural networks. *Nature* **337**(1), 129–132 (1989)
26. Rumelhart, D.E., Hinton, G.E., Williams, R.J.: Learning representations by back-propagating errors. *Nature* **323**(1), 533–536 (1986)
27. Siegelmann, H.T., Sontag, E.D.: On the computational power of neural nets. *J. Comput. Syst. Sci.* **50**(1), 132–150 (1995)
28. Teo, C.L., Lim, K.B., Hong, G.S., Yeo, M.H.T.: A neural net approach in analyzing photograph in PIV. In: *Conference Proceedings 1991 IEEE International Conference on Systems, Man, and Cybernetics*, pp. 1535–1538. IEEE, Charlottesville, VA, USA (1991)
29. Grant, I.: Particle image velocimetry: a review. *Proc. Inst. Mech. Eng. C J. Mech. Eng. Sci.* **211**(1), 55–76 (1997)
30. Baldi, P., Hornik, K.: Neural networks and principal component analysis: learning from examples without local minima. *Neural Netw.* **2**(1), 53–58 (1989)
31. Milano, M., Koumoutsakos, P.: Neural network modeling for near wall turbulent flow. *J. Comput. Phys.* **182**(1), 1–26 (2002)
32. Stone, P., Veloso, M.: Multiagent systems: a survey from a machine learning perspective. *Auton. Robot.* **8**, 345–383 (2000)
33. Kober, J., Peters, J.: Learning motor primitives for robotics. In: 2009 IEEE International Conference on Robotics and Automation, pp. 2112–2118. IEEE, Kobe, Japan (2009)
34. Pinto, L., Andrychowicz, M., Welinder, P., Zaremba, W., Abbeel, P.: Asymmetric Actor Critic for Image-Based Robot Learning. [arXiv:1710.06542](https://arxiv.org/abs/1710.06542) 2017 [cs.RO] (2017)
35. Mnih, V., Kavukcuoglu, K., Silver, D., Graves, A., Antonoglou, I., Wierstra, D., Riedmiller, M.: Playing Atari with Deep Reinforcement Learning. [arXiv:1312.5602](https://arxiv.org/abs/1312.5602) [cs.LG] (2013)
36. Silver, D., Schrittwieser, J., Simonyan, K., Antonoglou, I., Huang, A., Guez, A., Hubert, T., Baker, L., Lai, M., Bolton, A., Chen, Y., Lillicrap, T., Hui, F., Sifre, L., Van Den Driessche, G., Graepel, T., Hassabis, D.: Mastering the game of Go without human knowledge. *Nature* **550**, 354–359 (2017)
37. OPENAI 2018 OpenAI Five. <https://blog.openai.com/openai-five/>
38. Vinyals, O., Babuschkin, I., Czarnecki, W.M., et al.: Grandmaster level in StarCraft II using multi-agent reinforcement learning. *Nature* **575**, 350–354 (2019)

39. Collobert, R., Weston, J.: A unified architecture for natural language processing: deep neural networks with multitask learning. In: ICML '08: Proceedings of the 25th international conference on Machine learning, pp. 160–167. Association for Computer Machinery, Helsinki, Finland (2008)
40. Bahdanau, D., Brakel, P., Xu, K., Goyal A., Lowe, R., Pineau, J., Courville, A.C., Bengio, Y.: An Actor-Critic Algorithm for Sequence Prediction. [arXiv:1607.07086v3](https://arxiv.org/abs/1607.07086v3) [cs.LG] (2016)
41. Mitchell, T.M.: The discipline of machine learning. Machine learning department, Carnegie Mellon University (2006)
42. Cunningham, P., Cord M., Delany S.J.: Supervised learning. In: Cord M., Cunningham P. (eds) Machine Learning Techniques for Multimedia. Cognitive Technologies. Springer, Berlin, Heidelberg (2008)
43. Meijering, E.: A chronology of interpolation: from ancient astronomy to modern signal and image processing. In: Proceedings of the IEEE, vol. 90(3), pp. 319–342. IEEE (2002)
44. Hastie, T., Tibshirani, R., Friedman, J.: Overview of supervised learning. In: The Elements of Statistical Learning. Springer Series in Statistics. Springer, New York, NY (2009)
45. Wang, M., Hemati, M.S.: Detecting Exotic Wakes with Hydrodynamic Sensors. [arXiv:1711.10576](https://arxiv.org/abs/1711.10576) [physics.flu-dyn] (2017)
46. Prasetya, R., Ridwan, A.: Data mining application on weather prediction using classification tree, Naïve Bayes and K-nearest neighbor algorithm with model testing of supervised learning probabilistic brier score, confusion matrix and ROC. J. Appl. Inf. Commun. Technol. **4**(2), 25–33 (2019)
47. Gangopadhyay, S., Clark, M., Rajagopalan B.: Statistical downscaling using k-nearest neighbors. Water Resour. Res. **41**(2) (2005)
48. Hornik, K., Stinchcombe, M., White, H.: Multilayer feedforward networks are universal approximators. Neural Netw. **2**(5), 359–366 (1989)
49. Krizhevsky, A., Sutskever, I., Hinton, G.E.: ImageNet classification with deep convolutional neural networks. Commun. ACM **60**(6), 84–90 (2017)
50. Goodfellow, I., Bengio, Y., Courville, A.: Deep Learning. MIT Press, Cambridge, MA (2016)
51. Ranzato, M.A., Chopra, S., Auli, M., Zaremba, W.: Sequence level training with Recurrent Neural Networks. [arXiv:1511.06732v7](https://arxiv.org/abs/1511.06732v7) [cs.LG] (2016)
52. van den Oord, A., Kalchbrenner, N., Kavukcuoglu, K.: Pixel recurrent neural networks. [arXiv:1601.06759](https://arxiv.org/abs/1601.06759) [cs.CV] (2016)
53. Hochreiter, S., Schmidhuber, J.: Long short-term memory. Neural Comput. **9**(8), 1735–1780 (1997)
54. Graves, A.: Generating Sequences With Recurrent Neural Networks. [arXiv:1308.0850](https://arxiv.org/abs/1308.0850) [cs.NE] (2014)
55. Van Engelen, J.E., Hoos, H.H.: A survey on semi-supervised learning. Mach. Learn. **109**, 373–440 (2020)
56. Goodfellow, I.J., Pouget-Abadie, J., Mirza, M., Xu, B., Warde-Farley, D., Ozair, S., Courville, A., Bengio, Y.: Generative Adversarial Networks. [arXiv:1406.2661](https://arxiv.org/abs/1406.2661) [stat.ML] (2014)
57. Ledig, C., Theis, L., Huszar, F., Caballero, J., Cunningham, A., Acosta, A., Aitken, A., Tejani, A., Totz, J., Wang, Z., Shi, W.: Photo-realistic single image super-resolution using a generative adversarial network. In: 2017 IEEE Conference on Computer Vision and Pattern Recognition, pp. 4681–4690, IEEE, Honolulu, HI, USA (2017)
58. Li, J., Liang, X., Wei, Y., Xu, T., Feng, J., Yan, S.: Perceptual generative adversarial networks for small object detection. In: 2017 IEEE Conference on Computer Vision and Pattern Recognition, pp. 1951–1959. IEEE, Honolulu, HI, USA (2017)
59. Vondrick, C., Pirsaviash, H., Torralba, A.: Generating videos with scene dynamics. In: Lee, D.D., Luxburg, U., Garnett, R., Sugiyama, M., Guyon, I. (eds.) Proceedings of the 30th International Conference on Neural Information Processing Systems, pp. 613–621. Curran Associates Inc. Barcelona, Spain (2016)
60. Gui, J., Sun, Z., Wen, Y., Tao, T., Ye, J.: A review on Generative Adversarial Networks: Algorithms, Theory and Applications. [arXiv:2001.06937](https://arxiv.org/abs/2001.06937) [cs.LG] (2020)

61. Creswell, A., White, T., Dumoulin, V., Arulkumaran, K., Sengupta, B., Bharath, A.A.: Generative adversarial networks: an overview. *IEEE Signal Process. Mag.* **35**(1), 53–65 (2018)
62. Garnier, P., Viquerat, J., Rabault, J., Larcher, A., Kuhnle, A., Hachem, E.: A review on deep reinforcement learning for fluid mechanics. [arXiv:1908.04127v2](https://arxiv.org/abs/1908.04127v2) [physics.comp-ph] (2021)
63. Hu, J., Wellman, M.P.: Nash Q-learning for general-sum stochastic games. *J. Mach. Learn. Res.* 1039–1069 (2003)
64. Hado van Hasselt.: Double Q-learning. In: Lafferty, J.D., Williams, C.K.I., Shawe-Taylor, J., Zemel, R.S., Culotta, A. (eds.) *Proceedings of the 23rd International Conference on Neural Information Processing Systems*, vol. 2, pp. 2613–2621. Curran Associates Inc., Vancouver British Columbia Canada (2010)
65. Hasselt, H., Guez, A., Silver, D.: Deep reinforcement learning with double Q learning. [arXiv:1509.06461v3](https://arxiv.org/abs/1509.06461v3) [cs.LG] (2015)
66. Mnih, V., Kavukcuoglu, K., Silver, D., Rusu, A.A., Veness, J., Bellemare, M.G., Graves, A., Riedmiller, M., Fidjeland, A.K., Ostrovski, G., Petersen, S., Beattie, C., Sadik, A., Antonoglou, I., King, H., Kumaran, D., Wierstra, D., Legg, S., Hassabis, D.: Human-level control through deep reinforcement learning. *Nature* **518**, 529–533 (2015)
67. Riedmiller, M., Gabel, T., Hafner, R., Lange, S.: Reinforcement learning for robot soccer. *Auton. Robot.* **27**(1), 55–73 (2009)
68. Schembri, M., Mirolli, M., Baldassarre, G.: Evolving internal reinforcers for an intrinsically motivated reinforcement-learning robot. In: 2007 IEEE 6th International Conference on Development and Learning, pp. 282–287. IEEE, London, UK (2007)
69. Ghahramani, Z.: Unsupervised learning. In: Bousquet O., von Luxburg U., Rätsch G. (eds) *Advanced Lectures on Machine Learning. ML 2003. Lecture Notes in Computer Science*, vol. 3176. Springer, Berlin, Heidelberg. (2004)
70. Sirovich, L., Kirby, M.: Low-dimensional procedure for the characterization of human faces. *J. Opt. Soc. Am. A* **4**(3), 519–524 (1987)
71. Herman, A.: Nonlinear principal component analysis of the tidal dynamics in a shallow sea. *Geophys. Res. Lett.* **34**(2) (2007)
72. MacDorman, K.F., Chalodhorn, R., Asada, M.: Periodic nonlinear principal component neural networks for humanoid motion segmentation, generalization, and generation. In: *Proceedings of the 17th International Conference on Pattern Recognition*, vol.4. ICPR 2004, pp. 537–540. IEEE, Cambridge UK (2004)
73. Baldi, P.: Autoencoders, unsupervised learning, and deep architectures. In: Guyon, I., Dror, G., Lemaire, V., Taylor, G., Silver, D. (eds.) *Proceedings of ICML Workshop on Unsupervised and Transfer Learning*, PMLR, vol. 27, pp. 37–49. Bellevue, Washington, USA (2012)
74. Makhzani, A., Shlens, J., Jaitly, N., Goodfellow, I., Frey, B.: Adversarial Autoencoders. [arXiv:1511.05644](https://arxiv.org/abs/1511.05644) [cs.LG] (2015)
75. Burda, Y., Grosse, R., Salakhutdinov, R.: Importance Weighted Autoencoders. [arXiv:1509.00519v4](https://arxiv.org/abs/1509.00519v4) [cs.LG] (2016)
76. Hartigan, J.A., Wong, M.A.: Algorithm AS 136: A K-means clustering algorithm. *J. R. Stat. Soc. Series C Appl. Stat.* **28**(1), 100–108 (1979)
77. Bradley, P.S., Fayyad, U.M.: Refining Initial Points for K-Means clustering. In: Shavlik, J. (ed.) *Proceedings of the 15th International Conference on Machine Learning (ICML98)*, pp. 91–99. Morgan Kaufmann, San Francisco (1998)
78. Likas, A., Vlassis, N., Verbeek, J.J.: The global k-means clustering algorithm. *Pattern Recogn.* **36**(2), 451–461 (2003)
79. Zhou, H., Soh, Y.C., Wu, X.: Integrated analysis of CFD data with K-means clustering algorithm and extreme learning machine for localized HVAC control. *Appl. Therm. Eng.* **76**, 98–104 (2015)
80. Kaiser, E., Noack, B.R., Cordier, L., Spohn, A., Segond, M., Abel, M., Daviller, G., Osth, J., Krajnovic, S., Niven, R.K.: Cluster based reduced order modelling of a mixing layer. *J. Fluid Mech.* **754**, 365–414 (2014)
81. Ling, J., Kurzawski, A., Templeton, J.: Reynolds averaged turbulence modeling using deep neural networks with embedded invariance. *J. Fluid Mech.* **807**, 155–166 (2016)

82. Cheung, S.H., Oliver, T.A., Prudencio, E.E., Prudhomme, S., Moser, R.D.: Bayesian uncertainty analysis with applications to turbulence modeling. *Reliab. Eng. Syst. Saf.* **96**(9), 1137–1149 (2011)
83. Edeling, W.N., Cinnella, P., Dwight, R.P.: Predictive RANS simulations via Bayesian model-scenario averaging. *J. Comput. Phys.* **275**, 65–91 (2014)
84. Maulik, R., San, O., Rasheed, A., Vedula, P.: Sub-grid modelling for two-dimensional turbulence using neural networks. *J. Fluid Mech.* **858**, 122–144 (2018)
85. Ma, M., Lu, J., Tryggvason, G.: Using statistical learning to close two-fluid multiphase flow equations for a simple bubbly system. *Phys. Fluids* **27**(9), 092101 (2015)
86. Verma, S., Novati, G., Koumoutsakos, P.: Efficient collective swimming by harnessing vortices through deep reinforcement learning. *Proc. Natl. Acad. Sci. U.S.A. (PNAS)* **115**(23), 5849–5854 (2018)
87. Hwangbo, J., Sa, I., Siegwart, R., Hutter, M.: Control of a quadrotor with reinforcement learning. *IEEE Robot. Autom. Lett.* **2**(4), 2096–2103 (2017)
88. Fan, D., Yang, L., Triantafyllou, M.S., Karniadakis, G.E.: Reinforcement Learning for Active Flow Control in Experiments. [arXiv:2003.03419](https://arxiv.org/abs/2003.03419) [physics.flu-dyn] (2020)
89. Parezanović, V., Laurentie, J.-C., Fourment, C., Delville, J., Bonnet, J.-P., Spohn, A., et al.: Mixing layer manipulation experiment. *Flow Turbul. Combust.* **94**(1), 155–173 (2015)
90. Gautier, N., Aider, J.-L., Duriez, T., Noack, B.R., Segond, M., Abel, M.: Closed-loop separation control using machine learning. *J. Fluid Mech.* **770**, 442–457 (2015)
91. Makinen, R.A., Periaux, J., Toivanen, J.: Multidisciplinary shape optimization in aerodynamics and electromagnetics using genetic algorithms. *Int. J. Numer. Meth. Fluids* **30**(2), 149–159 (1999)
92. Xu, M., Song, S., Sun, X., Chen, W., Zhang, W.: Machine learning for adjoint vector in aerodynamic shape optimization. *Acta Mechanica Sinica* (2021)
93. Yan, X., Zhu, J., Kuang, M., Wang, X.: Aerodynamic shape optimization using a novel optimizer based on machine learning techniques. *Aerosp. Sci. Technol.* **86**, 826–835 (2019)

Influence of Gyroscopic Effect and Rotary Inertia on the Vibrations of a Continuous Rotor System



Amit Malgol and Ashesh Saha

Abstract The vibration characteristics of a rotor system consisting of a rigid disk mounted on the middle of a flexible shaft is studied to investigate the influence of gyroscopic effect and rotary inertia of the shaft. The bearings are replaced by linear springs. The partial differential equation (PDE) governing the beam vibrations is reduced to a set of ordinary differential equations (ODE) by modal analysis. A detailed parametric study is conducted and the dynamics of the system is studied through time-displacement responses, phase-plane and frequency response plots.

Keywords Continuous system · Gyroscopic effect · Rotary inertia · Vibration

1 Introduction

The rotating elements are used in a broad range of applications such as motor, generator, blower etc. The response of the rotary system depends on the excitation inputs and the system characteristics. In this paper, we primarily focus on the modeling and analysis of rotor system with the influence of gyroscopic effect and rotary inertia. A rotor system can be modeled either in the form of a discrete system or a continuous system. We consider the rotor system as a continuous one in this work. The partial differential equations (PDE's) governing the system vibrations are reduced to a set of ordinary differential equations (ODE's) by modal analysis.

There is a vast literatures on the analyses of a continuous rotor system considering different influencing factors. Only a handful of literatures are briefly discussed in this paper [1–6]. The dynamics of the rotor system with the combined effect of large deformations in bending, rotary inertia [1, 2], rotor unbalance, the gyroscopic effect [2, 3] along with the shear effects, and axial dynamic force are considered by Shad et al. [1–3]. The Euler Bernoulli beam equation theory are used to model

A. Malgol (✉) · A. Saha
National Institute of Technology Calicut, Kozhikode, Kerala 673601, India

A. Saha
e-mail: ashesh@nitc.ac.in

the continuous rotor system. Hamilton’s principle is applied to derive the governing equation using the kinetic and strain energy of the shaft [1–3].

Khanlo et al. [4] studied the dynamics of the flexible rotor system with the effect of disk position nonlinearity. Rayleigh’s beam theory is used to model the continuous rotor system. Different types of responses, such as the subharmonic motion, chaotic behavior, and quasi-periodic motion, etc. are observed [4]. Duchemin et al. [5] investigated the effect of base excitation and gyroscopic force on a flexible rotor system. The Lagrange principle is applied to derive the equation of motion from the kinetic and strain energies of the rotor system. Deb et al. [6] examined the Campbell diagrams to analyze the critical speeds of the rotating system with the gyroscopic effect.

The rotor system can be conveniently modeled in the form of a discrete system [7–9]. Cveticanin [7] considered the influence of gyroscopic force and some other effects for the analyses of free vibration of the rotor system. Matsushita et al. [8] explored the influence of gyroscopic force on the natural frequency of the rotating system. In some literatures, forward and backward whirling motions have been analyzed [8, 9].

The rest of the paper is organized as follows. The mathematical model is briefly discussed in Sect. 2. The analytical method for obtaining the closed form solutions is explained in Sect. 3. Some results are discussed in Sect. 4 followed by conclusions in Sect. 5.

2 Mathematical Modeling

The rotor model consists of a rigid disk mounted on the flexible shaft supported with linear springs, as shown in Fig. 1. Point S in Fig. 1c is the geometric center of disc where shaft axis passes, and point G is the center of gravity of disc. The eccentricity of G from S is denoted by e .

The governing eqns. of rotor system modeled with gyroscopic effect and rotary inertia are described as [1–3, 10]

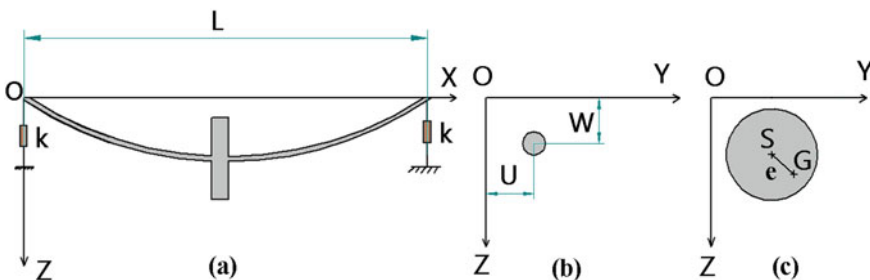


Fig. 1 a Schematic diagram of the rotor system b cross-sectional view of the shaft c cross-sectional view of disc

$$\begin{aligned} \rho A \frac{\partial^2 U}{\partial t^2} + EI \frac{\partial^4 U}{\partial X^4} + mR^2 \frac{\partial^4 U}{\partial t^2 \partial X^2} + 2mR^2 \omega \frac{\partial^3 W}{\partial t \partial X^2} \\ = m_u e \omega^2 \sin(\omega t) \delta\left(X - \frac{L}{2}\right), \end{aligned} \quad (1a)$$

$$\begin{aligned} \rho A \frac{\partial^2 W}{\partial t^2} + EI \frac{\partial^4 W}{\partial X^4} - mR^2 \frac{\partial^4 W}{\partial t^2 \partial X^2} + 2mR^2 \omega \frac{\partial^3 U}{\partial t \partial X^2} \\ = m_u e \omega^2 \cos(\omega t) \delta\left(X - \frac{L}{2}\right), \end{aligned} \quad (1b)$$

where U and W are the displacements in horizontal and vertical directions, respectively, ω is the rotational speed of the rotor, R is the radius of gyration of the shaft, m_u is unbalance mass, $m = \rho A$ is mass per unit length of the shaft, and L is the length of the shaft. The dirac delta function $\delta(X - \frac{L}{2})$ ensures that the centrifugal force $m_u e \omega^2$ is acting at the middle of the shaft. The governing equations in dimensionless form are obtained as

$$\frac{\partial^2 u}{\partial \tau^2} + \frac{\partial^4 u}{\partial x^4} - r^2 \frac{\partial^4 u}{\partial \tau^2 \partial x^2} + 2r^2 r_f \frac{\partial^3 w}{\partial \tau \partial x^2} = r_m r_e r_f^2 \sin(r_f \tau) \delta\left(x - \frac{1}{2}\right), \quad (2a)$$

$$\frac{\partial^2 w}{\partial \tau^2} + \frac{\partial^4 w}{\partial x^4} - r^2 \frac{\partial^4 w}{\partial \tau^2 \partial x^2} - 2r^2 r_f \frac{\partial^3 u}{\partial \tau \partial x^2} = r_m r_e r_f^2 \cos(r_f \tau) \delta\left(x - \frac{1}{2}\right), \quad (2b)$$

where $u = \frac{U}{L}$, $w = \frac{W}{L}$, $x = \frac{X}{L}$, $k = \frac{KL^3}{EI}$, $r_f = \frac{\omega}{\Omega}$, $r_m = \frac{m_u}{\rho AL}$, $r_e = \frac{e}{L}$, $r = \frac{R}{L}$, $T = \Omega t$, $\Omega = \left(\frac{EI}{\rho AL^4}\right)^{\frac{1}{2}}$. The partial differential Eq. (2) governing the system vibrations are reduced to a set of ODE's by modal analysis, the solutions are assumed as

$$u(x, \tau) = \sum_{i=1}^n \Psi_i(x) u_i(\tau), \quad (3a)$$

$$w(x, \tau) = \sum_{i=1}^n \Psi_i(x) w_i(\tau), \quad (3b)$$

where $\Psi_i(x)$ is the i th orthonormal mode shape of a simply supported beam with spring supported at the ends. The expression for $\Psi_i(x)$ is quite long and is given in Appendix. The mode shapes satisfy the following orthonormality conditions:

$$\int_0^1 \Psi_i \Psi_j dx = \delta_{ij}, \quad (4a)$$

$$\int_0^1 \Psi_i \frac{d^4 \Psi_j(x)}{dx^4} dx = \int_0^1 \Psi_j \frac{d^4 \Psi_i(x)}{dx^4} dx = p_i^4 \delta_{ij}, \quad (4b)$$

where the natural frequencies p_i are obtained from the following frequency equation

$$p_i^6(1 - \cos p_i \cosh p_i) + 2k^2 \sinh p_i \sin p_i + 2kp_i^3(\cos p_i \sinh p_i - \sin p_i \cosh p_i) = 0. \quad (5)$$

In the modal analysis [11], solutions (3) is first substituted into Eq. (2). Then, both sides of the equations are multiplied by Ψ_j and integrated over the domain $[0, 1]$. Subsequently, the orthonormality conditions (4) are applied to obtain the following governing equations for the first mode only

$$u_1'' + p_1^4 u_1 + 2\xi u_1' - R_I r^2 d_{11} u_1'' + 2Gr^2 d_{11} r_f w_1' = q_o \sin(r_f \tau), \quad (6a)$$

$$w_1'' + p_1^4 w_1 + 2\xi w_1' - R_I r^2 d_{11} w_1'' - 2Gr^2 d_{11} r_f u_1' = q_o \cos(r_f \tau), \quad (6b)$$

where R_I and G are rotary inertia and gyroscopic effect, respectively, and $q_o = r_m r_e r_f^2 \Psi_1(0.5)$. It is to be noted that modal damping terms ($2\xi u_1'$ and $2\xi w_1'$) are added in Eq. (6). R_I and G will be taken either as 1 or 0 depending on whether the inertia effect and/or gyroscopic effect are considered for the analysis or not.

3 Analytical Method

In this section, the exact closed form solutions of Eq. (6) are obtained using the the principle of superposition. Equation (6) are first simplified into

$$m_1 u_1'' + 2\xi u_1' + g_2 w_1' + k_1 u_1 = q_o \sin(r_f \tau) = q_o \text{Im}(e^{ir_f \tau}), \quad (7a)$$

$$m_2 w_1'' + 2\xi w_1' - g_1 u_1' + k_2 w_1 = q_o \cos(r_f \tau) = q_o \text{Re}(e^{ir_f \tau}), \quad (7b)$$

where $m_1 = m_2 = 1 - R_I r^2 d_{11}$, $g_1 = g_2 = 2Gr^2 r_f^2 d_{11}$, $k_1 = k_2 = p_1^4$. “Im” and “Re” in Eq. (7) refer to imaginary and real parts, respectively.

Equation (6) are written in matrix form as

$$[M]\ddot{\tilde{x}} + [G]\dot{\tilde{x}} + [k]\tilde{x} = \tilde{Q}_1 \text{Im}(e^{ir_f \tau}) + \tilde{Q}_2 \text{Re}(e^{ir_f \tau}), \quad (8)$$

where

$$[M] = \begin{bmatrix} m_1 & 0 \\ 0 & m_1 \end{bmatrix}, [G] = \begin{bmatrix} 2\xi & g_2 \\ -g_1 & 2\xi \end{bmatrix}, [k] = \begin{bmatrix} k_1 & 0 \\ 0 & k_1 \end{bmatrix},$$

$$\tilde{Q}_1 = \begin{bmatrix} q_0 \\ 0 \end{bmatrix}, \tilde{Q}_2 = \begin{bmatrix} 0 \\ q_0 \end{bmatrix}, \tilde{x} = \begin{bmatrix} x_1 \\ x_2 \end{bmatrix} = \begin{bmatrix} u_1 \\ w_1 \end{bmatrix}.$$

We will first solve Eq. (8) for the excitations $\tilde{Q}_1 \text{Im}(e^{ir_f\tau})$ and $\tilde{Q}_2 \text{Re}(e^{ir_f\tau})$ separately. As the system is linear, the method of superposition can be applied to obtain the solutions for the excitation $\tilde{Q}_1 \text{Im}(e^{ir_f\tau}) + \tilde{Q}_2 \text{Re}(e^{ir_f\tau})$. The steady-state solution of Eq. (8) for either form of the excitation can be assumed as

$$\tilde{x}(\tau) = \tilde{X}(ir_f)e^{ir_f\tau}. \quad (9)$$

Substituting Eq. (9) into Eq. (8) and separating the real and imaginary parts, we get

$$\tilde{Z}(ir_f)\tilde{X}_1(ir_f) = \tilde{Q}_1, \quad (10a)$$

$$\tilde{Z}(ir_f)\tilde{X}_2(ir_f) = \tilde{Q}_2, \quad (10b)$$

where $\tilde{Z}(ir_f) = r_f^2[M] + ir_f[G] + [k]$ is the impedance matrix. The solutions can then be obtained from [12] the following equations:

$$\tilde{x}_1(\tau) = \begin{bmatrix} x_{11} \\ x_{21} \end{bmatrix} = \frac{\tilde{Q}_1}{\tilde{Z}(ir_f)} = \text{Im}\left(\frac{\text{adj}\tilde{Z}(ir_f)}{\det\tilde{Z}(ir_f)}\tilde{Q}_1e^{ir_f\tau}\right), \quad (11a)$$

$$\tilde{x}_2(\tau) = \begin{bmatrix} x_{12} \\ x_{22} \end{bmatrix} = \frac{\tilde{Q}_2}{\tilde{Z}(ir_f)} = \text{Re}\left(\frac{\text{adj}\tilde{Z}(ir_f)}{\det\tilde{Z}(ir_f)}\tilde{Q}_2e^{ir_f\tau}\right), \quad (11b)$$

where

$$\text{adj}\tilde{Z}(ir_f) = \begin{bmatrix} k_1 - r_f^2m_1 + i2\xi r_f & -ir_f g_1 \\ ir_f g_1 & k_1 - r_f^2m_1 + i2\xi r_f \end{bmatrix}, \text{ and}$$

$$\det\tilde{Z}(ir_f) = (k_1 - r_f^2m_1)^2 - (2\xi r_f)^2 - (r_f g_1)^2 - i4r_f g_1(k_1 - r_f^2m_1).$$

Ultimately, the principle of super position is employed to obtain the solutions as

$$x_1(\tau) = x_{11}(\tau) + x_{12}(\tau) = X_1 \sin(r_f\tau - \phi), \text{ and} \quad (12a)$$

$$x_2(\tau) = x_{21}(\tau) + x_{22}(\tau) = X_1 \cos(r_f\tau - \phi), \quad (12b)$$

where X_1 is the amplitude of the vibrations in both the horizontal and vertical directions and ϕ is the phase angle which are obtained as

$$X_1 = \frac{q_0 \left\{ \left(k_1 - r_f^2 m_1 - r_f g_1 \right)^2 + \left(2\xi r_f \right)^2 \right\} \sqrt{\left(k_1 - r_f^2 m_1 - r_f g_1 \right)^2 + \left(2\xi r_f \right)^2}}{\left(\left(k_1 - r_f^2 m_1 \right)^2 - \left(2\xi r_f \right)^2 - \left(r_f g_1 \right)^2 \right)^2 + \left(4r_f \xi \left(k_1 - r_f^2 m_1 \right) \right)^2}, \quad (13a)$$

and

$$\phi = \tan^{-1} \left(\frac{2\xi r_f}{\left(k_1 - r_f^2 m_1 - r_f g_1 \right)} \right). \quad (13b)$$

Interestingly, the amplitude of vibration and the phase angle for both the horizontal and vertical oscillations are the same. All the results are now discussed in the next section.

4 Results and Discussion

In this section, a detailed parametric analysis is carried out to understand the effect of eccentricity ratio (r_e), damping factor (ξ), mass ratio (r_m), radius of gyration of shaft (r), support spring stiffness (k), and the rotary inertia and the gyroscopic effects of the shaft on the vibration of the rotor system. Note that k doesn't affect directly the values of the amplitude X_1 and phase angle ϕ in Eq. (13) and the parameter k_1 is not the same as k . The parameter k is coming into the frequency Eq. (5) and $k_1 = p_1^4$, where the natural frequency of the shaft for the first mode p_1 is to be determined from Eq. (5) for different values of support spring stiffness k .

4.1 Comparison of Numerical and Analytical Results

The phase plane plots of the rotor system obtained by numerically simulating the governing Eq. (5) are compared with the analytical results given by Eq. (12) in Fig. 2. Figure 2 verifies the correctness of the analytical solutions as they coincide with the responses obtained from numerical simulation. The time-displacement responses (not shown here) also coincide for numerical and analytical solutions.

In the forthcoming analysis, the effect of different parameters are analysed through the frequency response (X_1 vs. r_f) and phase angle (ϕ vs. r_f) plots. The effect of eccentricity ratio r_e on X_1 and ϕ are shown in Figs. 3. As expected, the amplitude of vibrations (X_1) increases with the increase of the eccentricity ratio (r_e). The resonance frequency is not much affected by r_e as all the resonance peaks occur almost for the same value of r_f . Moreover, the phase angle ϕ is also unaffected by r_e as all the

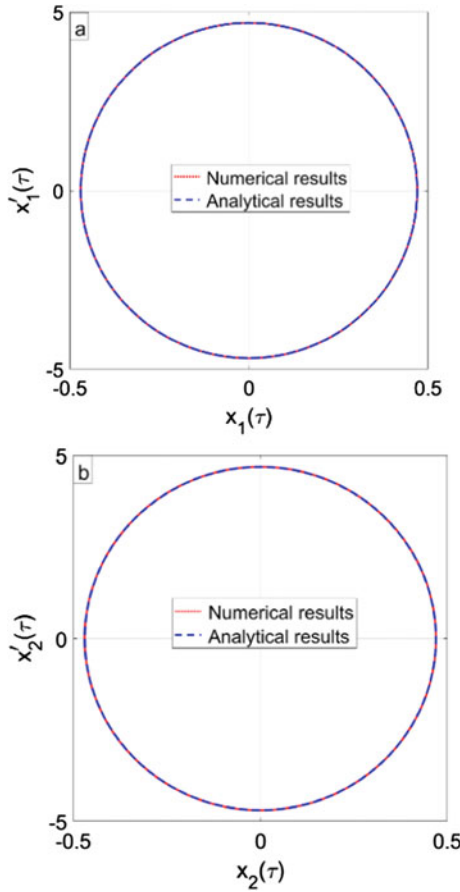


Fig. 2 Phase plane plots in the horizontal and vertical direction. Parameters: $r_m = r_f = 10$, $r = 0.02$, $\xi = 0.05$, $r_e = 0.001$, and $k = 6000$

curves for different values of r_e are coincident as shown in Fig. 3b. We will refer the resonance frequency as f_r for the subsequent analysis. It is to be noted that the phase angle ϕ obtained using the “MATLAB” command “atan2d” are in degrees and $\phi \rightarrow 0^\circ$ as $r_f \rightarrow 0$ and $\phi \rightarrow 180^\circ$ as $r_f \rightarrow \infty$ as the change is happening gradually near resonance. In fact, for all the forthcoming analysis also, the asymptotic values of phase angles are $\phi = 0^\circ$ for $r_f \rightarrow 0$ and $\phi = 180^\circ$ for $r_f \rightarrow \infty$.

Figure 4 show the influence of damping factor ξ on X_1 and ϕ . Increased value of ξ significantly reduces the vibration amplitude, particularly near resonance. However, the natural frequency/resonance frequency (f_r) is not much affected by ξ . Also, the change of phase angle from one asymptotic value $\phi = 0^\circ$ for $r_f \rightarrow 0$ to the other asymptotic value of $\phi = 180^\circ$ for $r_f \rightarrow \infty$ is more gradual for higher values of ξ .

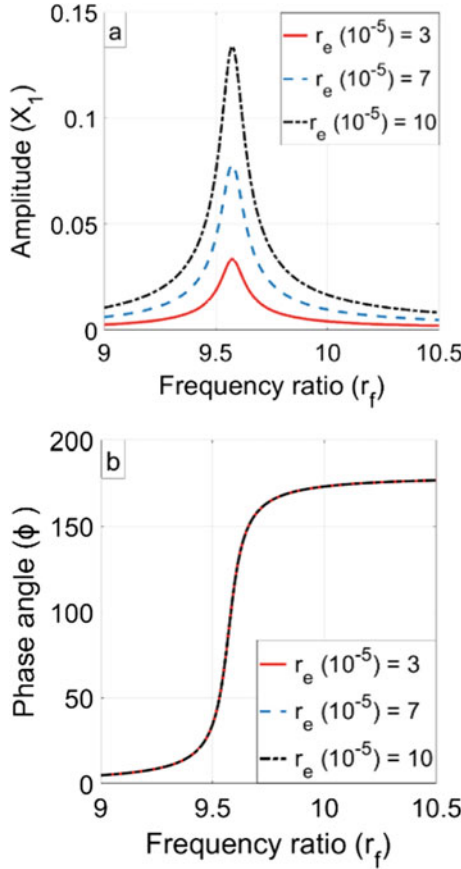


Fig. 3 **a** Frequency response and **b** phase angle plots for different values of r_e . Parameters: $r_m = 6$, $r = 0.02$, $\xi = 0.05$, $R_I = G = 1$, and $k = 600$

Increased value of mass ratio r_m significantly increases the amplitude of vibration without much affecting the resonance frequency (f_r) as shown in Fig. 5a. The phase angle though is independent of r_m which is clear from Fig. 5b.

From the previous analysis, we observed that f_r is not much affected by the parameters r_e , ξ and r_m . However, the influence of other parameters, like the radius of gyration (r), support spring stiffness (k), and the inertia and gyroscopic effect of the shaft on f_r are clearly noticeable from Figs. 6, 7 and 8. It is observed from Fig. 6 plotted for different values of r that f_r increases with the increase of r . Moreover, the peak amplitude at resonance also increases with the increase of r . This radius of gyration r appears in both the inertia and gyroscopic terms in Eq. (6). A very similar result is obtained when the support spring stiffness k is varied as shown in Fig. 7; f_r as well as the peak amplitude at resonance increase with the increase of k .

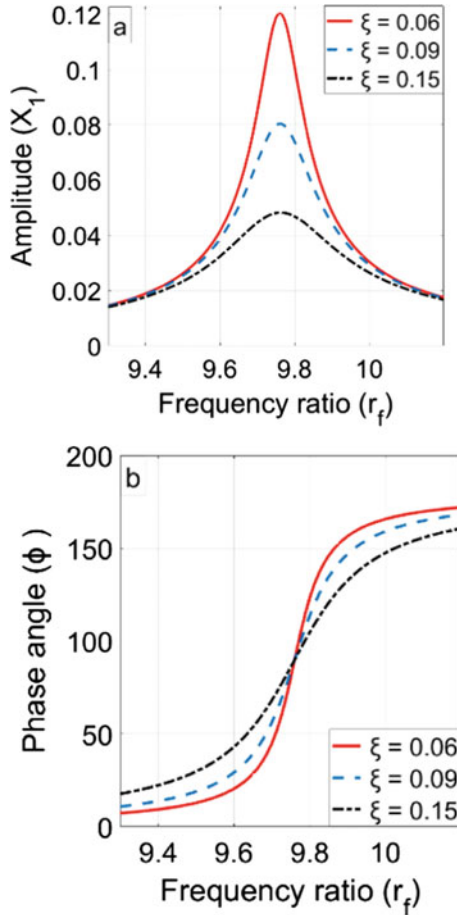


Fig. 4 **a** Frequency response and **b** phase angle plots for different values of ξ . Parameters: $r_m = 5$, $r_e = 0.00015$, $r = 0.02$, $R_I = G = 1$, and $k = 1500$

The influence of rotary inertia and gyroscopic effects of shaft are analysed in Figs. 8. As explained earlier, we will use $R_I = 1$ if the inertia effect of the shaft is considered and $R_I = 0$ if the inertia effect of the shaft is not considered. The same with the value of G for gyroscopic term. It is observed from Fig. 8 that the inertia effect of the shaft reduces the resonance frequency (f_r) whereas the gyroscopic effect of the shaft increases f_r . When both of them are considered together ($R_I = G = 1$), f_r slightly increases compared to the case when none of them are considered ($R_I = G = 0$), but this value of f_r is less than the value of f_r for $R_I = 0$, $G = 1$.

A better perspective about the effect of different parameters on f_r can be achieved by plotting the Cambell diagram which will be considered in future.

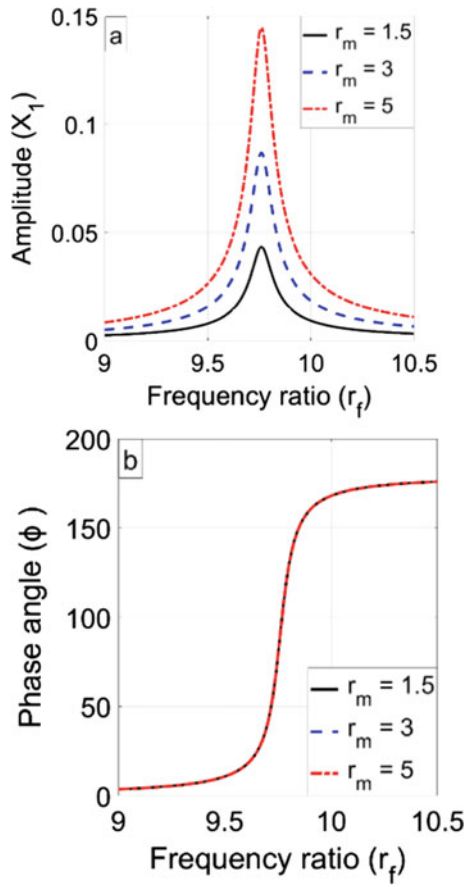


Fig. 5 **a** Frequency response and **b** phase angle plots for different values of r_m . Parameters: $r = 0.02$, $r_e = 0.00015$, $\xi = 0.05$, $R_I = G = 1$, and $k = 1500$

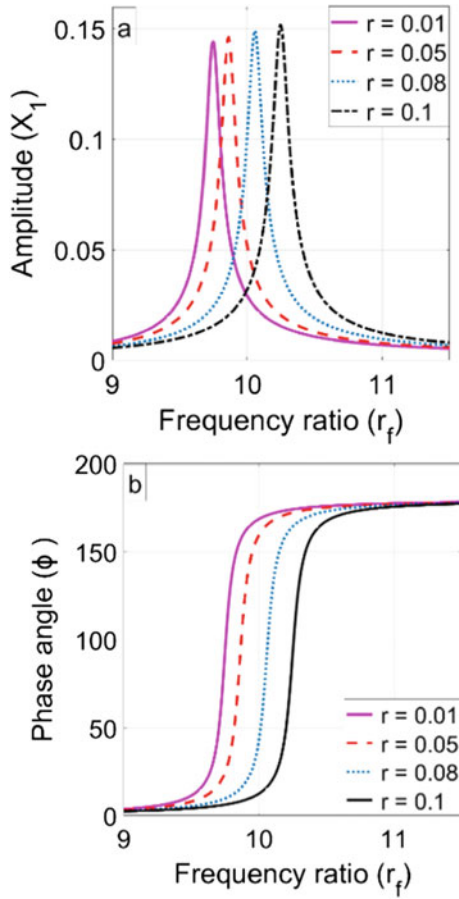


Fig. 6 **a** Frequency response and **b** phase angle plots for different values of r . Parameters: $r_m = 5$, $r_e = 0.00015$, $\xi = 0.05$, $R_I = G = 1$, and $k = 1500$

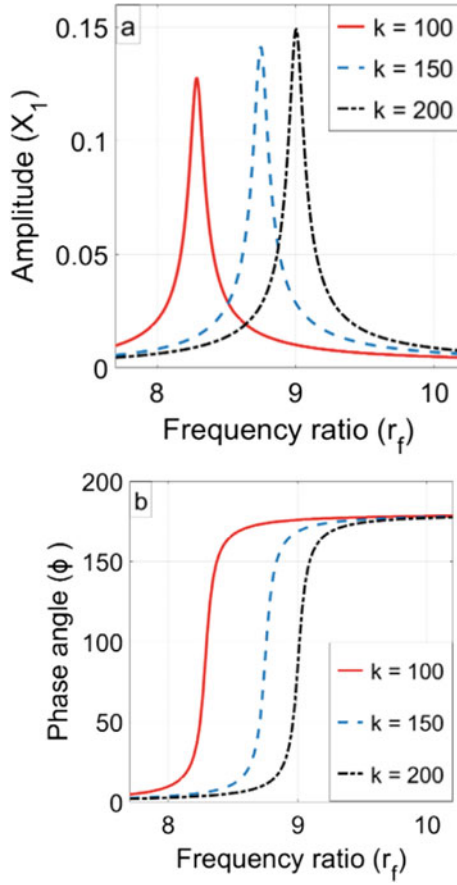


Fig. 7 **a** Frequency response and **b** phase angle plots for different values of k . Parameters: $r_m = 6$, $r_e = 0.00015$, $\xi = 0.05$, $R_I = G = 1$, and $r = 0.02$

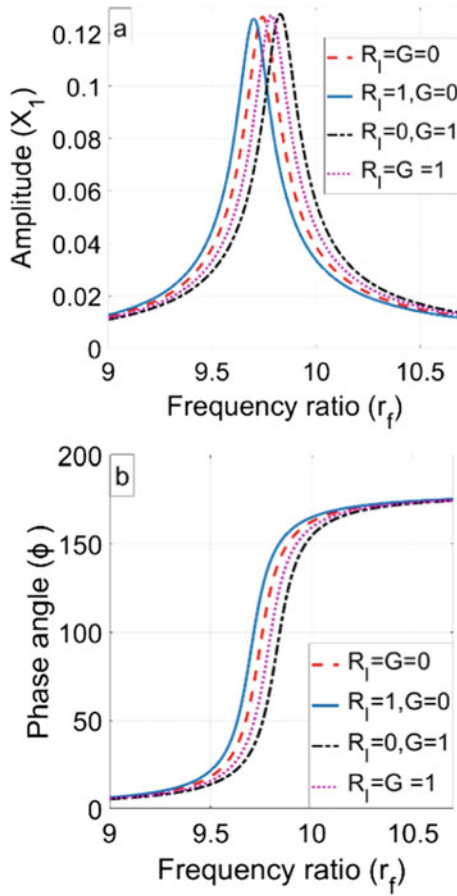


Fig. 8 **a** Frequency response and **b** phase angle plots for different values of R_I and G . Parameters: $r_m = 7$, $r_e = 0.00015$, $k = 1500$, $\xi = 0.08$, and $r = 0.03$

5 Conclusions

In this paper, we analysed the effect of different system parameters on the vibration characteristics of a rotor system consisting of a rigid disc mounted at the middle of a flexible shaft which is considered to be a continuous system. The system parameters considered are the eccentricity ratio (r_e), damping factor (ξ), mass ratio (r_m), radius of gyration of shaft (r), support spring stiffness (k), and the rotary inertia and the gyroscopic effects of the shaft. The bearings supporting the shaft at both ends are replaced by linear springs. The PDE governing the system vibration is reduced to a set of ODE's by modal analysis. The exact analytical solutions show that the expressions for the amplitude of vibrations and phase angle are the same for the vibrations of the disc along the horizontal and vertical directions. The influence of different parameters are analysed from the frequency response and phase angle plots. It is observed that even though the amplitude of vibrations are largely affected by the parameters r_e , ξ , and r_m , their influence on the resonance frequency (f_r) is hardly noticeable. The resonance frequency (f_r) as well as the peak amplitude at resonance increases with the increase of r and k . The rotational inertia of the shaft decreases f_r whereas the gyroscopic effect of shaft increases f_r , the influence of the later being the stronger. In all the cases, the phase angle gradually increases from one asymptotic value $\phi = 0^\circ$ for $r_f \rightarrow 0$ to the other asymptotic value of $\phi = 180^\circ$ for $r_f \rightarrow \infty$, r_f being the frequency ratio.

Acknowledgements This work has been supported by DST SERB—SRG under Project File no. SRG/2019/001445 and National Institute of Technology Calicut under Faculty Research Grant.

Appendix

The expression for $\Psi_i(x)$ and C_1 is written as

$$\begin{aligned} \Psi_i(x) = & C_1(2 \sin(p_1 x)k \sinh(p_1) + \sin(p_1 x)p_1^3 \cos(p_1) - \sin(p_1 x)p_1^3 \cosh(p_1) \\ & + 2 \sinh(p_1 x)k \sin(p_1) + \sinh(p_1 x)p_1^3 \cos(p_1 x) - \sin(p_1 x)p_1^3 \cos(p_1 x) \\ & + \sinh(p_1 x)p_1^3 \cos(p_1) - \sinh(p_1 x)p_1^3 \cosh(p_1) + \sinh(p_1 x)p_1^3 \cosh(p_1 x) \\ & - p_1^3 \cosh(p_1 x) \sin(p_1)) / (2 \sinh(p_1)k + p_1^3 \cos(p_1) - p_1^3 \cosh(p_1)), \end{aligned}$$

$$\begin{aligned} C_1 = & 2 / (-24p_1^6 z_1 - 8kp_1^3 z_2 + 64kp_1^3 z_4 + 16k^2 z_2 + 8k^2 p_1 e^{(2p_1)} \\ & - 32kp_1^3 z_1 - 16k^2 e^{(4p_1)} - 32kp_1^4 z_1 + 48kz_5 e^{(6p_1)} + 32kz_5 e^{(4p_1)} \\ & - 48kz_5 e^{(2p_1)} - 24k^2 z_0 e^{(2p_1)} + 16kp_1^4 \sin(p_1) e^{(3p_1)} + 16kp_1^4 \sin(p_1) e^{(3p_1)} \\ & + 16k^2 z_0 e^{(4p_1)} + 32k \sin(p_1) p_1^3 e^{(3p_1)} - 12p_1^6 z_0 e^{(2p_1)} - 8kp_1^4 e^{(6p_1)} \\ & - 16kp_1^4 \cos(p_1) e^{(3p_1)} + 32k^2 z_1 - 96kp_1^3 e^{(5p_1)} \sin(p_1)) \end{aligned}$$

$$\begin{aligned}
 &+ 16kp_1^4 e^{(5p_1)} \cos(p_1) + 8k^2 p_1 e^{(6p_1)} + 16kp_1^4 e^{(5p_1)} \sin(p_1) - 24k^2 z_0 e^{(6p_1)} \\
 &- 12z_0 p_1^6 e^{(6p_1)} + 8kp_1^3 z_2 + 32k^2 p_1 z_2 + 8kp_1^4 e^{(4p_1)} - 16k^2 z_2 \\
 &- 48k^2 p_1 e^{(4p_1)} + 16p_1^7 \sin(p_1) e^{(3p_1)} + 24p_1^6 \sin(p_1) e^{(3p_1)} \\
 &+ 4 \cos(p_1) p_1^6 e^{(3p_1)} - 16p_1^7 z_2 - 24k^2 e^{(2p_1)} - 16p_1^7 \sin(p_1) e^{(5p_1)} \\
 &+ 24p_1^6 \sin(p_1) e^{(5p_1)} - 24 \cos(p_1) p_1^6 e^{(5p_1)} + 20p_1^6 \cos(p_1) e^{(3p_1)} \\
 &- 11p_1^6 e^{(4p_1)} + 24k^2 e^{(2p_1)} (\cos(p_1))^2 - 12p_1^6 z_2 \\
 &+ 12p_1^6 e^{(6p_1)} (\cos(p_1))^2 x + 16k^2 e^{(4p_1)} - 16k^2 z_2 - 24k^2 e^{(6p_1)} (\cos(p_1))^2 \\
 &- 12p_1^6 e^{(2p_1)} (\cos(p_1))^2 + 24k^2 e^{(6p_1)} + 4p_1^7 e^{(2p_1)} + 4p_1^7 e^{(6p_1)} + 8p_1^7 e^{(4p_1)} \\
 &+ 11p_1^6 e^{(4p_1)} ((-24p_1^6 z_1 - 8kp_1^3 z_2 + 8k^2 p_1 e^{(2p_1)} + 64kp_1^3 e^{(3p_1)} \sin(p_1) \\
 &+ 16k^2 z_2 - 32kp_1^3 z_1 - 16k^2 e^{(4p_1)} - 32kp_1^4 z_1 + 48kp_1^3 z_0 e^{(6p_1)} + 32kp_1^3 z_1 \\
 &- 48kp_1^3 z_0 e^{(6p_1)} + 32kp_1^3 z_1 - 48kp_1^3 z_0 e^{(2p_1)} - 24k^2 z_0 e^{(2p_1)} \\
 &+ 16k \sin(p_1) p_1^4 e^{(3p_1)} + 16k^2 z_1 - 12p_1^6 z_0 e^{(2p_1)} + 32k \sin(p_1) p_1^3 e^{(3p_1)} \\
 &- 16kp_1^4 \cos(p_1) e^{(3p_1)} + 32k^2 z_1 - 96kp_1^3 \sin(p_1) e^{(5p_1)} + 48k^2 p_1 e^{(4p_1)} \\
 &+ 16kp_1^4 \cos(p_1) e^{(5p_1)} + 16k \sin(p_1) p_1^4 e^{(5p_1)} - 24k^2 z_0 e^{(6p_1)} - 12p_1^6 z_0 e^{(6p_1)} \\
 &+ 8k^2 p_1 e^{(6p_1)} + 8k^2 p_1^3 e^{(4p_1)} \cos(p_1) + 32k^2 p_1 z_2 + 8kp_1^4 e^{(2p_1)} - 8kp_1^4 e^{(4p_1)} \\
 &- 8kp_1^4 e^{(6p_1)} + 16p_1^7 \sin(p_1) e^{(3p_1)} + 4 \cos(p_1) p_1^6 e^{(3p_1)} - 16p_1^7 \sin(p_1) e^{(5p_1)} \\
 &+ 24p_1^6 \sin(p_1) e^{(5p_1)} - 24p_1^6 \sin(p_1) e^{(5p_1)} - 24 \cos(p_1) p_1^6 e^{(5p_1)} \\
 &+ 20 \cos(p_1) p_1^6 e^{(3p_1)} + 24p_1^6 \sin(p_1) e^{(3p_1)} - 16k^2 z_2 + 12p_1^6 z_2 \\
 &+ 24k^2 e^{(2p_1)} (\cos(p_1))^2 - 16p_1^7 z_2 - 12p_1^6 z_2 + 12p_1^6 (\cos(p_1))^2 e^{(6p_1)} \\
 &- 24k^2 e^{(6p_1)} (\cos(p_1))^2 - 12p_1^6 (\cos(p_1))^2 e^{(2p_1)} + 24k^2 e^{(6p_1)} \\
 &+ 4p_1^7 e^{(2p_1)} + 4p_1^7 e^{(6p_1)} + 8p_1^7 e^{(4p_1)} + 11p_1^6 e^{(4p_1)} + 16k^2 e^{(4p_1)} \\
 &- 24k^2 e^{(2p_1)} - 11p_1^6 e^{(4p_1)} p_1)^{0.5} (-p_1^3 - 2k + 2p_1^3 e^{(p_1)} \cos(p_1) \\
 &+ 2ke^{(2p_1)} \cos(p_1) + 2ke^{(2p_1)} - p_1^3 e^{(2p_1)} e^{(p_1)},
 \end{aligned}$$

where,

$$Z_0 = \cos(p_1) \sin(p_1), Z_1 = \cos(p_1) e^{(4p_1)} \sin(p_1), Z_2 = (\cos(p_1))^2 e^{(4p_1)}, Z_3 = (\sin(p_1))^2 e^{(4p_1)}, Z_4 = (\sin(p_1))^2 e^{(3p_1)}, Z_5 = \cos(p_1) p_1^3 \sin(p_1).$$

References

1. Shad, M.R., Michon, G., Berlioz, A.: Nonlinear dynamics of rotors due to large deformations and shear effects. *Appl. Mech. Mater.* **110**(116), 3593–3599 (2012)
2. Shad, M.R., Michon, G., Berlioz, A.: Modeling and analysis of nonlinear rotordynamics due to higher order deformations in bending. *Appl. Math. Model.* **35**, 2145–2159 (2011)

3. Shad, M.R., Michon, G., Berlioz, A.: Analytical study of the dynamic behavior of geometrically nonlinear shaft-disk rotor systems. *Mec. Ind.* **12**, 433–443 (2011)
4. Khanlo, H.M., Ghayour, M., Ziaei-Rad, S.: Disk position nonlinearity effects on the chaotic behavior of rotating flexible shaft-disk systems. *J. Mech.* **28**(3), 513–522 (2012)
5. Duchemin, M., Berlioz, A., Ferraris, G.: Dynamic behavior and stability of a rotor under base excitation. *J. Vib. Acoust. Trans. ASME.* **128**(5), 576–585 (2006)
6. Deb, F., Jegadeesan, K., Shrivankumar, C.: Analysis of a rotor supported in bearing with gyroscopic effects. *IOP Conf. Ser.: Mater. Sci. Eng.* **402**, 012059 (2018)
7. Cveticanin, L.: Free vibration of a jeffcott rotor with pure cubic non-linear elastic property of the shaft. *Mech. Mach. Theory.* **40**, 1330–1344 (2005)
8. Jahromi, A.F, Bhat, R.B, Xie, W.F.: Forward and backward whirling of a rotor with gyroscopic effect. In: Sinha, J.K. (ed.) *Vibration Engineering and Technology of Machinery, Mechanisms and Machine Science*, vol. 23, pp. 879–887. Springer International Publishing, Switzerland, (2015)
9. Matsushita, O., Tanaka, M., Kanki, H., Kobayashi, M., Keogh, P.: Gyroscopic effect on rotor vibrations. In: *Mathematics for Industry*, pp. 153–180 (2017)
10. Ghosh, A., Mallik, A.K.: *Theory of Mechanisms and Machines* (2015)
11. Saha, A., Pandey, S.S., Bhattacharya, B., Wahi, P.: Analysis and control of friction-induced oscillations in a continuous system. *J. Vib. Cont.* **18**(3), 467–480 (2011)
12. Meirovitch, L.: *Principles and Techniques of Vibrations*. Prentice Hall (1997)

Friction Stir Welding of IS:65032 Aluminum Alloy and Predicting Tensile Strength Using Ensemble Learning



Kaveti Upender , B. V. R. Ravi Kumar, M. S. Srinivasa Rao,
and M. Venkata Ramana

Abstract Joining two metals play a significant role in the automobile and aerospace industries and it is a challenging job. To overcome the challenges, Friction Stir Welding (FSW) is considered as the solid-state joining technique in the industries as it is a new and unique way. As the field of machine learning is extending its applicability to different fields, it can even be applied in the field of welding. The objective of this paper is to give a review of FSW of aluminum alloys. In addition, machine learning regression models are developed to predict the tensile strength of IS:65032 aluminum alloy by taking rotational speed, welding speed, tool tilt angle, and tool pin shoulder diameter as the input parameters. In this work, the ensemble learning approach is adopted to develop models as it uses the wisdom of many learning algorithms to achieve better performance by filling in the gaps of learning ability. A comparative study was done by considering coefficient of determination and Root Mean Square Error (RMSE) of the Bagging and Boosting models in order to determine a robust regression model for predicting the tensile strength. From the conducted experiment it was concluded that Gradient Boosting Regressor performed better than the other ensemble models and feature importance of independent variables is also evaluated.

Keywords Frictions stir welding (FSW) · IS:65032 aluminum alloy · Ensemble learning · Tensile properties

1 Introduction

Welding is widely used by engineers and manufacturers to connect metal structures for assembling cars and aircraft, building bridges, etc. For many years joining of similar and dissimilar metals was achieved by melting the metals. In the early 1990s,

K. Upender (✉) · B. V. R. R. Kumar · M. S. S. Rao
Department of Mechanical Engineering, VNR Vignana Jyothi Institute of Engineering and Technology, Hyderabad, India

M. V. Ramana
Department of Automobile Engineering, VNR Vignana Jyothi Institute of Engineering and Technology, Hyderabad, India

[1] a new and unique welding technique was developed instead of melting metals to join them using high temperatures. This method is known as Friction Stir Welding (FSW). FSW makes use of friction to generate heat, it uses high forces and relative motion to join the metals. In the FSW process, both the metals parts are in a stationary position, a non-consumable pin which is also known as a tool pin is rotated by penetrating it into the interface of two abutting metal plates and stirred from one end to the other end of the metal in order to join the metals together. The tool pin is a little shorter than the depth of the metal. Friction generated through the tool pin heats the atoms inside the base metal. These heated atoms move around from one metal to another metal and create a strong bond without melting the metals. Besides getting a smooth weld surface, the bond created by this process is as strong as the parent material. The weld surface which is heated due to friction is plastically deformed. In a matter of seconds, the metals are welded and are cool enough to touch. FSW is superior as it leaves a clean and neat appearance along the face of the weld. Apart from conventional welding, FSW joins metals without emitting toxic fumes or gases while welding. With this process, engineers and manufacturers have much more flexibility in the metals they use.

As the field of machine learning is extending its applicability to different fields, it can even be applied in the field of welding. For FSW, by taking rotational speed (RPM), welding speed (mm/min), tool tilt angle, and tool pin shoulder diameter (mm) as the input parameters a machine learning regression model can be developed to predict the tensile strength (MPa) of the weldments. In this work Ensemble learning is used which is a part of machine learning which improves the predictive performance of the model by combining multiple learning algorithms to solve a problem. The main principle behind ensemble learning is to group weak learning algorithms together to form a strong learning algorithm that achieves a better performance than the individual weak learning algorithm. In ensemble learning, weak learning algorithms are referred to as the models that cannot perform well by themselves because they have a high bias or they have high variance and strong learning algorithms are referred to as the ensemble models.

Bagging and Boosting are the two ensemble learning approaches used in the experimentation.

1.1 Bagging Approach

The bagging method is focused to produce an ensemble model with low variance than its components as it learns from several homogeneous weak learners with high variance and then combines them by using an averaging process as shown in Fig. 1. The bagging method is also known as parallel ensemble learning because the base models are trained independently from each other. Random Forest, Bagging, etc. are few examples of bagging.

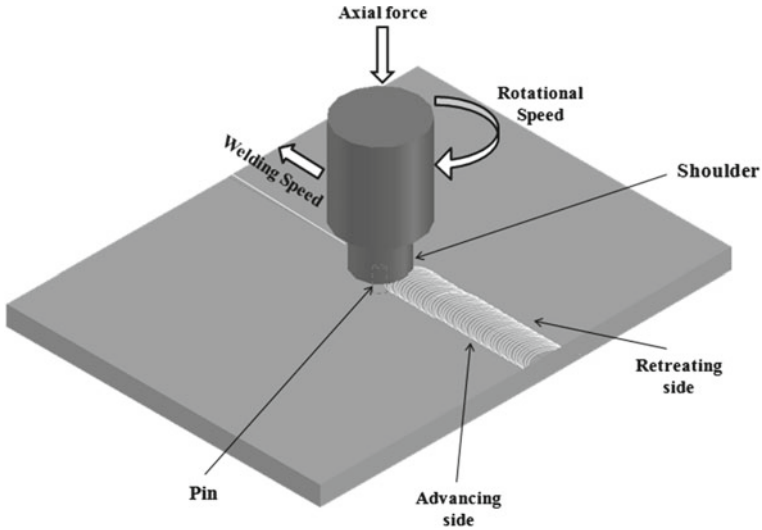


Fig. 1 FSW process

1.2 Boosting Approach

The boosting method is focused to produce an ensemble model with low bias than its components as multiple homogeneous weak learners are combined to obtain a strong learner that performs better than any individual weak learner as shown in Fig. 2. The boosting method is also known as sequential ensemble learning because the base models are trained sequentially. AdaBoost, Gradient Boosting, etc. are few examples of boosting (Fig. 3).

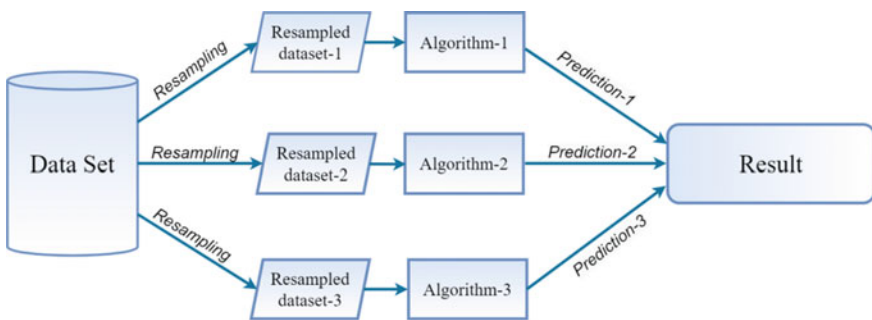


Fig. 2 Bagging diagram

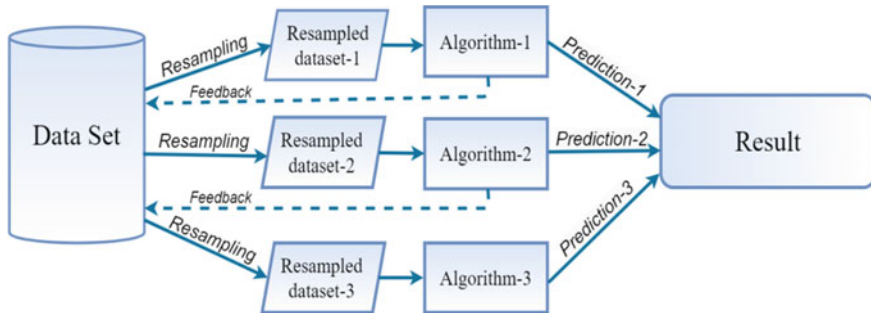


Fig. 3 Boosting diagram

2 Literature Review

Verma et al. [2] performed FSW on AA6082 alloy to determine the ultimate tensile strength (UTS) of the butt joint. Process parameters like rotational speed and welding speed were varied for each butt joint. The joint is fabricated with a tilt angle of 2° and 30 s dwell time. H13 die steel is used as the tool pin with 20 mm diameter, 6.1 mm pin length, 6 mm pin diameter, and hardness of 54-56HRC. According to ASTM E8M-04, tensile specimens were prepared to perform UTS in the universal testing machine (UTM). The UTS of the weldments were recorded to train Gaussian process regression (GPR), support vector machining (SVM), and multi-linear regression (MLR) machine learning models to predict the ultimate tensile strength of the material. The conclusion was given that GPR model with RBF and Pearson VII kernel performed better than SVM and MLR regression models for predicting the values of UTS of welding joints [2]. Mishra and Jain [3] focused to study the single response optimization of FSW on AA 6082-T6 using the Taguchi techniques to yield favorable UTS. The tool used in the experiment was made of high-carbon steel. During the welding process cylindrical, cylindrical with threaded, square, and trapezoidal are used as the tool pins with a diameter of 6 mm in cylindrical tool pin, 6 mm side for square tool pin, 6 mm side of the base in trapezoidal, and 3 mm tapered at the tip. An experiment was conducted with different combinations of rotational speeds, welding speeds, profile pin, and shoulder diameter. The conclusion was drawn that all the parameters which were selected have a significant effect on UTS. With rotational speed of 1200 rpm, welding speed of 30 mm/min, cylindrical threaded tool pin and 16 mm shoulder diameter optimum UTS was obtained [3].

Silva et al. [4] presented an optimization study of friction stir welded joints through the Taguchi and Artificial Neural Network methods. AA6082 material with the dimension of $380 \times 150 \times 3$ mm was used to weld on a modified milling machine. The experiment was performed by varying the tool rotational speed, welding speed, tilt angle, probe distance from the root surface and shoulder/probe diameters ratio (D/d). After the experimentation temperature, tensile properties, hardness profile and bending properties were recorded. An equation with regression coefficients was

developed to estimate the joint properties and other process parameters are dependent on each other. A conclusion was made that the tools diameters ratio was the most influential factor in the joint quality and also that the weld speed, the tool rotational speed and the probe/shoulder diameters ratio are dependent on each other [4]. Garg and Goyal [5] worked on 6 mm thick AA6082-T6 alloy as the base material and tool pin made up of H13 steel with 16 mm shank diameter, 20 mm shoulder diameter, 40 mm shoulder length, 6 mm pin diameter, square tool pin and pin length 5.75 mm. Few FSW process parameters like plunge depth, welding speed, dwell time, and tilt angle are kept constant throughout the fabrication. Welding was done by varying the number of passes and rotational speed. For the tensile test, the specimens are sliced according to the ASTM-E8 M04 standard. Tensile strength, yield strength, % elongation, and micro-hardness were recorded and inspected by plotting graphs. Finally, the conclusion was made that the defected welds are produced at low rotational speed [5].

3 Material

Aluminum alloy IS:65032 is most widely used in the area of manufacturing of structures as it has moderately high strength with excellent corrosion resistance. It even exhibits good weldability and extrudability. Tool pins with shoulder diameter of 12 mm, 14 mm and 16 mm were used to perform a butt weld on Aluminum alloy IS:65032. These tool pins were made up of high carbon steel. These butt weldments were machined to the required dimensions as mention in Fig. 4 using CNC wire cut EDM [6–8] (Figs. 5 and 6; Tables 1 and 2).

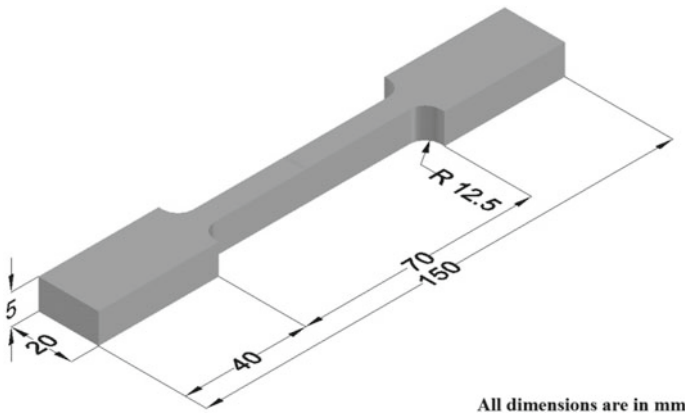


Fig. 4 Tensile specimen dimensions (ASTM E8M-04)

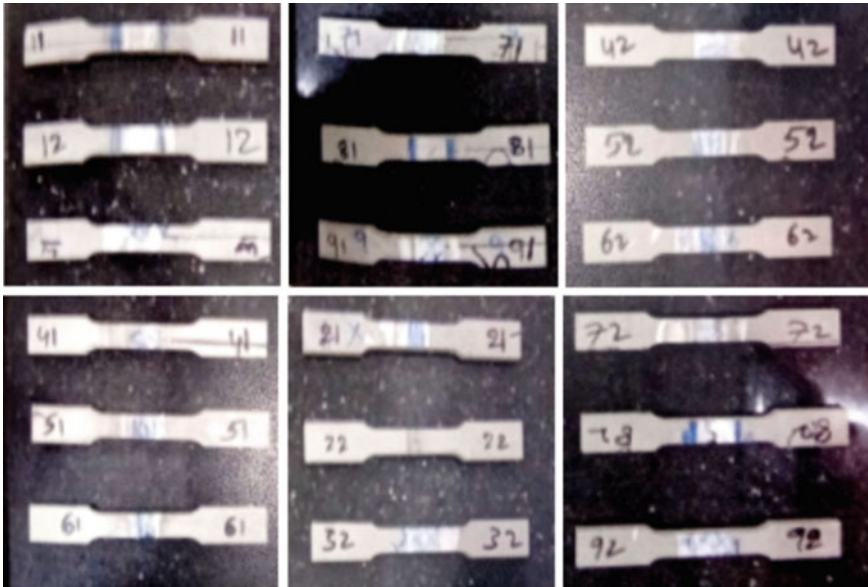


Fig. 5 Few tensile specimens before tensile test



Fig. 6 Few tensile specimens after tensile test

Table 1 Chemical composition of the base material IS:65032 aluminum alloy [6]

Element	Al	Si	Fe	Cu	Mn	Mg	Zn	Cr	Ti
Weight (%)	97.1	0.545	0.534	0.224	0.362	0.916	0.245	0.005	0.016

Table 2 Mechanical properties of the base material IS:65032 aluminum alloy [6]

Property	Yield strength (MPa)	UTS (MPa)	% Elongation
Value	266.6	308.5	16.28

Table 3 Few experimental values from the data set

S. No.	Factors				Output response weld strength (MPa)	
	Rotational speed (RPM)	Travel speed (mm/min)	Tool tilt angle (Degrees)	Tool pin shoulder diameter (mm)	Sample 1	Sample 2
1	1000	60	0	12	204.5	213.3
2	1000	80	1	12	200.3	210.7
.
.
.
.
27	1600	100	1	16	270.5	278.3

4 Dataset

The data set was created by taking the experimental values of Rao et al. [6]. By analyzing all the experiments values rotational speed (RPM), welding speed (mm/min), tool tilt angle (degrees), and tool pin shoulder diameter (mm) was considered as input variables and tensile strength (MPa) of sample 1 and sample 2 as the target variable. The data set consists of 27 samples and it is split into training and testing dataset in the ratio of 8:1. All the samples are stored in CSV files, the training file has 24 rows * 6 columns and the testing file has 3 rows * 6 columns (Table 3).

5 Methodology

Initially, in the training phase the training data set is passed to the Decision Tree Regressor (DTR), Random Forest Regressor (RFR), Bagging Regressor (BR), AdaBoost Regressor (AR), and Gradient Boosting Regressor (GBR) algorithms for training the models. As there are two target variables in the dataset, multi output regressor models are developed. After training the multi output regressor models with the training data set, the best model is selected for predicting the tensile strength. Best model was selected by comparing the coefficient of determination or R^2 and Root mean square error (RMSE) of the models. The coefficient of determination tells us how well the model predicts the target variable. As the value of the R^2 error approaches to one then it is said that the developed model is a generalized model. RMSE talks about how the data is around the best fit line and it penalizes large errors. In the testing phase, the test data set is passed to the best model for predicting the tensile strength (Fig. 7).

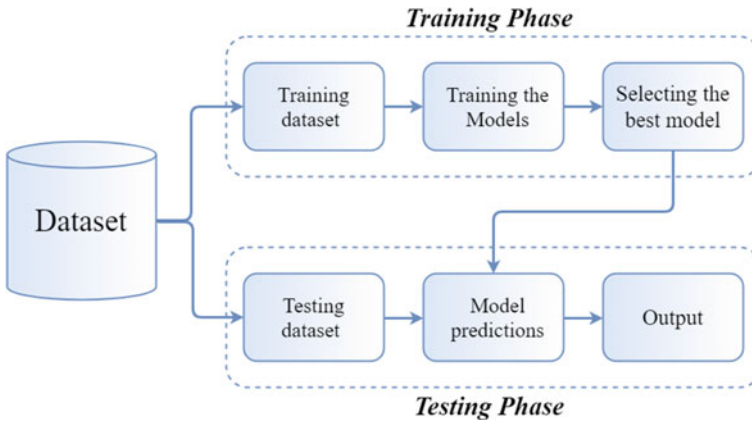


Fig. 7 Block diagram for predicting the tensile strength

$$R^2 = 1 - \frac{\sum_i^n (y_i - \hat{y}_i)^2}{\sum_i^n (y_i - \bar{y})^2} \tag{1}$$

$$RMSE = \sqrt{\frac{1}{n} \sum_i^n (y_i - \hat{y}_i)^2} \tag{2}$$

‘n’ is the number of samples,
 ‘ y_i ’ is the actual value,
 ‘ \hat{y}_i ’ is the predicted value and
 ‘ \bar{y} ’ the average predicted value.

6 Results

R^2 error and RMSE of the experimented algorithms are recorded in Table 4. Based on the R^2 error and RMSE of the Regression algorithms a conclusion can be drawn that Gradient Boosting Regressor is the best model.

Table 4 R^2 error and RMSE values of the experimented algorithms

S. No.	Algorithm	R^2 error	RMSE
1	Decision Tree Regressor	0.962	6.565
2	Random Forest Regressor	0.976	5.219
3	Bagging Regressor	0.978	4.97
4	AdaBoost Regressor	0.970	5.83
5	Gradient Boosting Regressor	0.992	2.895

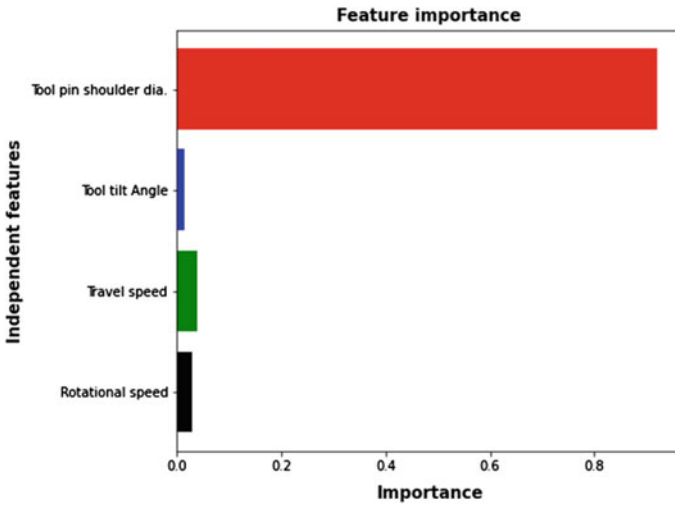


Fig. 8 Feature importance sample—1

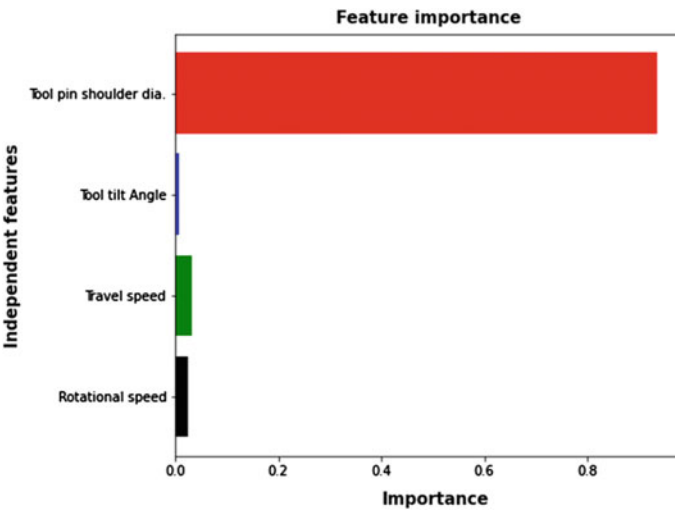


Fig. 9 Feature importance sample—2

Table 5 Feature importance of the independent attributes

Sample No.	Rotational speed	Travel speed	Tool tilt angle	Tool pin shoulder diameter
1	0.027	0.038	0.013	0.921
2	0.025	0.030	0.007	0.937

Table 6 Independent features of the test dataset

S. No.	Rotational speed (RPM)	Travel speed (mm/min)	Tool tilt angle (Degrees)	Tool pin shoulder diameter (mm)
1	1300	60	1	14
2	1300	100	0	16
3	1600	80	0	12

In Figs. 8, 9 and Table 5 feature importance of GBR is plotted and recorded respectively. From these plots and values, it can be confirmed that the independent feature Tool pin shoulder diameter is contributing more to the formation of the model.

The test data set is passed to the GBR model to predict the tensile strength. In Table 6 test data sets independent features are tabulated and in Table 7 test data sets dependent features are tabulated along with the model predicted values.

In Figs. 10 and 11 the actual UTS and the predicted values of samples 1 and 2 are plotted and the plots show that the predicted results are nearer to the experimental results.

Table 7 Target variables and predicted values

S. No.	Actual sample 1	Actual sample 2	Predicted of sample 1	Predicted of sample 2
1	257.5	262.2	261.71	261.90
2	280.2	284.1	277.46	285.79
3	200.1	204.2	203.26	207.67

Fig. 10 Tensile strength versus sample 1 in the test dataset

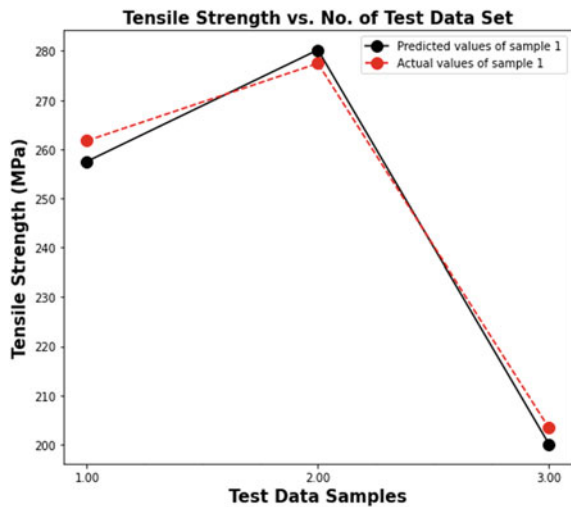
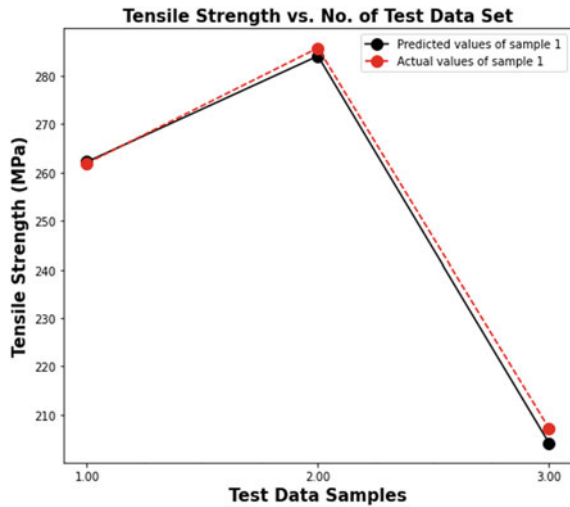


Fig. 11 Tensile strength versus sample 2 in the test dataset



7 Conclusions

In this study, a comparative study on DTR, RFR, BR, AR, and GBR models were evaluated by measuring the R^2 error and RMSE of each model. From this study the drawn conclusions are:

- The GBR model performed better than other models as it achieved 0.992 R^2 error and 2.895 RMSE.
- Among the independent features Tool pin shoulder diameter is contributing more to the formation of the robust model. From this it can be inferred that tool pin has major effect on the UTS of the FSW weldments.

In future, algorithms related Bagging and Boosting approaches can be implemented on large datasets. By tuning the hyper parameters of the selected model the predicting ability of the developed model can be enhanced to a greater extent.

References

1. Marathe, S.: A review paper on: friction stir welding (FSW). *Int. J. Adv. Res. Eng. Sci. Manage* **2** (2016)
2. Verma, S., Gupta, M., Misra, J.P.: Performance evaluation of friction stir welding using machine learning approaches. *MethodsX* **5**, 1048–1058 (2018)
3. Mishra, R., Jain, S.: Friction stir welding (FSW) process on aluminum alloy 6082-T6 using taguchi technique. *Int. J. Res. Eng. Inno.* **3**, 301–305 (2019). <https://doi.org/10.36037/IJREI.2019.3503>
4. Silva, L.F.M., Braga, D.F.O., Miguel, Moreira, P.: Integrity, reliability and failure of mechanical systems AA6082-T6 friction stir welded butt joints optimization (2013)

5. Garg, R.K., Goyal, A.: Experimental investigations on FSW of AA6082-T6 aluminum alloy (2020). https://doi.org/10.1007/978-981-15-4748-5_1
6. Rao, M.S.S., Kumar, B.V.R.R., Hussain, M.M.: Experimental study on the effect of welding parameters and tool pin profiles on the IS:65032 aluminum alloy FSW joints. *Mater. Today: Proc.* **4**, 1394–1404 (2017). <https://doi.org/10.1016/j.matpr.2017.01.161>
7. Elangovan, K., Balasubramanian, V.: Influences of tool pin profile and welding speed on the formation of friction stir processing zone in AA2219 aluminium alloy. *J. Mater. Process. Technol.* **200**, 163–175 (2008). <https://doi.org/10.1016/j.jmatprotec.2007.09.019>
8. Rao, M.S.S.: Experimental study of weld characteristics during friction stir welding (FSW) of aluminum alloy (AA6061-T6). *Int. J. Res. Eng. Technol.* **1**, 469–473 (2012). <https://doi.org/10.15623/ijret.2012.0103046>

Experimental Investigation on Nozzle Flow at Different Levels of Jet State at Supersonic Mach Numbers with Sudden Expansion



Ridwan, J. I. Suheel, Hamza Afser Delvi, M. MashtaqAhamed Attar, Sher Afghan Khan, and Mohammed Faheem 

Abstract This study depicts the experiment's outcomes to assess the control mechanism efficacy when activated at the base recirculation zone for an area ratio of 4.84. The convergent-divergent (CD) nozzles with Mach numbers considered were from 1.25 to 3, and experiments were done for correctly, imperfectly, and under-expanded cases. For low Mach numbers, namely $M = 1.25$ and 1.3, variation in the duct's flow is identical, and control is not applicable. However, there is an increase in the fluctuation level from Mach 1.6, and its growth continues until the study's highest Mach number. For Mach 1.48 and 1.6, the flow management scores increased the pressure in the pipe. For Mach 1.8, the effectiveness shows a mixed trend. This trend gets reversed at Mach 2, and when the flow control mechanism is used, it reduces pressure. For the largest Mach 3 of the study, the control efficacy is negligible, and the microjet does not negatively impact the flow field.

Keywords Wall pressure · Area ratio · Supersonic jet · Active control · Microjets · Sudden expansion

1 Introduction

The jets are utilized to propel jet liquids at high pressures and are applied in industrial and end-user products such as gasoline injectors, water jet cutters, showers, etc. The CDs are used to propel gasses to extreme velocity, exceeding the sonic speed to

Ridwan · S. A. Khan · M. Faheem (✉)

Department of Mechanical Engineering, Faculty of Engineering, IIUM, Kuala Lumpur, Malaysia
e-mail: faheem.mech@pace.edu.in

J. I. Suheel

Department of Mechanical Engineering, BMS College of Engineering, Bangalore, India

H. A. Delvi

Department of Thermal Power, VTU Regional Centre, Mysuru, India

M. M. Attar · M. Faheem

Department of Mechanical Engineering, P. A. College of Engineering, Mangalore, India

obtain the most considerable amount of thrust for an aircraft. The airline industry employs CDs for aircraft, missiles, and unguided rockets [1]. An elaborate structure representing the flow separation and recirculation in an abruptly extended flow is shown. The flow gets re-connected after the breakup, and the viscous seam will split into twin areas. It gets divided into the recirculation region and the main jet area. The attachment juncture is where the splitting streamline meets the wall of the tube of the extended duct. Figure 1 explains the suddenly expanded flow range characteristics [2–7].

It is noticeable that the combustion mechanisms are preferred by a substantial decrease of the base drag, while a growing trend of base drag decreases net drag in air-moving bodies. Equally notable is the absence of oscillations of flow preceding base drag control. In the sudden expansion of flows, Sethuraman et al. [8] explored the usage of dynamic and submissive monitor approaches to investigate pressure inside the pipe. The analysis shows that the active stream management technique controls the pressure in the wake effectively. A study of Pathan et al. [9] extended duct optimization shows that the enlarged tube portrays a vital role in improving the driving force and attachment on the flow path while exiting the nozzle. By increasing the Mach, the force of the thrust increases. It is observed that the thrust increases after a certain ideal level with the increasing duct length. Microjets regulated the wall pressure of the suddenly long nozzle. The extreme variation in the pipe pressure is during the re-connection duration when the duct size $L = 10D$ is higher.

Wall pressure improvements are between 50 and 60% in this situation [10–13]. It was reported that the duct size could be distinguished for a fixed level of expansion, which ends in the most incredible increment or reduction of pressure in the wake. Usually, duct size $L = 5D$ seemed to be the threshold for manipulating the region's vortex. Except for $NPR = 3$, the limit is reduced to $L/D = 2$ at supersonic Mach numbers. The pipe size $<5D$ showed to be inadequate for the stream to be reattached in nearly all instances [14–18]. Flow expansion plays a crucial role in determining baseline pressure values. For the lower relief of 2.56 and 3.24, control is quite useful.

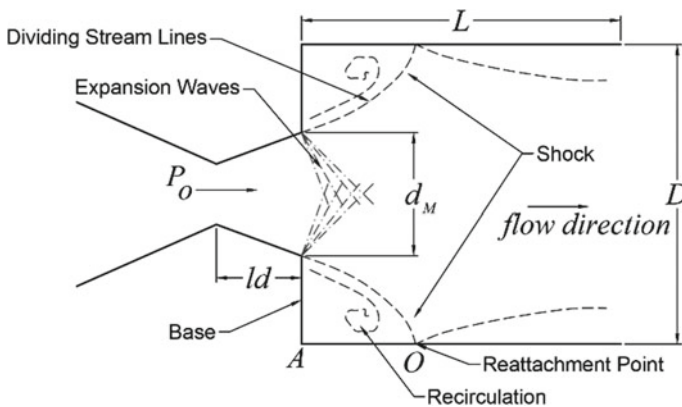


Fig. 1 Flow with sudden expansion [9, 19]

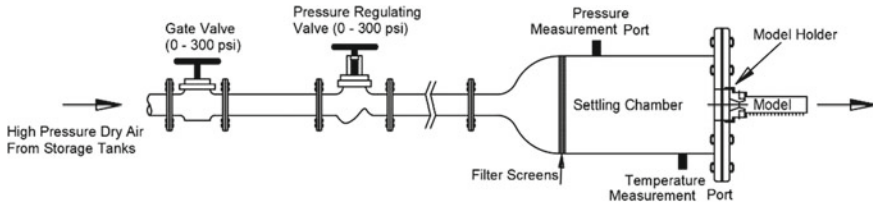


Fig. 2 Jet facility [20, 21]

Microjets in the range of 2.6 and 3 for each Mach $M = 2.2$ have been proved to be helpful [2]. The study uses microjets for the base region to increase the pressure and the tube section of the conduit utilizing supersonic CD nozzle Mach numbers.

2 Experimental Setup

2.1 Jet Facility

Experiments were carried at the IIT, Kanpur, India, utilizing an accessible jet lab. The research lab comprises a storage facility of 85 m^3 . A multi-stage compressor that generates a maximum of developing $0.17 \text{ m}^3/\text{s}^3$ air at a gauge pressure of 300 psi is delivered onto the containers. Under pressure, air from the tank is transported through the pressure regulator via a nozzle, across the seating partition. An appropriate mixing span is placed between the valve and the storage tank to relieve the regulatory valve's stream disturbances. The test section is a cylindrical portion with a wire knit inside, which screens the air before transferring to the nozzle and tube [1, 20]. A blowing control tank was used to trigger tiny jets to determine the pressure under control (Fig. 2).

2.2 Experimental Model

Convergent-divergent nozzles and circular ducts are produced from brass. An increased pipe with a step height of 2.5 was fitted at the exit of the chamber, utilizing a flange at the exit of the nozzle to perform the tests. The nozzles were regulated after fabrication to confirm the design Mach ($M = 1.25$ to 3.0) to establish the definite Mach at the exit of the nozzle. The detailed procedure for manufacturing the nozzle and tube is reviewed in the literature [22–26] (Fig. 3).

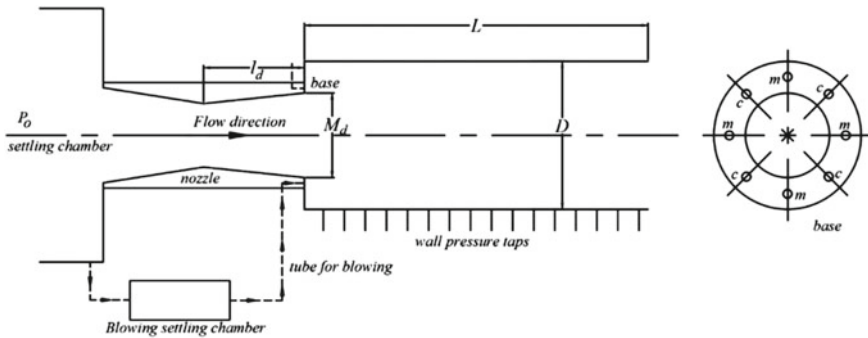


Fig. 3 Nozzle and duct [27, 28]

3 Results and Discussion

The pressure of the tube is standardized by dividing it with the freestream pressure. The study was carried out for Mach 1.25, 1.3, 1.48, 1.6, 1.8, 2, and 3. The experiments were done for Mach 1.25 to 2.0 when nozzles are correctly expanded. At Mach 1.8 and 2.0, the nozzles were underneath the effect of a beneficial pressure ascent. For the highest Mach number of the study, the nozzle is imperfectly expanded. Findings for $M = 1.25$ are exhibited in Fig. 4a, b for duct segments $L = 8D$ and $4D$ for perfectly expanded case. For the greatest duct stretch, there are variations in the pressure of the duct by thirty-three percent. However, such variations are not seen for $L = 4D$. These fluctuations are attributed owing to the interactions of the shock in the interior of the reattachment duration. Once the flow crosses the reattachment length, there is

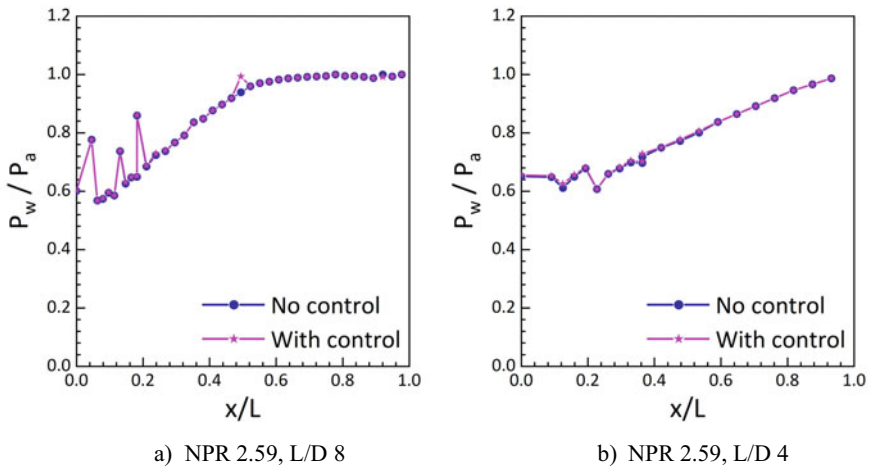


Fig. 4 Results at Mach 1.25 at design NPR

an effortless growth of pressure till it achieves the ambient requirements. The flow patterns are identical—control increases the pressure inside the pipe.

With a further escalation in the inertia levels, the effect of a rise in inertia level is visible in Fig. 5a, b. There are considerable changes and variations in the wall pressure, and the fluctuations are more than a hundred percent. The fields are identical, and the control mechanism has no adverse impact on the flow field. When we look at the findings of this study at Mach 1.8 are shown in Fig. 6a, b for duct size $L = 10D$ to $4D$ for design NPR. The control’s outcome is to decrease the wall pressure

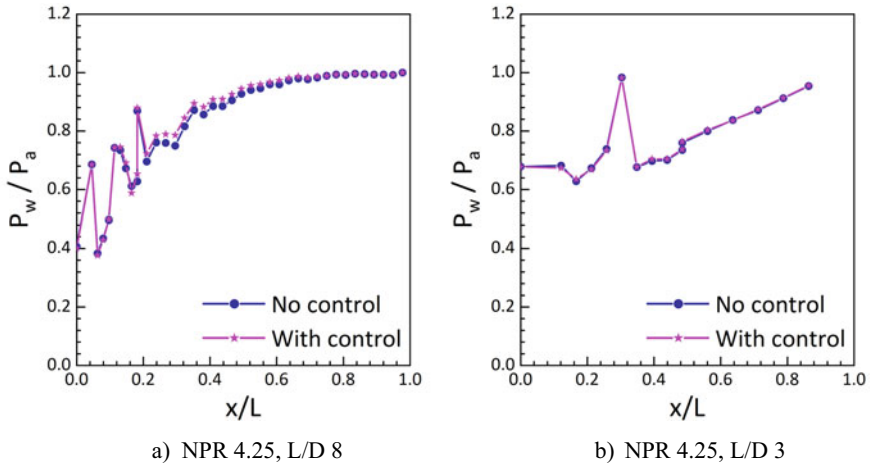


Fig. 5 Results at $M = 1.6$ at design NPR

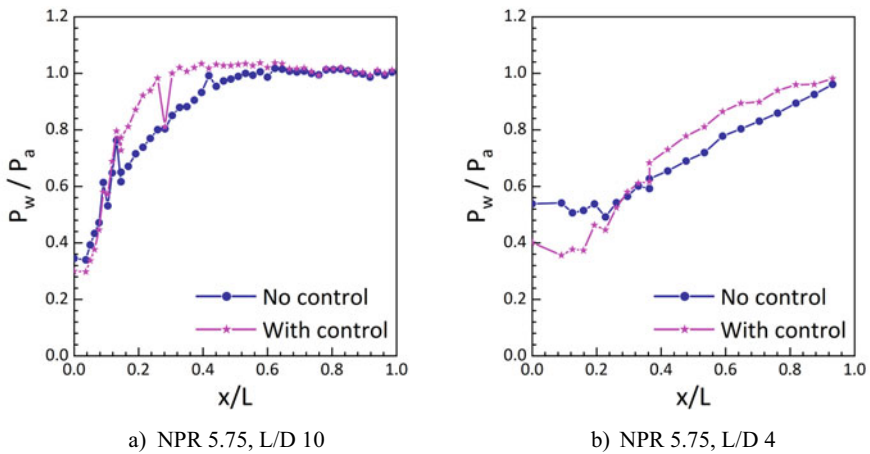


Fig. 6 Results at $M = 1.8$ at design NPR

within the reattachment length, whereas, in the regions beyond $x = 0.3L$, the flow management effect is to raise the wall pressure.

Results for Mach 1.8 for a favorable pressure gradient for four different duct lengths are presented in Fig. 7a–d. The study aims to assess the control mechanism’s effect at a predetermined intensity of the beneficial pressure grade. When the pipe’s length is considerable, the pressure fluctuations are dominant due to the shock waves’ interface, dividing streamline, and reflecting the waves’ reflections from the wall. The flow control management efficiency is insignificant. For lower duct length due to the backpressure’s influence, the duct’s pressure variations are declined.

Figures show that results at Mach 2 for duct dimensions $L = 8D$ to $2D$. Figure 8a–d for correctly expanded cases. As the nozzle flow is at the design NPR, the shear tier departing from the nozzle’s exit will pass through the weak waves. These waves will

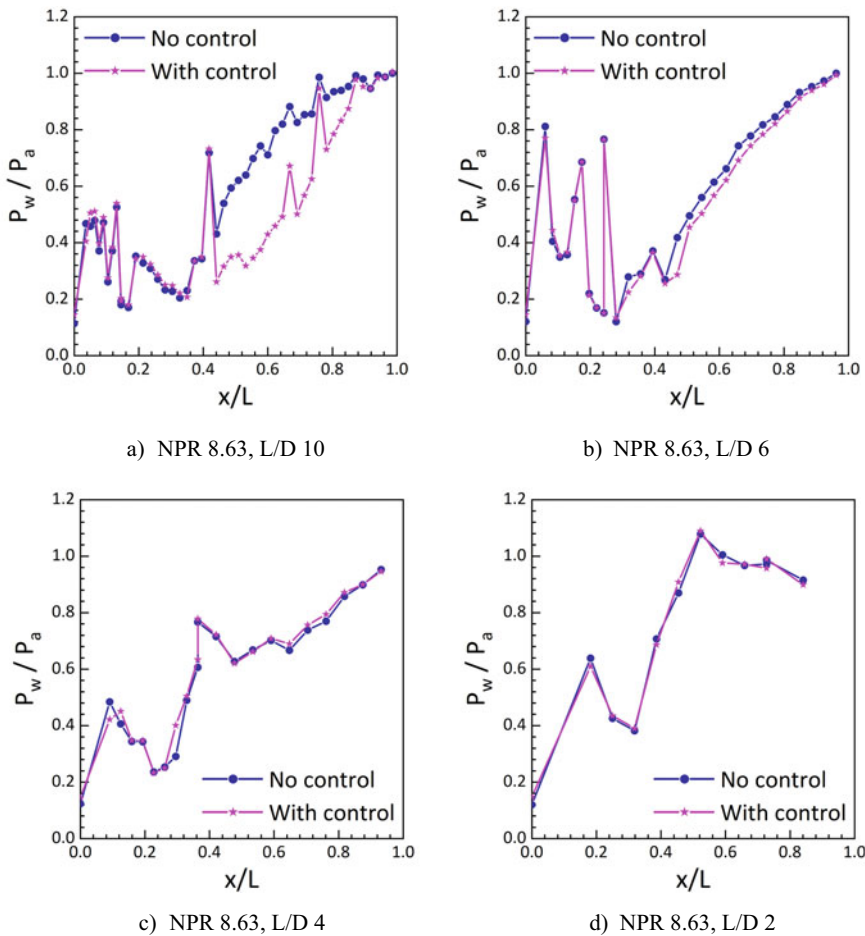


Fig. 7 Results at $M = 1.8$ for under-expanded case

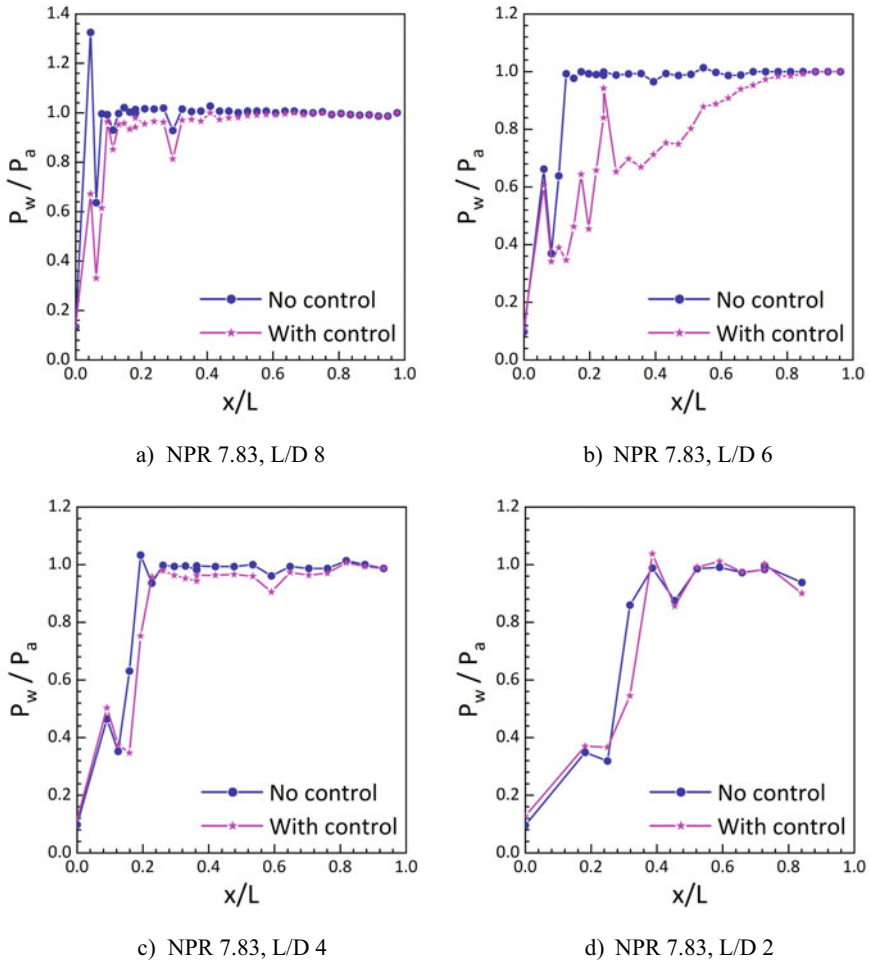


Fig. 8 Results at $M = 2$ at design NPR

have a negligible influence on the flow pattern of the duct. That may be the reason for minimal variations in the pressure field inside the enlarged duct. Once again, these findings at design NPR have demonstrated that the flow field will not be free from the waves. Rather, the Mach waves are noticed in the flow field. Normally the flow field remains similar before and after the control mechanism's presence—the dynamic flow control management scores in a decline of the duct pressure. The extent of the reduction of the duct pressure is mostly related to the duct size. For large duct length, control impact is more as compared to the smaller duct length. For smaller duct lengths, the backpressure influence will be more. It is also seen that the pressure fluctuations are limited within the reattachment length of the duct.

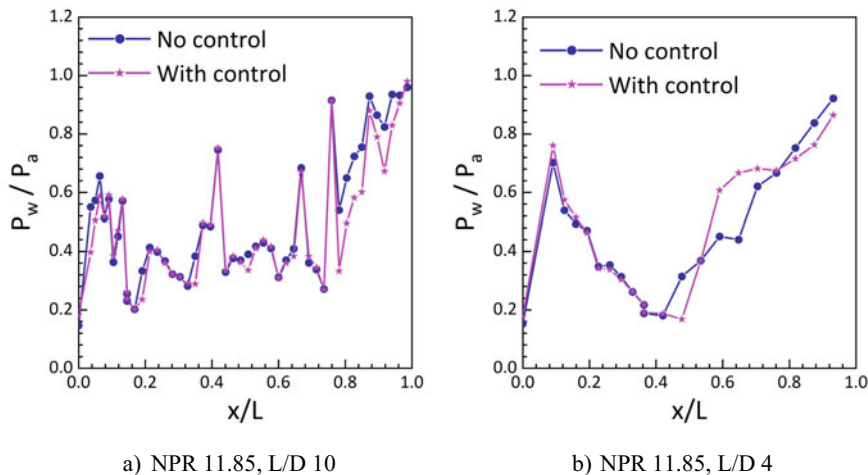


Fig. 9 Results at Mach 2 for under-expanded case

Results for the under-expansion case at Mach 2.0 are shown in Fig. 9a, b for conduit lengths $L = 10D$ to $4D$. Once the jets are undergoing the expansion fan due to a favorable pressure gradient, the pressure has decreased and reached a low level while departing from the nozzle departure—the value of the pressure at the departure end is twenty percent of the freestream value. When the duct length is ten times the diameter, the fluctuations are highest. The control does not show any definite trend when the flow regulation mechanism is employed for these duct lengths. This trend's physical reasons may be the high Mach number, the duct length, and the flow's relief. Established on the directly above findings, we can declare that control may not give the desired results when the area ratio is beyond a certain limit. Because of the large area ratio, the flow may propagate without influencing the duct's flow field.

The findings of this investigation at Mach 3 for $L = 10D$, $6D$, and $3D$ at NPR = 10 are shown in Fig. 10a–c when the adverse pressure exists. The level of over-expansion is 0.277. These figures show that the normalized pressure's magnitude has different values at the shear layer's exit position. Their values are 0.45, 0.8, and 0.7 for tube size $L = 10D$, $6D$, and $3D$. Variation in the pressure values is due to the ambient pressure, the strength of the oblique shock wave, the manifested shock wave's strength the vortex's strength within the reattachment length. Major oscillations are noticed for $6D$ duct length. For the largest duct length of $10D$ small fluctuations, ten percent duct length is seen to be contained. Later a smooth recovery of the pipe pressure takes place. The duct length $L = 3D$ seems barely adequate for the stream to continue to be connected to the pipe.

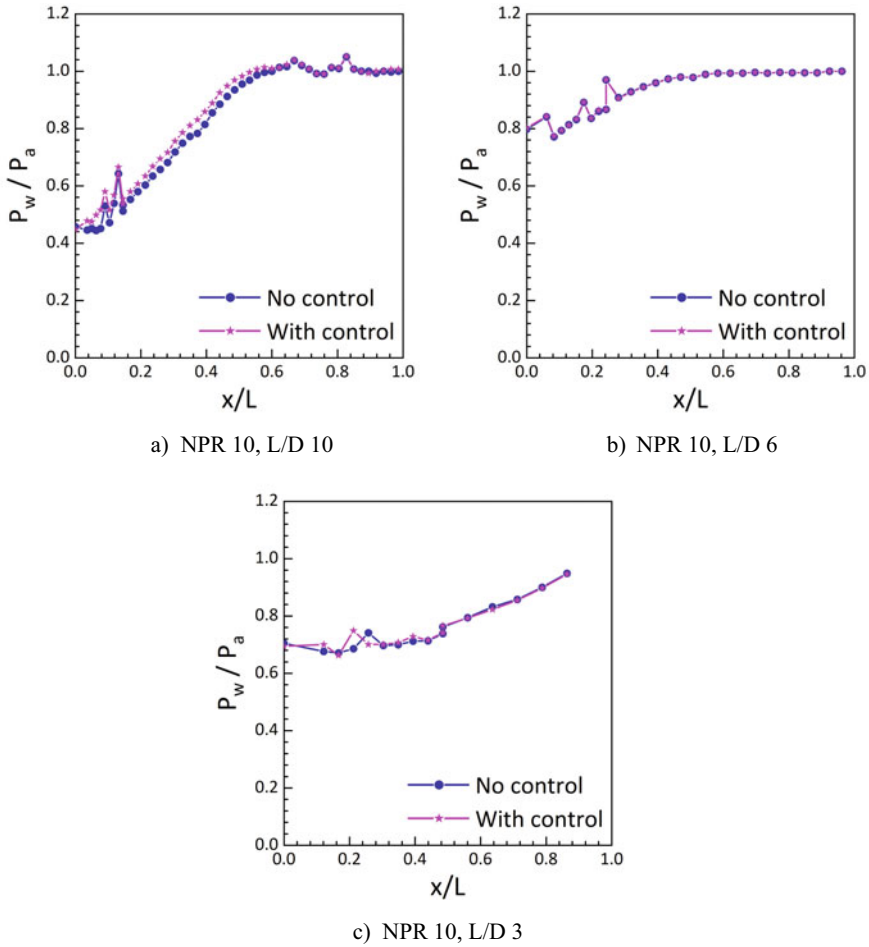


Fig. 10 Results at $M = 3$ for over-expanded case

4 Conclusion

Built on the directly above conversation, we can bring in the following inferences. For low Mach numbers, namely $M = 1.25$ and 1.3 , variation in the duct's flow is identical, and control is not valid. For Mach 1.48 and 1.6 , the flow control management increases the pipe pressure. However, around $M = 1.6$, the fluctuation level from Mach 1.6 and its growth continues until the study's highest Mach number. For Mach 1.8 , the effectiveness shows a mixed trend. This trend gets reversed at Mach 2 , and when the flow control mechanism is used, it reduces pressure. That indicates that under-expanded jets need not increase the ducts inside pressure, which is a standard perception. This study demonstrated that for smaller Mach $M = 1.25$ to 1.6 , the jets

with favorable pressure gradient increases wall pressure inside the duct. Here the relief available to the flow additionally portrays a vital part. For the largest Mach 3 of the current investigation, the flow control management efficacy is insignificant, and the microjets do not negatively affect the pipe's flow.

References

1. Faheem, M., Khan, A., Kumar, R., Khan, S.A.: Experimental study of supersonic multiple jet flow field. In Proceedings of the 32nd International Symposium on Shock Waves (ISSW32), July 2019, pp. 2725–2731. https://doi.org/10.3850/978-981-11-2730-4_0362-cd
2. : Analysis of Area Ratio in a CD Nozzle with Suddenly Expanded Duct using CFD Method, vol. 5, no. 5, pp. 61–71 (2019)
3. Pathan, K.A., Dabeer, P.S., Khan, S.A.: Optimization of area ratio and thrust in suddenly expanded flow at supersonic Mach numbers. *Case Stud. Therm. Eng.* **12**(September), 696–700 (2018). <https://doi.org/10.1016/j.csite.2018.09.006>
4. Aabid, A., Mazlan, N.M., Ismail, M.A.: Numerical Simulation of Suddenly Expanded Flow at Mach 2.2 (March 2019)
5. Asadullah, M., Khan, S.A., Asrar, W.: Low-cost base drag reduction technique. *Int. J. Mech. Eng. Robot. Res.* **7**(4), 428–432 (2018). <https://doi.org/10.18178/ijmerr.7.4.428-432>
6. Khan, A., Aabid, A., Khan, S.A.: CFD analysis of convergent-divergent nozzle flow and base pressure control using micro-JETS. *Int. J. Eng. Technol.* **7**(3.29), 232–235 (2018)
7. Baig, M.A.A., Al-Mufadi, F., Khan, S.A., Rathakrishnan, E.: Control of base flows with micro jets. *Int. J. Turbo Jet Engines* **28**(1), 59–69 (2011). <https://doi.org/10.1515/TJJ.2011.009>
8. Sethuraman, V., Rajendran, P., Khan, S.A.: Base and wall pressure control using cavities and ribs in suddenly expanded flows-an overview. *J. Adv. Res. Fluid Mech. Therm. Sci.* **66**(1), 120–134 (2020)
9. Pathan, K.A., Dabeer, P.S., Khan, S.A.: Enlarge duct length optimization for suddenly expanded flows. *Adv. Aircr. Spacecr. Sci.* **7**(3), 203–214 (2020). <https://doi.org/10.12989/aas.2020.7.3.203>
10. Bashir, M., Khan, S.A., Chaudhary, Z.I., Shinde, V.: Wall pressure measurements beneath the supersonic jets in an abruptly augmented nozzle. *J. Adv. Res. Fluid Mech. Therm. Sci.* **66**(2), 20–31 (2020)
11. Benefit of Mach number and expansion level on the flow development in a cylindrical tube diameter of 18 mm. *Mater. Today Proc.* (Inpress, 2021). <https://doi.org/10.1016/j.matpr.2021.05.167>
12. : Significance of dynamic control on suddenly expanded flow when nozzles are over, under, and perfectly expanded. *Mater. Today Proc.* (Inpress, 2021). <https://doi.org/10.1016/j.matpr.2021.05.655>
13. Khan, S.A., Chaudhary, Z.I., Baig, M.A.A., Delvi, H.A., Faheem, M.: Impact of Mach number on the flow pattern in suddenly expanded duct. *Mater. Today Proc.* (Inpress, 2021). <https://doi.org/10.1016/j.matpr.2021.06.149>
14. Saleel, A., Baig, M.A.A., Khan, S.A.: Experimental investigation of the base flow and base pressure of sudden expansion nozzle. *IOP Conf. Ser. Mater. Sci. Eng.* **370**(1) (2018) <https://doi.org/10.1088/1757-899X/370/1/012052>
15. Khan, S.A., Chaudhary, Z.I., Shinde, V.B.: Base pressure control by supersonic micro jets in a suddenly expanded nozzle. *Int. J. Mech. Mechatronics Eng.* **18**(4), 101–112 (2018)
16. Khan, S.A., Aabid, A., Saleel, C.A.: Influence of Micro Jets on the Flow Development in the Enlarged Duct at Supersonic Mach Number 01 (2019)
17. Aabid, A., Chaudhary, Z.I., Khan, S.A.: Modelling and analysis of convergent divergent nozzle with sudden expansion duct using finite element method. *J. Adv. Res. Fluid Mech. Therm. Sci.* **63**(1), 34–51 (2019)

18. Quadros, J.D., Khan, S.A.: Prediction of base pressure in a suddenly expanded flow process at supersonic mach number regimes using ANN and CFD. *J. Appl. Fluid Mech.* **13**(2), 499–511 (2019). <https://doi.org/10.29252/jafm.13.02.30049>
19. Aabid, A., Khan, S.A.: Determination of wall pressure flows at supersonic Mach numbers. *Mater. Today Proc.* (2020). <https://doi.org/10.1016/j.matpr.2020.06.538>
20. Faheem, M., Khan, A., Kumar, R., Khan, S.A., Asrar, W., Sapardi, A.M.: Experimental study on the mean flow characteristics of a supersonic multiple jet configuration. *Aerosp. Sci. Technol.* **108**(106377), 1–13 (2021). <https://doi.org/10.1016/j.ast.2020.106377>
21. Faheem, M., Khan, A., Kumar, R., Khan, S.A., Asrar, W., Sapardi, M.A.M.: Experimental investigation of the effect of cross wire on the flow field of elliptic jet. *Int. J. Heat Fluid Flow* **90**(August), 1–12 (2021). <https://doi.org/10.1016/j.ijheatfluidflow.2021.108834>
22. Azami, M.H., Faheem, M., Aabid, A., Mokashi, I., Khan, S.A.: Experimental research of wall pressure distribution and effect of micro jet at Mach 1.5. *Int. J. Recent Technol. Eng.* (2019). <https://doi.org/10.35940/ijrte.B1187.0782S319>
23. Khan, S.A., Mokashi, I., Aabid, A., Faheem, M.: Experimental research on wall pressure distribution in C-D nozzle at mach number 1.1 for area ratio 3.24. *Int. J. Recent Technol. Eng.* (2019). <https://doi.org/10.35940/ijrte.B1182.0782S319>
24. Azami, M.H., Faheem, M., Aabid, A., Mokashi, I., Khan, S.A.: Inspection of supersonic flows in a CD nozzle using experimental method. *Int. J. Recent Technol. Eng.* (2019). <https://doi.org/10.35940/ijrte.B1186.0782S319>
25. Faheem, M., Kareemullah, M., Aabid, A., Mokashi, I., Khan, S.A.: Experiment on of nozzle flow with sudden expansion at mach 1.1. *Int. J. Recent Technol. Eng.* **8**(2S8), 1769–1775 (2019). <https://doi.org/10.35940/ijrte.B1150.0882S819>
26. Faheem, M., Muneer, R., Avvad, M., Aneeque, M., Khan, S.A.: Influence of microjets on flow development for diameter ratio of 1.6 for correctly expanded nozzles. *Mater. Today Proc.* **46**(7), 2549–2556 (2021). <https://doi.org/10.1016/j.matpr.2021.01.834>
27. Faheem, M., Suheel, J.I., Delvi, H.A., Khan, S.A.: Studies on nozzle flow at beneficial and adverse flow conditions and effectiveness of flow control management. In 2020 IEEE 7th International Conference on Engineering Technologies and Applied Sciences (ICETAS) Studies, pp. 20–24 (2021)
28. Delvi, H.A., Muneer, R., Faheem, M., Khan, S.A.: Influence of microjets on flow development at supersonic mach numbers with sudden expansion. *IOP Conf. Ser. Mater. Sci. Eng.* **1057**, 012051 (2021). <https://doi.org/10.1088/1757-899x/1057/1/012051>

Multi Objective Optimization Using Artificial Neural Networks in the Cutting Parameters of Machining of Heat Treated Be-Cu Alloy



Manda Sreeja, K. Devaki Devi, and M. Naga Phani Shastry

Abstract Metal cutting is a complex process which affects the quality of a finished product. While, quality is the measure of performance and production rate. This paper describes an efficient model of optimizing cutting parameters in machining of heat-treated Beryllium Copper Alloy to minimize surface roughness (Ra), cutting forces (Fc) and maximize Metal Removal Rate (MRR). The input parameters are speed, feed, depth of cut, nose radius and heat treatment. This study presents Multi Objective Optimization (MOO) which includes generating Analysis Of Variance (ANOVA) and Artificial Neural Networks (ANN) is used to predict the output, which is then verified with the experimental results and the model is then monitored for desired accuracy levels.

Keywords MOO · Ra · Fc · ANOVA · MRR

1 Introduction

Machining is the process used in manufacturing to remove unwanted material for forming desired shape. Its main objective is to form the structure of required dimensions with enhanced finishing. As it is the production process which is carried out by cutting, use of machine tool is unavoidable and hence we can either use manual or automatic control. Irrespective of control machining is to be carried out by optimal usage of parameters so that suitable finishing and material removal rate can be acquired. This paper presents one of such optimal conditions of cutting parameters in heat treated beryllium copper alloy.

Multi Objective optimization is said to be the process of optimizing one or more parameters to enhance the desired output in this context Multi Objective Optimization is nothing but minimizing the selected input parameters to achieve the maximization in output parameters. The input parameters considered are speed, feed, depth of cut, nose radius and heat treatment. Each of these parameters has its own impact

M. Sreeja (✉) · K. Devaki Devi · M. Naga Phani Shastry
G Pulla Reddy Engineering College, Kurnool, Andhra Pradesh, India
e-mail: sreejareddy.manda@gmail.com

© The Author(s), under exclusive license to Springer Nature Singapore Pte Ltd. 2022
K. C. Popat et al. (eds.), *Advances in Mechanical Engineering and Material Science*,
Lecture Notes in Mechanical Engineering,
https://doi.org/10.1007/978-981-19-0676-3_10

in machining process if it comes to speed, variation in speed leads to irregularities in material removal rate and feed impacts over the finishing of the material so the consideration of parameters is a major task and is to be given equal importance dependent on the output. Here, the output parameters are Material removal rate, surface roughness and cutting force.

1.1 Nomenclature

s	Speed, rpm
f	Feed, mm/min
doc	Depth of cut, mm
ns	Nose radius, mm
ht	Heat treatment
MRR	Material removal rate, mm ³ /min
Ra	Surface roughness, microns
Fc	Cutting force, KN

Beryllium copper alloy has wide range of applications due to its extensive properties. Some of the sectors where beryllium alloy used are automotive, electrochemical, aerospace, medical and telecommunication industries. This be-cu alloy offers enhanced results in mechanical properties like strength and hardness after heat treatment.

1.2 Objectives Presented in This Paper

Maximization of Metal removal rate.

Minimization of surface roughness and cutting force.

2 Literature Review

According to Devaki Devi [1], multi objective optimization of process parameters is a suitable method to improve quality of outputs in machining of beryllium copper alloy. In her research work she proposed several methods to optimize process parameters, namely response surface methodology and genetic algorithms.

In his paper, Krishna Prasad [2], presented the influence of cutting parameters using Anova. The conclusion of his paper includes that the parameters like speed, feed, and depth of cut affects surface finish and in order to get minimum surface roughness it is equally important to consider these parameters at suitable parameters. He stated that feed is a suitable parameter in influencing surface roughness.

Shivade [3] in his paper on optimization of machining parameters using Taguchi approach claimed that optimum combinations give best results. It may be of single response or multi response but optimization of design gives enhances results. A combination of input parameters was suggested to minimize surface roughness.

Shihab [4] presented a survey on cutting temperature in turning process by utilizing RSM as an endeavor was composed to explore the effect of cutting parameters on cutting temperature while turning of compound steel using multilayer covered carbide (TiN/TiCN/Al₂O₃/TiN) embeds. For performing machining analysis, the Central composite construct (CCD) was used to huddle information. A few analytic tests were performed to check the legitimacy of suspicions. Importance of cutting parameters was decided using measurable investigation.

3 Methodology

Cutting parameters were analyzed in machining of heat-treated beryllium copper alloy. Experimental data is required along with which investigated selection of experiments is desirable. To accomplish the task of selection of experiments design of experiments plays a crucial role and to carry out optimization Response surface methodology and artificial neural networks.

3.1 Design of Experiments

Experiments have been conducted for finding the variations and to analyze the results. In this perspective experimental trials are to be performed, experiments trails with variations are designed with an effective techniques said to be design of experiments. Design of Experiments (DOE) is carried out with the help of design expert software to draw optimal design in central composite design.

3.2 Optimal Design in CCD

See Table 1.

3.3 Response Surface Methodology

It gives the relationship between one or more response variables. This model was introduced by Box and William in 1951 who called this model as an approximation. Suggestion is with using a second-degree polynomial.

Table 1 Design matrix in composite design

Run	A:s (Rpm)	B:f (mm/rev)	C:doc (mm)	D:ns (mm)	E:ht
1	910	0.053	0.4	0.8	1
2	1200	0.129	0.2	0.4	1
3	1200	0.053	0.4	1.2	-1
4	700	0.129	0.2	0.4	1
5	700	0.053	0.6	0.4	1
6	700	0.129	0.2	1.2	-1
7	700	0.129	0.2	0.4	1
8	700	0.053	0.6	0.4	1
9	1200	0.129	0.2	1.2	1
10	700	0.129	0.6	0.4	-1
11	700	0.053	0.2	0.4	-1
12	1200	0.053	0.2	0.4	1
13	1200	0.053	0.6	0.4	-1
14	1200	0.129	0.4	0.8	-1
15	700	0.053	0.6	1.2	-1
16	1200	0.053	0.6	1.2	1
17	1200	0.092	0.2	0.8	-1
18	1200	0.129	0.6	1.2	-1
19	1200	0.129	0.6	0.4	1
20	700	0.129	0.6	0.4	-1
21	910	0.092	0.4	0.4	-1
22	1200	0.092	0.4	1.2	1
23	700	0.053	0.6	1.2	-1
24	1200	0.053	0.2	0.4	1
25	700	0.053	0.2	1.2	1
26	700	0.092	0.2	0.8	-1
27	910	0.053	0.2	1.2	-1
28	910	0.092	0.6	0.8	1
29	700	0.129	0.6	1.2	1
30	700	0.092	0.4	1.2	1

3.3.1 Experimental Design

A design matrix with 30 runs is obtained after considering the following input factors with ranges (Tables 2, 3, 4, 5 and 6).

The F-test and P-test conducted on MRR, Ra, Fc in relation with input parameters depicts that there is a significant variation due to these parameters speed, feed, depth of cut, nose radius and heat treatment in the model.

Table 2 Input factors with ranges

Factor	Name, units	Minimum value	Maximum value
A (s)	Speed, rpm	700	1200
B (f)	Feed, mm/min	0.053	0.129
C (doc)	Depth of cut, mm	0.2	0.6
D (ns)	Nose radius, mm	0.4	1.2
E (ht)	Heat treatment	-1	1

Table 3 Experimental design matrix

Run	Input factors					Responses		
	A:s (Rpm)	B:f (mm/rev)	C:doc (mm)	D:ns (mm)	E:ht	MRR (mm ³ /min)	Ra (microns)	Fc (N)
1	910	0.053	0.4	0.8	1	1923	0.112	84.928
2	1200	0.129	0.2	0.4	-1	853	1.335	52.271
3	1200	0.053	0.4	1.2	-1	2219	0.075	130.72
4	700	0.129	0.2	0.4	1	1792	1.335	26.086
5	700	0.053	0.6	0.4	1	2152	0.225	111.1
6	700	0.129	0.2	1.2	-1	1561	0.445	94.7
7	700	0.129	0.2	0.4	1	1788	1.335	39.2
8	700	0.053	0.6	0.4	1	2062	0.225	166.7
9	1200	0.129	0.2	1.2	1	3063	0.445	45.8
10	700	0.129	0.6	0.4	-1	4657	1.335	124.1
11	700	0.053	0.2	0.4	-1	633	0.225	45.7
12	1200	0.053	0.2	0.4	1	1134	0.225	35.9
13	1200	0.053	0.6	0.4	-1	3144	0.225	39.2
14	1200	0.129	0.4	0.8	-1	5261	0.667	88.2
15	700	0.053	0.6	1.2	-1	1796	0.075	160.1
16	1200	0.053	0.6	1.2	1	3743	0.075	117.7
17	1200	0.092	0.2	0.8	-1	1817	0.339	62
18	1200	0.129	0.6	1.2	-1	7282	0.445	166.7
19	1200	0.129	0.6	0.4	1	8216	1.335	150.3

3.4 Artificial Neural Networks

To validate the results, neural networks are adopted in which validation set is used for tuning the parameters of a model. Test set is used for performance evaluation. **The validation set** is used to compare their performances and decide to select a model among different models (In ANN, comparison of ANN models with different number of hidden layers for instance). Figure 1 shows the neuron setup in ANN.

Table 4 Analysis of variance for Ra

Source	Sum of squares	df	Mean square	F-value	p-value	
Model	6.09	15	0.4059	51.53	<0.0001	Significant
A-s	0.0002	1	0.0002	0.0297	0.8655	
B-f	2.81	1	2.81	356.19	<0.0001	
C-doc	0.0069	1	0.0069	0.8818	0.3636	
D-ns	1.59	1	1.59	202.25	<0.0001	
E-ht	0.0146	1	0.0146	1.85	0.1951	
AB	0.0001	1	0.0001	0.0105	0.9199	
AC	0.0009	1	0.0009	0.1125	0.7423	
AD	0.0001	1	0.0001	0.0168	0.8988	
AE	0.0042	1	0.0042	0.5314	0.4780	
BC	0.0004	1	0.0004	0.0469	0.8317	
BD	0.7257	1	0.7257	92.14	<0.0001	
BE	0.0004	1	0.0004	0.0457	0.8338	
CD	0.0008	1	0.0008	0.1071	0.7483	
CE	0.0037	1	0.0037	0.4647	0.5066	
DE	0.0027	1	0.0027	0.3398	0.5692	
Residual	0.1103	14	0.0079			
Lack of fit	0.1103	9	0.0123			
Pure error	0.0000	5	0.0000			
Cor total	6.20	29				

As the input parameters considered are five in number and output parameters are 3 in number then the hidden neurons considered to be 2/3rd size of input added with size of output. This results in 6.33 hidden neurons as of the criteria least number of hidden neurons acceptable is 10. When these neurons are trained the performance is as shown in Fig. 2. The convergence is at epoch 2, which can be read from the plot.

In Fig. 3 rating factor is given for training, testing and validation and can be compared (Figs. 4 and 5).

4 Optimization of Process Parameters

Optimal process parameters are setup using response surface methodology, the desirability obtained is as follows which can be stated as 0.670 (Table 7).

Table 5 Analysis of variance for mrr

Source	Sum of squares	df	Mean square	F-value	p-value	
Model	9.732E+07	15	6.488E+06	21.40	<0.0001	Significant
A-s	1.429E+07	1	1.429E+07	47.12	<0.0001	
B-f	2.732E+07	1	2.732E+07	90.10	<0.0001	
C-doc	4.424E+07	1	4.424E+07	145.90	<0.0001	
D-ns	59977.75	1	59977.75	0.1978	0.6633	
E-ht	6.815E+05	1	6.815E+05	2.25	0.1561	
AB	1.594E+06	1	1.594E+06	5.26	0.0379	
AC	4.734E+06	1	4.734E+06	15.61	0.0014	
AD	5.770E+05	1	5.770E+05	1.90	0.1894	
AE	5.862E+05	1	5.862E+05	1.93	0.1861	
BC	5.932E+06	1	5.932E+06	19.56	0.0006	
BD	55596.14	1	55596.14	0.1833	0.6750	
BE	45732.58	1	45732.58	0.1508	0.7036	
CD	5.474E+05	1	5.474E+05	1.81	0.2005	
CE	5.014E+05	1	5.014E+05	1.65	0.2194	
DE	9.574E+05	1	9.574E+05	3.16	0.0973	
Residual	4.245E+06	14	3.032E+05			
Lack of fit	4.205E+06	9	4.673E+05	58.46	0.0002	Significant
Pure error	39967.50	5	7993.50			
Cor total	1.016E+08	29				

Table 6 Analysis of variance for Fc

Source	Sum of squares	df	Mean square	F-value	p-value	
Model	36471.28	5	7294.26	6.70	0.0005	Significant
A-s	181.49	1	181.49	0.1667	0.6866	
B-f	372.28	1	372.28	0.3420	0.5641	
C-doc	31991.57	1	31991.57	29.39	<0.0001	
D-ns	416.52	1	416.52	0.3827	0.5420	
E-ht	2629.53	1	2629.53	2.42	0.1332	
Residual	26122.02	24	1088.42			
Lack of fit	21657.92	19	1139.89	1.28	0.4258	Not significant
Pure error	4464.10	5	892.82			
Cor total	62593.30	29				

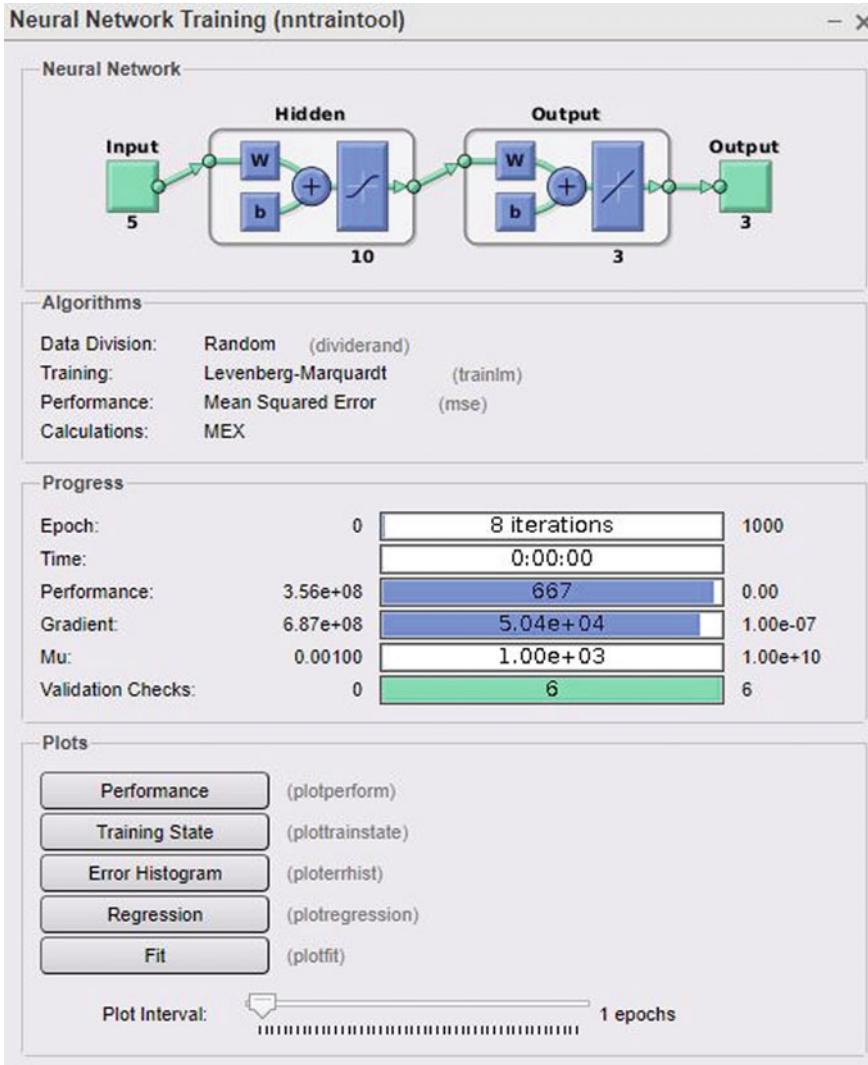


Fig. 1 Neuron setup in ANN

5 Conclusion and Future Scope

This study demonstrated a successful use of Response Surface Methodology for determining optimal performance parameters with suitable input parameters (speed, feed, depth of cut, nose radius and heat treatment-annealed and hardened). Furthermore, the individual and cumulative impacts of the input variables on the output

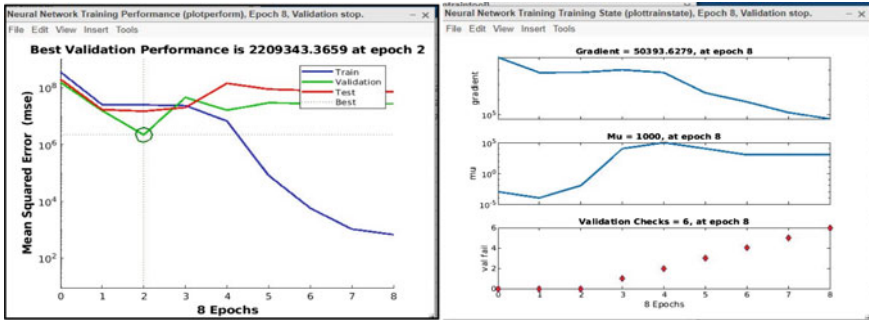


Fig. 2 Training performance plots in ANN

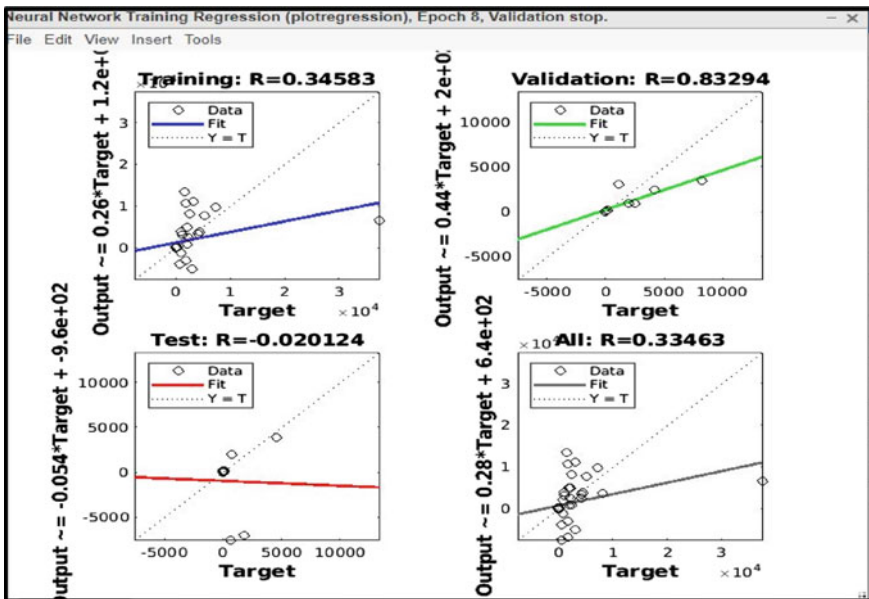


Fig. 3 Regression plot using ANN

factors are being investigated. Data validation has been performed using ANOVA and ANN, which shown that experimental data is valid and convergent.

The optimum values of performance measures are identified and the best combination of the input parameters for the specified turning process has been anticipated. Confirmation tests were carried out to assess the efficiency of optimization, which was shown to be efficient with a 5% inaccuracy. There is always room for improvement in any research project, and as part of that, heuristic approaches with the inclusion of additional factors such as tool signature and other tool materials may be used to improve the process and generalize the uses of beryllium copper alloy.

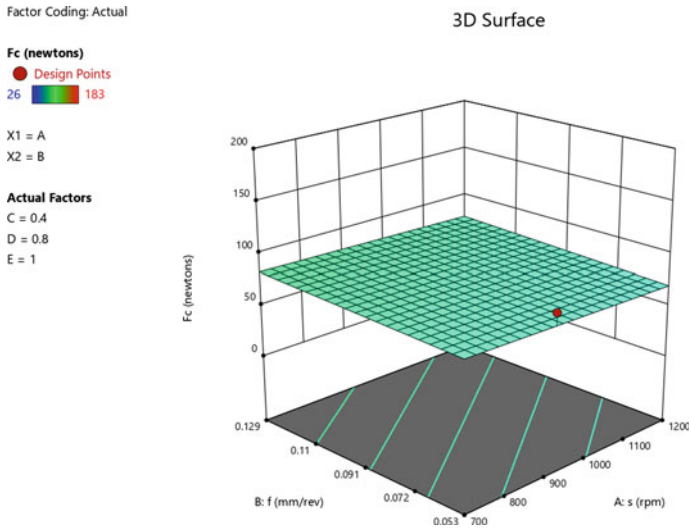


Fig. 4 Response for Fc

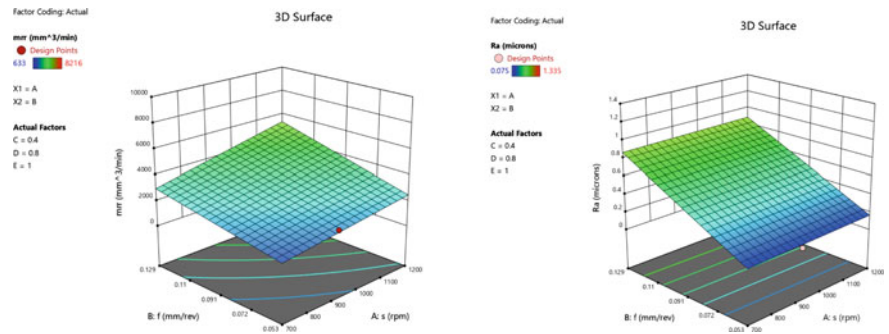


Fig. 5 Specific response graphs for output parameters MRR, Ra

Table 7 Optimal solutions for 2 combinations of categoric factor levels

No.	s	f	doc	ns	ht	mrr	Ra	Fc	Desirability
1	1199.998	0.129	0.454	1.200	1	6027.893	0.419	91.653	0.670
2	1200.000	0.129	0.474	1.200	1	6244.852	0.419	95.349	0.670

References

1. Devaki Devi, K.: Statistical approach for multi criteria optimization of cutting parameters of turning on heat treated beryllium copper alloy. *J. Eng. Sci. Technol.* **12** (2017)
2. Krishna Prasad, D.V.V., Bharathi, K.: Multi-objective optimization of milling parameters for machining cast iron on machining centre. *Res. J. Engineering Sci.* **2**(5), 35–39 (2013)

3. Shivade, A.S., Bhagat, S., Jagdale, S., Nikam, A., Londhe, P.: Optimization of Machining Parameters for Turning using Taguchi Approach (2014). ISSN: 2277-3878
4. Shihab, S.K., Khan, Z.A.: Mohammad, A., Siddiqueed, A.N.: RSM based study of cutting temperature during hard turning with multilayer coated carbide insert. *Procedia Mater. Sci.* **6**:1233–1242 (2014)
5. Sridhar, G., Venkateswarlu, G.: Multi objective optimization of turning process parameters on en8 steel using grey relational analysis. *Int. J. Eng. Manuf.* **4**(4), 14–25 (2014)
6. Das, S.R., Kumar, A., Dhupall, D., Mohapatra, S.K.: Optimization of surface roughness in hard turning of AISI 4340 steel using coated carbide inserts. *Int. J. Inf. Comput. Technol.* **3**(9), 871–880 (2013)
7. Devaki Devi, K., Satish Babu, K., Hemachandra Reddy, K.: Mathematical modelling and optimization of turning process parameters using response surface methodology. *Int. J. Appl. Sci. Eng.* (2015)
8. Murali Mohan, M., Sagar, N.V.S.S. Lava Kumar, M., Venugopal Goud, E.: Multi-Objective Optimization of Machining Parameters of EN36 steel using RSM, *IJERT* (2015)
9. Magdum, V.B., Naik, V.R.: Evaluation and Optimization of Machining Parameter for turning of EN 8 Steel. *IJETT* (2013)
10. Dhavamani, C., Alwarsamy, T.: Optimization of cutting parameters of composite materials using genetic algorithm. *Eur. J. Sci. Res.* (2011)

Fabrication of Highly Oriented Piezoelectric Nanofibers Using a Low Cost and Lab-Scale Electrospinning System



Duc-Nam Nguyen , Van-Tuan Nguyen, Ich-Hung Dam, and Van-Huong Vu

Abstract A large number of piezoelectric polymers have been studied and applied widely recently and become an attractive topic in both material science and applied engineering fields. Piezoelectric polymers such as Poly(vinyl fluoride) and Poly(γ -benzyl, L-glutamate) fabricated in nanofibers have shown impressive properties in the aspect of low weight, high flexibility and high piezoelectricity. One of the major parameters influencing to the piezoelectricity of electrospun fibers is the orientation. This paper reviews the contribution of fiber orientation to the piezoelectricity properties and the technique to manipulate the orientation. The research group introduces for the first time a fully integrated and compact electrospinning system which is low cost and suitable for both lab-scale and large-scale purpose.

Keywords Piezoelectric fibers · Electrospinning · Fiber orientation · Nanofibers · Electromechanical sensors

1 Introduction

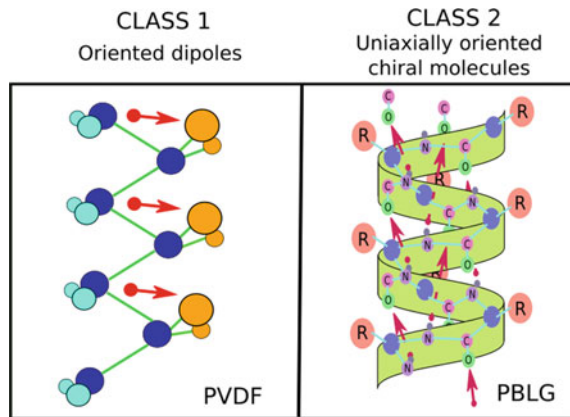
Since 1990s, the use of functional materials such as piezoelectric polymer has extensively increased in a variety of fields such as nano-energy harvesting, flexible vibration, force sensors, tissue engineering, biocompatible devices, tactile sensors, wound healing, etc. (Fig. 1) [1–9]. Piezoelectric polymers fibers are attractive because of their dedicated properties, such as large surface area, low weight, high endurance, high flexibility, high piezoelectric voltage generation, and high capability to integrate with the flexible and complex substrates. Poly(vinyl fluoride) (PVDF) and its co-polymer such as Poly[(vinylidene fluoride)-co-trifluoroethylene] [P(VDF-TrFE)]

D.-N. Nguyen (✉) · V.-T. Nguyen
Phenikaa University, Hanoi 12116, Vietnam
e-mail: nam.nguyenduc@phenikaa-uni.edu.vn

Phenikaa Research and Technology Institute (PRATI), Hanoi 11313, Vietnam

I.-H. Dam · V.-H. Vu
University of Transport and Communications, Hanoi 12116, Vietnam

Fig. 1 Piezoelectric formation of PVDF and PBLG molecular (Reprinted from [12])



are one of the typical piezoelectric polymers which have received a lot of attention for various sensor applications [5, 8, 10]. PVDF-based polymers consist of four main crystalline phases (α , β , γ and δ phase). Unlike non-polar and most stable phases including α -, γ -, and δ -phase, the β -phase PVDF produces electrical polar structure during different processing techniques such as mechanical stretching, electrical poling and thermal treatment (Fig. 1). On the other hand, P(VDF-TrFE) copolymer containing trifluoroethylene (TrFE) content, can be crystallized in β -phase easily. P(VDF-TrFE) is even more advanced than PVDF in the aspect of high crystallinity and better chemical stability.

Recent discover of piezoelectric polymer is Poly(γ -benzyl, L-glutamate) (PBLG) [11–13]. PBLG is one of Poly(α -amino acid) groups, or polypeptide, and is a synthetic biopolymer made from amino acid repeating units, i.e. $-\text{[NH-CHR-CO]}_x-$. The unique characteristic of PBLG molecular is the well-defined confirmation of long-range chain and persisted this structure in both solution and solid state. In the PBLG molecular conformation, parallel and directional alignment of hydrogen bonds along the helical axis collectively expose strong electric dipole moments (Fig. 1). Such strong dipole moments contribute mainly to the high piezoelectricity and its high thermal stability over long time. As the result, electrospun PBLG fibers produced impressive piezoelectric coefficient $d_{33} = 27 \text{ pC N}^{-1}$ [12] and exhibited ultra-sensitivity up to 615 mV N^{-1} as integrated into composite structure [11].

Fiber orientation is not the main parameter in some research aspects such as gas sensor, filter membranes, etc. However, piezoelectric fibers' performance is inherited from the direction of the polar crystalline or dipole moment. Hence, the fiber orientation and the piezoelectricity have inherent correlation. Recent publications have been reported that the orientation or alignment of electrospun fibers govern the stiffness and piezoelectric character of fibers significantly [2]. Nguyen et al. [12] proved the correlation between increment of alignment level of electrospun PBLG with the piezoelectricity. Highly oriented PVDF-fiber based composite generated piezoelectric voltage constant $g_{31} = 33.9 \text{ mV N}^{-1}$ and $g_{33} = 61.2 \text{ mV N}^{-1}$ which is

suitable for high-performance energy harvesting devices [14]. Lee et al. [15] demonstrated the importance of orientation of electrospun P(VDF-TrFE) nanofiber on tissue engineering via annealing process on neurite growth. Highly oriented P(VDF-TrFE) fibers can direct the neurite outgrowth while the randomly oriented fibers promoted the neurite extending in radial direction. The aligned P(VDF-TrFE) fiber is capable of restoring the anatomical structure of damage spinal cord tissue [16].

One of the greatest challenges of nanofibers fabricated by ES is how to manipulate the fibers to the ordered structure precisely. In this study, we present brief explanation of physical principle of fiber formation in ES process. This study focuses on highlighting and explaining the recent progress in ES in which the orientation of electrospun nanofibers can be controlled effectively and how the orientation influences the electro-mechanical characteristic of nanofibers. We also introduced the design of a lab-scale ES system with low cost but high robustness.

2 Electrospinning Principle and Fibers Orientation

2.1 Principle of Electrospinning Process

In the ES setup, a metal nozzle is connected to a positive high voltage source. The ground is connected to a collector which is several millimeters to tens of centimeters from the syringe. The polymer solution is pumped out from the nozzle with a constant feed rate and electrified by the electrical field. As the result, formation of nanofiber is majored by the interaction of surface tension and electrical forces on the change of fluidic viscosity. The entire process can be divided into seven stages as shown in Fig. 2 and elaborated as followed.

Stage 1: The electrical charges inside the polymer solution is electrified intensively and causes phenomena namely “excess charges”. The excess charges accumulate on the surface of the fluid, but are constrained by surface tension.

Stage 2: Once the charges concentrated over a small volume and lead to an intensive interaction of static charges, there will be a “breaking effect” happening at the end of a droplet because of the Coulomb force. This “breaking effect” is called Taylor cone.

Stage 3: The surface tension and viscosity are larger than the Coulomb force. As the result, the fluid jet experiences a short and straight path.

Stage 4: At a point when the Coulomb force starts dominating other factors and causes an imbalance state, the first bending instability happens. The jet starts whipping or coiling. The jet is elongated and decreases its diameter from hundreds of micrometers to tens of micrometers.

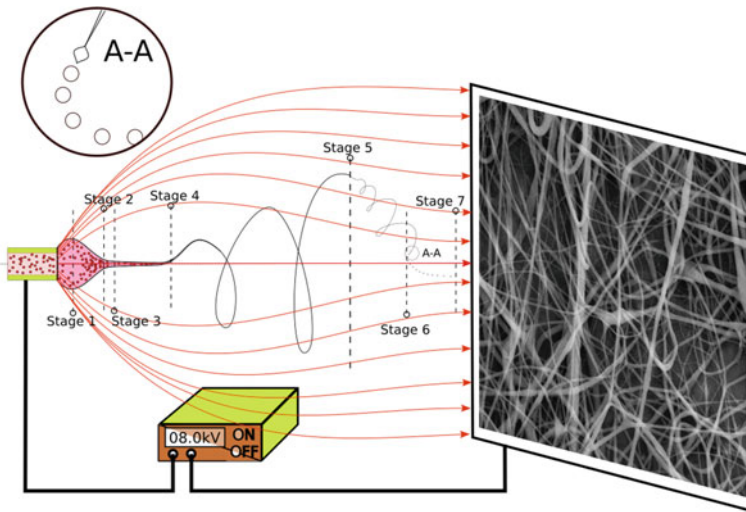


Fig. 2 Working principle of ES process

Stage 5: The jet now is elongated to sub micrometer level and the dynamic energy increases tremendously. While the main jet whips, a second bending instability starts processing.

Stage 6: As the jet gets much thinner, there is a chance that the jet might be broken into tiny droplets. If this process happens, then the process will be called electrospaying.

Stage 7: At the collector, bundles of fibers in nano- or sub-micro scale are deposited in a random orientation. Hence, from a small amount of polymer solution, solid state of fibers is processed in the form of continuous and nano/microfibers.

Many researchers have established the theory for the formation of fibers during ES process [17]. Models for ES contain numbers of parameters including: voltage, tip-to-collector distance, solution concentration, solution viscosity, humidity, temperature, solvent evaporation rate, feed rate, etc. However, researchers have proven that the instability of fluidic jet is unavoidable to fabricate nanofibers using conventional ES. Therefore, new techniques have been developed to manipulate the fiber formation process and achieve the structured fibers.

2.2 Fiber Orientation and the Influence to the Piezoelectricity

For years, controlling the fiber orientation with stable fabrication technique was the bottle neck in ES method practically. Farrar et al. [13] discovered the piezoelectricity of electrospun PBLG fibers for the first time; however, the authors were unable to explain the large variation of piezoelectricity of samples. In 2018, Nguyen et al.

[12] invented End-point Control Assembly (EpCA) method which allows to manipulate the fiber formation effectively. The EpCA method is based on the electrostatic concentration effect to target the fiber to a determined position. As the result, both the level of orientation and the collected area can be controlled precisely (Fig. 3). It has been proven that the piezoelectric of electrospun fibers composes of large number of dipole moments along the Carbon chain. Therefore, when every single fiber is parallel, the overall effect of polar effect is magnified. This is the first time the correlation between fiber orientation and piezoelectric coefficient is presented (Fig. 4).

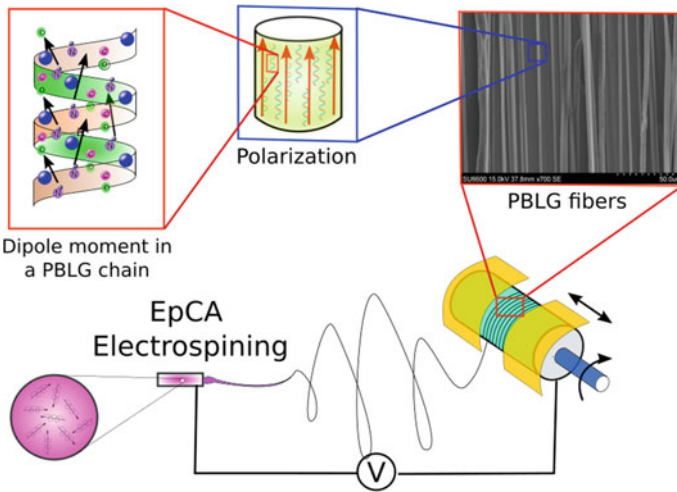
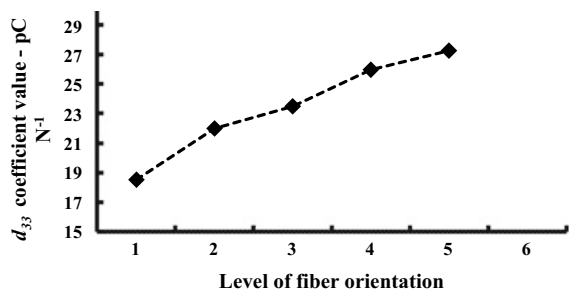


Fig. 3 Principle of polarized PBLG nanofibers via EpCA process

Fig. 4 The dependence of fiber orientation to the piezoelectricity (Reprinted from [12])



3 Manipulation of Electrospun Nanofibers

Followed by the need of manipulating electrospun fibers effectively, several techniques had been presented. Some of the most popular ones are (a) centrifugal ES [18], (b) rotating disk collector [19], (c) auxiliary electrodes [20], and (d) rotating cylinder collector [21] (Fig. 5). The common advantage of these configurations is the ease of obtaining parallel nanofibers in a large area. However, monitoring and controlling the exact position of the fibers are not possible as applying these techniques.

Applying the invention of Nguyen et al. [22] on manipulation the deposition of fibers on a rotating collector, researchers at Applied Mechatronics Lab (AML) (Phenikaa University) has introduced a large-scale ES system namely ESA01 (Fig. 6). This is a compact, integrated system with dedicated functions such as real-time monitoring process, video streaming, fume ventilation system, integration with EpCA method, etc. (Table 1). The functional block diagram was shown in Fig. 7. Comparing to the equivalent functional electrospinning models, the ESA01 provides better performance with lower cost. The ESA01 has been used to fabricate core-shell fibers and parallel nanofibers with highly stable results (Fig. 8).

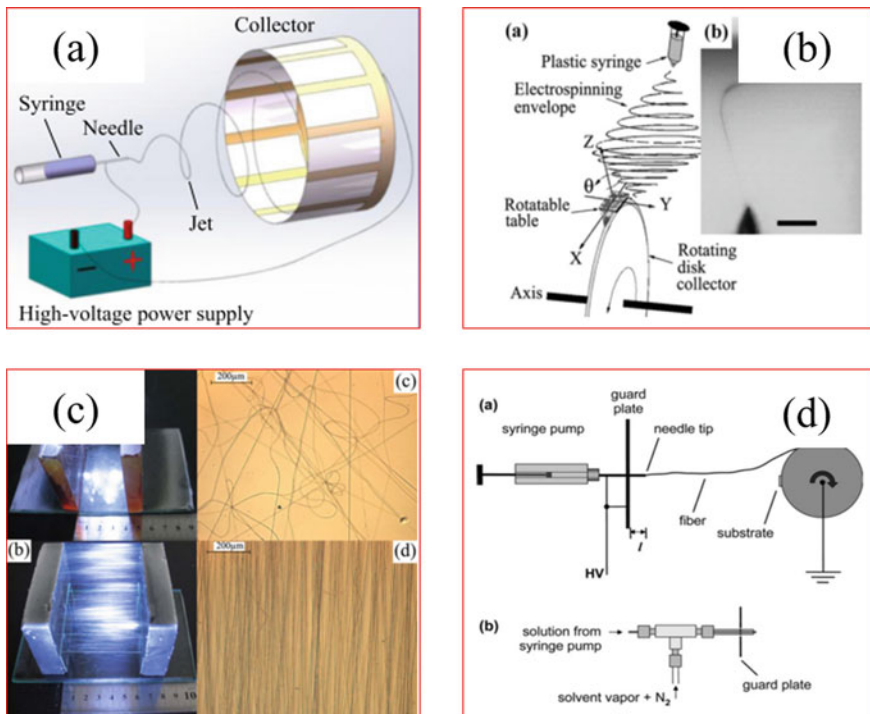


Fig. 5 Some of the most popular ES setup to archive highly oriented nanofibers

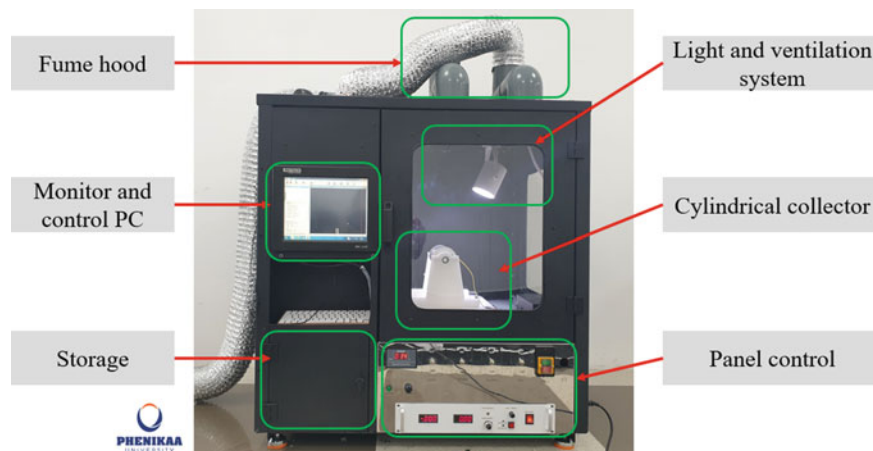


Fig. 6 The ESA01 system manufactured by AML at Phenikaa University

Table 1 Main specifications of ESA system

Specification	Unit	ESA01 Phenikaa University, Vietnam	ESR200P2R2D NanoNC, Korea	Nanospinner-1 Plus Invenso, USA
Dimension	mm	1000 × 1000 × 1000	950 × 640 × 1150	740 × 645 × 770
Weight	kg	120	–	60
Input	VAC	220 @60 Hz	220 @60 Hz	220 @60 Hz
Rotation speed	Rpm	4000	2500	500
Independent pumps	Axis	2	1	3
Feeding rate resolution	μl/h	0.01	0.01	0.01
Voltage	kV	30	30	30
Additional functions				
Humidity control	Yes	30 ÷ 85 RH,	N/A	N/A
Camera monitoring	Yes	5 × camera with real-time HD video streaming	N/A	N/A
Temperature control	Yes	20 ÷ 50 degC	N/A	N/A
Air ventilation		Yes	Yes	Yes
Coaxial fibers fabrication capability	Yes	Yes	N/A	N/A
Cost	USD	12,000	30,000	28,450

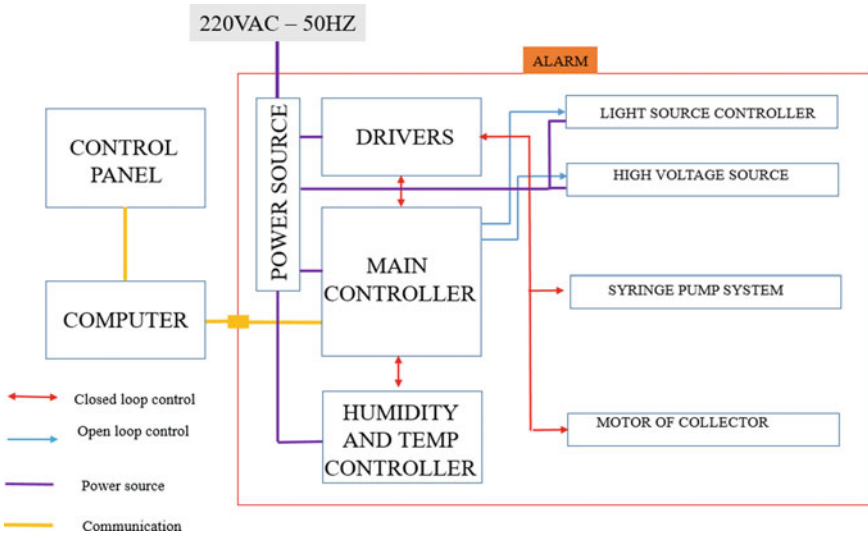
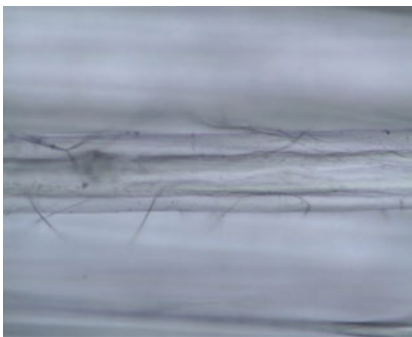
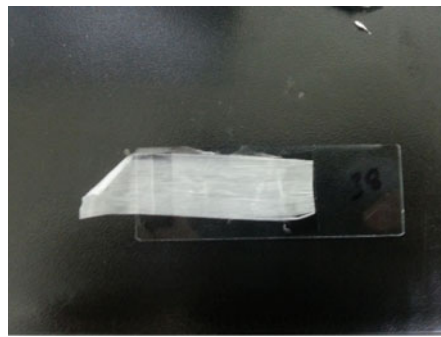


Fig. 7 The functional block diagram of the ESA01



A sample of coaxial fibers



A sample of parallel nanofibers membrane

Fig. 8 Samples fabricated by ESA01

4 Conclusion and Discussion

Nanofibers of piezoelectric polymers such as PVDF, PBLG still remain lots of potential applications in biosensors, electro-mechanical sensors, wound healing, etc. The orientation of fibers is currently considered as one of the key parameters to improve the performance of piezoelectric nanofibers. Therefore, the robustness in controlling the fabrication process and its relation with other characteristic such as orientation can be only obtained through a stable and advanced system. In this paper, we introduced a low-cost and lab-scale electrospinning system named as EAS01. By integrated real-time video streaming processing algorithm, ESA01 can be upgraded to apply

artificial intelligence in control the jet formation automatically in the future. It is expected that the EAS01 can support the study of electrospun fibers which requires extreme fabrication conditions.

References

1. Azimi, B., Maleki, H., Zavagna, L., De la Ossa J.G., Linari, S., Lazzeri, A., Danti, S.: Bio-based electrospun fibers for wound healing. *JFB* **11**(3), 67 (2020)
2. Azimi, B., Milazzo, M., Lazzeri, A., Berrettini, S., Uddin, M.J., Qin, Z., Buehler, M.J., Danti, S.: Electrospinning piezoelectric fibers for biocompatible devices. *Adv. Healthcare Mater.* **9**(1), 1901287 (2019)
3. Kalimuldina, G., Turdakyn, N., Abay, I., Medeubayev, A., Nurpeissova, A., Adair, D., Bakenov, Z.: A review of piezoelectric PVDF film by electrospinning and its applications. *Sensors* **20**(18), 5214 (2020)
4. Khadka, D.B., Donald, M.S., Haynie, T.: Protein- and peptide-based electrospun nanofibers in medical biomaterials. *Nanomedicine* **8**(8), 1242–1462 (2012)
5. Mokhtari, F., Shamshirsaz, M., Latifi, M., Foroughi, J.: Nanofibers-based piezoelectric energy harvester for self-powered wearable technologies. *Polymers* **12**(11), 2697 (2020)
6. Huang, Y.A., Ding, Y., Bian, J., Su, Y., Zhou, J., Duan, Y., Yin, Z.: Hyper-stretchable self-powered sensors based on electrohydrodynamically printed, self-similar piezoelectric nano/microfibers. *Nano Energy* **40**, 432–439 (2017)
7. Lang, C., Fang, J., Shao, H., Ding, X., Lin, T.: High-sensitivity acoustic sensors from nanofibre webs. *Nat. Commun.* **7** (2016)
8. Persano, L., Dagdeviren, C., Su, Y., Zhang, Y., Girardo, S., Pisignano, D., Huang, Y., Rogers, J.A.: High performance piezoelectric devices based on aligned arrays of nanofibers of poly(vinylidene fluoride-co-trifluoroethylene). *Nat. Commun.* **4** (2013)
9. Filippin, A.N., Sanchez-Valencia, J.R., Garcia-Casas, X., Lopez-Flores, V., Macias-Montero, M., Frutos, F., Barranco, A., Borrassa, A.: 3D core-multishell piezoelectric nanogenerators. *Nano Energy* **58**, 476–483 (2019)
10. Ren, G., Cai, F., Li, B., Zheng, J., Xu, C.: Flexible pressure sensor based on a Poly(VDF-TrFE) nanofiber web. *Macromol. Mater. Eng.* **298**(5), 541–546 (2013)
11. Nguyen, D.-N., Moon, W.: Piezoelectric polymer microfiber-based composite for the flexible ultra-sensitive pressure sensor. *J. Appl. Polym. Sci.* **137**(29), 48884 (2019)
12. Nguyen, D.-N., Yu, S.M., Moon, W.: Electrospinning of poly(γ -benzyl- α ,L-glutamate) microfibers for piezoelectric polymer applications. *J. Appl. Polym. Sci.* **135**(27), 46440 (2018)
13. Farrar, D., Ren, K., Cheng, D., Kim, S., Moon, W., Wilson, W.L., West, J.E., Yu, S.M.: Permanent polarity and piezoelectricity of electrospun alpha-helical poly(alpha-amino acid) fibers. *Adv. Mater.* **23**(34) (2011)
14. Nguyen, D.N., Moon, W.: Fabrication and characterization of a flexible PVDF fiber-based polymer composite for high-performance energy harvesting devices. *Journal of Sensor Science and Technology* **28**(4), 205–215 (2019)
15. Lee, Y.-S., Collins, G., Arinze, T.L.: Neurite extension of primary neurons on electrospun piezoelectric scaffolds. *Acta Biomater.* **7**(11), 3877–3886 (2011)
16. Wu, S., Chen, M.-S., Maurel, P., Lee, Y.-S., Bunge, M.B., Arinze, T.L.: Aligned fibrous PVDF-TrFE scaffolds with Schwann cells support neurite extension and myelination in vitro. *J. Neural Eng.* **15**(5), 056010 (2018)
17. Reneker, D.H., Yarin, A.L.: Electrospinning jets and polymer nanofibers. *Polymer* **49**(10), 2387–2425 (2008)
18. Lei, T., Peng, Q., Chen, Q., Xiong, J., Zhang, F., Sun, D.: Alignment of electrospun fibers using the whipping instability. *Mater. Lett.* **193**, 248–250 (2017)

19. Zussman, E., Theron, A., Yarin, A.L.: Formation of nanofiber crossbars in electrospinning. *Appl. Phys. Lett.* **82**(6), 973–975 (2003)
20. Yan, H., Liu, L., Zhang, Z.: Alignment of electrospun nanofibers using dielectric materials. *Appl. Phys. Lett.* **95**(14), 143114 (2009)
21. Kiselev, P., Rosell-Llompart, J.: Highly aligned electrospun nanofibers by elimination of the whipping motion. *J. Appl. Polym. Sci.* **125**(3), 2433–2441 (2012)
22. Nguyen, D.-N., Hwang, Y., Moon, W.: Electrospinning of well-aligned fiber bundles using an end-point control assembly method. *Eur. Polymer J.* **77**, 54–64 (2016)

Visual Product Assessment by Using the Eye-Tracking Equipment to Study the Effect of Product Shapes on consumer's Thinking



Jitender Singh  and Prabir Sarkar

Abstract Product design has become a significant tool for successful companies. Products arouse emotional feelings in consumers. Emotions can effect buying decisions of consumers as well as product assessments. It is broadly recognized that higher user satiation and better product performance can be reached through product aesthetic design. Integrating emotional value into tangible products has become an important approach for increasing a product's emulative power in the retail market. Therefore, it is a need of manufactures to understand how product aesthetics impact the consumer's emotions. On the other hand, when designing a new product, maximum time focus is paid for the enhancement of its usability and functionality, and very little attention is paid to consumers' emotional desires. In this paper, we investigate the relationship between product structure/features and consumer emotions. Two different products are considered in this study. In addition, by using the four basic pleasures model of Jordan a closed list of product-specific semantic descriptors is developed. An eye-tracker-based experiment and open-ended survey were performed during this study, where substantial connections between product geometry and semantic were found. In this study, we find out the emotional responses for geometric features from users, and the major finding of eye-tracker is discussed in brief in the results section. The study results are helpful in future product development and reduce the failure rate of the product.

Keywords Product design · Aesthetics · Consumer appeal · Eye-tracker

1 Introduction

In the current competitive marketplace, fulfill customer desires and taste has become a key role for every product design industry [21]. Current time customers not only choose products that provide them physical pleasure in term of quality, price, and function, but they also seek for cognitively pleasure too. And these play a huge role at

J. Singh (✉) · P. Sarkar

Department of Mechanical Engineering, Indian Institute of Technology, Ropar, Punjab, India
e-mail: jitendernit1724@gmail.com

© The Author(s), under exclusive license to Springer Nature Singapore Pte Ltd. 2022
K. C. Popat et al. (eds.), *Advances in Mechanical Engineering and Material Science*,
Lecture Notes in Mechanical Engineering,
https://doi.org/10.1007/978-981-19-0676-3_12

149

the time of purchase and it is also known as a sentimental purchase [11]. To provide product aesthetics designs with an additional sense of qualities, affective design has been useful, and this shift has received immense responsive in the area of industrial design [4, 5, 19].

1.1 Perceptual Matching

A term perceptual matching term is known as when one stimuli must be concluded as same as the second stimuli or differ from the second stimuli, has been an essential tool for evaluating the cognitive/intellectual and ability to interpretation of human being. Specifically, this type of works have been used to examine visual product recognition [7, 8, 12, 13], categorization, relational perception learning [3, 6], and perceptual learning [6]. One of the most contrary to intuition process of close observation in perceptual matching is that the easiness of finding the dissimilarities among two consequently observed objects can change in a serial manner as they can see—although the same looking objects are related [9, 18]. In this work, we are taking the help of perceptual matching to define the interaction among the opinion that industrial designers purpose to convey with the help of product aesthetic design and the customer insight aroused by the product. We cover the product area and the customer area.

2 Product Field

A specific object observed in a two perspectives in the product field: the product area (design area/field and targeted emotion/sentiment) and the customer area (object type and attained sentiment/emotion).

2.1 Product Design

Incorporating emotional values in objects/products is necessary to several diverse research capacities. It comprises quality research, consumer behaviour research, and ergonomics research for finding consumer desires by using the product design. [14, 17, 20]. The research work in these areas helps social scientific theories to find out consumers' emotional feelings and demands. Incorporating consumer market research results in product design needs a perfect pathway with various areas, such as social, psychology, physiology, marketing, and engineering. In product design, the prime target is to decipher the feelings, individual experiences, and perceptions. Based on customer's requirements, designers then use their personal experiences related to product designs and various aesthetics skills to generate a physical product.

As its name suggests, the physical design represents the outer look of the product, which is a collection of different design elements [1, 10].

2.2 Target Emotion

Individual product/object has an affinity to deliver customers with a design conception, to an equal degree like taglines/advertisements actively encourage its virtues. This emotive appeal is planned to serve customer requirements and thus generate an attraction. The product gesture and charm can be concise as the target emotion (TE), which is laid down by the product characteristics and can be expressed in a systematic way by using a marketing approach [15, 16].

2.3 Visual Perception

To illustrate a product with the help of visual insights, humans collect the information in their mind which they see and provide explanations or descriptions of the product's qualities based on the attributes of its look. Because of the practices of cognition, humans are trained their mind to store the product description by using attributes of a product and they take help to identify or categories the new product with the previous information which they were already stored in their mind. To be precise, to describe a category is the most natural mode for persons to define something that is visually accessible to them. For instance, when persons are asked to relate to a hot cup of coffee, most of the time consumers link the cup of coffee with a relaxing time or relax their mind, another example is Coco-Cola linked with carbonated drinks.

2.4 The Two Matching Relations

Corresponding to the two mood of opinion described in Sect. 2.2, relating to the ability to interpret the comparison is separated into two aspects: affective comparison and visual comparison.

2.4.1 Visual Comparison

Nowadays in human cognition a visual comparison is a very hot topic of research. For instance, as detailed in colour science, visual comparison testing and following colour-comparison purposes worked as the building blocks of recent time's colorimetry [2] and Zotkin [22] visual comparison among visual and actual pictures led to image-guided neurosurgery. During this work, visual comparison defines the

relationship among the consumer area and the product area with regards to visual opinion. The bond between this matching relationships shows the capability of a product design to lead customer to understand its characteristics specifically and accurately. As an assessment tool, visual comparison estimate the perfection at what level the group of a product considered by customers is the similar as it's of their base group. On the other hand, there is a chance of misunderstandings, when the matching strength is weak and customers interpret the product in a wrong way. For instance, the well-known design of "Tuborg" bottle design shows youthful image and Nestle water bottle which shows pureness and healthy environment. On the other hand, if the bottle fill with a coffee, it produce a melody emotion, the silhouette of a coffee and carbonated drink might be create confusion among the present customers. For that reason, understandable and specific shape could make customers immediately find the intended perception of coffee as well as beverage product and increase its identification, and this will provide considerable help for the development of that specific brand.

3 Aim and Methodology

As we know, in the current scenario, product design has become a significant tool for the success of any product base company. Products arouse emotional feelings in consumers. Emotions can effect buying decisions and product assessments of consumers. Therefore, it is a need of manufactures to understand how product aesthetics impact the consumer's emotions. This paper investigates the relationship between product structure/features and their relation to consumer emotions. For that, we considered the different shapes of beverage bottles for this study. An open-ended survey and eye-tracker-based experiment were performed in this study, where substantial connections between product geometry and consumer perception were found. We use twelve different silhouette shapes of bottles from different beverage categories.

4 Results and Discussion

4.1 Open-Ended Results

For experiment purpose, all the image is downloaded from "PNGWing" with a standard size. The bottle belongs to different categories like juice bottle (Ju), coffee/milk (C/M) bottle, carbonated (soft drink) (SD) bottle, wine bottle (W), energy drink (ED), etc. After selection of different categories of silhouette images, we made six slides and on each slide, we paste two different silhouette image. We conducted an open-ended survey among the young generation to collect consumer affective responses

because today’s generation is more connected with each beverage category. For first of experiment, a total twenty respondent took participation, their average age is 29 years, and all are working in multinational companies.

During the survey, we requested all the participant to provide your consent for each categories of the silhouette. i.e., Question: Do you thinking, from which category of beverage this silhouette is belonging and please write your response for each image below the silhouette. After completion of the survey, we find the frequency ratio (FR), for the consumer responses with respect to the different beverage bottle categories. In the second phase, we conducted an eye-tracker experiment with the same set of images/slides with a different sets of respondents. We find out their emotional responses for geometric features from users. From the first phase of experiment, we find fourteen responses out of twenty respondents. The response of all the participants is given in Table 1.

In Table 1 we can see that in the first slide, respondents provide a very high FR with the AI bottle silhouette compared to the other six categories. For the second image of the first slide, the juice silhouette image gets a 35.71% FR which is top in their categories. Similarly, the juice image gets 21.43% of the FR with the second priority in ED categories, then 14.29% of FR with CD and M/C categories. In the second slide, we paste CD and ED silhouette images. For CD bottle image respondents provide 85.71% of FR with their respective categories, for second image i.e. ED bottles, respondents provide 50% of FR (to ED category) and 21.43% to both Ju and W silhouette bottle. In the third slide, we paste M/C bottle and ED bottle silhouette image. For M/C silhouette, respondents provide 71.43% of FR with their respective categories, and for ED bottle silhouette, respondents provide 57.14% of FR. In the fourth slide, CD and M/C bottle silhouette paste on the white sheet. In the open-ended survey, for CD, respondents provide an 85.71% of FR with their respective categories. Similarly, for M/C silhouette respondents provides 28.57% with their

Table 1 The FR on 6 categories for each sample after classification task (partial)

Type of products image	AI (%)	Ju	CD	ED	M/C	T	W
AL	100	0	0	0	0	0	0
Ju	0	35.71%	14.29%	21.43%	14.29%	7.14%	7.14%
CD	0	7.14%	85.71%	0	0	0	7.14%
ED	0	21.43%	7.14%	50.00%	0	0	21.43%
M/C	0	7.14%	0	0	71.43%	21.43%	0
ED	0	7.14%	14.29%	57.14%	0	0	14.29%
CD	0	0	85.71%	7.14%	0	0	7.14%
M/C	7.14	21.43%	14.29%	7.14%	28.57%	21.43%	0
M/C	0	14.29%	14.29%	14.29%	28.57%	14.29%	7.14%
AL	100	0	0	0	0	0	0
CD	7.14	0	92.86%	0	0	0	0
AI	100	0	0	0	0	0	0

respective category and 21.43% with Ju category. In fifth slide, Ju and AL bottle silhouette is paste on the white paper, and respondents 28.57% of FR with M/C category bottle and 14.29% with Ju, CD, and ED bottle silhouette. On the other hand, a 100% of FR is provided by the respondents for the AL bottle silhouette with their respective category. In the last slide, we paste CD bottles and AL bottle silhouettes. Respondents provide a 92.86% FR for a CD and a 100% equal for AL for the respective categories i.e. CD and AL category, respectively.

4.2 Eye-Tracking Results

In the second phase of this study, we conducted an ET experiment. After completing an experiment, we request all the respondents to provide their valuable consent for the same slides shown to them in the ET equipment. We requested all the eight respondents just after the ET experiment to give their response for the same images in the open-ended survey and the FR is provided in Table 2.

In the ET experiment, a heat map is generated to note down the consumer eye movement during the ET experiment, which is shown in Figs. 1, 2, 3, and 4, which is shown in a respective manner as the slide shows in the second phase of the experiment (open-ended experiment, just after the ET experiment).

We have seen Fig. 1 and FR in Tables 1 and 2 for open-ended and ET experiments (open-ended experiment, just after the ET experiment). We found that, left silhouette image of slide A, shown a 100% of match in both of phase of experiment and the heat effected zone is formed in the right side of bottle which is above of centroid section of bottle till the neck section. But, in the case of the right silhouette bottle (Slide A) the respondents during the first phase of the experiment, attain 35.71% of

Table 2 FR of eye-tracking respondents

Type of products image	Al (%)	Ju (%)	CD (%)	ED (%)	M/C (%)	T (%)	W (%)
AL	100	0	0	0.00	0.00	0	0
Ju	0	25	0	25	25	0	25
CD	0	0	100	0	0	0	0
ED	0	25	0	75	0	0	0
M/C	0.00	0.00	0	0.00	75.0	12.5	12.5
ED	0.00	50.0	12.5	37.5	0.00	0.00	0.00
CD	0.00	0.00	100	0	0	0	0
M/C	0	0.00	0.00	12.5	87.5	0.00	0.00
M/C	0.00	12.5	12.5	0.00	25.0	37.5	12.5
AL	100	0	0	0.00	0	0	0
CD	12.5	0.00	87.5	0.00	0.00	0.00	0.00
Al	100	0	0	0.00	0	0	0

Fig. 1 Slide A and slide B shown the images four different categories

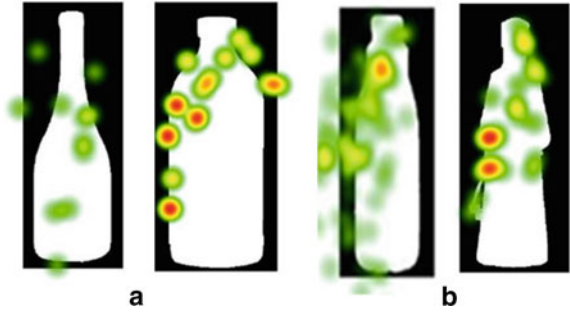


Fig. 2 Slide C and slide D shown the images four different categories

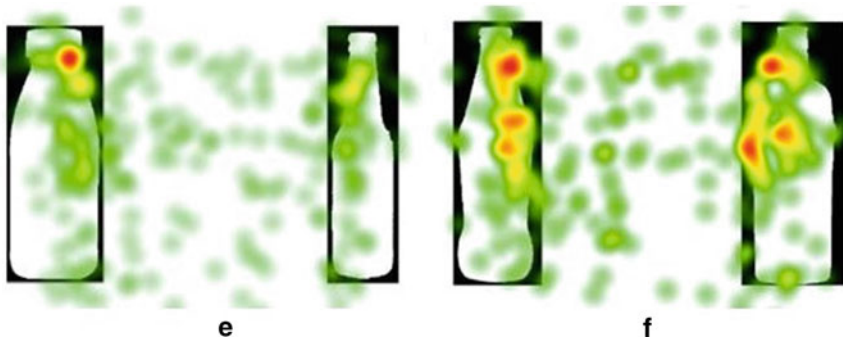
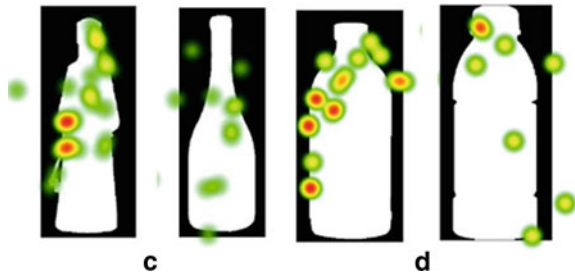


Fig. 3 Slide E and slide F shown the images four different categories

FR. On the other hand, during the second phase of the experiment, we attain a 25% of FR with actual bottle categories.

The heat-affected zone for the right side of the silhouette is the left side of the bottle like below the neck of the bottle and centroid section. In the case of right section of Fig. 1, in slide B, we paste the silhouette image of CD (Limca bottle on left side) and ED bottle.

In the first and second phase experiment, for the left side of the bottle, 85.71% of the open-ended participants and 100% of ET respondents recognize this silhouette with their actual category i.e. CD. On the other hand, there were little contradiction

between the respondents of the first phase and ET i.e. 50% for the first phase and 75% for the second phase. And, from the figure, we can be justified that the deep curve of the CD bottle area is a more important part for identifying the product category, and similarly, in the case of energy drink bottle, a spiked area which shows robustness is the more essential part during the ET experiment as described in the heat map in Fig. 1.

In the case of Fig. 2, in slide D, we present the M/C bottle silhouette (left side), ED (right side), and in slide C, we present the CD (right side), M/C bottle silhouette (left side), respectively. The FR is shown in Tables 1 and 2, from the open-ended survey and ET experiment (open-ended experiment, just after the ET experiment). We analyse that, left image (M/C bottle) of slide D, shown a 71.43% and 75% of FR in both of phase of the experiment and the heat effected zone is formed in the right side of the bottle, from bottom to neck section. In the case of the right side silhouette bottle (Slide D) the respondents during the first phase of the experiment, 57.14% of FR with their respective category of beverages.

On the other hand, during the second phase of the experiment, we attain a 50% of FR with other beverage categories and 37.5% with the respective category. As we can see that, the heat effected zone covers the neck section, just below the neck section, and a straight and angular section is just the middle of the bottle spline section.

As in the silhouette image, we can see the spike as well as curve section which were partly related to the robustness and curvy shape of any fruit. In the case of slide C, we analyse that, left image (CD bottle), showing an 87.5% and 100% of FR in both phases of the experiment, and the heat effected zone is formed on the right side of the bottle, from the bottom to the neck section. Similarly, for the right image (milk/coffee bottle), shown a 28.75% and 87.5% of FR in both phases of the experiment, and the heat effected zone is formed on a chamfered zone of spline more like coffee beans.

In Fig. 3, we present the two images in slide E, i.e., the Ju bottle silhouette in the left section, and the AL bottle silhouette (Beer) in the right section of the same slide. In slide E, the highest FR for juice bottles is 28.57% with M/C and 37.5% with tea category for the first phase and second phase of the experiment, respectively. On the right side of slide E, the FR for the AL bottle is 100% for the first as well as the second phases of the experiment. And the heat map formation happens over the slant height of the bottle. Similarly, in last slide F, we paste two different silhouette. The left side silhouette is of CD bottle and the right side is of AL bottle. In slide E, the highest FR for a CD bottle is 92.86% as compared to 87.5% for the second phase of the experiment with the CD bottle category. On the right side of slide F, the FR for the AL bottle is 100% for the first as well as the second phase of the experiment. By seeing the heat map, we can predict that the neck section and just below the neck section provide a piece of huge information related to the product category.

5 Conclusion

As we can see the results and discussion in Sect. 4, we analyse that there is a huge need for each product-related industry to gather the consumer cognitive information for designing a new product related to the future consumer with a high level of acceptance rate. Previous researchers use various methods to gather the consumer response for the development of a new product like Kansei engineering, Semantic differential method, and Fuzzy AHP, etc.

In this study, we use unique techniques to gather the information and correlate the information for finding its accuracy. By using FR, we can relate the consumer response with product black and white images. After that, we use ET for the same experiment to gather consumer cognitive responses. From that, we can note down the consumer eye movement on the same image, from that we know that, how consumer eyes responded to image of the product. And, by using ET, we can find out which section of product the respondent is looking for. This think, will help for designing the new product, which was increased the product demand in the current and upcoming market as well. Ultimately, this will helps to increase the industry profits.

References

1. Agost, M.-J., Vergara, M.: Relationship between meanings, emotions, product preferences and personal values. Application to ceramic tile floorings. *Applied Ergonomics* **45**(4), 1076–1086 (2014). <https://doi.org/10.1016/j.apergo.2014.01.008>
2. Billmeyer, F.W.: *Color Science: concepts and methods, quantitative data and formulae*, 2nd ed., by Gunter Wyszecki and W. S. Stiles, John Wiley and Sons, New York, 1982, 950 Pp. Price: \$75.00. *Color Res. Appl.* **8**(4), 262–263 (1983). doi: <https://doi.org/10.1002/col.5080080421>
3. Blaisdell, A.P., Cook, R.G.: Two-Itemsame-different concept learning in pigeons. *Anim. Learn. Behav.* **33**(1), 67–77 (2005). <https://doi.org/10.3758/BF03196051>
4. Chang, H.-C., Lai, H.-H., Chang, Y.-M.: A measurement scale for evaluating the attractiveness of a passenger car form aimed at young consumers. *Int. J. Ind. Ergon.* **37**(1), 21–30 (2007). <https://doi.org/10.1016/j.ergon.2006.09.014>
5. Chuang, M.-C., Ma, Y.-C.: Expressing the expected product images in product design of micro-electronic products. *Int. J. Ind. Ergon.* **27**(4), 233–245 (2001). [https://doi.org/10.1016/S0169-8141\(00\)00053-6](https://doi.org/10.1016/S0169-8141(00)00053-6)
6. Goldstone, R.L.: Perceptual learning, **28** (1998)
7. Graf, M.: Form, space and object: geometrical transformations in object recognition and categorization (2002)
8. Graf, M.: Coordinate transformations in object recognition. *Psychol. Bull.* **132**(6), 920–945 (2006). <https://doi.org/10.1037/0033-2909.132.6.920>
9. Hodgetts, C.J., Hahn, U.: Similarity-based asymmetries in perceptual matching. *Acta Physiol. (Oxf)* **139**(2), 291–299 (2012). <https://doi.org/10.1016/j.actpsy.2011.12.003>
10. Jitender, P.S.: Understanding the relationship between aesthetics and product design. *International Journal of Engineering Technology Science and Research* **5**(3), 6 (2018)
11. Lai, H.-H., Lin, Y.-C., Yeh, C.-H., Wei, C.-H.: User-oriented design for the optimal combination on product design. *Int. J. Prod. Econ.* **100**(2), 253–267 (2006). <https://doi.org/10.1016/j.ijpe.2004.11.005>

12. Lamberts, K., Kent, C.: The time course of object-feature retrieval in recognition. *J. Exp. Psychol. Learn. Mem. Cogn.* **34**(3), 688–695 (2008). <https://doi.org/10.1037/0278-7393.34.3.688>
13. Lawson, B.: *How designers think: the design process demystified*, 4th edn. Elsevier, Amsterdam (2006)
14. Moulson, T., Sproles, G.: Styling strategy. *Bus. Horiz.* **43**(5), 45–52 (2000). [https://doi.org/10.1016/S0007-6813\(00\)80008-7](https://doi.org/10.1016/S0007-6813(00)80008-7)
15. Nagamachi, M.: Kansei engineering: a new ergonomic consumer-oriented technology for product development. *Int. J. Ind. Ergon.* **15**(1), 3–11 (1995). [https://doi.org/10.1016/0169-8141\(94\)00052-5](https://doi.org/10.1016/0169-8141(94)00052-5)
16. Nagamachi, M.: Kansei engineering as a powerful consumer-oriented technology for product development. *Appl. Ergon.* **33**(3), 289–294 (2002). [https://doi.org/10.1016/S0003-6870\(02\)00019-4](https://doi.org/10.1016/S0003-6870(02)00019-4)
17. Peighambari, K., Sattari, S., Kordestani, A., Oghazi, P.: Consumer behavior research A synthesis of the recent literature. *SAGE Open* **6**(2), 215824401664563 (2016). <https://doi.org/10.1177/2158244016645638>
18. Rothkopf, E.Z.: A measure of stimulus similarity and errors in some paired-associate learning tasks. *J. Exp. Psychol.* **53**(2), 94–101 (1957). <https://doi.org/10.1037/h0041867>
19. Seva, R.R., Helander, M.G.: The influence of cellular phone attributes on users' affective experiences: a cultural comparison. *Int. J. Ind. Ergon.* **39**(2), 341–346 (2009). <https://doi.org/10.1016/j.ergon.2008.12.001>
20. Simmonds, G., Spence, C.: Thinking inside the box: how seeing products on, or through, the packaging influences consumer perceptions and purchase behaviour. *Food Qual. Prefer.* **62**, 340–351 (2017). <https://doi.org/10.1016/j.foodqual.2016.11.010>
21. Yan, H.-B., Huynh, V.-N., Murai, T., Nakamori, Y.: Kansei evaluation based on prioritized multi-attribute fuzzy target-oriented decision analysis. *Inf. Sci.* **178**(21), 4080–4093 (2008). <https://doi.org/10.1016/j.ins.2008.06.023>
22. Zotkin, D.N., Duraiswami, R., Davis, L.S., Mohan, A., Raykar, V.: Virtual audio system customization using visual matching of ear parameters. In: *Object Recognition Supported by User Interaction for Service Robots*, vol. 3, pp. 1003–1006. IEEE Computer Society, Quebec City (2002)

Neural Network (NN) Based Qualitative Assessment of Bone Growth Over Textured Implant Surfaces



Rajdeep Ghosh , Souptick Chanda, and Debabrata Chakraborty

Abstract Implants are widely used in the restoration of failed joints and bone fractures across the globe. The success of an orthopaedic intramedullary or extramedullary implants depends considerably on various design parameters. The surface texture on implant surfaces is known to influence primary (mechanical) as well as secondary (biologic fixation) stability. Finite element (FE) based biomechanoregulatory schemes were earlier employed while investigating the qualitative trends of bone growth over implant surfaces. Such in silico methodologies, although an efficient process to assess bone growth at the bone-implant interface, involve manually intensive modelling owing to large number of design variables and consequently, demand higher computational time. Machine Learning (ML) based approaches such as Neural Networks (NN) modelled around a wide range of experimental or computational database may be a viable alternative to minimize the complication related to tedious FE runs. The aim of this study thus is to assess the efficiency of using a trained and tested NN while predicting bone growth for unknown data of design parameters for two distinctly textured implant surfaces. The results obtained from FE analyses for an unlabeled dataset and bone growth predictions from the NN for the same dataset for both the implant models were found to be strongly correlated. Although all design morphologies cannot be incorporated in a generalized NN, the methodology appears to be an efficient strategy to predict optimal design features for a specific implant morphology without the need for an exhaustive in vitro or in silico study.

Keywords Implant · Macro-textures · Finite element analysis · Mechanobiology · Bone growth · Neural networks

R. Ghosh (✉) · D. Chakraborty
Department of Mechanical Engineering, Indian Institute of Technology Guwahati, Guwahati,
Assam 781 039, India
e-mail: rajdeep.mech@iitg.ac.in

S. Chanda
Department of Biosciences and Bioengineering, Indian Institute of Technology Guwahati,
Guwahati, Assam 781 039, India

1 Introduction

Lack of biological fixation is one of the major causes of aseptic loosening of cementless implants. Such failure in implant fixation can be minimized to certain extent by realistic design changes in the implant morphology [1, 2]. Surface design features such as surface roughness [3] and macro-textures [1, 2] can be tailor-made to promote sufficient bone growth around a cementless prosthesis. The design evaluation for a large set of implant designs with similar surface morphology need an iterative FE modeling which would be manually exhaustive and computationally expensive. In view of this, developing a predictive mathematical [4, 5] model might be a viable option for establishing a link between implant surface morphology and quantifiable degrees of ossification while retaining the accuracy of FE analysis.

The non-primitive nature of most surface features on implant surfaces, together with a variety of important design considerations, could result in complex non-linear correlations with ossification levels. Neural networks (NNs) are a type of biologically inspired machine learning (ML) technique that can be used to create complicated relationships as predictive mathematical models [5]. NNs were employed in biomechanical design evaluation on many prosthesis [6–9] earlier. NN was used effectively by Cilla et al. [8] to design a single objective shape optimization model for a short-stem femoral stem. Roy et al. [6] utilized NN to convert FE results to the desirability function of an optimization problem on dental implant. Chatterjee et al. [9] also used a trained NN to predict microstrains of a femur-implant system from data as predicted by FE analysis.

Backpropagation algorithms are widely employed in machine learning to train NNs. Several generalization approaches, including as Bayesian regularization (BR) and Levenberg–Marquardt (LM), are employed with NNs to reduce the error associated with backpropagation procedures. Overfitting the training data is also less likely using generalization techniques. Because of their benefit in producing a reduced mean squared error, both the BR and LM techniques are often used [7]. However, Bayesian regularization outperforms LM [7], with BR attaining the best correlation coefficient and the smallest sum of square errors. However, there are hardly any literatures that formulates ML techniques towards assessment of secondary stability of a cementless prosthesis based on implant design variables. Furthermore, to the best of the authors' knowledge, there has been little research on the usefulness of NN models for predicting osseointegration over geometrically diverse macro-textured implant surfaces.

The fundamental purpose of this research is to create new predictive mathematical models premised on BR-BPNN that correlate significant design variables for two commercially feasible implant surface textures to ossification levels during a short healing period. Finally, the utility of the proposed frameworks has been extended to predict bone growth for those unlabeled data sets formed by Design of Experiment (DOE) approach.

2 Materials and Method

Two different representative 3D macro-textured implant models (**RVM1** and **RVM2**) were created based on commercially viable implant textures. **RVM1** contains uniformly spaced rectangular ribs which partially mimics the proximal anterior–posterior surfaces of CORAIL [1, 2] hip stem. On the contrary, **RVM2** contains equally spaced hemispherical grooves of equal radius which represents the proximal region of SP-CL [1] hip stem. **RVM#** stands for Representative Volume Model ‘Number’.

To maintain clinical authenticity, the significant dimensions for the 3D parametric models were extracted from a radiological image [10] of an implanted CLS Spotorno using ImageJ v1.53a (National Institutes of Health and Laboratory for Optical and Computational Instrumentation, University of Wisconsin, USA). The range of the parameters were decided by the authors based on average width of an intramedullary hip prosthesis inside a femoral cavity, maximum allowable gap between the bone and the implant for ossification and ease of manufacturability with the traditional manufacturing processes.

The representative volumes of bone-implant interface models encompass a fabricated macro-texture covering the implant surface, while the mid-portion representing granulation tissue (which is the prime site of bone growth) and the bone representing the portion at the other side (Fig. 1).

2.1 Dataset for “Training” and “Validation” of the NN

The dataset obtained for training and validation was obtained from FE-based biomechanoregulatory algorithm of bone growth as developed earlier by the same authors [1, 2]. The dataset for both the models were created based on 3 factors 4 levels full-factorial design for **RVM1** and 2 factors 4 levels full-factorial design for **RVM2**. A significance of the set of chosen parameters were analyzed using analysis of variance (ANOVA) test.

2.1.1 Parametric NN Modelling for RVM1

To train the NN, data points were taken from 44 FE-based bio-mechanoregulatory assessments of ossification. While, 20 FE-based results were used for validation. Three statistically significant design parameters (*p*, *q* and *r*) as input nodes with one output node corresponding to percentage of bone growth as obtained from FE results were chosen while training the network. *p*, *q* and *r* are also found to be clinically significant design parameters to estimate bone growth at bone-tissue interface. The input (\mathbf{I}_{RVM1}) and output (\mathbf{O}_{RVM1}) strings for training the NN [5] of **RVM1** can be expressed as follows:

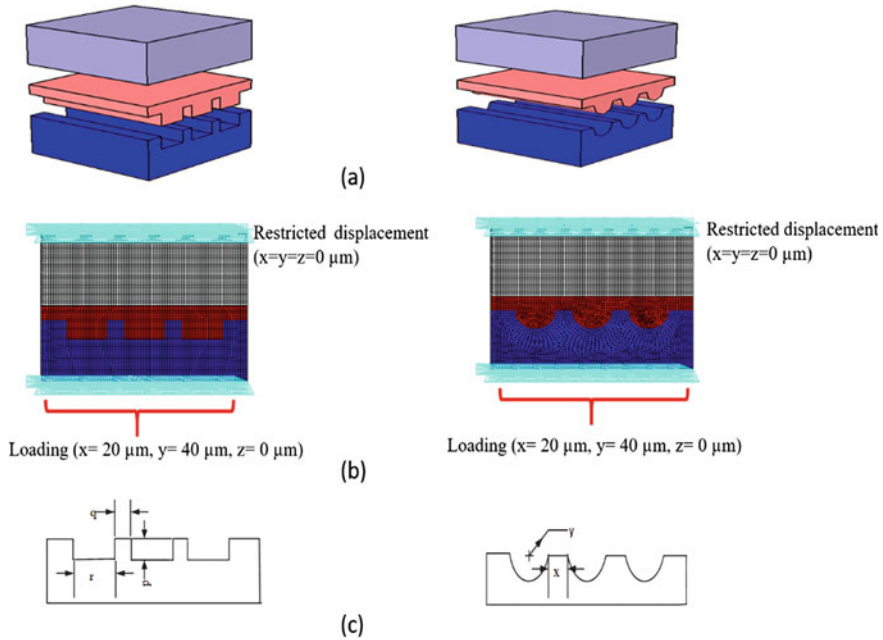


Fig. 1 CAD and FE models of the two bone-implant interface with macro-textures over the implant surfaces: **a RVM1, b RVM2** (mapped colors: blue for implant; red for granulation tissue; grey for bone)

$$I_{RVM1} = [p \ q \ r], \quad \mathbf{O}_{RVM1} = [BG_{RVM1}] \tag{1}$$

subject to constraints [5]:

$$\begin{aligned} 1.0 &\leq p \leq 2.5 \\ 1.0 &\leq q \leq 2.5 \\ 2.0 &\leq r \leq 5.0 \end{aligned}$$

2.1.2 Parametric NN Modelling for RVM2

The network was trained using data from 11 FE-based bio-mechanoregulatory assessments of ossification, whereas 5 of these analyses were used for validation. As input nodes, two statistically significant design variables ('x' and 'y') were chosen. Similar to the earlier model, design parameters 'x' and 'y' are found to be clinically significant. The input (\mathbf{I}_{RVM2}) and output (\mathbf{O}_{RVM2}) strings for the NN [5] of **RVM2** can be expressed as:

Table 1 Levels of design variables (in mm) chosen while creating the dataset for the models

RV M1		Level 1	Level 2	Level 3	Level 4
Design parameters (mm)	<i>p</i>	1.0	1.5	2.0	2.5
	<i>q</i>	1.0	1.5	2.0	2.5
	<i>r</i>	2.0	3.0	4.0	5.0
RV M2		Level 1	Level 2	Level 3	Level 4
Design parameters (mm)	<i>x</i>	1.0	1.5	2.0	2.5
	<i>y</i>	1.0	1.5	2.0	2.5

$$I_{RV M2} = [x \ y], \mathbf{O}_{RV M2} = [BG_{RV M2}] \tag{2}$$

subject to constraints [5]:

$$1.0 \leq x \leq 2.5$$

$$1.0 \leq y \leq 2.5$$

Table 1 shows the levels of design variables chosen while creating the dataset for both the models.

2.2 Preparation of FE Models Along with Loading and Boundary Conditions

As illustrated in Fig. 1, CAD models were first created in CATIA® v5R20 software (Dassault Systèmes, France) and then transferred to ANSYS V14.5 FE software (ANSYS Inc., Canonsburg, PA, USA). FE models were discretized with eight-noded hexahedral elements (SOLID185). For each of the FE models, a mesh sensitivity analysis was performed in order to determine definitive grid sizes and achieve acceptable accuracy in the findings.

All of the models’ regions (implant section, granulation tissue, and host bone) were assigned linear elastic, isotropic material properties [2]. The Young’s modulus of the stainless steel implants used in this research was 195 GPa [2, 5]. The Young’s modulus of bone was determined as 500 MPa [1, 2, 5], while the Young’s modulus of granulation tissue was determined as 1 MPa [2, 5]. For the implant and bone, the Poisson’s ratio was set to 0.3, whilst for the granulation tissue, it was set to 0.167 [5]. The interfaces between bone and tissue and between implant and tissue were considered to be bonded [1, 2, 5].

The top surface of the host bone was restrained in all feasible orientations, whilst a radial (gap opening/closing) displacement of 40 μm and a tangential (bone-implant micromotion) displacement 20 μm [1, 2, 5], were given to the bottom surface of the implant.

2.3 Differentiation of Tissues Using Mechano-biological Principles

A sequential bio-mechanoregulatory algorithm was used to model evolutionary bone growth (Fig. 2). A diffusion model was used to simulate the movement of multipotent mesenchymal stem cells (MSCs) inside the bone-implant interface space as performed in an earlier computational scheme [2, 5] as:

$$\psi \nabla^2 c = \frac{dc}{dt} \tag{3}$$

where Ψ is the coefficient of diffusion ($0.1 \text{ mm}^3/\text{day}$), and the element-specific number of undifferentiated MSCs is represented by c [5]. The value of Ψ was set so that the entire stem cell migration process occurs within the granulation tissue layer within 16 weeks [2, 5], imitating the initial healing period.

Initially, it was hypothesized that the interlayer space between the bone and the implant was filled with granulation tissue, which is made up of enough blood vessels

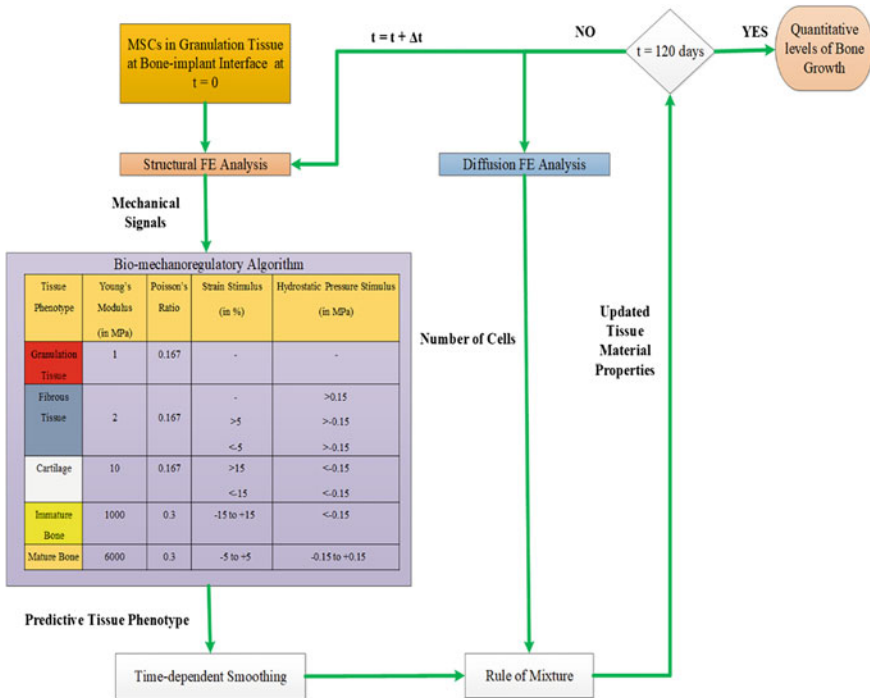


Fig. 2 Numerical scheme implemented to estimate amount of bone formation at the site of defect through a bio-mechanoregulatory model

generated by angiogenesis to feed nutrients to recently created cells and few other inflammatory cells that eliminate wounded tissue [2]. The differentiation of MSCs into distinct osteogenic cellular phenotypes is governed by localised mechanical stimuli (dilatational hydrostatic pressure and deviatoric strain) [2, 5]. Fibrous tissue, cartilage, and immature bone are formed from these cellular phenotypes [5]. The effective material properties (E_{n+1} and ν_{n+1}) of the formed tissues [5] were estimated based on a rule of mixtures as in Eq. 4:

$$E_{n+1} = \left(\frac{c_{\max} - c_{tissue}}{c_{\max}} \right) \Big|_n E_{granulation} + \left(\frac{c_{tissue}}{c_{\max}} \right) \Big|_n E_{tissue} \quad (4)$$

where the material properties of the granulation tissue and generated tissue, respectively, are $E_{granulation}$ (also $\nu_{granulation}$) and E_{tissue} (also ν_{tissue}); c_{\max} and c_{tissue} are the maximum cell concentration and the actual element-specific cell concentration, respectively [5]. Equation 5 shows how the model's material characteristics were updated using a temporal smoothing method [2, 5] as:

$$E_{n+1, smoothed} = \frac{1}{10} \sum_{i=n}^{n-9} E_i \quad (5)$$

In the numeric scheme, one iterative process represents a single post-surgical day. The entire healing simulation was developed to run for 120 iterations, which equates to a post-surgical time of around 16 weeks [2, 5].

2.4 Process Modeling with Neural Network

A single hidden layer of 'N' nodes was considered in the study for both the models. The output node is represented by the percentage of bone growth (BG). Initialization of weights for the datasets have been carried out to achieve better training performance. Tan-sigmoidal and linear functions were chosen as activation functions for the hidden and output layers of the network respectively. Output (O_{NN}) computed from the NN are compared with the target output (T_O) to estimate the error. The algorithm minimizes a loss function, ξ , a linear combination of sum of squared errors and sum of squared network weights. When the computed ξ for a specific combination of errors and weights satisfies a convergence criterion, training of the NN stops, else weights were updated iteratively through back propagation of errors with LM algorithm. In the present analysis, mean squared error (MSE) is considered at the point of convergence for the network and estimated by:

$$MSE = \frac{1}{N} \sum_{i=1}^N (T_O - O_{NN})^2 \quad (6)$$

The NN models developed in the present study were run in MATLAB environment (MATLAB 2017a, The MathWorks Inc., Natick, MA, USA). Parametric investigations were carried out for each of the networks by trial-and-error method so as to achieve maximum predictability of the models.

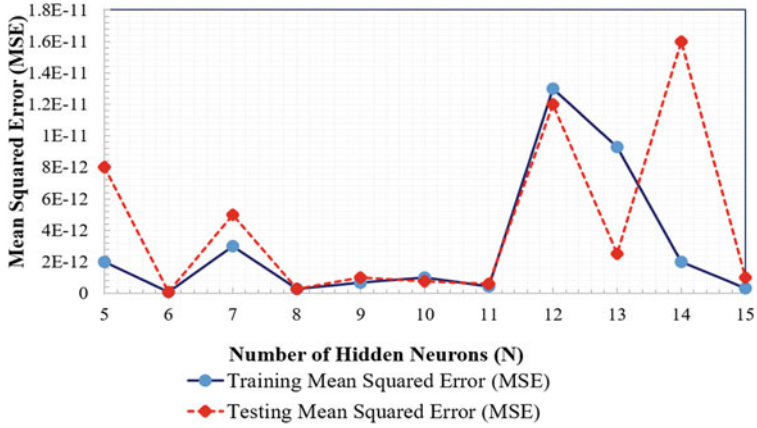
2.5 Design of Experiment (DOE) Approach to Assess Bone Growth

Design of Experiment (DOE) is a statistical technique through controlled tests to identify the influence of several parameters to a desired output or response. There are several types of DOE techniques used presently such as full-factorial, fractional factorial, Taguchi, Plackett–Burman and response surface methodology (RSM). Although a full-factorial DOE becomes cumbersome for a large number of parameters with their corresponding levels, it is extensively used to study the influence of all significant parameters on a desired response comprehensively. In the present study, 2^k full-factorial DOE was employed with number of input design parameters as mentioned earlier in the implant models i.e. (2^3) 8 models for **RVM1** and (2^2) 4 models for **RVM2**. Unlabeled (unseen) input data was chosen for both the models and FE analysis was performed so as to validate the results with those obtained through trained NNs.

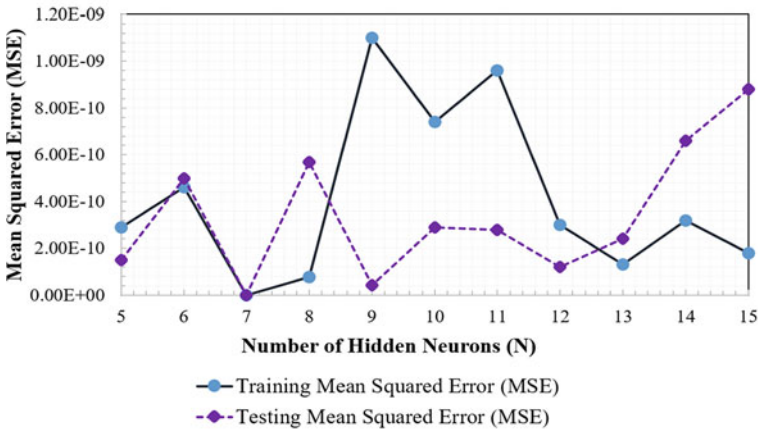
3 Results and Discussion

3.1 Performance Analysis of NN Architecture

The near-optimal BPNN architecture with BR for **RVM1** was obtained through a parametric analysis as presented in Fig. 3. BR was chosen as it can provide a better generalization and minimal over-fitting for a small and difficult dataset. While performing the parametric study, the number of neurons in the hidden layer (N) was altered in the range of (5, 15). It can be observed that NN with 6 hidden neurons showed the least mean squared error (MSE) in testing (Fig. 3). Optimal NN architecture as obtained for **RVM1** is found to be 3-6-1 with training MSE to be $1.0\text{E}-13$ and testing MSE to be $8.0\text{E}-14$. Similarly, by altering N, the optimal NN-architecture for **RVM2** (Fig. 3) is found to be 2-7-1 with training MSE to be $1.9\text{E}-13$ and testing MSE to be $4.1\text{E}-14$. Finally, significance of design parameters was analyzed using ANOVA test in terms of F and p values. ANOVA test was performed at 95% confidence interval i.e. if p -value is less than 0.05, null hypothesis is rejected and all parameters are considered statistically significant. Moreover, if calculated F is more than F_{crit} , the design parameters are considered significant. Table 2 ANOVA test for chosen design parameters for both models. Thus, it is clear from the Table 2 that,



(a)



(b)

Fig. 3 Parametric analysis to find the optimal NN architecture

Table 2 ANOVA test for chosen design parameters for both models

RVM1		DF	SS	MS	F	p	F _{crit}
Design parameters	p	1	2009.61	2009.61	1054.41	0.00	3.93
	q	1	1976.78	1976.78	1039.09	0.00	3.93
	R	1	1258.57	1258.57	585.55	0.01	3.93
RVM2		DF	SS	MS	F	p	F _{crit}
Design parameters	X	1	819.00	819.00	481.98	0.00	4.30
	Y	1	830.72	830.72	477.27	0.00	4.30

p -values for all the design parameters are found to be below 0.05 thus rejecting the null hypothesis while, F -values were found to be more than F_{crit} which gives the confidence for all the design variables of the models to be statistically significant.

3.2 DOE Versus Trained NN for Qualitative Assessment of Bone Growth

Tables 3 and 4 shows the comparison of the results of bone growth over implant surfaces as estimated through conventional FE analysis and the trained NNs. The results from the table clearly shows that, a trained NN is equally efficient in assessment of bone growth over implant surfaces while reducing computational cost over conventional FE based bio-mechanoregulatory algorithms for further analysis of a large scale of implant designs.

Table 3 Prediction of bone growth by FE analysis versus NN for model **RVM1**

Models	Control factors			Bone growth %	
	p	Q	r	FE analysis	From NN
RVM1.1	1.1	2.1	4.1	10.5	10.6
RVM1.2	1.1	1.1	4.1	15.2	15.2
RVM1.3	2.1	2.1	4.1	16.2	16.1
RVM1.4	2.1	1.1	4.1	16.3	16.3
RVM1.5	1.1	2.1	3.1	16.6	16.5
RVM1.6	1.1	1.1	3.1	13.4	13.6
RVM1.7	2.1	2.1	3.1	14.4	14.1
RVM1.8	2.1	1.1	3.1	14.7	14.5

Table 4 Prediction of bone growth by FE analysis versus NN for model **RVM2**

Models	Control factors		Bone growth %	
	x	y	FE analysis	From NN
RVM2.1	1.8	1.1	16.9	16.8
RVM2.2	2.1	1.1	14.7	14.6
RVM2.3	1.8	2	16.3	16.3
RVM2.4	2.1	2	13.2	13.2

4 Conclusion

The present investigation exploits the application of ML techniques such as NN to the estimation of bone growth. BR-BPNN was obtained for two distinct implant surface morphologies to test the efficacy of using NN. The amount of bone growth as predicted by NN was found to have significant correlation with the results obtained from FE based mechanoregulatory analysis. The present analysis will further assist in topology optimization of implant surfaces from a wide range of implant models.

Acknowledgements The authors would highly acknowledge the Composite Structures and Fracture Mechanics Laboratory, Department of Mechanical Engineering, Indian Institute of Technology Guwahati, India, for providing required computational facilities to carry out the research study successfully. The study was partially funded by SPARC, MHRD (Presently Ministry of Education), Government of India (Project ID: SPARC/P705).

References

1. Ghosh, R., Chanda, S., Chakraborty, D.: The influence of macro-textural designs over implant surface on bone on-growth: a computational mechanobiology based study. *Comput. Biol. Med.* **124**, 103937 (2020)
2. Ghosh, R., Chanda, S., Chakraborty, D.: Influence of sequential opening/closing of interface gaps and texture density on bone growth over macro-textured implant surfaces using FE based mechanoregulatory algorithm. *Comput. Methods Biomech. Biomed. Eng.*, 1–15 (2021)
3. Mukherjee, K., Gupta, S.: Bone ingrowth around porous-coated acetabular implant: a three-dimensional finite element study using mechanoregulatory algorithm. *Biomech. Model. Mechanobiol.* **15**(2), 389–403 (2016)
4. Chanda, S., Gupta, S., Pratihari, D.K.: A combined neural network and genetic algorithm based approach for optimally designed femoral implant having improved primary stability. *Appl. Soft Comput.* **38**, 296–307 (2016)
5. Ghosh, R., Chanda, S., Chakraborty, D.: Qualitative predictions of bone growth over optimally designed macro-textured implant surfaces obtained using NN-GA based machine learning framework. *Med Eng Phys.* **95**, 64–75 (2021)
6. Roy, S., Dey, S., Khutia, N., Chowdhury, A.R., Datta, S.: Design of patient specific dental implant using FE analysis and computational intelligence techniques. *Appl. Soft Comput.* **65**, 272–279 (2018)
7. Kayri, M.: Predictive abilities of bayesian regularization and levenberg–marquardt algorithms in artificial neural networks: a comparative empirical study on social data. *Math. Comput. Appl.* **21**(2), 20 (2016)
8. Cilla, M., Borgiani, E., Martínez, J., Duda, G.N., Checa, S.: Machine learning techniques for the optimization of joint replacements: application to a short-stem hip implant. *PLoS One* **12**(9), e0183755 (2017)
9. Chatterjee, S., Dey, S., Majumder, S., Chowdhury, A.R., Datta, S.: Computational intelligence based design of implant for varying bone conditions. *Int J Numer Method Biomed Eng.* **35**(6), e3191 (2019)
10. Zimmer Biomet, UK, Product brochure. <https://www.zimmer.co.uk/medical-professionals/products/hip/cls-spotorno.html>. Last accessed 2020/06/08

Study and Investigation of Tribological Functions of Nano Additive with SAE 40/W20 Oil on EN 19



A. Vinothkumar, R. Ruban , H. Mohit, and G. R. Arpitha

Abstract High operating conditions of moving machine components leads various wearing and failure mainly due to friction. Lubricants are widely used to overcome the friction of the components. Poor performance of lubricant plays a significant energy and material losses. Hence the lubricant needs to synthesis for desirable high working conditions. When the Nano particles introduced into the lubricant matrix, it adheres on one of the moving parts and changes sliding friction to rolling friction resulting in reduced friction losses, wear and increased life of bearing. This research focuses on usage of SAE 40/w20 oil as a lubricant with addition of Multi Walled Carbon Nano Tubes (MWCNTs) as Nano particles. Ultrasonic agitator and Pin on Disk apparatus were used for testing of material EN 19. This study concluded that addition of MWCNTs to the lubricating oil results in considerable decreases in friction, wear rate and increases the load carrying capacity of the lubricant.

Keywords MWCNT · Nano additive · Tribological functions

1 Introduction

Friction is generated when mechanical components come in contact and when there is a relative motion between them. The tribological interaction of a solids surfaces exposing surface with interacting materials and environment resulting in loss of material from the surface. The surface properties of the materials are improved either

A. Vinothkumar · R. Ruban (✉)

Department of Mechanical Engineering, National Institute of Technology, Tiruchirappalli,,
Tamilnadu 620015, India

e-mail: rubanmechanicaler@gmail.com

H. Mohit

Department of Mechanical Engineering, Alliance College of Engineering and Design, Alliance
University, Bengaluru, Karnataka 562106, India

G. R. Arpitha

Department of Mechanical Engineering, Presidency University, Bengaluru, Karnataka 560064,
India

by surface finishing process or by the use of lubricants for reducing the friction and wear [1]. The study of friction phenomenon at the nanometer scale helps us to further promote the performance of the machine components. This leads to the idea of using nanoparticles as lubricants [2].

The nanoparticles as lubricant additives can improve the wear resistance, reducing friction between the adjoining surfaces and load bearing capacity of the oil arousing interest among the researchers. Nano-lubricants with metallic additives have been studied along with the rapid development of technology. The nanoparticles are involved as additive in lubricant involving carbon nanotubes [3–5]. The nanoparticles are added to the oils to improve the anti-wear properties under extreme pressure conditions which was reported under experimental results [6]. The nanoparticles containing anti-wear additives have been very effective in improving the tribological performance [7, 8]. Typically, SAE 20W40 is used in industrial bearing oils, automobiles and hydraulics is chosen as base oil [9]. Since due to humidity environment, low speed and heavy load conditions, it was advisable to use lubricated with the mineral containing wear additives. Traditionally, in order to protect materials from wear and seizure, additives such as chlorides, sulphates and phosphates have been used [10].

It has been perceived that carbon nanotubes specially of multiwalled provides the desirable performance. Typically, carbon Nano Tubes (CNTs) are allotropes of carbon with a cylindrical microstructure. The aspect ratio of nanotubes are constructed upto 1,32,000,000:1. The carbon nanotubes are employed as additions to many structural materials because of their exceptional thermal conductivity, tensile, and electrical properties. Multiwalled carbon nano tubes is a stack of graphene sheets rolled into concentric cylinders [11]. The multiwalled carbon nanotubes due to its physical and chemical properties raised its possibility of use in various applications such as in sensors and field emission displays [12, 13]. In this work, multi walled carbon nanotubes of 20 nm diameter are employed for testing of wear on bearing materials.

2 Experimental Details

The friction and wear properties of the pin material are determined by conducting wear test using Pin-On-Disk tribometer apparatus conforms to ASTM G99 standards shown in Fig. 1. The pin and disc material are wisely chosen in such a way that Pin material hardness should not exceed the hardness of disc. Because this may result in incorrect readings [14]. The Pin Material used in here is EN 19 which has high-quality tensile strength along with the good ductility and shock resisting properties. It also possesses wear resistance. The material E19 provides high quality quenched and alloy tempered structural steel. The material EN19 finds its applications in various machine tools and motor industries for gears, crankshafts, shafts and bearings. It is used predominantly in deep groove ball bearings and magneto type bearings, where high tensile strength steel at good quality is desirable. The composition of the pin material

Fig. 1 Pin on disc tribometer

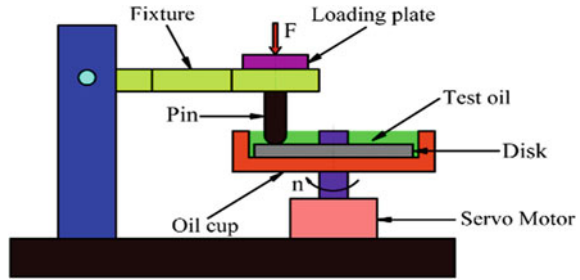


Table 1 Composition of pin material

Element	Min (in %)	Max (in %)
Carbon	0.35	0.45
Manganese	0.50	0.80
Silicon	0.10	0.35
Nickel	–	–
Molybdenum	0.20	0.40
Chromium	0.90	1.50
Sulphur	–	0.05
Phosphorus	–	0.05

EN19 is shown in Table 1. As per the specification of the apparatus, the pin diameter considered here for wear testing is 8 mm and the length is 34 mm with a surface finish of 10 microns (RA 10) which is prepared according to ASTM G99 Standards. The Disc Material considered here is EN 31 which is an alloy martensitic steel equivalent to AISI 52,100 steel. This material possesses higher degree of hardness with compressive strength and abrasion resistance.

This material is applied where higher level of friction coefficient and surface loading is required [15]. EN 31 is used extensively in automobile industry in ball and roller bearings, spinning tools, beading tools, punches and dies. The composition of disc material EN31 is shown in Table 2. Therefore, EN 19 is chosen as pin material and EN 31 is chosen as disc material due to their extensive use in bearing materials and handling of high surface loading. SAE 20/W40 oil as a base oil which is used as lubricant. The Nano Particles are mixed with the lubricant with the help of sonicator. Sonication is the process of agitating particles in a sample with the help of applying sound energy. Water bath is initially prepared and is used to neutralize the heat produced by the ultrasonic waves. Water is filled upto a certain level in order to complete the water bath. The tank of the sonicator is filled with crushed ice before the sonication process is started. The Nano lubricant is placed on the sonicator tray and the probe is inserted into the Nano lubricant. A frequency of 20 Hz is set using the control unit. The Ultra-sonication process is done for 30 min. The properties of multiwalled carbon nanotubes significant in nanolubricants are shown in Table 3. Due to the production of Ultrasonic waves, the nano particles are agitated causing them to

Table 2 Properties of disc material

Element	Min (in %)	Max (in %)
Carbon	0.90	1.20
Manganese	0.30	0.75
Silicon	0.10	0.35
Nickel	–	–
Molybdenum	0.20	0.40
Chromium	1.00	1.60
Sulphur	–	0.40
Phosphorus	–	0.40

Table 3 Properties of multiwalled carbon nanotubes

MCNT	Description	Characteristic method
Production	Chemical vapor deposition	Proprietary method
Available form	Black powder	Visual
Diameter	Outer Dia: 20 nm	TEM, SEM
Length	20 μm	TEM, SEM
Nano tube purity	>98%	TGA, Raman
Metal particles	<1%	TGA
Surface area	220 m^2/gm	BET

move around the lubricant and thus ensuring proper mixing of the nano particles and the lubricant. The Nano particles is again placed in a water bath in order to reduce the heat after mixing of nano particles for 30 min. It is found acceptable for use once the lubricant is properly cooled. It was observed that there is negligible amount of sedimentation which is a result of proper mixing due to ultrasonic waves.

Pin on Disc Tribometer consists of a stationary pin under an applied load in contact with a rotating disc. The Pin can have any shape to simulate a specific contact, but spherical tips are often used to simplify the contact geometry. The parameters to be considered for wear testing in pin on disc tribometer are load, speed and sliding distance. Load here refers to the amount of load which is given on the disc by the pin and speed refers to the speed at which the disc rotates. Sliding distance refers to the distance between the center of the disc and the position of the pin. The Pin on Apparatus is used to test abrasive wear. Abrasive wear occurs when a hard rough surface slides across a softer surface. Abrasive wear is generally of two types. The two modes of wear are two body wear and three body wear. Three body wear occurs when the particles are not constrained and are free to roll and slide down a surface.

Two body wear occurs when the grit or hard particles remove material from the opposite surface. The contact environment determines whether the wear is classified as open or closed. An open contact environment occurs when the surfaces are

Table 4 Properties of lubricant SAE 40/w20 oil

Characteristics	SAE40/ W20 oil
Kinematic viscosity	13–16
Viscosity index (min)	110
Pour point degree (°C)	–21
Flash point (°C)	200
Total base number	4–5

sufficiently displaced to be independent of one another. It was concluded that the main objective of this wear is to compare and analyze the wear which is caused due to normal lubricant and Nano-lubricant. Here, regular SAE 20W40 which is considered normally as normal lubricant. This causes certain amount of wear while during testing conditions. It is the constant against which the nano lubricant is tested to determine whether it is advantageous or not. Nano-lubricant consists of 500 ml of SAE 20w40 mixed with 2.5015gm of Carbon Nanotubes which is of 0.5% of its weight and the mixing is done in the sonicator at a frequency of 20 kHz for thirty minutes. As per the specifications of the apparatus, the pin diameter is 8 mm and the length is 34 mm, with a surface finish of 10 μm (RA 10), prepared according to ASTM G99 standards (Table 4).

3 Experimental Procedures

The Pin on Disk Tribometer is prepared by washing the arm and reciprocating module with diesel. The Pin and the disk are rubbed with emery sheet in order to provide good surface finish. The weight of the Pin are checked in the digital balance by replacing one by one. The Pin is fixed on to the pin holder by tightening the lock screws on either side of the arm. The wear has been checked for three loads such as 10, 20 and 30 N. Three speeds are used for each load which is of mainly 750, 1000 and 1250 rpm. A total of Nine Pins are required for each cycle of tests—for dry test, test with normal lubricant (SAE 20w40 oil) and test with nano-lubricant. The Pins are labelled with a marker and kept in different zip lock bags. These are separated into three groups of 9 for each cycle. The disk is washed with NaOH to remove external impurities and it is fixed to the disc holder. The three types of wear test is conducted, one with dry wear test, another wear test with the use of regular SAE 20w40 as a lubricant and finally with wear test with usage of nano-lubricant. In case of dry wear test, testing is done on the absence of lubrication and in the case of wet wear test, testing is done on the presence of lubrication.

3.1 Dry Wear Test

The load, speed and sliding distance is entered and the pin is made to be in contact with the disc. The Disc starts to rotate once the necessary parameters are entered. Dry wear is easily seen on the surface of the Pin due to the absence of lubrication in case of dry wear test. The Pin is removed from the pin holder after the time taken to cover the sliding distance is determined. The weight is taken in the digital balance once again and this is repeated for the remaining eight pins.

3.2 Wet Test

Lubricant is first filled into a bottle and kept at a high height. Using an Inlet valve port, a tube is inserted into the bottle and the lubricant is made to flow through the tube. The other end of the disk is kept near the disk. The lubricant can be controlled with the help of regulator. The Disc starts to rotate and the pin is in contact once the parameters are entered and the lubricant is made to flow through the tube. The Pin is removed from the pin holder after the time taken to cover the sliding distance is determined. The weight is taken in the digital balance once again and this is repeated for the remaining eight pins.

4 Results and Discussions

When the Pin and Disc are in contact, control unit is affixed to the Pin on Disc apparatus which shows the amount of wear occurring on the pin. It is certain that frictional force and coefficient of friction can be determined after the calculation of wear rate. The wear rate is calculated based on the volume of the pins. In order to confine the experimental study within a periphery, the results are calculated from the data acquisition system of Pin on disk Tribometer. The few trials of the study are carried out by varying the load such as (10, 20, 30 N) with sliding constant distance of 750 mm. The Physical Parameters such as Wear, coefficient of friction and frictional force are shown in Figs. 2a, b, 3a, b and 4a, b. Here, the main concern of this study is the determination of wear rate using volume reduction method.

By this investigation, the load is gradually increased to access the determination of wear rate occurring over the surface under three set of lubricants. The three set of lubricants are Dry lubricant, SAE 40/w20 Oil + Nano Oil (0.5% weight). The wear rate increases with increase in load range from 10 to 50 N, but with the addition of Nano additives there is a drastic reduction in wear rate by 94.58% by keeping sliding distance and speed constant shown in Fig. 5. It also perceives that there is a drastic reduction in wear rate of 96% with the use of Nano lubricants with increase in speed in the range of (400–800) rpm by keeping load and speed constant is shown in Fig. 6.

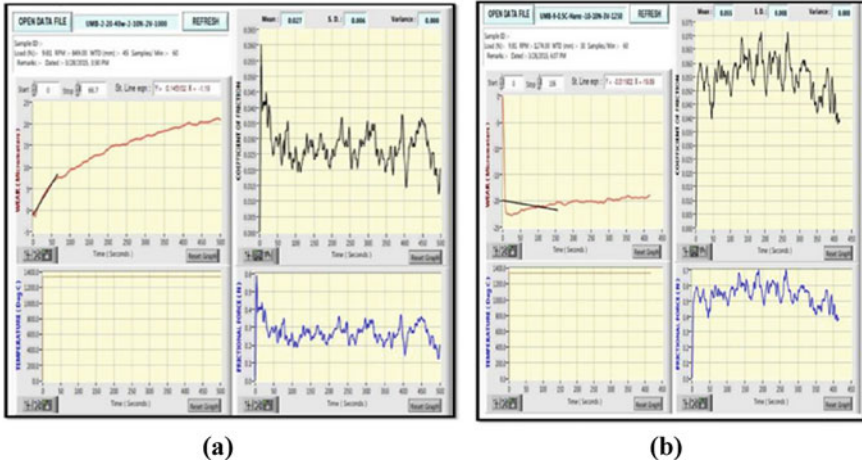


Fig. 2 Wear characteristics on 10 N, 750 mm, SAE 40w/20 oil **a** without MWCNT, and **b** with MWCNT

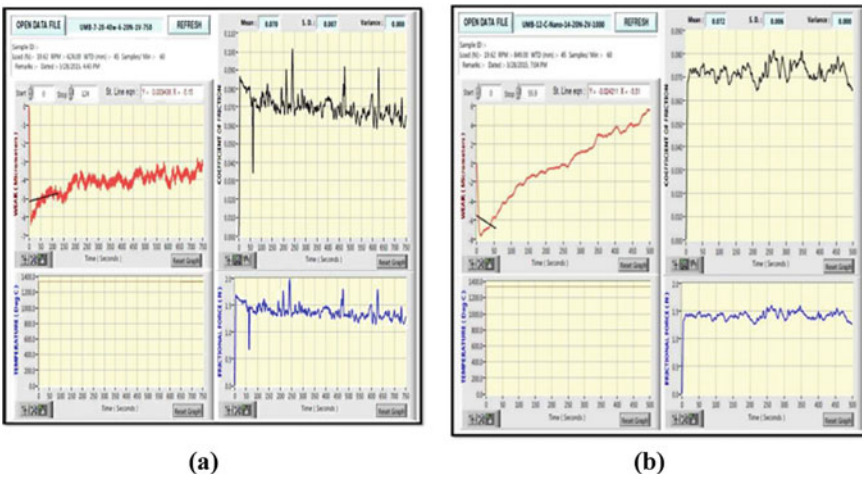


Fig. 3 Coefficient of friction characteristics on 10 N, 750 mm, SAE 40w/20 oil, **a** without MWCNT, and **b** with MWCNT

With the incremental sliding distance from 750 to 1750 mm, it clearly depicts there is a reduction in wear rate in a steady manner around 37% upon the addition of nano Lubricant to the SAE 40/w20 Oil shown in Fig. 7.

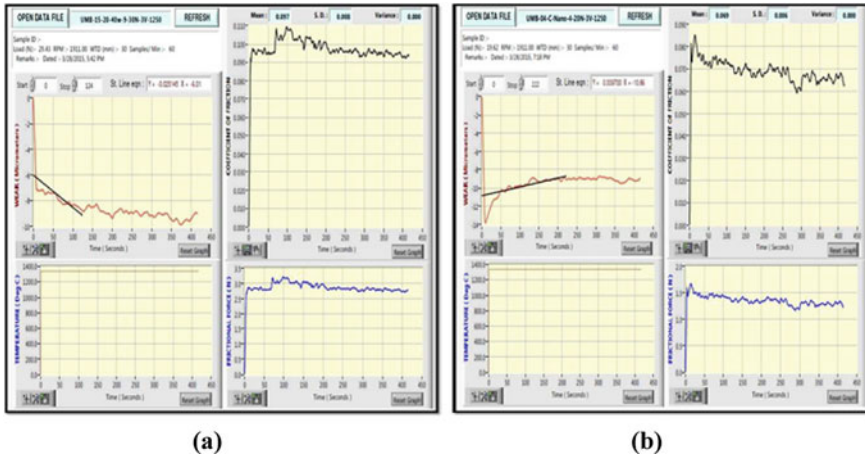


Fig. 4 Frictional force on 10 N, 750 mm, SAE 40w/20 oil a without MWCNT, and b with MWCNT

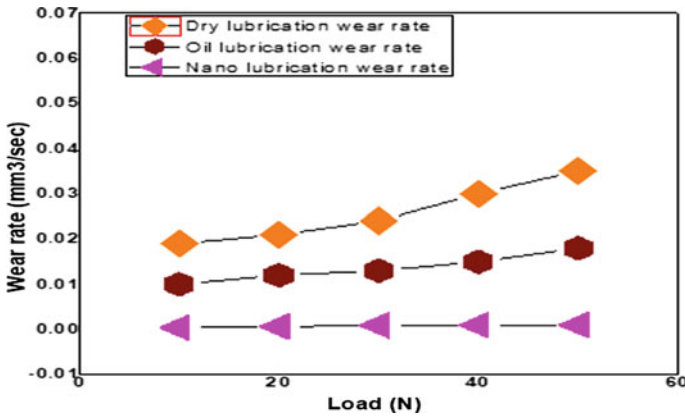


Fig. 5 Wear rate in varying load (sliding distance 750 mm, speed 400 rpm)

5 Conclusion

The motivation for conducting this wear test is stemmed from the increasing amounts of wear seen in EN19. Even during the usage of lubricants, it is seen that the wear is only reduced to some extent and that too only for a short span of time. So, it arises the need of new alternative engineered lubricant. From our study, MWNCT's is the best additive additive to overcome the existing concerns. From our study, it is evident that the use of nanoparticles as an additive in lubricants can help in reducing friction between the moving parts which ultimately reduces the wear rate. It is normally observed that wear rate increases with increase in load but with the addition of nano additives it is seen that wear rate drastically reduces by 94.58% by keeping sliding

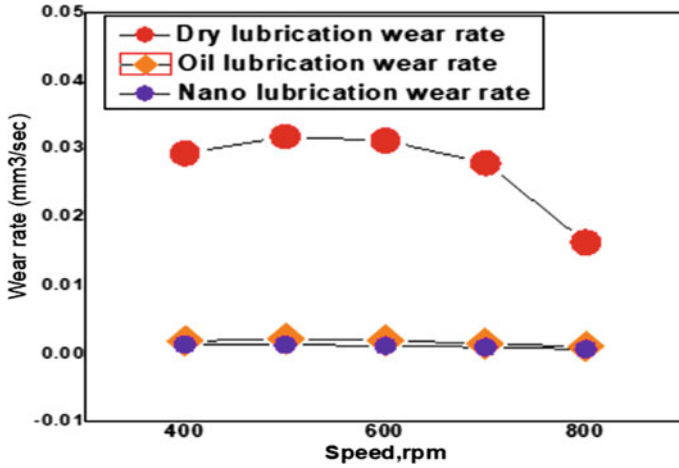


Fig. 6 Wear rate in varying speed (10 N load, 750 mm)

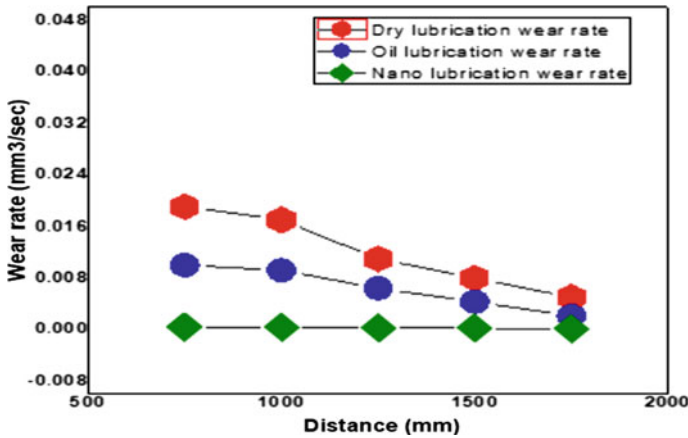


Fig. 7 Wear rate in varying sliding distance (load 10 N, Speed 400 rpm)

distance and speed constant. It is also perceived that there is a drastic reduction in wear rate of 96% with the use of Nano lubricants with increase in sliding distance by keeping load and speed constant. It is observed that with the incremental sliding distance from 750 to 1750 mm, it clearly depicts there is a reduction in wear rate in a steady manner around 37% upon the addition of nano lubricant to the SAE 40/w20 Oil. The study concludes that the addition of MWNCTs to SAE 40/w20 oil reduces the wear rate and opens the way to handle the case where extreme wear prone scenarios which ultimately enhances the mechanical life of the component.

References

1. Bhaumik, S., Prabhu, S., Singh, K.J.: Analysis of tribological behavior of carbon nanotube based industrial mineral gear oil 250 cSt viscosity. *Adv. Tribol.* **1**, 2014 (2014)
2. Kalita, P.A., Malshe, A.P., Jiang, W.E., Shih, A.J.: Tribological study of nano lubricant integrated soybean oil for minimum quantity lubrication (MQL) grinding. *Trans. NAMRI/SME* **38**(313), 137–144 (2010)
3. Yu, B., Liu, Z., Ma, C., Sun, J., Liu, W., Zhou, F.: Ionic liquid modified multi-walled carbon nanotubes as lubricant additive. *Tribol. Int.* **1**(81), 38–42 (2015)
4. Pei, X., Hu, L., Liu, W., Hao, J.: Synthesis of water-soluble carbon nanotubes via surface initiated redox polymerization and their tribological properties as water-based lubricant additive. *Eur. Polymer J.* **44**(8), 2458–2464 (2008)
5. Nunn, N., Mahbooba, Z., Ivanov, M.G., et al.: Tribological properties of polyalphaolefin oil modified with nanocarbon additives. *Diam. Relat. Mater.* **54**, 97–102 (2015)
6. Kalita, P., Malshe, P.: Tribological study of nano lubricant integrated soybean oil for minimum quantity lubrication grinding. *Trans. North American Manuf. Res. Inst.* 137–144 (2010)
7. Muzakkir, S.M., Hirani, H., Thakre, G.D.: Lubricant for heavily loaded slow-speed journal bearing. *Tribol. Trans.* **56**(6), 1060–1068 (2013)
8. Muzakkir, S.M., Hirani, H.: Experimental investigation on effect of particle sizes of molybdenum disulphide on wear under heavy load and slow speed conditions. *IJMER* **4**(12), 46–49 (2014)
9. Woma, T.Y., Lawal, S.A., Abdulrahman, A.S., Olutoye, M.A., Ojapah, M.M.: Vegetable oil based lubricants: challenges and prospects. *Tribol. Online* **14**(2), 60–70 (2019)
10. Liu, L., Fang, Z., Gu, A., Guo, Z.: Lubrication effect of the paraffin oil filled with functionalized multiwalled carbon nanotubes for bismaleimide resin. *Tribol. Lett.* **42**(1), 59–65 (2011)
11. Saifuddin, N., Raziah, A.Z., Junizah, A.R.: Carbon nanotubes: a review on structure and their interaction with proteins. *J. Chem.* **1**, 2013 (2013)
12. Bekyarova, E., Davis, M., Burch, T., Itkis, M.E., Zhao, B., Sunshine, S., Haddon, R.C.: Chemically functionalized single-walled carbon nanotubes as ammonia sensors. *J. Phys. Chem. B* **108**(51), 19717–19720 (2004)
13. Yu, W., Xie, H.: A review on nanofluids: preparation, stability mechanisms, and applications. *J. Nanomater.* (2012)
14. Rasheed, A.K., Khalid, M., Rashmi, W., Gupta, T.C., Chan, A.: Graphene based nanofluids and nanolubricants—review of recent developments. *Renew. Sustain. Energy Rev.* **1**(63), 346–362 (2016)
15. Rajaparthiban, J., Ravichandran, M., Stalin, B., Kumar, P.R., Mohanavel, V.: Machining of EN31 steel using carbide insert—a statistical approach. *Mater. Today: Proc.* **22**, 2559–2564 (2020). Author, F.: Article title. *Journal* **2**(5), 99–110 (2016)

A Review on Advances in Friction Welding of Dissimilar Metals



Deepansh Gill  and M. K. Pradhan 

Abstract Friction welding is classified as one of the most definitive and cost-effective processes when it comes to welding different materials. Solid State welding processes undergo intermetallic compound layering and avoid the melting phase, which is usually seen in fusion welding processes. The study of friction behaviour, joining methodology, contact zone temperatures, and interfacial heat production becomes necessary. This document links the finite element analysis in terms of the thermal behaviour of the joint to the experimental analysis of the distribution of the temperature field. The aim is to perform the welding of Aluminium and Stainless Steel by taking the research a step further than the previously done researches by mapping thermal data with mechanical behaviour and establish stresses in the joints.

Keywords Finite element method (FEM) · Aluminium alloy (AA) · Stainless steel (SS) · ANSYS

1 Introduction

Friction welding is a non-conventional method of welding in which joining occurs in solid state of structure itself allowing various combinations in both similar and dissimilar fashion. One workpiece is continuously rubbed against the other with certain rotational velocity which generates the frictional heat and softens the workpiece then, forging pressure is applied axially. Thus, coalescence is accomplished by thermo-mechanical means. A similarity can be drawn between friction welding and forging process but the basic underlying principle in friction welding is that it converts mechanical energy into frictional heat. Friction welding holds several advantages over fusion welding in terms of lesser heat affected zone (HAZ) formation and

D. Gill (✉) · M. K. Pradhan
Maulana Azad National Institute of Technology, Bhopal, Madhya Pradesh 462003, India
e-mail: deepansh.gill@gmail.com

M. K. Pradhan
e-mail: mohanrkl@gmail.com

© The Author(s), under exclusive license to Springer Nature Singapore Pte Ltd. 2022
K. C. Popat et al. (eds.), *Advances in Mechanical Engineering and Material Science*,
Lecture Notes in Mechanical Engineering,
https://doi.org/10.1007/978-981-19-0676-3_15

overcoming the challenging task owing to the verity that these two materials have varying thermophysical and mechanical properties which makes them relatively less soluble with fusion welding, that's why friction welding becomes a suitable process.

Friction welding is branched in three categories namely: rotary friction welding (RFW), linear friction welding (LFW) and orbital friction welding (OFW). RFW limits itself to cylindrical geometry workpieces and is operated in three ways namely: inertia friction welding (Fig. 2) (developed around 1960s), direct/continuous drive friction welding (Fig. 1) (developed around 1940s) and combined (hybrid) friction welding [1]. Inertia method has variable speed due to employment of a flywheel which stores surplus energy and delivers during deficiency while direct drive operates with a motor providing constant speed. LFW (developed around 1980s) welding is employed for non-cylindrical (rectangular) shaped workpiece in which friction is generated by reciprocated rubbing and axial pressure is applied. OFW (developed around 1970s) is a hybrid of both RFW and LFW which is generally employed for non-cylindrical cross section and both workpiece are rotated in same sense to generate the friction followed by axially applied pressure [2]. Most widely used process in the study is RFW with individual categories despite of the fact that the thickness of HAZ developed is non-uniform as heat generation rate is non-uniform. There are some welding parameters which decide the quality of weld namely: relative velocity between work-materials, process time duration, axial force and amplitude of translation (especially for LFW, OFW) [2].

Aluminium alloys and stainless steels are conventionally used group of metals in industries like automotive, aerospace, oil etc. [3]. due to their remarkable properties and weldability. These possess phenomenal resistance under axial pressure and torque thus displaying apt strength and deformation capability. Density differences are taken into consideration which hybridize the material properties of both base metals which include light weight and corrosion resistance along with strength of joint [3]. This configuration forms a brittle intermetallic compound (IMC) with lesser tensile strength than base metal upon the fusion welding, so a solid-state welding

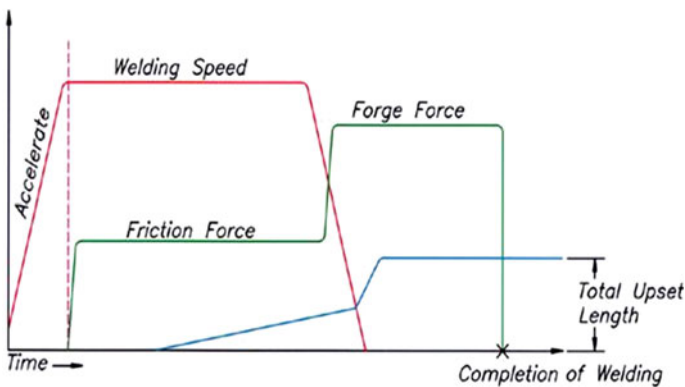


Fig. 1 Direct/continuous drive friction welding

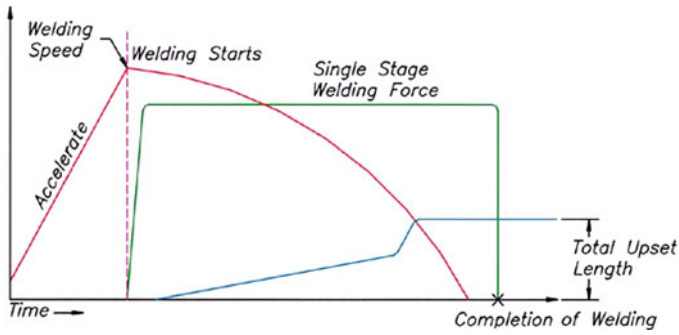


Fig. 2 Inertia friction welding

proves to be an effective method in which temperature range is lesser. The study becomes complicated due to its nature and difference in properties of aluminium and stainless steel such as melting point, thermal conductivity and coefficient of thermal expansion, so a proper optimization of input parameters is required to obtain an equally optimized weld joint [4].

1.1 Finite Element Method

Finite element analysis/modelling (FEA/FEM) is a very powerful mathematical tool used to solve computational complex problems. FEM is a prominent example of rapid technological development in the field of science and technology. It provides suitable flexibility in approximating the behaviour of a system under certain stimulus and establishing the phenomenon under changing stimuli. Analyzing the system computationally becomes important in terms of feasibility of the process and changing the parameters to optimize the output as to experimental process is not very economical and usually takes much greater amount of time. FEM process for a friction welding process is convoluted one and usually needs a well-defined pattern of algorithms so, most of the authors who performed FEM in any respective software package have tried to develop the Temperature versus Welding time curve in order to know the peak values of temperature reached during welding and accordingly the mechanical deformation (upsetting) and forge effect (plastic behaviour) can be modelled in a coupled way as thermo-mechanical FEM. Adaptive mesh (Fig. 4) design was chosen in all the papers in such a way that its refined at the junction but relatively coarse at the ends in order to compute the results accurately and economize the process wherever needed (Fig. 4).

Frictional contact interface initially was considered as coulombic in nature when the deformation is elastic in nature (Fig. 3), some papers mentioned it [5–7]. While others took it by default. Later stage is to be modelled with the fact that as material

Fig. 3 Shear stress versus normal stress curve

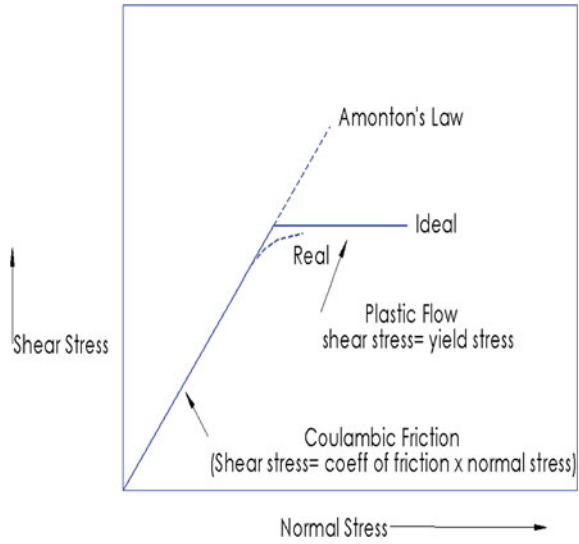
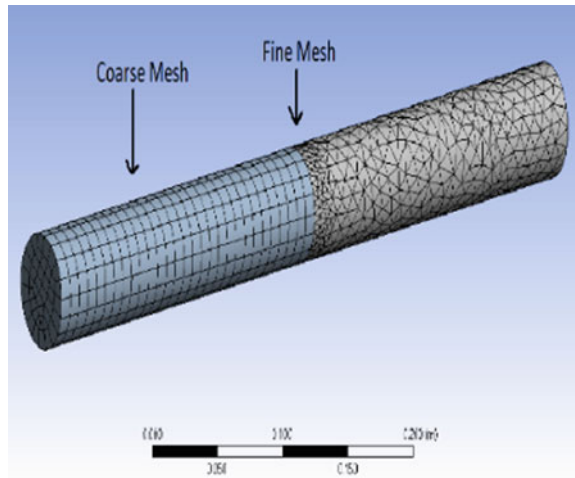


Fig. 4 Adaptive mesh representation



softens the plastic behaviour is incorporated into it so it follows plastic flow rule (Fig. 3).

1.2 Experimental Validation

Experimental validation becomes an important tool in terms of establishing a fact. It depicts actual reality of the system which is usually predicted from FEM and we can

quantify the deviation from the correctness. All the authors focused on optimizing the process parameters such as: rotational velocity, forging pressure, upsetting (axial shortening), welding time. They plotted the optimization with different parameters some authors plotted equivalent stress [6, 8–10]. Some plotted shear stress (frictional stress) [5, 8, 11]. And residual stress analysis [12, 13]. Temperature profile was plotted by each author versus various factors such as distance of weld [9, 10, 14, 15], welding time [5, 6, 8, 10, 11, 13], frictional pressure [9, 10], RPM [9, 10, 14], yield [6], flow stress [11, 15]. And specific heat [7, 15]. Aiming of finding an optimum peak value of each of the aforementioned parameters in the plot.

Most of the authors mentioned here have used metallographic testing to determine microstructure by using SEM–EDX (Scanning electron microscopy–energy dispersion X-ray) and physical properties of weld by testing it for hardness in HAZ and base metal zone. Many have performed tensile, shear and bending tests to determinate the strength of the weld zone and compare it with base metal.

1.3 Process Applications

Friction welding discovers its application in various industries such as automotive, aerospace, electrical and agro. Butt joints in drive shafts, oil drill pipes and aircraft engine components find an extensive use. Agro industries use friction welding for engine valves, gears, hydraulic piston rods and axles. In aerospace it's used for joining turbine blades with discs [2]. Some other applications include cryogenic heat exchangers's transition joints, vacuum applications and rocket propulsion systems which is specifically for Al and steel [16].

2 Review of Application of Methods and Materials in Friction Welding in the Descending Order of Development of Process

References	Material used	Mechanism	Testing performed	FEM method	Aim	Remarks
Rao et al. [17]	AA2219 with SS304	Rotary friction continuous drive welding	Hardness tests, tensile testing, microstructural observations.	N/A	Outcomes of process parameters on friction welding.	
Benkherbache et al. [18]	Similar and dissimilar aluminium and steel	Rotary friction welding	Hardness tests, ultrasonic testing, tensile strength & micrographic tests.	N/A	Evaluation of rigidity of RFW cylindrical samples manufactured on a parallel lathe.	Reduce RPM to increase the friction in order to reach temperature in the contact surface w/o reaching melting point.
Senkathir and Siddharth [19]	AA 6061-T6 and stainless steel AISI 304	Rotary friction welding	Metallographic tests, SEM-EDX, tensile test (yield, ultimate), UTS versus Forge load by ANOVA Distribution.	N/A	Encapsulates summary of the trials and process parameter optimization.	Highest value of tensile strength is 179 MPa, friction pressure = 1500 Nm, friction time = 10 s and Forge load = 1600 Nm.
Hincapié et al. [14]	Aluminium with carbon steels	Rotary friction continuous drive welding	Optical microscopy, SEM, hardness tests, tensile test, temperature profile distribution.	ANSYS Steady state thermal convection	Study the development of solid-state joints for process parameter optimization & inter-metallic compounds.	Fluidity and measure of flash depends on heat contribution controlled by RPM. As, low RPM has low heat with it Low heat input prevents the formation of IMCs.

(continued)

(continued)

References	Material used	Mechanism	Testing performed	FEM method	Aim	Remarks
Khalfallah et al. [20]	AA1100 & mild steel	Rotary friction welding	Metallographic tests, SEM-EDX, hardness tests, tensile test using RSM.	N/A	Investigate the RFW of AA1100 with mild steel, and process variable optimization using RSM.	Highest strength observed under the highest forge pressure/time, min. value leads to a minimum hardness in the weld joints.
Mehta [3]	AA compositions & carbon steels	FW, FSW, hybrid FSW, FS spot welding, FS welding, FS scribe welding, FS brazing, friction melt bonding, FS dovetailing, friction-bit joining, FS extrusion, & FS assisted diffusion welding	Micrographic tests	N/A	Assessing fabrication activity, influence of variables, microstructural disparities, Formation of intermetallic compounds (IMCs), and dissimilitude in mechanical properties.	For Al-steel welds, the interfacial reaction coverings are formed of different IMC phases, must be as minimal as possible. Use interlayer material, given heat control, and post weld heat treatment to inhibit the advancement of IMCs

(continued)

(continued)

References	Material used	Mechanism	Testing performed	FEM method	Aim	Remarks
Wan and Huang [21]	AA6061 & SS316L	Rotary friction welding	Metallographic tests, SEM-EDX, hardness tests, joint strength, temperature profile distribution.	N/A	Study the development of solid-state joints for process parameter optimization & inter-metallic compound.	Size of IMC layers elevates with increased friction time At 15° groove, tensile strength approximates to 166.32 MPa
Mani and Ananthapadmanaban [22]	Aluminium alloys (6061, 2024, 5083) & C-steels (AISI4340 and Austenitic steels)	Rotary friction welding	Microstructure analysis	N/A	Methods of FW of Aluminium to steel in reference with to inter-metallic formation.	Strength of the joint is subject to the type and thickness of intermetallic formed at the welded joint
Pravala, and UdayKiran [23]	H30 aluminium and BS970 mild steel Kimuraa	Rotary friction continuous drive welding	Hardness tests, tensile test & metallographic tests,	N/A	Assess the development of weld for process parameter optimization.	Testing the welding, showed the best results in tensile tests.
Kimuraa et al. [24]	Pure Aluminium-SS304	Rotary friction continuous drive welding	Metallographic tests, SEM-EDX, hardness tests, tensile test, temperature profile distribution.	N/A	Effect of FW on connection aspect, tensile strength, and bend ductility & process parameter optimization was done.	Friction torque was local to the initial maximum at friction time of 0.6 s, Forge pressure of 150 MPa, the bend ductility is 90 deg at 1.0 s.

(continued)

(continued)

References	Material used	Mechanism	Testing performed	FEM method	Aim	Remarks
Torun [25]	Al 7075 Alloy and 316 L stainless steel	Rotary friction welding	Optical metallographic tests and SEM-EDX, hardness tests, shear tests.	N/A	Study the development of solid-state joints for process parameter optimization.	Friction time has a key part in flash development and joining shear strength.
Hynes et al. [12]	Hybrid AA6063-6SiCp-3Grp composite and AISI 1030 steel with AA1100 as interlayer	Rotary friction welding	Metallographic tests, SEM-EDX, hardness tests, joint strength (residual impact strength, tensile strength).	Regression Analysis for axial shortening, temperature distribution, impact strength	Study the development of solid-state joints for process parameter optimization.	Rotational velocity and interlayer bulk width contribute 39% and 36% respectively in impact strength, 71% in upsetting.
Nimesh et al. [8]	AA 6061 and mild steel	Rotary friction inertia friction welding	Hardness tests, temperature profile distribution.	ANSYS, ABAQUS Mathematical modelling (thermal), 3D FEM- (Load distribution wrt time, Temp. distribution wrt time)	Study the development of solid-state joints for process parameter optimization comparing FEM and experiments.	Peak temperatures achieved in the range of 527–627 °C & from simulation at HAZ is 480–490 °C, experimental data shows a temperature of 450 at HAZ.
Alavala [9]	AA2024 & SS304	Rotary friction welding	N/A	ANSYS WORKBENCH (15.0) Assessed strength, bulk deformation piercing and flange generation	Evaluate the weldability of AA2024 and SS304 for process parameter optimization using FEM.	Weldability of AA2024 and SS304 depend on RPM, time for friction and the ratio of forge pressure/friction pressure.

(continued)

(continued)

References	Material used	Mechanism	Testing performed	FEM method	Aim	Remarks
Asif et al. [15]	UNS S31803 duplex stainless steel	Rotary friction welding	Metallographic tests, SEM-XRD & temperature profile distribution	ANSYS Mathematical modelling (friction, strain hardening), 3D non-linear FEA for thermal distribution	Thermal history, upsetting profiles prediction & validated using experimental results.	Maximum temperature gained while frictional heating, at zenith temperatures less than melting point.
Reddy [10]	AA2024 and AISI 1021 Steel	Rotary friction continuous drive welding	N/A	ANSYS (15.0) 3D FEM (influence of process parameters on temperature, equivalent stress)	Process parameters have been optimized using Taguchi techniques.	Friction based pressure of 35 MPa, frictional duration of 3 s, RPM of 1500 rpm & forge pressure 37.5 MPa.
Meshram and Reddy [26]	AA6061 with AISI 4340	Rotary friction continuous drive welding	Metallographic tests, SEM, XRD and scanning electron probe microanalysis (SEPM), fractography (fracture tests), hardness tests.	N/A	Study the development of solid-state joints for process parameter optimization & introducing silver inter-metallic layer on 4340 and test that.	With Ag as intermetallic layer, greater strength and ductility of Al to low alloy steel welds was accredited to the ductile form of phase.
Ambroziak et al. [27]	Aluminium alloys with different compositions & Austenitic Stainless Steel	Rotary friction and linear friction welding (less often)	Hardness tests, shear, tensile & bending tests	N/A	During welding, structural effects and various organizations of the methodology were analysed.	Long time and high temperatures lead to the creation of intermetallic stages.

(continued)

(continued)

References	Material used	Mechanism	Testing performed	FEM method	Aim	Remarks
Bennett et al. [5]	Compositions of austenitic and martensitic steels	Rotary friction inertia friction welding	Synchrotron X-ray, neutron diffraction techniques, EDXRD, hardness tensile & bending tests, temperature profile distribution with post weld cooling model, residual stress.	<i>DEFORM 2D</i> (<i>v10.0</i>), Mathematical modelling (thermal, friction, stress), phase transformation modelling	FEM model validation against experimental data for process parameter optimization and FEM model was validated for residual stresses against experimental process.	Data structure constitute for materials, allow microstructural consequences of two is included in model, and the change in volume relates with the martensite transformation incorporated with post-weld cooling analysis.
Alves et al. [28]	AA1050 & 304 SS	Rotary friction welding	Metallographic tests, SEM-EDX hardness tests.	N/A	Evaluate the formation of solid-state weld joints for process parameter optimization.	Vickers microhardness measured on the edge of AA1050 & AISI 304 near the bond junction, centre, and were greater than in the base of metal.

(continued)

(continued)

References	Material used	Mechanism	Testing performed	FEM method	Aim	Remarks
Maalekian et al. [6]	Similar steel bars	Orbital friction welding	Temperature profile distribution, heat generation and axial shortening.	<i>DEFORM 3D</i> Mathematical modelling (Heat generation, interfacial friction), Thermo-Mechanical FE based on heat input	Heat-generation rate is analysed using: constant coulomb friction, sliding–sticking friction, and an inverse heat analysis.	Sliding–sticking & the sustained friction coefficient ways provide lesser precise data, of heat-generation rate if apt value for is chosen. Inverse heat analysis can give much accurate results.
Maalekian et al. [7]	Similar eutectoid steel bars	Orbital friction welding	Micrographic, macro-graphic tests, hardness test, temperature profile, heat flux distribution and stress–strain curve.	<i>DEFORM 3D</i> Mathematical modelling (thermal), Thermomechanical FE based on phase transformation, flash formation in HAZ, axial shortening	OFW probing using experimental and numerical analysis, friction-based heat production by inverse heat-transfer analysis.	Inverse heat analysis can give much accurate results for heat generation.
Zhang et al. [11]	Nickel based super alloy GH4169 and C25 steel	Rotary friction continuous drive welding	Temperature profile distribution, frictional stress and upsetting velocity.	<i>DEFORM 2D</i> Mathematical modelling (3D-viscoplastic constitutive equation, thermal analysis), thermomechanical FEA	3D rigid viscoplastic FEM model was established to describe FW process. Temperature measured and compared to calculations.	Stress by friction is greater in the inland of friction junction than at edge. Deformation phase of friction stress remain almost same, varies during heating stage.

(continued)

(continued)

References	Material used	Mechanism	Testing performed	FEM method	Aim	Remarks
Alvise et al. [13]	N/A	Rotary friction inertia friction welding	Rotational deceleration, upset curves, temperature & elasto-viscoplastic residual stress analysis	<i>P1+P1 formulation</i> (for velocity and pressure), Glerkin (SG) method coupled asynchron Taylor discontinued Galerkin (TDG) method for thermal shocks	Building and experimentally validating a FE code for the IFW process to analyse it.	Numerical multi-material model in terms of multi-body contact has proved to be numerically ordered and experimental validation was done.
Fukumoto et al. [29]	AA5052 & SS304	Continuous drive friction welding process	Metallographic tests, SEM-EDX, TEM, hardness tests, joint strength	N/A	Assess the development of weld strength for process parameter optimization.	Weld strength heightens and reaches the highest, and thereafter reduces again as time for friction increased.

3 Results and Discussions

Benkherbache et al. [18] obtained a sound weld using rotary friction welding and did the process in combination with aluminium and steel for varying RPM and found that increase in RPM reduces the tensile strength of interface. Senkathir and Siddharth [19] performed a study on AA-SS and optimized it using design of experiment method—ANOVA and found that friction loading had the maximum influence on the ultimate tensile strength amongst input parameters, whereas friction time had the minimum. Hincapié et al. [14] performed an validation study on AA-SS using three input parameters and found burn-off length is not a decisive criteria for defect free joint and RPM plays a key role in flash expulsion and heat generation. Oscar was able to formulate an equation of IMC thickness which depends on temperature rise as well. Khalfallah et al. [20] used design of method technique called Response surface methodology (RSM) to optimize the input parameters and found tensile strength increases with increase in friction pressure/ time and forge pressure/time, while micro-hardness reduces with increase in friction pressure/time and RPM. Wan and Huang [21] performed weld parameter optimization and found that short friction time leads to low temperature rise and less plastic deformation while longer friction durations would facilitate IMC formation. Kimuraa et al. [24] performed weld parameter optimization using 1650 RPM, 30 MPa friction pressure, a series of friction durations from 0.04 to 3.0 s, a series of forge pressures from 30 to 150 MPa, and forge time of 6.0 s, joint efficiency for both tensile and bend increased upon increasing the forge pressure. Torun [25] tried to establish an effect of increasing friction time and burn-off length and found that shear strength increases while hardness showed negligible effect to time. Hynes et al. [12] carried out process parameter optimization by using ANOVA on AA composite and steel stud by varying it in three ranges low, medium and high respectively. RPM and interlayer sheet thickness play significant role in impact strength while friction time plays least. EDX analysis shows the presence of IMC which is orthorhombic. Nimesh et al. [8] performed FEM on ABAQUS and experimental testing to determine strength and hardness respectively. Maximum temperature, stress (Von-Mises and Tresca's), elastic–plastic strains were obtained between 2nd and 3rd second of process initiation. Alavala [9] performed FEM on ANSYS and performed process parameter optimization using ANOVA design of experiments which stated that friction stress and RPM increase the equivalent stresses but an increase in frictional time reduces it and directional deformation increases with increase in RPM but reduces with increase in forge load. Asif et al. [15] performed FEM on ANSYS and validated the results experimentally for optimized values, with increase in frictional, forge pressure/time the axial shortening values increase and IMC formation was not found. Reddy [10] performed FEM on ANSYS and validated the results experimentally for optimized values, friction pressure/time, RPM, forge pressure play 43.74%, 26.21%, 12.97%, & 16.96% respectively towards deviation in the effective stress and 38.18%, 38.18%, 26.20% and 16.45% respectively towards total deformation. Meshram and Reddy [26] performed study on effects of silver interlayer on hybrid weld and suggested

that silver interlayer improves ductility in weld zone along with improved tensile strength. Silver act as a barrier in between base metals thus prevents brittle inter-layer formation. Non formation of IMC results in loss in hardness but silver IMC takes it to a tolerant level. Bennett et al. [5] modelled the process in 2D FEM using DEFORM and experimentally validating the results for temperature and upset rate in three samples with sizes 5, 10, 15 mm respectively. FEM formulation also depicted austenite concentration and Heat affected zones (HAZs). Maalekian et al. [6] did a comparative study of FDM and FEM using OFW, maximum effective stress rises with friction time while effective strain rates reduce. A trivial peak temperature difference is there between center and base metal at the same time. Maalekian et al. has used three approaches to model the process- firstly, coulombic law for friction coefficient. Secondly, sticking and sliding friction modelling being done separately by utilizing the effects in different regions. Thirdly, experimental method of inverse analysis. Maalekian et al. [7] has done FEM on DEFORM and experimental testing of hardness profile and microstructure establishment. Experiment and FEM are in close agreement with peak temperature obtained between 3rd and 4th second near 1000 °C while size of HAZ is 2.8 mm. Maximum hardness is obtained at weld interface and then falls to a constant value while headed for base metal. Zhang et al. [11] performed the FEM on DEFORM and has modelled the process in three stages and temperature rise along with plastic softening. Peak temperature achieved is 1130 °C. Experimental validation of flash shape formation and directional deformation are in a close agreement with FEM.

4 Conclusion

- (i) Works have been done on DEFORM software in initial and mainly by using viscoplastic material modelling but later on authors switched to much user-friendly software like ABAQUS and ANSYS.
- (ii) Friction coefficient is influenced by numerous aspects such as RPM, axial pressure, temperature profile, plastic deformation etc. Determining the exact value at different phases of welding is slightly out of league.
- (iii) Higher temperature results in more tendency of IMC formation and lower temperatures results in improper plastic yielding. RPM and frictional loading are deciding parameters for heat generation. So, they must be controlled by in such a way that sound weld is obtained.
- (iv) RPM, friction pressure and forge pressure play important role in joint strength while friction and forge timings play key role in microstructural features of weld joint.
- (v) New mathematical techniques like: Taguchi design, Response surface methodology (RSM) and Artificial neural network (ANN) are developed as design of experiments to improvise the optimization method by increasing the accuracy computationally.

- (vi) Inverse heat analysis method [2, 6, 7] is a very fine technique being used by some authors to obtain temperature values much closer to that of the accurate.

References

1. Uzkut, M., Ünlü, B., Yilmaz, S., Akdağ, M.: Friction welding and its applications in today's world. *Sarajev. Int. Symp. Sustain. Dev.* 710–724 (2010) [Online]. Available: <http://eprints.ibu.edu.ba/621/>
2. Maalekian, M.: Friction welding—critical assessment of literature. *Sci. Technol. Weld. Join.* **12**(8), 738–759 (2007). <https://doi.org/10.1179/174329307X249333>
3. Mehta, K.P.: A review on friction-based joining of dissimilar aluminum-steel joints. *J. Mater. Res.* **34**(1), 78–96 (2019). <https://doi.org/10.1557/jmr.2018.332>
4. Vyas, H., Mehta, K.P., Badheka, V., Doshi, B.: Pipe-to-pipe friction welding of dissimilar Al-SS joints for cryogenic applications. *J. Braz. Soc. Mech. Sci. Eng.* **42**(2), 1–12 (2020)
5. Bennett, J., Attallah, M.M., Preuss, M., Shipway, P.H., Hyde, T.H., Bray, S.: Finite element modeling of the inertia friction welding of dissimilar high-strength steels. *Metall. Mater. Trans. A Phys. Metall. Mater. Sci.* **44**(11), 5054–5064 (2013). <https://doi.org/10.1007/s11661-013-1852-2>
6. Maalekian, M., Kozeschnik, E., Brantner, H.P., Cerjak, H.: Comparative analysis of heat generation in friction welding of steel bars. *Acta Mater.* **56**(12), 2843–2855 (2008). <https://doi.org/10.1016/j.actamat.2008.02.016>
7. Maalekian, M., Kozeschnik, E., Brantner, H.P., Cerjak, H.: Finite element modeling of orbital friction welding of eutectoid steel bars. *Metall. Mater. Trans. A Phys. Metall. Mater. Sci.* **39**A(4), 844–852 (2008). <https://doi.org/10.1007/s11661-008-9481-x>
8. Nimesh, P., Chaudhary, R., Singh, R.C., Ranganath, M.S.: Simulation of inertia friction welding of mild steel and aluminium 6061 using finite element method on ABAQUS. *Int. J. Adv. Prod. Ind. Eng.* **1**(4), 29–39 (2016)
9. Alavala, C.R.: Weldability of friction welding process for AA2024 alloy and SS304 stainless steel using finite element analysis. *Int. J. Eng. Dev. Res.* **6**(3), 53–57 (2016)
10. Reddy, C.: Finite element analysis of friction welding process for AA7020-T6 and Ti-6Al-4V alloy: experimental validation. *Int. J. Sci. Res.* **4**(8), 947–952 (2015). Available: <https://www.ijsr.net/archive/v4i5/SUB154501.pdf>
11. Zhang, Q.Z., Zhang, L.W., Liu, W.W., Zhang, X.G., Zhu, W.H., Qu, S.: 3D rigid viscoplastic FE modelling of continuous drive friction welding process. *Sci. Technol. Weld. Join.* **11**(6), 737–743 (2006). <https://doi.org/10.1179/174329306X153222>
12. Rajesh Jesudoss Hynes, N., Vivek Prabhu, M., Nagaraj, P.: Joining of hybrid AA6063-6SiCp-3Grp composite and AISI 1030 steel by friction welding. *Def. Technol.* **13**(5), 338–345 (2017). <https://doi.org/10.1016/j.dt.2017.05.014>
13. D'Alvise, L., Massoni, E., Walloe, S.J.: Finite element modelling of the inertia friction welding process between dissimilar materials. *J. Mater. Process. Technol.* **125–126**, 387–391 (2002). [https://doi.org/10.1016/S0924-0136\(02\)00349-7](https://doi.org/10.1016/S0924-0136(02)00349-7)
14. Hincapié, O.D., Salazar, J.A., Restrepo, J.J., Graciano-Urbe, J.A., Torres, E.A.: Weldability of aluminum-steel joints using continuous drive friction welding process, without the presence of intermetallic compounds. *Eng. J.* **24**(1), 129–144 (2020). <https://doi.org/10.4186/ej.2020.24.1.129>
15. Asif, M., Shrikrishana, K.A., Sathiya, P.: Finite element modelling and characterization of friction welding on UNS S31803 duplex stainless steel joints. *Eng. Sci. Technol. an Int. J.* **18**(4), 704–712 (2015). <https://doi.org/10.1016/j.jestch.2015.05.002>
16. Vyas, H.D., Mehta, K. P., Badheka, V., Doshi, B.: Processing and evaluation of dissimilar Al-SS friction welding of pipe configuration: nondestructive inspection, properties, and microstructure. *Measurement* **167**, 108305 (2021)

17. Anand Rao, G., Mahender, P., Rohit Kumar, B.: Study the effect of process parameters on friction welding of dissimilar metals AISI304 with AA2219 aluminium. In: AIP Conference Proceedings, vol. 2317, p. 030013 (2021). <https://doi.org/10.1063/5.0036450>
18. Benkherbache, H., Amroune, S., Zouai, M., Mohamad, B., Silem, M., Saidani, H.: Characterization and mechanical behaviour of similar and dissimilar parts joined by rotary friction welding. *Eng. Solid Mech.* **9**(1), 23–30 (2020). <https://doi.org/10.5267/j.esm.2020.6.002>
19. Senkathir, S., Siddharth, V.B.: Friction welding of dissimilar metals (aluminium AL 6061 T6 and stainless steel AISI 304). *IOP Conf. Ser. Mater. Sci. Eng.* **912**(3) (2020). <https://doi.org/10.1088/1757-899X/912/3/032043>
20. Khalfallah, F., Boumerzoug, Z., Rajakumar, S., Raouache, E.: Optimization by RSM on rotary friction welding of AA1100 aluminum alloy and mild steel. *Int. Rev. Appl. Sci. Eng.* **11**(1), 34–42 (2020). <https://doi.org/10.1556/1848.2020.00005>
21. Wan, L., Huang, Y.: Friction welding of AA6061 to AISI 316L steel: characteristic analysis and novel design equipment. *Int. J. Adv. Manuf. Technol.* **95**(9–12), 4117–4128 (2018). <https://doi.org/10.1007/s00170-017-1505-5>
22. Mani, D., Ananthapadmanaban, D.: Welding mechanisms during friction welding of aluminium with steel. *J. Chem. Pharm. Sci.* (7), 53–55 (2017)
23. Pravalala, E.K., Udaykiran, A.: Studies on joining of aluminium to mild steel using friction welding process, vol. 5(4), pp. 365–371 (2017)
24. Kimura, M., Suzuki, K., Kusaka, M., Kaizu, K.: Effect of friction welding condition on joining phenomena, tensile strength, and bend ductility of friction welded joint between pure aluminium and AISI 304 stainless steel. *J. Manuf. Process.* **25**, 116–125 (2017). <https://doi.org/10.1016/j.jmapro.2016.12.001>
25. Torun, O.: “Friction welding of AL 7075 and 316L stainless steel. *Online J. Sci. Technol.* **7**(2), 56–59 (2017)
26. Meshram, S.D., Madhusudhan Reddy, G.: Friction welding of AA6061 to AISI 4340 using silver interlayer. *Def. Technol.* **11**(3), 292–298 (2015). <https://doi.org/10.1016/j.dt.2015.05.007>
27. Ambroziak, Korzeniowski, M., Kustron, P., Winnicki, M., Sokołowski, P., Harapińska, E.: Friction welding of aluminium and aluminium alloys with steel. *Adv. Mater. Sci. Eng.* **2014** (2014). <https://doi.org/10.1155/2014/981653>
28. Alves, E.P., Neto, F.P., An, C.Y.: Welding of AA1050 aluminum with AISI 304 stainless steel by rotary friction welding process. *J. Aerosp. Technol. Manag.* **2**(3), 301–306 (2010). <https://doi.org/10.5028/jatm.2010.02037110>
29. Fukumoto, S., Tsubakino, H., Okita, K., Aritoshi, M., Tomita, T.: Friction welding process of 5052 aluminium alloy to 304 stainless steel. *Mater. Sci. Technol.* **15**(9), 1080–1086 (1999). <https://doi.org/10.1179/026708399101506805>

Conceptual Design and Development of Automated Waste Segregator



Vishwas Mahesh , Manoj D. Yadav, T. C. Sinchana, S. R. Subhash, and S. Sushmitha

Abstract The current research focuses on the conceptual design and development of an automatic trash segregator machine that uses a parallel resonant impedance sensing mechanism to detect metallic objects and capacitive sensors to discriminate between wet and dry waste. Currently there is no proper access to waste disposal services which in turn affects appropriate waste management. Majority of the waste collected are either dumped unscientifically or disposed to water resource thereby leading to environmental hazards. Various conceptual sketches are developed for segregating the waste automatically and the best concept is selected based on the pros and cons on the developed concepts. The required components are procured and the selected concept is developed and successfully demonstrated for various wastes such as metallic, dry and wet wastes. The outcome of the present work helps in managing and segregating the garbage without spoiling the environment. It also reduces the man power and makes the process of recycling and reuse easier.

Keywords Conceptual design · Waste segregator · Product design

1 Introduction

The amount and varieties of solid and hazardous garbage are constantly increasing as a result of continued economic expansion, urbanisation, and industrialization, national and municipal governments face a new problem in ensuring effective and long-term waste management [1]. Waste must be properly sorted, handled, transported, and disposed of in order to reduce dangers for the patients, common people and the surrounding. After sorting, garbage's value is determined economically. At the moment, there is no home waste separation system for dry, wet, and metallic garbage [2].

V. Mahesh (✉) · M. D. Yadav · T. C. Sinchana · S. R. Subhash · S. Sushmitha
Department of Industrial Engineering and Management, Siddaganga Institute of Technology,
Tumakuru 572103, India
e-mail: vishwasm@sit.ac.in

© The Author(s), under exclusive license to Springer Nature Singapore Pte Ltd. 2022
K. C. Popat et al. (eds.), *Advances in Mechanical Engineering and Material Science*,
Lecture Notes in Mechanical Engineering,
https://doi.org/10.1007/978-981-19-0676-3_16

The curse of garbage will become a benefit for civilization if a good recycling system is implemented. Recycling will be more efficient as a result of the sorting operation. The old trash management system will be changed into an intelligent system using this type of garbage sorter. This SMART system will contribute to a more livable environment, reduced global warming, and a healthier world. People have employed numerous garbage disposal technologies to remove undesired materials since the dawn of civilization. Animals are fed or burned after it is buried in the earth or thrown into the sea. One of the key problems of modern society has always been getting rid of unneeded things. Throughout history, garbage has played a vital role. Diseases such as bubonic plague, cholera, and typhoid fever, to name a few, all threaten Europe's people and monarchy. They have existed for a long time as a result of the filth associated with rat breeding and contaminated water supplies. As witnessed in 1350, if garbage is not adequately managed, it can cause serious harm. The "Black Plague" erupted, killing over 25 million people. Bangladesh's garbage generation rate is growing, and by 2025, it is predicted to reach 47,064 tonnes per day. The rate of waste generation (kg/upper limit/day) is expected to climb to 0.6 by 2025. Wet trash, dry waste, garden waste, E waste, sanitary waste, and home hazardous waste are some of the several sorts of waste [3].

Daniel Hoornweg and Perinaz Bhada-"What Tata's a Waste: A Global Review of Solid Waste Management" examines how the growing urban population is producing a growing number of waste management issues in cities all around the world. Surprisingly, the author discovered that global urban inhabitants produce substantially more waste today than they did ten years ago. While trash output in upper-middle and upper-income countries is predicted to remain stable in 2025, rubbish production in lower- and lower-middle-income countries such as India, Nigeria, and Kenya is expected to more than double [4]. The authors contemplated using a wireless sensor network to keep track of the bin's status. However, the researchers employed Argos mote, which has a geographical coverage of only 430 m and only considers a single parameter for bin status [5].

The total amount of rubbish produced in 2006 was estimated to be around 2.02 billion tonnes, up 7% from 2003. Segregation, treatment, and transportation of waste must all be done properly. To reduce the risk to the public's health and to maintain environmental safety. When garbage is correctly classified, its economic worth is maximised. Poor garbage disposal practises cause serious environmental issues in a given location. Improper waste disposal is defined as the disposal of waste in a manner that has negative environmental consequences. Hazardous garbage thrown in the ground is one example, as is not recycling items that should be recycled [6, 7].

Clean Ahmadabad Abhiyan, Trash-Wise, Mumbai Environmental Action Group, Vatavaran, and Srishti are among the non-governmental groups working in the subject of waste management. They have all succeeded in raising public understanding of their rights and obligations in relation to solid waste management and the cleanliness of their city. These organisations encourage community participation in solid waste management by promoting education and awareness in schools [8, 9].

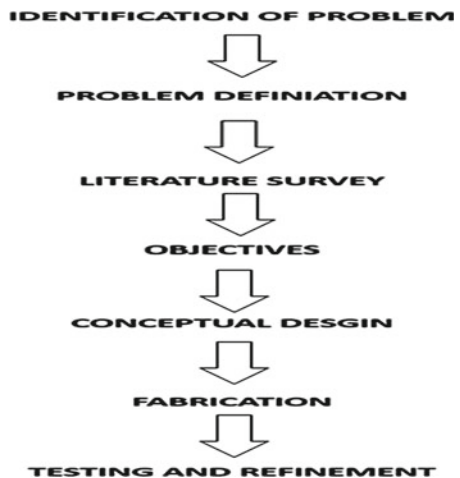
According to the literature, the contemporary population lacks access to proper garbage disposal services, resulting in a waste management issue. The majority of

garbage collected is discarded or leaks into bodies of water, resulting in poor living conditions and a contaminated, unhealthy environment. As part of a smart waste management system, there is no trash sorting technology that may be utilised in homes, offices, or industries. As a result, the current project aims to design and build an automated trash segregator system for various forms of garbage.

2 Methodology

Figure 1 depicts the approach used in this research. The sensation of awareness of a pervasive social problem, a social phenomenon, or a notion that is worth studying—as it takes investigation to understand—is referred to as problem identification. Observation, knowledge, wisdom, and skills are used to identify such a situation. The systematic step that the proposed project will follow to solve a problem is known as problem statement. The main focus of the problem statement will be on the negative aspects of the existing condition and it concentrates on what is leading to it. A literature review is a systematic review of scholarly sources (such as books, journal articles, and theses) that are pertinent to a certain topic or research question. It's frequently written as part of a thesis, dissertation, or research paper to assist you put your work in context with other works. The project objectives are the aims you intend to achieve by the project's conclusion. This could include tangible goods such as deliverables and assets, as well as intangible goals such as improving productivity or inspiring others. At the end of the project, your project goals should be measurable, attainable, time-bound, and unambiguous. Concept research, also known as conceptual design, is a stage of project planning that entails creating ideas and analysing the advantages and disadvantages of putting those ideas into action. In fact, this stage is sometimes referred to as "Ideation" or "Concept Generation." Fabrication is the process

Fig. 1 Methodology adopted for developing automatic waste segregator



of making anything from raw or semi-finished materials rather than pre-assembled parts. To put it another way, it is the process of creating something from the ground up rather than putting something together. The goal of the Testing/Refinement phase is to find any and all issues that prohibit the new application from being utilised in production successfully.

2.1 Requirement Specification

The components used in proposed automatic waste segregator is shown in Fig. 2

Arduino is an open-source computer hardware and software company. The Arduino community is a project and user organisation that develops and uses development boards based on microcontrollers. These development boards are built using Arduino Modules, which are open-source prototyping platforms. For the simplified microcontroller board, a variety of development board packages are available. The most common way to programme is through the Arduino IDE, which employs the embedded C programming language. This gives you access to the Arduino Library, which is constantly growing thanks to the open-source community's contributions.

Moisture is detected using the Moisture Sensor. The sensor's two huge exposed pads serve as probes and act as a variable resistor. It calculates the volumetric moisture/water content indirectly by using some of the object's characteristics as proxies for moisture content, such as electrical resistance, dielectric constant, or neutron interaction. The relationship between the measured property and moisture must be calibrated, and it can vary depending on environmental factors such as electric conductivity, temperature, and so on.

The search coil of a metal detector sends an electromagnetic field into the ground. Any metal objects (targets) that come into touch with the electromagnetic field become energised and produce their own electromagnetic field. Unlike photoelectric

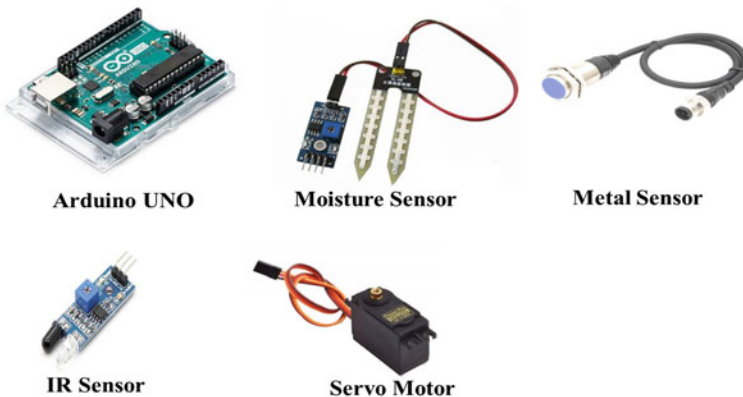


Fig. 2 Components used in automatic waste segregator

sensors, inductive proximity sensors can detect a metal object through opaque plastic. Plastic, wood, paper, and ceramics are not detected as non-metal targets. Because these sensors exclusively detect metal objects, accumulated dust or oil splash on the sensor head has no effect on detection.

To sense a specific phase in the environment, an IR sensor generates and/or detects infrared radiation. Thermal Radiation is emitted by all objects in the infrared spectrum in general. This type of radiation, which is invisible to the naked eye, is detected by the infrared sensor. A detector that reacts to infrared (IR) radiation is known as an infrared detector. The existence of an impediment is detected using infrared sensors.

A rotary or linear actuator with the ability to precisely control angular or linear position, velocity, and acceleration. It is made up of an appropriate motor and a position feed-back sensor. It also demands a sophisticated controller, which is often a separate module designed specifically for servo motors. It can be rotated between 0° and 180° in any direction. By providing a power-width electric pulse to the control pin, the degree of rotation can be regulated.

2.2 Concept Generation and Fabrication

In this phase, four different concepts are generated based on the authors' brainstorming, as shown in Fig. 3. The idea A operates by detecting the type of garbage

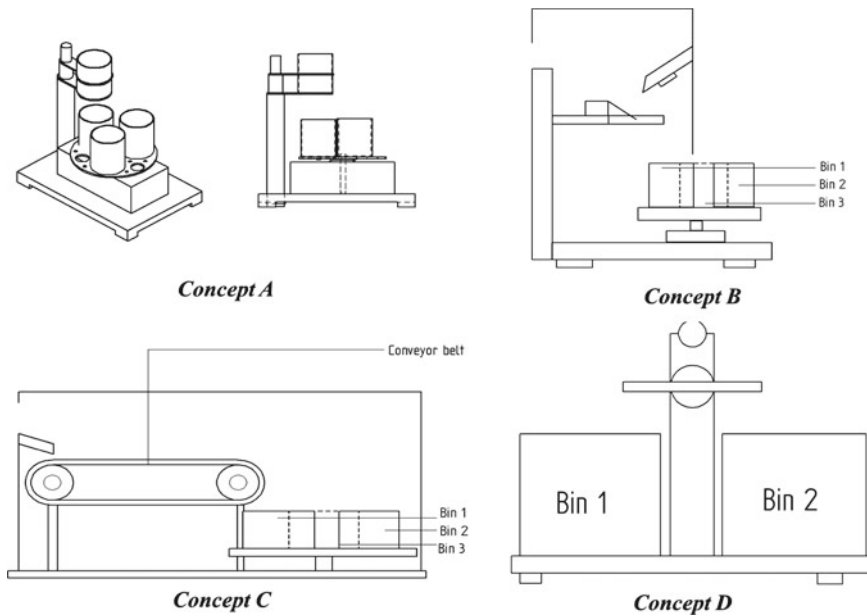
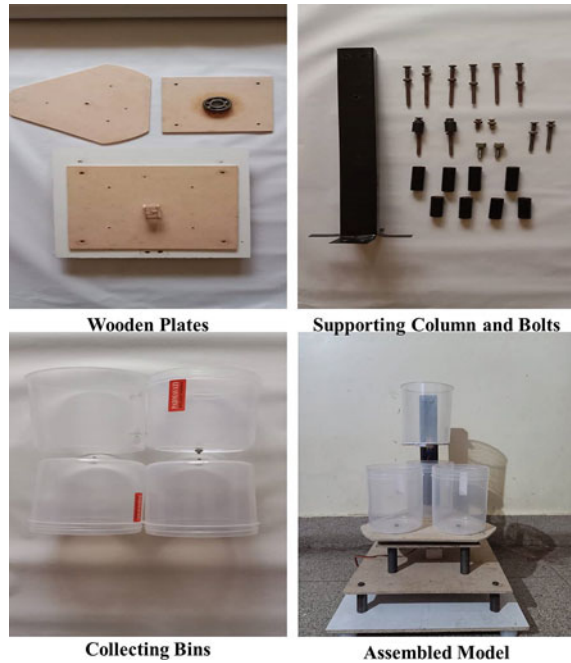


Fig. 3 Concepts generated for automatic waste segregator

Fig. 4 Fabrication of proposed equipment



and then rotating the disc to place the proper container at the disposal site. Concept B is a slightly modified version of concept A that is enclosed and uses an angled sensor for sensing. Concept C uses a conveyor belt to transport waste, whereas concept D uses two bins and a tilting lever to dispose of it. After weighing the advantages and disadvantages of each concept, it was determined that concept A is the best fit for the proposed automatic waste segregator, and fabrication began. Figure 4 depicts the many steps of the proposed machine's fabrication.

3 Results and Discussion

The proposed working model of automatic waste segregator is designed and developed. At the household level, an automatic trash separator has been effectively adopted to separate waste into metal waste, dry waste, and wet waste. Only one sort of waste can be separated at a time, because metal, wet waste, and dry waste have different priorities. Wet, dry, and metal waste were used in the experiment. It is discovered that the capacitance count of wet rubbish changes more, whereas the capacitance count of dry waste changes significantly less. Other objects are identified as dry debris because their relative dielectric constant is moderate. The automatic garbage sorter successfully sorted the waste into glass, metal, moist garbage, and dry rubbish, according to the experimental results. Table 1 shows the results obtained.

Table 1 Results obtained for different types of waste

Sl. No	Metallic waste	Discarded or not
1	Coke tin	YES
2	Nut and bolt	YES
3	Metal scrap	YES
<i>Dry waste</i>		
4	Dry leaves	YES
5	Paper cups	YES
6	Clothes	YES
<i>Wet waste</i>		
7	Wet paper	YES
8	Kitchen waste	YES

4 Conclusions

Various conceptual designs have been developed for automatic waste segregator. The best concept among the proposed concepts is selected. The working model of automated waste segregator is successfully development and demonstrated. The designed automatic trash segregator aids in the management and segregation of rubbish without harming the environment, as well as the segregation of metallic, dry, and wet wastes at the household level. One type of garbage can be separated at a time using the designed technology. The automatic segregation method saves time and effort for humans. The procedure of recycling and reusing becomes simple. The system is completely automated, efficient, time-saving, and simple to operate. We can check on the status of the bins after they've been separated at any moment.

References

1. Damghani, A.G. Savarypour, E.Z., Deihimfard, R.: Municipal solid waste management in Tehran: current practices, opportunities and challenges. *Waste Manag.* **28**, 929–934 (2008)
2. Praveen, Y.T., Byrappa, C.: Design and modelling of automated waste management system with crusher and pneumatic compactor. *Int. Res. J. Eng. Technol.* **7**, 1284–1289 (2020)
3. Naveen, B., Kavya, G.K., Kruthika, S.N., Ranjitha, K., Sahana, C.: Automated waste segregator using Arduino. *Int. J. Adv. Eng. Res. Dev.* **5**, 255–261 (2018)
4. Hoorweg, D., Tata, P.B.: What a waste A global review of solid waste management (2012). <https://doi.org/10.1201/9781315593173-4>
5. Nagaraj, D., Shivaprasad, B., Santosh, H.: Automated waste segregator using renesas microcontroller. *Int. J. Innov. Res. Technol.* **4**, 603–608 (2017)
6. Ranjitha, C., Sarga, V., Sreelakshmi, P.K., Vishnu, S., Arya, P.: Real time waste segregation. *Int. J. Futur. Revolut. Comput. Sci. Commun. Eng.* **4**, 1–3 (2018)
7. Prashanth, H., Ballur, A., Sadapur, D., Ranjanagi, M., Nimbalkar, R.: Design, fabrication and analysis of fully automatic solid waste segregationsystem. *Int. Innov. Sci. Res. Technol.* **3** (2018)

8. Shivakumar, N., Kunwar, A.R., Patel, S. kumar, Pushpa mala, S.: Design and development of an automatic clustered, assorted trash segregation system. In: 2016 IEEE International Conference on Recent Trends in Electronics, Information & Communication Technology (RTEICT) (2016)
9. Sharanya, M., Harika, M., MN, S., Kochuvila, S.: Automatic waste segregator. In: 6th International Conference on Advances in Computing, Communications and Informatics (ICACCI'17) (2017)

Design and Analysis of Car Brake Rotor and Brake Caliper for Efficient Braking



J. Karthik and Manas Kumar Pal

Abstract Road accidents have become very common nowadays. Therefore, safety has become a priority for vehicle drivers as well as passengers. The idea behind this work is to improve the safety parameters of a brake system. There are different reasons why accidents happen and one of them is improper timing of applying brakes by the driver. Any sudden obstacles appearing to the driver leads to panic, and this situation results in accidents as the driver cannot apply brakes in time due to panic. Taking the driver reaction time into consideration, this work leads to modifying the brake design to avoid accidents and hence can increase safety. A car braking system consists of a brake rotor and brake caliper. In this paper, an efficient braking system is presented where the design of the brake rotor and the brake caliper is modified by considering the stopping distance and driver's reaction time. It is seen that the modified design is safe and able to perform efficiently without any failure.

Keywords Brake rotor · Brake caliper · Stopping distance

1 Introduction

The modern automobile is one of the most complex machines on earth with thousands of parts each with specific design functions. Passenger cars have emerged as the primary means of family transportation, with an estimated 1.4 billion in operation. Earlier, automobiles were not as efficient as they are now. Many breakthroughs have come into light with constant research on different components. Though the automobile industry has grown in terms of size and quality, there is still a lot of research and room for development. Safety of the driver and the passengers are the most important factor which is take care during the design of a automobiles. Several authors discussed different types of brake design which can be implemented by the automobile industry [1–5]. Patel et al. [1] has designed and modelled a brake caliper and has calculated the corresponding factors which are important for brakes. These

J. Karthik · M. K. Pal (✉)

School of Mechanical Engineering, VIT-AP University, Amaravati, Andhra Pradesh 522237, India
e-mail: manaspal2015iit@gmail.com

© The Author(s), under exclusive license to Springer Nature Singapore Pte Ltd. 2022
K. C. Popat et al. (eds.), *Advances in Mechanical Engineering and Material Science*,
Lecture Notes in Mechanical Engineering,
https://doi.org/10.1007/978-981-19-0676-3_17

207

included calculation of bore area of master cylinder, pressure at caliper end, area of caliper piston, total force on brake pad by single piston, and clamping force on disc. Vinay et al. [2] studied the design and the analysis of the disc brake rotor and they also studied the thermomechanical analysis of the brake rotor. This paper showed the calculations to find the kinetic energy (K.E.) of the vehicle, the stopping distance of the vehicle, braking force, the angular velocity of the rotor, and the heat flux. These parameters determine the performance of the brake rotor. The factor which has been included in my project is the new and sleek design with different dimensions and materials.

Amrishi et al. [5], studied the brake design and the brake rotors used in this paper are both solid disc rotors as well as a drilled rotor. This paper is only based on the design and analysis of drilled rotors i.e. ventilated disc rotors. These drilled ventilators are placed in a specific and unique way in our design and are very different from the referred papers. The disc used in their paper was slightly bigger with an outer diameter of 381 mm and inner diameter of 125 mm whereas this paper displays the design dimensions with an outer diameter of 256 mm and inner diameter of 153 mm.

The paper written by Shah et al. [3], does not include the thermal analysis of the brake caliper. Their paper has only considered stress distribution and deformation analysis. Our paper is trying to fill this gap by showing the thermal analysis of the brake caliper along with the static structural analysis. Our thermal analysis includes Temperature analysis and Total Heat Flux analysis.

Upon close observation and review of the papers it has been found that several papers discuss the calculations for stopping distance, etc. but the reaction time of the driver has not been considered in most of the calculation. Hence this parameter has been considered in our paper. The reaction time in this paper is taken to be 2.5 s which is considered as the worst-case scenario.

The main objective of this project is to consider the driver reaction time and design an efficient system that can reduce the braking distance as well as the braking time. Also, this project is focused on designing a brake rotor that is structurally and thermally stable when different boundary conditions are placed. Finally, this project aims to analyze the results which are obtained from the analysis of the brake rotor and brake caliper.

2 Design Procedure

2.1 Working Methodology

The working methodology of this type of brake system is simple. It consists of a brake rotor and a brake caliper. Firstly, when the car driver applies force on the brake pedal or applies brakes, these brake pedals push themselves back applying pressure on the brake fluid which is at the end of the brake pedal. Now, this pressure pushes the liquid further and reaches the brake caliper. This pressure builds up or amplifies

as it travels towards the brake caliper following Pascal’s principle. Pistons are placed inside the brake caliper which pushes the brake pads attached to the brake caliper against the brake disc to slow down the vehicle. Therefore, the pressure applied by the driver goes to all four wheels simultaneously and results in slowing the vehicle.

2.2 Design Parameters

Hyundai i20 model with 1510 kg weight and 50 m/s maximum speed are considered for design. Deceleration, stopping distance and stopping time of vehicle is calculated after considering the braking force, kinetic energy and equations of motion. Considering driver reaction time and the stopping distance the required braking force is calculated and both the brake rotor and the brake caliper are newly designed with different dimensions for better performance. The design criteria include the parameters and dimensions used to design the components. The outer diameter of the brake rotor is 256 mm whereas the inner diameter is 153 mm. The ventilated disc rotors help the heat to dissipate faster than the normal one so, for heavy vehicles it is important to have them. In this work, we have considered the ventilated disc.

2.3 Material Selection

Gray Cast Iron is used as a material for the brake rotor because of its high thermal conductivity due to its higher graphite content. Due to its structure, it allows low heat to transfer, therefore, giving it greater life than many other materials. The material used for the brake caliper is aluminum alloy because of its lower weight than other metals, therefore, reducing the overall weight of the car. The properties are given in Tables 1 and 2.

Table 1 Mechanical properties of gray cast iron for brake rotor

Properties	Value	Units
Elastic modulus	6.61787e+010	N/m ²
Poisson’s ratio	0.27	–
Shear modulus	5e+010	N/m ²
Tensile strength	151,258,000	N/m ²
Mass density	7200	kg/m ³

Table 2 Mechanical properties of aluminum alloy for brake caliper

Properties	Value	Units
Tensile yield strength	2.8e+08	Pascals (Pa)
Density	2770	kg/m ³

3 Results and Discussion

3.1 Results for Brake Rotor

When the component is subjected to different loading conditions, the material should be capable of withstanding all the stress and strain. Therefore, for the results to be obtained few boundary conditions are being put on the brake rotor. These boundary conditions include load and pressure which have different directions. For this project, the worst-case scenario is considered where the load is 400 Newtons which is acting along the 'Z' axis whereas the pressure is 1,000,000 N/m² acting normal to the brake rotor under static structural analysis.

Von Mises Stress Analysis of Brake Rotor

Von mises stress is a value to determine whether a given material will yield or fracture. It is mostly used for ductile materials such as metals. The von-mises yield criterion states that 'if the von mises stress of a material under load is equal or greater than the yield limit of the same material under simple tension then the material will yield.

Figure 1 represents the von-mises stress of the brake rotor when the load of 400 N and pressure of 1,000,000 N/m² are applied on it. It also shows the maximum and minimum stress experienced by the brake rotor where the maximum stress is 3.893e+007 N/m² whereas the minimum stress is 2.100e+004 N/m². As the stress reaches a higher value, the color of the component in the analysis changes from blue to red. Different parts of the component experience different stress such as the middle part of the rotor. It experiences higher values of stress as it is fixed to the wheel and

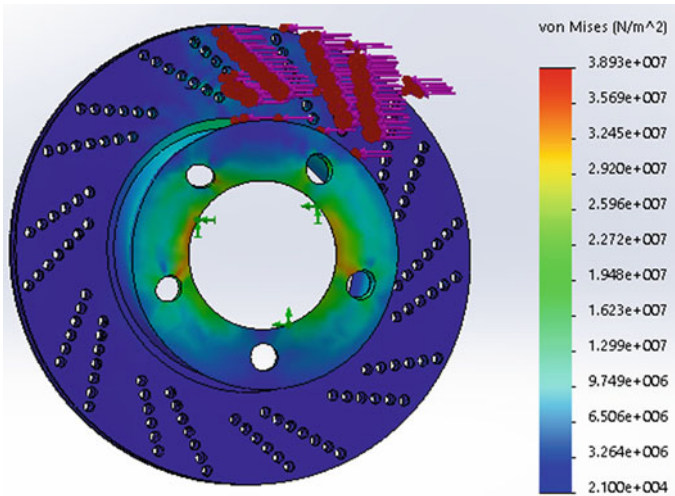


Fig. 1 Von mises stress analysis of brake rotor

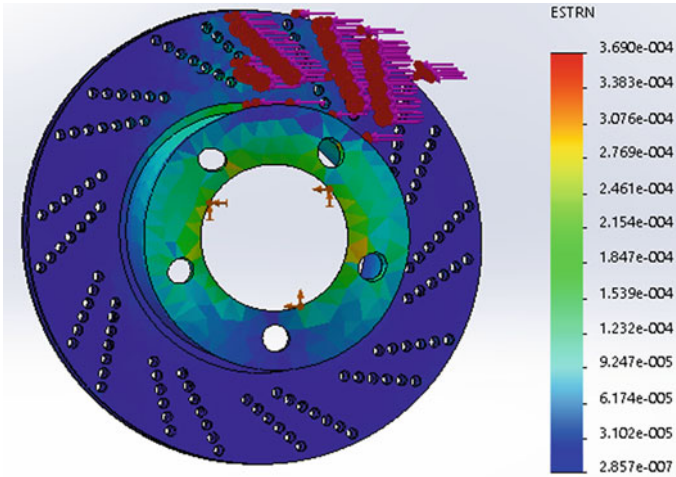


Fig. 2 Equivalent strain analysis of brake rotor

shows chances of deformation. The green part represents that the component has an average impact on that part.

Equivalent Strain Analysis of Brake Rotor

Equivalent strain is a scalar quantity and is also called von mises equivalent strain. It has no units and is the ratio of change in length to actual length. The results can be seen in the figure where the maximum and minimum values are shown. The strain does not have any units and therefore is a constant.

Figure 2 shows the equivalent strain analysis of the brake rotor under various loading conditions. It represents the values ranging from minimum to maximum with colour coding. The blue colour represents parts with low stress whereas the red colour represents high stress. As the value increases, the colour changes from blue to red.

In this analysis, the minimum value of the strain occurs on the disc of the brake rotor with the value $2.857e-007$. The maximum strain occurs at the part where the brake rotor is fixed i.e., somewhere in the middle of the brake rotor with the value $3.69e-004$. This happens because when the brakes are applied, the brake pads press against the brake rotor during its rotation therefore, the part where it is fixed is the most affected.

Displacement Analysis of Brake Rotor

Displacement plots are similar to contour plots but simpler in terms of plotting, they show the deformed model geometry either alone, with the undeformed edge, or overlaid on an outline of the undeformed geometry. These displacement plots are particularly useful for reviewing the mode shapes from the modal analysis.

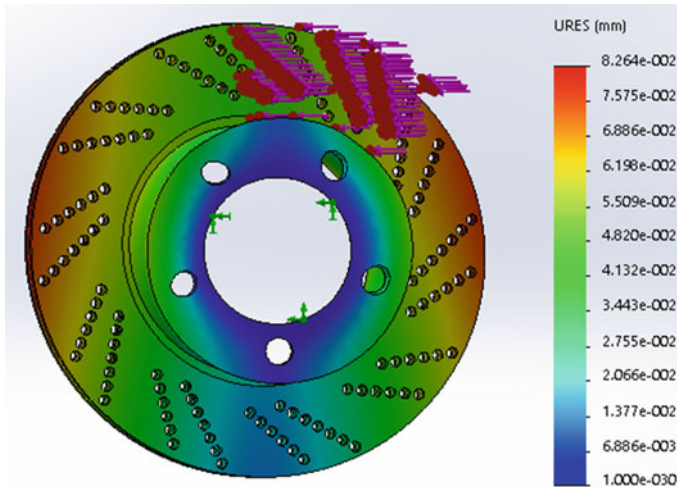


Fig. 3 Displacement analysis of brake rotor

Figure 3 shows the range of values which are in between maximum and minimum values which are $8.264e-002$ and $1.000e-030$ mm respectively. In the picture, it can be observed that this range of colours is evenly distributed throughout the component whereas the highest displacement is only seen on the corners of the brake rotor. This is because most of the loads are acting towards the ends.

3.2 Results for Brake Caliper

In this section, both structural analysis and thermal analysis have been performed on the component to obtain the corresponding results.

Total Deformation Analysis of Brake Caliper (Static Structural analysis)

In simple words, total deformation analysis shows all the parts where the deformation has occurred on the component. Here, this deformation is represented in the form of colours, and values are mentioned corresponding to the colours. Loads are applied to the brake caliper to obtain the results. Two forces of 1241.1 Newtons each are being applied in the opposite directions on the inner side of the brake caliper. These forces are applied in such a way because when the brake pads press against the brake rotor during braking, the resultant force acts normal to the force applied.

Figure 4 shows the parts of the components where the deformation occurred. The component is colour-coded where the blue colour shows the parts with minimum deformations whereas the red shows the parts with maximum deformation. As the deformation values increase, the colour changes from blue to red. In Fig. 4, the part where the brake pads are pressed against the brake rotor shows the maximum

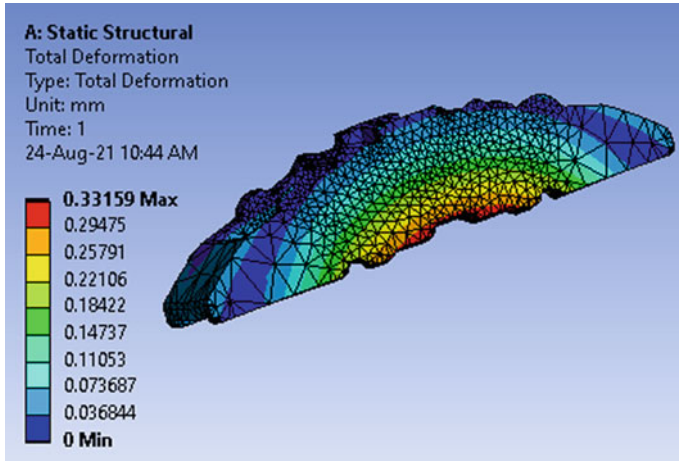


Fig. 4 Total deformation analysis of brake caliper

deformation as most of the force is taken by that part. The rest of the brake caliper shows minimum deformation. Here as shown in Fig. 4, the maximum deformation occurred is 0.33159 mm.

Equivalent Elastic Strain Analysis

The equivalent elastic strain can be defined as the limit for the values of strain up to which the object will rebound and come back to the original shape upon removal of the load. It does not have any units, therefore, it is a constant.

Figure 5 shows different values each corresponding to a different colour. It shows that the component has a minimum elastic strain in all parts. Here, the maximum and minimum values are 0.015212 and 2.1229e−8 respectively. This means when the brakes are applied, the brake caliper experiences minimum elastic strain for this particular material.

Total Heat Flux

Heat flux is also referred to as heat flux density or heat-flow density. It is the flow of energy per unit of area per unit of time. Its units are watts per square meter (W/m²) (Fig. 6).

For the brake caliper, the total heat flux is minimum throughout the length whereas, it experiences a little higher heat flux in the ends showing in colours light blue and green. Also, the inner sides of the component are affected with higher than minimum heat flux. Nowhere with the current load maximum heat flux is experienced by the brake caliper. The minimum heat flux is 2.4242e−7 W/mm² and the maximum is 9.5012 W/mm².

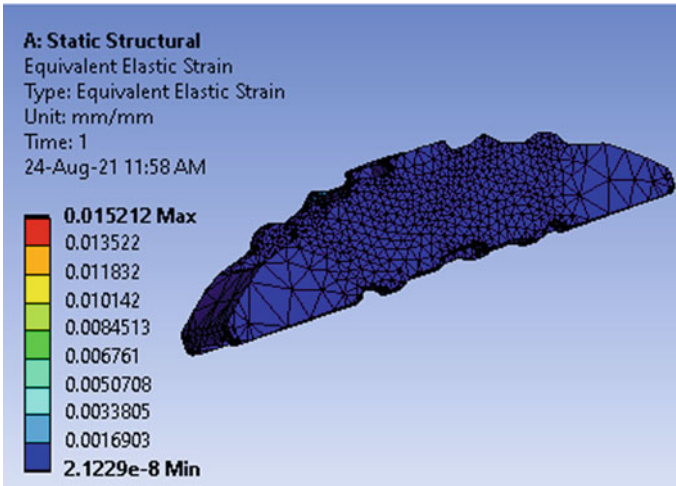


Fig. 5 Equivalent elastic strain analysis of brake caliper

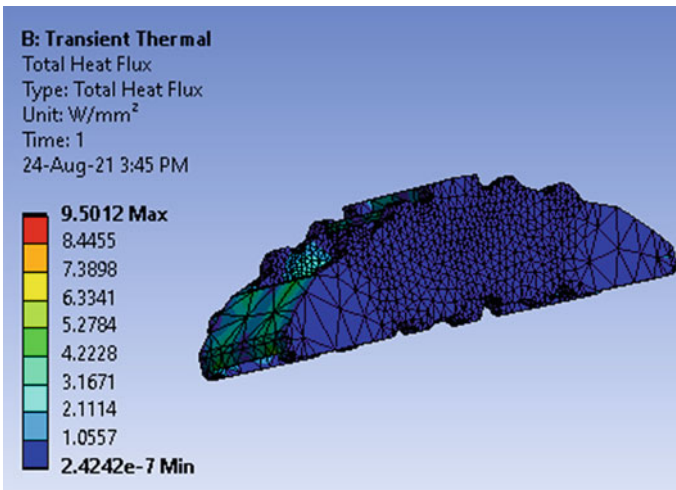


Fig. 6 Total heat flux analysis of brake rotor

4 Conclusion

The brakes are the most important component of a vehicle and one of the main mechanisms which are taken into consideration when safety is considered. The main objective of this work is to design an efficient system that can reduce the braking distance as well as the braking time. This project shows the new design and analysis of the brake rotor and brake caliper in detail. The braking time and braking distance are

considered during the design of the brake rotor and the brake caliper. These are done through calculations including various parameters such as the driver's reaction time. The brake caliper has also been designed which has the capability to press against the braking pads and stop the car at a lesser time than normal. All the components are made of Grey Cast Iron and analysis is done with various boundary conditions. The results show that the newly designed disc brake rotor and brake caliper would be suitable for implementation.

References

1. Prof. Patel, M., Patel, M.R.J.: Design of disc brake's rotor. *Int. J. Eng. Develop. Res.* **4** (2016)
2. Naik, V.K.M., Ramesh, K.M.: Design of effective hydraulic braking system for formula motorsport car. In: *IOP Conference Series Materials Science and Engineering* (2018)
3. Shah, R., Shah, C.: Design and analysis of hydraulic brake calipers. *Int. J. Mech. Eng. Technol. (IJMET)* **8** (2017)
4. Golhar, S.P., Rakhonde, A.R.: Design of Brake Caliper, Department of Mechanical Engineering, *International Research Journal of Engineering and Technology (IRJET)*, Volume-6, 2019.
5. Amrishi, P.N.: Computer-aided design and analysis of disc brake rotors. *Adv. Automob. Eng.* **5** (2016)

Effect of Impact Angles on the Frontal Structure of a Vehicle



Rudolf Ragis, Akshaykumar Khatane, Kesav Chandran, and P. Baskar 

Abstract Recent initiatives by organizations such as Global NCAP have revealed that the sub-par standards of safety of the Indian automobile market had conformed to. The base model vehicles from our manufacturers could not conform to the international crash test standards. Thus, the study of the crash and its effect is imperative. This work is an attempt to analyze the crash by varying the angle of impact and the velocity of impact. The idea behind the variation in the angle of impact is based on the response to an approaching threat. On seeing an approaching obstacle, the driver might swerve and crash the vehicle in at an angle. This is an attempt to analyze the crash by varying the angle of impact and the velocity of impact. The current research also looked at the variation brought on by material. A standard Front structure of a chassis is modeled and is meshed in ANSYS. It is then put under the required loading conditions and variations are recorded based on the angle of impact, velocity and material.

Keywords Crash test · Angle of impact · Frontal structure

1 Introduction

Alekhya et al. [1] reports that, in recent years, the main purpose of Automobile sectors have transformed into altering the design features of a vehicles regularly, for instance, the chassis, braking system, suspension system, air bag, seat belt and others. The motive of the vehicle designer is to mitigate the probability of susceptible injuries during varying impacts of collision. There is an increasing average Global Road Crash Rate of 3700 deaths per day as per world health organization road safety report 2018. To initially alleviate the fatality rate, experimental and virtual analysis study the car dynamics, velocity, repercussions of a vehicle collision, crash sensors, and personal injuries. The speed of the vehicle is the key factor which increases

R. Ragis · A. Khatane · K. Chandran · P. Baskar (✉)

School of Mechanical Engineering, Vellore Institute of Technology, Tamil Nadu, Vellore 632014, India

e-mail: pbaskar@vit.ac.in

the risk of the crash and severity of injuries and that could possibly result in death. Only 46 countries have laws to meet the speed criteria of the vehicles. As most of the countries don't have set speed limits, especially at high speeds it is necessary to decelerate and control the vehicle in order to avoid fatal crashes.

Safety of a vehicle has become a primary concern for the automotive industry, especially in the recent years, with the increase in the number of cars on the road and the awareness of the public towards the lack safety norms of the vehicles compared to global market. Thus, it is of utmost importance to provide for life saving technologies and designs for the automobiles that are to run on roads. For a safe design, an energy absorbing structure is required to reduce peak force by gradual dissipation of force over time.

In the early years, crash safety evaluations of a vehicle were conducted using manufactured prototypes. This was both time consuming and expensive. The advancements in the computing and simulation have made it possible to perform safer and more economical analysis on the vehicles. To put in perspective a single regulation in 1985 would have to have 150 prototype cars to be required to destroy to yield result as FE model size was 10,000 Elements. Comparing it to just 20 years down the line, 20 Regulations are checked using only 20 prototypes as the FE Model size crosses 5 million elements. Thus it is much easier to perform crash test on various structures and chassis without actual destruction of prototypes. This procedure is carried out in stages, i.e. Modelling and Analysis. The Model creation is done using various tools/software. Kiran et al. [2] considered the various types of car body structures and modelled in CAD and crash analysis is done in ANSYS software. Aluminum and Concrete are considered as materials for car body and wall respectively. Car outer body and wall is modeled in SOLIDWORKS. A SOLID186 Element is used as it is higher order 3D with 20 nodes. This element supports large deflection, plasticity, large strain capabilities, hyper elasticity, stress stiffening, and creep.

Kirkpatrick et al. [3] modeled an existing vehicle in a short time digitization was carried out. The first step in digitization of the car model was to find the mass and locate the center of mass of the vehicle. Then, the non-structural parts were removed and weighed. The vehicle was stripped down to its structural components for the digitization process. A global coordinate system was needed as the vehicle had to be moved multiple times during the process. The vehicle was also rested on blocks that were inserted directly beneath the frame, thus removing the movement caused by suspension. Digitization was performed using a Faro Arm 3D coordinate measuring instrument. After digitizing the exterior surfaces, the body panels were detached and the newly exposed internal surface was also digitized. Finally, the body was fully detached to expose the frame, suspension and drivetrain. The engine was considered as a rigid body in the finite element model. Hyper Mesh pre-processing software is used to scan the model statically before starting the simulation.

Any analysis is as good as its mesh and boundary condition. A smarter meshing of the vehicle structure will lead to less load and solving time and more accurate results. Therefore, in certain cases altogether different software is used for meshing. The type of element used for meshing the structures also defines the behavior of the model.

Modelling and meshing of the chassis use SOLID45 element for the modeling of solid structures and shell63 element for shell as both bending and membrane properties are available.

Atahan et al. [4] model was generated using True Grid mesh generation program and LS-DYNA 3D finite element code was used for crash simulations. The vehicle model contained 125,000 nodes with 25,000 brick elements and 88,000 shell elements. The simulations showed a good correlation with the crash test and component tests, except for time of response. This was attributed to approximations in the modelling of bumper isolators and engine mounts.

Material selection is an integral part of the design procedure and analysis procedure as well, as the variation in material yields different results leading to changes in design on iteration. Comparing isotropic metals to composite materials drastically changes the design on the vehicle. Side impact beams made of composites may help to increase protection during lateral impact, by virtue of their high energy absorbing capacity. Injuries in rollover incidents can be reduced by using material with high strength-to-weight ratio. Yadav et al. [5] found that crashworthiness of vehicle structure made of carbon composite and E Glass composite, with a much lower weight, was superior to typical structural steel and aluminum alloy.

Marzbanrad et al. [6] analyzed the front bumper beams made of aluminum; glass mat reinforced thermoplastic and high strength sheet moulding composite. They compared using impact simulation. The results showed that the high-strength sheet moulding composite minimized the deflection, impact force and stress distribution of the damping beam, and maximize the elastic energy.

According to Ambati et al. [7] it is critical to simulate the right conditions for the right results. The idea behind the variation in angle of impact is based on the response to an approaching threat. On seeing an approaching obstacle, the driver might swerve and crash the vehicle in at an angle. Thus, at the obstacle or the wall has to be at an angle from the center line of the front impact structure. Fixing the rear mounting point and providing the velocity to the entire structure towards the inclined wall will solve the problem. The velocity given is found as the component of velocity of the vehicle going straight. The angled impact is simulated at $+0^\circ$, $+5^\circ$, $+10^\circ$, $+15^\circ$, $+20^\circ$, $+30^\circ$, $+40^\circ$ and $+50^\circ$. Both positive and negative angles are considered because the vehicle models are not laterally symmetric. The offset impact is carried out at 20%, 40%, 60%, 80%, 90% and 100% overlap.

Abdel-Nasser et al. [8] found out on observing the effects on design by using deflection as a major criterion. The Energy stored in the material is also a crucial indication of ability of energy dissipation. Results are taken as mass of the geometry using various materials listed previously. Energy absorbed by the materials play an important part in safety during the simulation. Total energy is measured as well. But the specific energy of each material is the real measurement of the energy absorption. Thus, deflection/deformation and the energy stored in the material together give an accurate idea of what the intensity of the crash would be.

2 Methodology

Behaviour of a design before its manufacture is a very important trait to study, as sometimes desired traits are achieved only after previous tries. Since it is not possible to manufacture every iteration of the design, it is analysed using various methods. Theoretical analysis and Computerised simulation cum analysis are the two basic methods by which most of the design are analysed in recent years. Moreover, complicated designs are not always easy to be analysed by manual analytical calculation. Therefore, computerized analysis is widely used in most industries and engineering design works. There are various software available for analysis. Some of the most commonly used are Hypermesh, Abaqus, Autodesk Simulation, Ansys, NASTRAN and LS-DYNA.

Ansys is selected as software for the current analysis. Selection of module purely depends on the type of analysis to be performed on the component, whether it is thermal, magnetic, Dynamic, Static or Structural. In the current case the vehicle crash is a highly nonlinear transient dynamics phenomenon [9]. Therefore Explicit Dynamics is a natural selection for the Analysis. The Explicit Dynamics module requires part input in the form of material data and part geometry. Ansys itself has a large library of a variety of materials with different applications; it also has an option to add library or materials into the library. This gives us the freedom to add as many materials as needed.

The Part geometry can be imported from various software including Autocad, CATIA, and in Creo. However it is possible to link the Creo geometry file to ansys for faster alterations and analysis, providing a seamless experience of design and analysis. Even Ansys provides a Designing interface for modelling, Known as the Design Modeller. The Models which were designed for the research were designed in Creo as it is shown in Fig. 1. The inclusion of angle between the wall and the

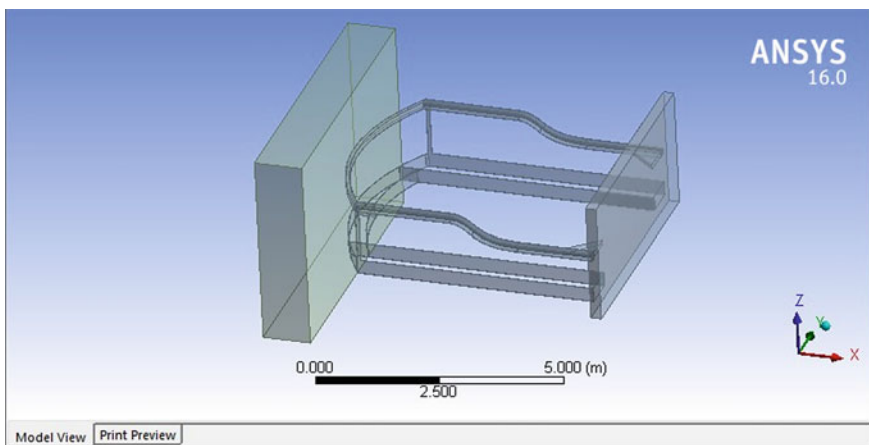


Fig. 1 Design modeler interface

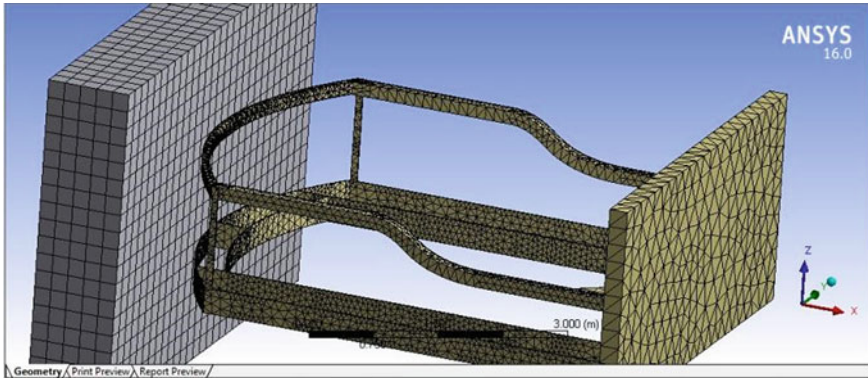


Fig. 2 Mesh generated model (Nodes: 11,625, Elements: 25,747)

Impact structure is done during the assembly after the modeling. Various assemblies varying in angle of offset 0° , 10° , 20° and 30° are saved in STP format.

The Part is then discretized or meshed into smaller elements and it is viewed in Fig. 2, to ease analysis, the areas around the curves and the step areas are taken care of specially to provide proper results for the analysis, since these areas are the areas where stress behavior is different [10] and is to be studied properly, as there are many substructures such as ribs and reinforcements.

Any analysis is as good as it's boundary conditions, the closer to real life the better the results is. So Boundary conditions are important factor in the analysis. Ansys provides a wide variety of tools for the application of boundary conditions. The wall is given fixed support at the bottom as planted on the ground. The impact structure is restricted the vertical movement using displacement condition as 0. The impact structure is given the velocity in the angle specified in the assembly. That is maintained using a local coordinate system to provide the velocity along the x axis. This changes in every assembly as changed. This ensures the closeness to the real life operating conditions. The analysis starts at the moment of contact, thus the impact force is seen low.

The front structure of the vehicle is subjected to impact from various angles [11]. The modelled front structure is assumed to be made of aluminum alloy. This is made to impact a steel wall at a velocity of 100 m/s. Solutions were obtained using LS-Dyna solver in ANSYS workbench. The results required for the analysis were to observe the stress and deformation and verify the safety of the components.

The results are then taken in the form of highest values along with the graphical representation of the stress, deformation and strain. This representation is very helpful in understanding the stress behavior of the component which in turn is very useful for the designer to understand the crash and failure of the component [4]. Deformation is necessary as it gives us the idea of the safety of the survival cell.

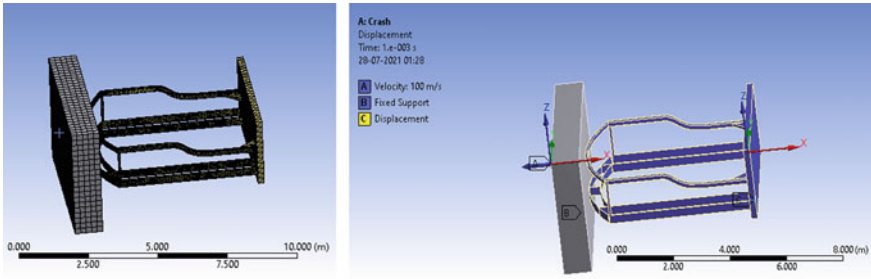


Fig. 3 Crash analysis at an angle of 0°—meshed structure with boundary condition

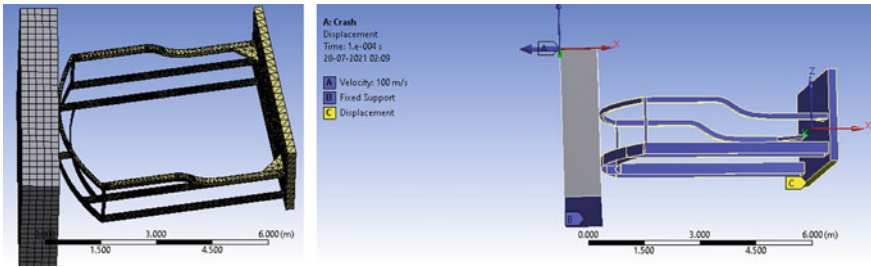


Fig. 4 Crash analysis at an angle of 10°—meshed structure with boundary condition

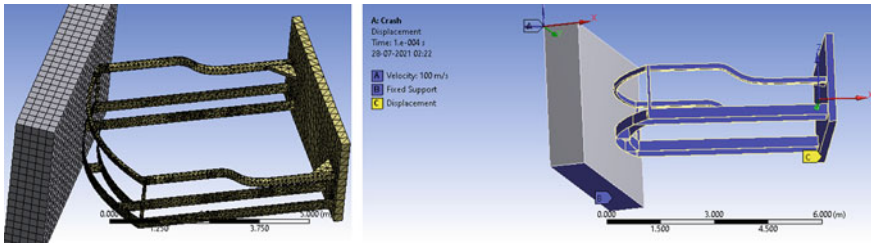


Fig. 5 Crash analysis at an angle of 20°—meshed structure with boundary condition

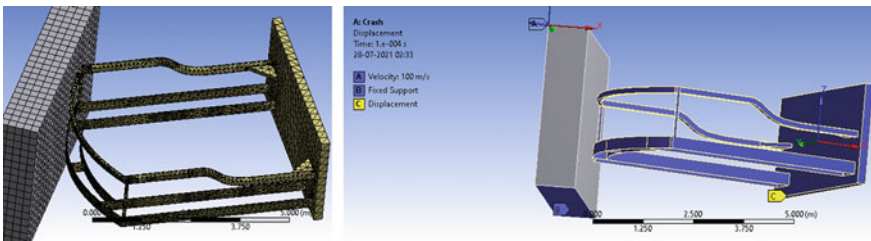


Fig. 6 Crash analysis at an angle of 30°—meshed structure with boundary condition

In order to analysis the vehicle body structure at different angle of impact the model is made in Creo and imported into Ansys. Figures 3, 4, 5 and 6 shows the meshed structure and boundary conditions at 0°, 10°, 20°, and 30° impact.

3 Results and Discussion

The area of Safety and crash analyses has grown by heaps and bounds in the past few decades. The advancement in Computing and Simulation has made it possible to perform safer, and move economic analysis. With the advancement in computing technologies it's the only becoming more and more realistic to simulate so many modal Points and the growth has been exponential. It is now entirely possible to extremely realistic conditions and situations to study mean. All that is required is a Computer powerful enough to do so.

The Introduction of composite material to Automobiles in the past 2 Decades has revolutionized Safety in high and Race cars and formula Cars Soon his will be Seen in the vehicles of the future. Due to me focus of greener lighter and more efficient vehicles. The Constant Development in Active Safety Systems has silently but surely saving lives with the drastic elimination of human Error factors from the vehicle. CAS, ABS, ACC, is some examples of the lifesaving Safety systems.

3.1 *Crash at Zero Degrees*

The results of analysis are exhibited in Fig. 7. The stress values are shown at the end time instant. It was observed that the end time of analysis plays a vital role in the results displayed and the computing time. The deformation difference between the end times is because the structure keeps moving with the velocity even after 0.0001 s. The lower value of stress at 0.001 s is due to the plastic deformation.

3.2 *Crash at 10°*

Figure 8 shows the crash analysis at 10°. The Angle offset leads to lower stress as the deformation is marginally higher. As there is no direct impact on the rib the stress concentration is lower. This is marginally safer as the non-reinforced lower structure absorbed energy for plastic deformation.

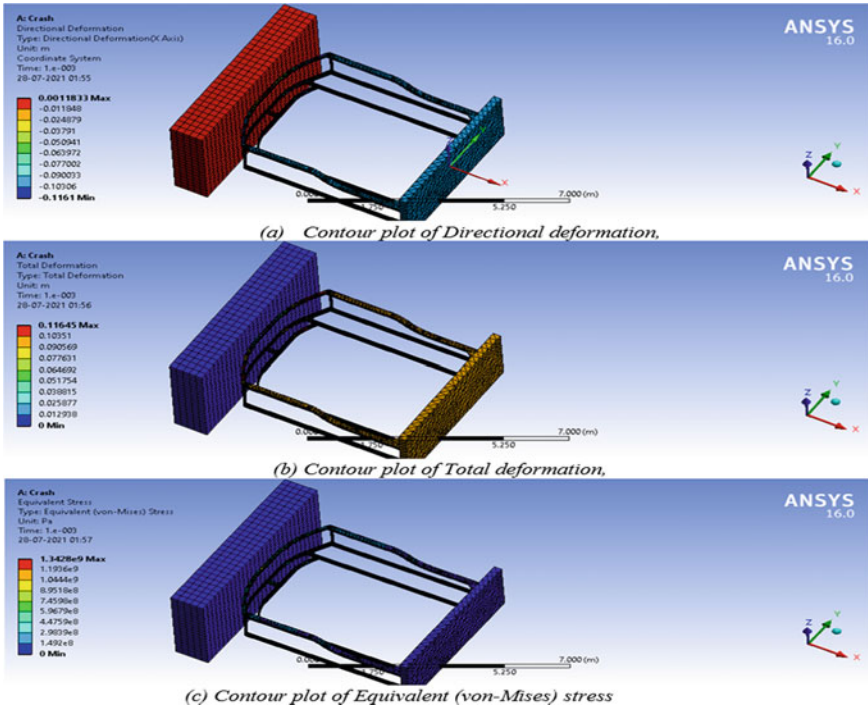


Fig. 7 Contours of crash analysis at zero degrees

3.3 Crash at 20°

Figure 9 shows the crash analysis at 20°. The angle offset leads to lower stress as there is no direct impact on the rib. The non-reinforced lower structure is deformed over a large area.

3.4 Crash at 30°

Figure 10 shows the crash analysis at 30°. The angle offset is such that the impact is on the area where the structure changes shape and direction on the upper structure and the left side rib is directly impacted on the lower structure. This leads to high stress concentration and low deformation. This is unsafe as the reinforcement will not crumple and thus transfer the shock of the crash.

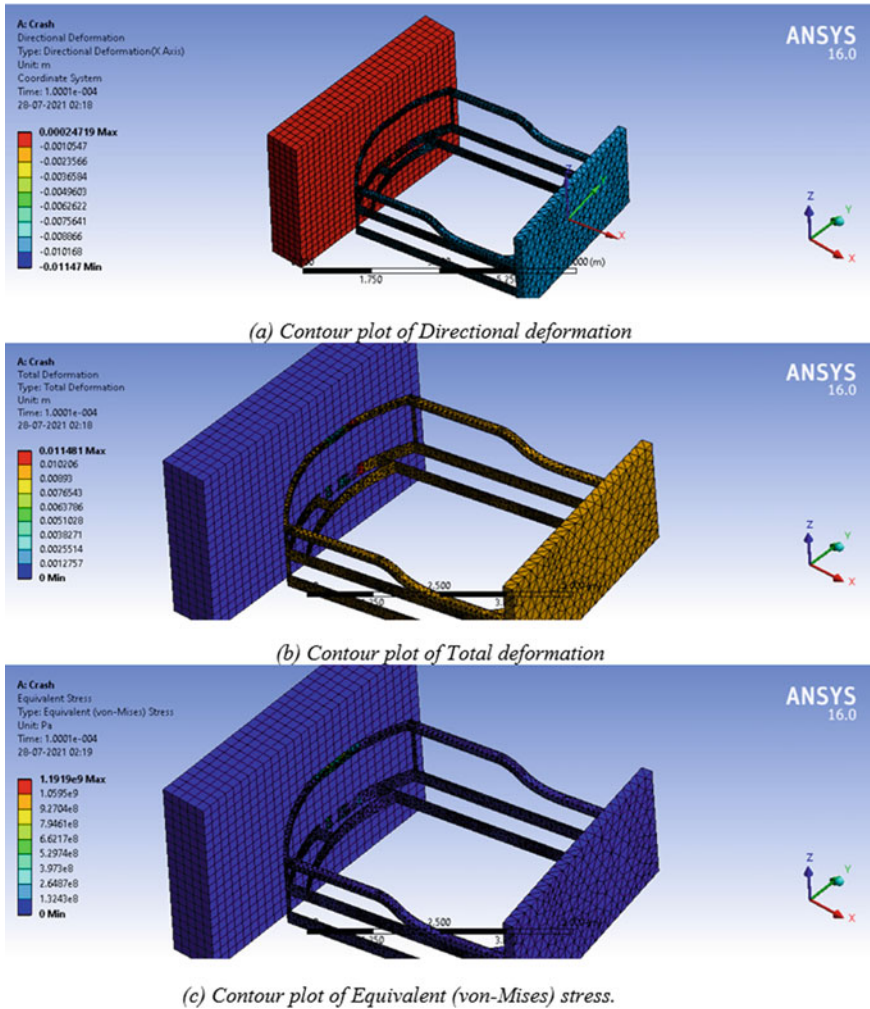


Fig. 8 Contours of crash analysis at 10°

4 Conclusions

Results from the analysis show that the higher angles of impact can slow down dissipation of energy and reduce severity of impact. The Convergence could not be reached due to lack of computing power. Based on the analysis performed here, the following conclusions can be drawn:

- The angle offset has the impact on the crash. It alters the area of the impact zone. Although the complexity of the design suggests that assumption is not advised, but on analysis it is observed that the more the area is in contact with the obstacle

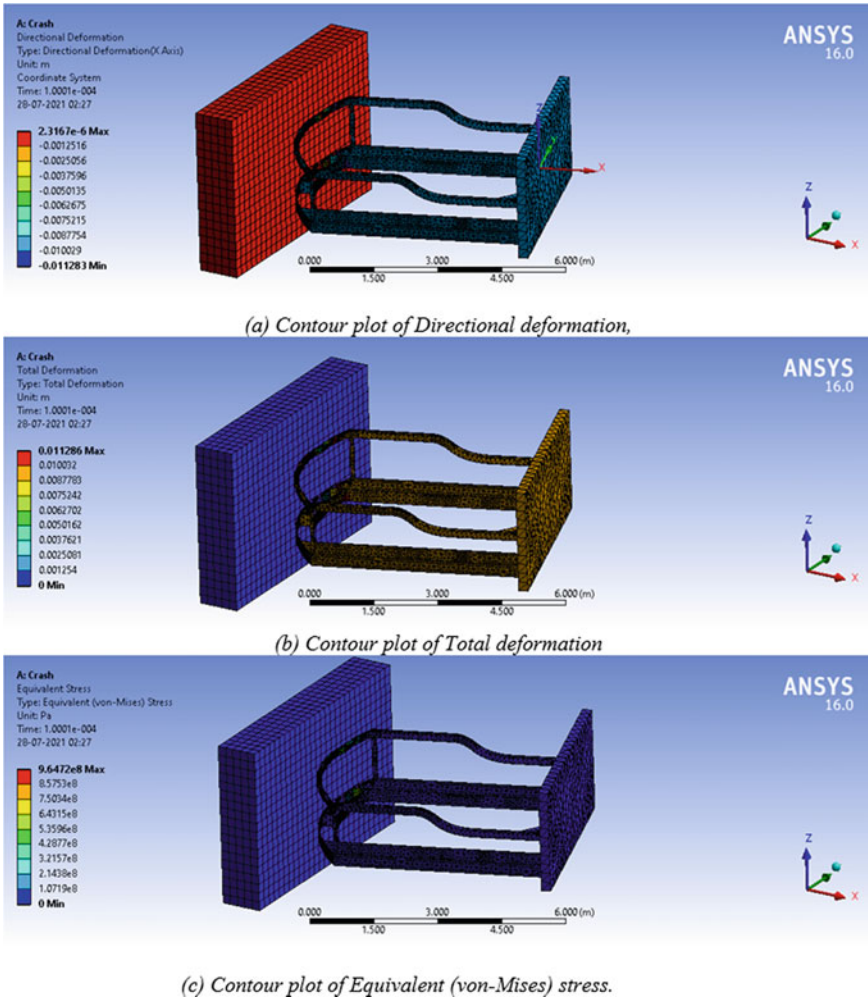


Fig. 9 Contours of crash analysis at 20°

the more the area of dispersion will be high which will lead to lower value of stress. The angle of Impact has a major effect on crash [12]. The structures that come in first contact with the obstacles vary with the angle of Impact and this leads to different in crash performance.

- However, it cannot be generalized for complex structures, as there are many sub structures in a total structure which provide strength and rigidity, and it is difficult to predict which angle will lead to a contact with the substructure. Complexity of frontal structures of different vehicle due to difference in design will cause varying performance and it cannot be generalized at which angle the crash is likely to have less Impact.

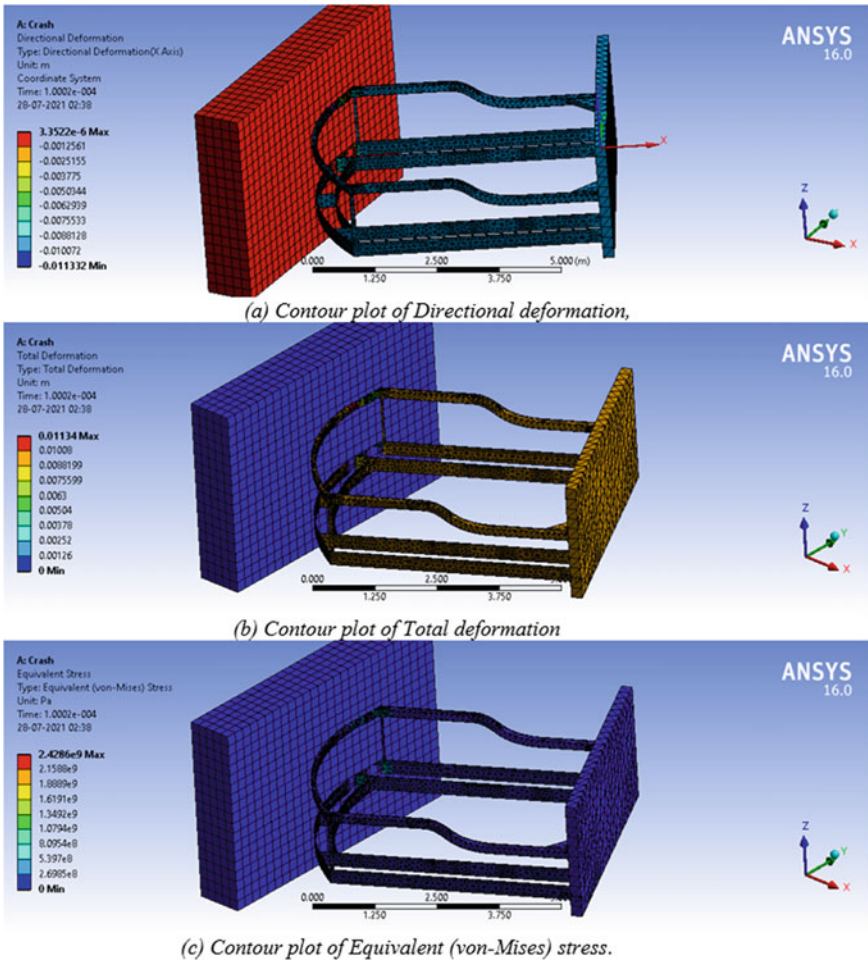


Fig. 10 Contours of crash analysis at 30°

- It is observed from the results of the research that, when the deformation is high the stress is low and vice versa.
- The dissipation due to plastic deformation plays a major role in the safety of the vehicle. Crumble zone plays a major role in the front impact safety. Here too the zones/structure which deform more are seem to have induced less damage to the structure connected to it.
- It's also not proper to predict a trend that an increase or decrease of the impact angle, the stress will be high or low due to the placement of substructures and reinforcement. The support structures such as ribs and reinforcements should be rigid enough to take the impact. But they should also be able to collapse at high stress so as to not transfer the load to the passengers.


- Due to complexity of design it is not advisable to assume but on analysis it is observed that, more the area in contact with the obstacles better the dissipation of energy leading to Lower values of stress.

References

1. Alekhya, G.N., Abhishikt, C.B.N.S., Ramachandran, B.: A recent investigation on design aspects of vehicle crash analysis in India. *Mater. Today Proc.* <https://doi.org/10.1016/j.matpr.2020.07.713>
2. Kiran, C.S., Sruthi, J., Balaji, S.C.: Design and crash analysis of a passenger car using ANSYS workbench. *CVR J. Sci. Technol.* **13**, 96–100
3. Kirkpatrick, S.W., Simons, J.W., Antoun, T.H.: Development and validation of high fidelity vehicle crash simulation models. *Int. J. Crashworthiness* **4**(4), 395–406. <https://doi.org/10.1533/cras.1999.0114>
4. Atahan, A.O.: Vehicle crash test simulation of roadside hardware using LS-DYNA. A literature review. *Int. J. Heavy Veh. Syst.* **17**(1), 52–75
5. Yadav, S., Pradhan, S.K.: Investigations into dynamic response of automobile components during crash simulation. *Proc. Eng.* <https://doi.org/10.1016/j.proeng.2014.12.404>
6. Marzbanrad, J., Alijanpour, M., Saeid Kiasat, M.: Design and analysis of an automotive bumper beam in low-speed frontal crashes. *Thin Walled Struct.* <https://doi.org/10.1016/j.tws.2009.02.007>
7. Ambati, T., Srikanth, K.V.N.S., Veeraraju, P.: Simulation of vehicular frontal crash-test. *Int. J. Appl. Res. Mech. Eng. (IJARME)* **2**(1), 37–42
8. Abdel-Nasser, Y.A.: Frontal crash simulation of vehicles against lighting columns using FEM. *Alexandria Eng. J.* **52**(3), 295–299. <https://doi.org/10.1016/j.aej.2013.01.005>
9. Belingardi, G., Obradovic, J.: Design of the impact attenuator for a formula student racing car: numerical simulation of the impact crash test. *J. Serbian Soc. Computational Mech.* **4**(1), 52–65
10. Supriya, B., Venkat Prasat, S.: Static, modal and impact analysis of car bumper using varied parameters. *Int. Res. J. Eng. Technol.* **8**(03), 111–119
11. Bhardawaj, S., Sharma, R.C., Sharma, S.K.: Analysis of frontal car crash characteristics using ANSYS. *Mater. Today Proc.* **25**, 898–902
12. Pal, C., Narahari, S., Vimalathithan, K., Manoharan, J., Hirayama, S., Hayashi, S., Combest, J.: Real world accident analysis of driver car-to-car intersection near-side impacts: focus on impact location. Impact Angle and Lateral Delta-V. Society of Automotive Engineers, SAE Technical Paper 2018-01-1328

Finite Element Analysis of High-Density Polyethylene (HDPE) Nanocomposite for Potential Use as Dental Implant



Mayank Dey, Rahul Vamsi Katabathuni, Nitesh Dhar Badgayan,
and Santosh Kumar Sahu 

Abstract The present investigation is oriented towards finite element analysis of High Density Polyethylene (HDPE) based polymer nanocomposite for potential usage as the dental implant. The polymeric nanocomposite was 0.1CNT/HDPE was chosen for the dental implant analysis. The modelling of the implant was carried out in CATIA V5 R20 software, and the analysis was performed using commercial FEA (Finite Element Analysis) software i.e. Ansys Workbench 2019 R1 GUI. The structural analysis was performed at various loading condition i.e. 50, 100, 150, 200, 250 and 300 N. The results indicates that the equivalent Von-Mises stress at 50 N was 8.6 MPa increased to 500.5% when the load increased to 300 N. Similar trend was observed for contact pressure and load. It is also noted that the equivalent Von Mises stress results are below the yield stress of 0.1 CNT when the load is below 250 N. It has potential application as dental implant material when bite force value below 250 N.

Keywords High density polyethylene · Nanocomposite · CNT · Ansys workbench · Finite element analysis · Equivalent Von-Mises stress · Bio-implant material · Dental implant

1 Introduction

Biomaterials are a unique material that is proposed to interact with bio-based systems without triggering any major side effects or ailments [1, 2]. The application includes joint replacement, bone cement, heart valves, stents, contact lenses, surgical clips, dental implants etc. [3, 4]. Among the different bio-materials available, polymeric based material specifically, HDPE based thermoplastic polymer is the prime choice

M. Dey · R. V. Katabathuni · S. K. Sahu (✉)

Department of Mechanical Engineering, Amrita School of Engineering, Amrita Vishwa Vidyapeetham, Bengaluru, India
e-mail: sksahumech@gmail.com

N. D. Badgayan

Centurion University of Technology and Management, Bhubaneswar, Odisha, India

© The Author(s), under exclusive license to Springer Nature Singapore Pte Ltd. 2022
K. C. Popat et al. (eds.), *Advances in Mechanical Engineering and Material Science*,
Lecture Notes in Mechanical Engineering,
https://doi.org/10.1007/978-981-19-0676-3_19

229

due to specific properties like non-corrosive, high hardness, superior impact strength and easily formable [5, 6]. In addition, it is also biocompatible, chemically stable and well-tolerated with surrounding tissue [7]. The application of virgin HDPE polymer hinders in many fields, including dental implant due to lower wear [8], mechanical [9, 10], rheological and thermal properties [11, 12].

The lacuna is fulfilled when suitable nanofillers are added with a virgin polymer matrix [13, 14] to form a nanocomposite. The subsequent paragraph discusses the brief literature review in the above perspective.

Garmabi et al. [15] reported mechanical properties of HDPE/nanoclay/nanoCaCO₃ hybrid composite. It was observed that at 5 wt.% nanoclay, 8 wt.% nano CaCO₃ enhanced the tensile modulus by 65% due to the large aspect ratio and reinforcing effect of CaCO₃ on nanoclay. Sahu et al. [16] investigated the wear performance and damping properties of HDPE/0.1 ND/MWCNT/GNP nanocomposite and their hybrids. It was observed that the addition of 0.1 ND significantly improved the wear performance of composite and among the hybrids HDPE/0.1 GNP/ND has shown best wear performance and damping abilities due to intercalation of ND between GNP layer. Badgayan et al. [17] performed the mechanical and thermal properties of HDPE polymer matrix composite filled with 1D (MWCNT) and 2D (h-BNNP) nanocomposite. The results suggested that the addition of MWCNT has significantly improved the nanocomposite and the best performance was seen for 0.15 h-BNNP/0.25 MWCNT hybrid nanocomposite. Mechanical properties of HDPE/MWCNT/Al₂O₃ for potential use in hip joint replacement was investigated by Dabees et al. [18]. Sahu et al. [19] carried out mechanical properties evaluation of HDPE based polymeric composite reinforced with 0.1 wt.% of 0D, 1D and 2D nanofillers i.e. ND, MWCNT and GNP nanocomposite respectively. The best mechanical performance was noted for 0.1 wt.% ND composite, with a considerable rise of hardness, fracture stress and Young's modulus i.e. 34, 42, 23% compared to virgin HDPE. Dimple et al. [20] evaluated HDPE based composite and hybrid for possible application in total hip prosthesis using finite element analysis. It was observed that 0.15 h-BNNP/0.25 MWCNT hybrid nanocomposite is suitable for all human actions i.e. jogging, cycling, stair climbing and walking as the stress value lies below the safer value.

Based on the above literature studies, it is inferred that HDPE based polymer nanocomposite specifically 0.1 CNT/HDPE nanocomposite exhibited the best mechanical, wear properties along with its biocompatible, which was chosen for the material for finite element analysis of dental implant. Among the tooth, the molar tooth was chosen for dental implant analysis as humans mostly use the molar tooth for chewing and breaking the hard food entity. The static structural analysis is performed on the molar tooth and the results like equivalent von Mises and contact pressure results were accessed.

Table 1 Material properties adopted [19]

Material properties	Values
Density (g/cm ³)	0.974
Young's modulus (GPa)	1.2
Poisson's ratio	0.44
Tensile yield strength (MPa)	42

2 Materials and Methods

2.1 Materials

Material for simulation of dental implant is 0.1 CNT/HDPE nanocomposite is used. The material properties were chosen from literature Sahu et al. [19] and represented in Table 1.

2.2 CAD Modeling and Finite Element Simulation

2.2.1 CAD Modeling

The 2D diagram of a molar tooth is shown in Fig. 1a, where it shows the different parts of a single molar tooth. A Three-dimensional (3D) model of a molar tooth is modelled using CATIA V5 R20 software is shown in Fig. 1b. The detail dimension is represented in Table 2.

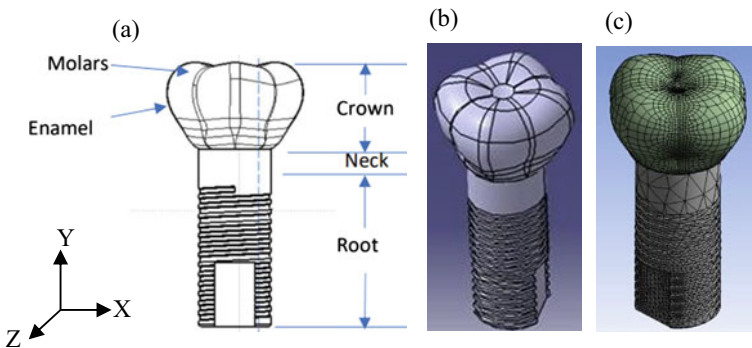


Fig. 1 a 2D model; b 3D model c Meshed model of a molar tooth

Table 2 Geometrical Dimensions of the molar tooth [21]

Parts	Actual molar teeth	Geometric modelling by CATIA V5 R20
Height of crown (mm)	5.2	5.2
The perimeter of the crown at the middle (mm)	18.4	18.42
Height of implant (mm)	10.89	11
Perimeter of implant (mm)	13.50	13.51
Pitch of implant thread (mm)	0.61	0.60

2.2.2 Boundary Condition and Finite Element Analysis

The 3D model discussed in the previous section is imported to the ANSYS Workbench environment as IGES format in the static structural environment and further analysis is performed. The boundary condition is set by creating a similar molar tooth in the inverted direction on the top of the considered base molar tooth. The base molar tooth is fixed in all direction and the various load of 50 N to 300 N is applied along the Y-direction on the top tooth.

The load value chosen here can be referred to as Fernandes et al. [22]. The meshing is performed by taking *quadrilateral* element for crown section and *tetrahedral element* for neck and root section, which is shown in Fig. 1c. The mesh convergence analysis was performed and there were 12,751 nodes, 7172 elements considered, whereas 7731 nodes, 4363 elements considered for the neck and root section. The equivalent von-Mises stress and the contact pressure is accessed from the simulation test.

3 Results and Discussion

Figure 2a shows the load vs. equivalent Von-Mises stress (EVS) at various load conditions. It is observed that at 50 N load the EVS is 8.6 MPa, which is increased to 100.1, 200.3, 300.5, 400.6 and 500.5% respectively. The EVS criteria give the deterministic characteristic for the material ability to sustain the loading. The value of yield stress for the material used i.e. 0.1 CNT/HDPE is 42 MPa, whereas the highest obtained EVS is 51.6 MPa, which indicates the failure of material at the highest load. However, at a load lower than 250 N, the yield stress is far away from the EVS, indicating its safer usage at a load lower than 250 N. Figure 2b represents the load vs contact pressure at various loads i.e. 50, 100, 150, 200, 250 and 300 N load. It is observed that at 50 N load the contact pressure is 60.6 MPa, which is increased to 121.2, 181.8, 242.4, 303.1 and 363.7 MPa respectively. There is an increase in the trend of contact pressure is seen with an increase in load similar to EVS, which is shown in Fig. 2c. The contact pressure is generally measured normal

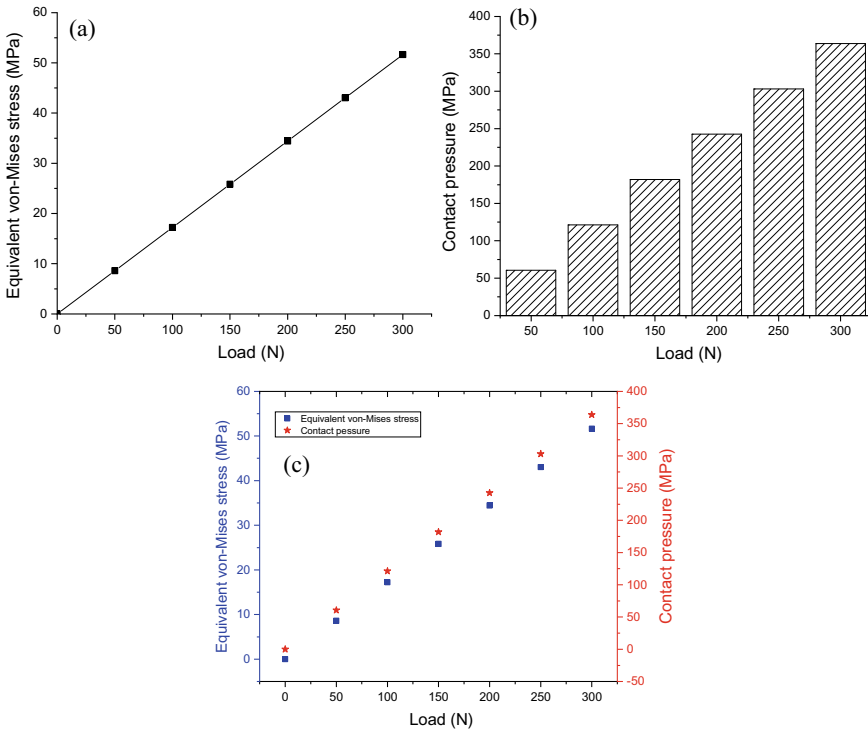


Fig. 2 a Equivalent Von-Mises stress versus load; b Contact pressure versus load; c Equivalent Von-Mises stress versus contact pressure versus load

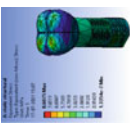
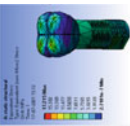
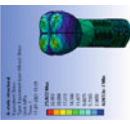
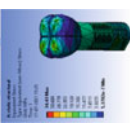
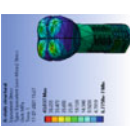
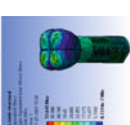
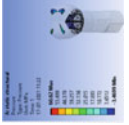
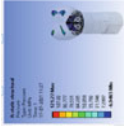
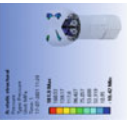
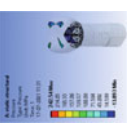
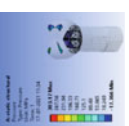

load vs contact area, which indicates proportional to load. Hence the increase in load causes an increase in contact pressure. The stress distribution results for EVS and contact pressure is shown in Table 3. There is no significant stress intensity is seen in both EVS and contact pressure distribution results, which indicates the dental implants are shaped to use in the current loading condition.

4 Conclusions

The structural analysis of molar tooth dental implant at various load conditions 50, 100, 150, 200, 250 and 300 N using Ansys static structural was analyzed. The material for the dental implant simulation was 0.1 CNT/HDPE nanocomposite was selected. Based on the current investigation following the inferences are drawn

- (a) Equivalent Von-Mises stress increases with increase in load and at higher load i.e. 300 N, the value was 51.6 MPa, which lies above yield stress of

Table 3 Simulation results at various load condition

Load (N) →	50	100	150	200	250	300
Equivalent von-Mises stress (MPa) →	 <p> Equivalent (von-Mises) Stress Max. (MPa) 1.07E+01 Min. (MPa) 0.00E+00 Avg. (MPa) 0.10E+00 Max. (N/mm²) 1.07E+01 Min. (N/mm²) 0.00E+00 Avg. (N/mm²) 0.10E+00 1.07E+01 MPa 1.07E+01 N/mm² </p>	 <p> Equivalent (von-Mises) Stress Max. (MPa) 2.14E+01 Min. (MPa) 0.00E+00 Avg. (MPa) 0.20E+00 Max. (N/mm²) 2.14E+01 Min. (N/mm²) 0.00E+00 Avg. (N/mm²) 0.20E+00 2.14E+01 MPa 2.14E+01 N/mm² </p>	 <p> Equivalent (von-Mises) Stress Max. (MPa) 3.21E+01 Min. (MPa) 0.00E+00 Avg. (MPa) 0.30E+00 Max. (N/mm²) 3.21E+01 Min. (N/mm²) 0.00E+00 Avg. (N/mm²) 0.30E+00 3.21E+01 MPa 3.21E+01 N/mm² </p>	 <p> Equivalent (von-Mises) Stress Max. (MPa) 4.28E+01 Min. (MPa) 0.00E+00 Avg. (MPa) 0.40E+00 Max. (N/mm²) 4.28E+01 Min. (N/mm²) 0.00E+00 Avg. (N/mm²) 0.40E+00 4.28E+01 MPa 4.28E+01 N/mm² </p>	 <p> Equivalent (von-Mises) Stress Max. (MPa) 5.35E+01 Min. (MPa) 0.00E+00 Avg. (MPa) 0.50E+00 Max. (N/mm²) 5.35E+01 Min. (N/mm²) 0.00E+00 Avg. (N/mm²) 0.50E+00 5.35E+01 MPa 5.35E+01 N/mm² </p>	 <p> Equivalent (von-Mises) Stress Max. (MPa) 6.42E+01 Min. (MPa) 0.00E+00 Avg. (MPa) 0.60E+00 Max. (N/mm²) 6.42E+01 Min. (N/mm²) 0.00E+00 Avg. (N/mm²) 0.60E+00 6.42E+01 MPa 6.42E+01 N/mm² </p>
Contact pressure (MPa) →	 <p> Contact Pressure Max. (MPa) 1.07E+01 Min. (MPa) 0.00E+00 Avg. (MPa) 0.10E+00 Max. (N/mm²) 1.07E+01 Min. (N/mm²) 0.00E+00 Avg. (N/mm²) 0.10E+00 1.07E+01 MPa 1.07E+01 N/mm² </p>	 <p> Contact Pressure Max. (MPa) 2.14E+01 Min. (MPa) 0.00E+00 Avg. (MPa) 0.20E+00 Max. (N/mm²) 2.14E+01 Min. (N/mm²) 0.00E+00 Avg. (N/mm²) 0.20E+00 2.14E+01 MPa 2.14E+01 N/mm² </p>	 <p> Contact Pressure Max. (MPa) 3.21E+01 Min. (MPa) 0.00E+00 Avg. (MPa) 0.30E+00 Max. (N/mm²) 3.21E+01 Min. (N/mm²) 0.00E+00 Avg. (N/mm²) 0.30E+00 3.21E+01 MPa 3.21E+01 N/mm² </p>	 <p> Contact Pressure Max. (MPa) 4.28E+01 Min. (MPa) 0.00E+00 Avg. (MPa) 0.40E+00 Max. (N/mm²) 4.28E+01 Min. (N/mm²) 0.00E+00 Avg. (N/mm²) 0.40E+00 4.28E+01 MPa 4.28E+01 N/mm² </p>	 <p> Contact Pressure Max. (MPa) 5.35E+01 Min. (MPa) 0.00E+00 Avg. (MPa) 0.50E+00 Max. (N/mm²) 5.35E+01 Min. (N/mm²) 0.00E+00 Avg. (N/mm²) 0.50E+00 5.35E+01 MPa 5.35E+01 N/mm² </p>	 <p> Contact Pressure Max. (MPa) 6.42E+01 Min. (MPa) 0.00E+00 Avg. (MPa) 0.60E+00 Max. (N/mm²) 6.42E+01 Min. (N/mm²) 0.00E+00 Avg. (N/mm²) 0.60E+00 6.42E+01 MPa 6.42E+01 N/mm² </p>

0.1 CNT/HDPE polymer nanocomposite, indicates the failure of material at higher load.

- (b) The contact pressure value showed proportional relation with load and equivalent Von-Mises stress.

It is concluded that the molar dental tooth with 0.1 CNT/HDPE polymer nanocomposite is safe to use when the load is below 250 N. The further experimental and simulation study will supplement the above suggestion and feasibility of adoption as dental implant material.

References

1. Gollapudi, V.R., Mallavarapu, U., Seetha, J., Duddela, V., Amara, V.R., Vatti, C.S., Anumakonda, V.: In situ generation of antibacterial bimetallic silver and copper nanocomposites using *Tinospora cordifolia* leaf extract as bio reductant. *Biointerface Res. Appl. Chem.* **10**, 5569–5574 (2020)
2. Das, R.K., Ngaihte, S.K., Prasad, R., Kakoti, A., Hoque, R., Sahu, S.K., Badgayan, N.: Experimental Investigation into electric discharge machining of Ti-6Al-4 V ELI alloy: an insight into biomedical applications. *Mater. Today Proc.* **46**, 30–35 (2021)
3. Roy, A.K., Kumar, K.: Visualization of thermal distribution during machining of dental implants. *Biointerface Res. Appl. Chem.* **12**(4), 4637–4648 (2021)
4. Zindani, D., Kumar, K.: Graphene-based polymeric nano-composites: an introspection into functionalization, processing techniques and biomedical applications. *Biointerface Res. Appl. Chem.* **9**, 3926–3933 (2019)
5. Sahu, S.K., Badgayan, N.D., Samanta, S., Sahu, D., Sreekanth, P.R.: Influence of cell size on out of plane stiffness and in-plane compliance character of the sandwich beam made with tunable PCTPE nylon honeycomb core and hybrid polymer nanocomposite skin. *Int. J. Mech. Sci.* **148**, 284–292 (2018)
6. Badgayan, N.D., Sahu, S.K., Sreekanth, P.S.R.: Investigation of wetting behavior of HDPE reinforced with nanoscopic 1D/2D filler system using contact angle goniometry. *Mater. Today Proc.* **26**, 331–334 (2020)
7. Rai, A., Datarkar, A., Arora, A., Adwani, D.G.: Utility of high density porous polyethylene implants in maxillofacial surgery. *J. Maxillofac. Oral Surg.* **13**(1), 42–46 (2014)
8. Badgayan, N.D., Samanta, S., Sahu, S.K., Siva, S.V., Sadasivuni, K.K., Sahu, D., Sreekanth, P.S.R.: Tribological behaviour of 1D and 2D nanofiller based high density poly-ethylene hybrid nanocomposites: a run-in and steady state phase analysis. *Wear* **376**, 1379–1390 (2017)
9. Badgayan, N.D., Sahu, S.K., Samanta, S., Sreekanth, P.S.R.: Assessment of bulk mechanical properties of HDPE hybrid composite filled with 1D/2D nanofiller system. *Mater. Sci. Forum* **917**, 12–16 (2018)
10. Sahu, S.K., Badgayan, N.D., Samanta, S., Sreekanth, P.S.R.: Quasistatic and dynamic nanomechanical properties of HDPE reinforced with 0/1/2 dimensional carbon nanofillers based hybrid nanocomposite using nanoindentation. *Mater. Chem. Phys.* **203**, 173–184 (2018)
11. Badgayan, N.D., Sahu, S.K., Samanta, S., Sreekanth, P.S.R.: An insight into mechanical properties of polymer nanocomposites reinforced with multidimensional filler system: a state of art review. *Mater. Today Proc.* **24**, 422–431 (2020)
12. Sahu, S.K., Badgayan, N.D., Sreekanth, P.S.R.: Rheological properties of HDPE based thermoplastic polymeric nanocomposite reinforced with multidimensional carbon-based nanofillers. *Biointerface Res. Appl. Chem.* **12**(4), 5709–5715 (2022)
13. Anandarao, R.K.R., Srinivasan, S., Rommala, H.R., Deepthi, Y.P.: Experimental investigation on influence of molybdenum content on tribological properties of hybrid PTFE composite. In: *AIP Conference Proceedings*, vol. 2080, No. 1, p. 020017 (2019)

14. Sahu, S.K., Badgayan, N.D., Samanta, S., Sreekanth, P.S.R.: Evaluation of cell parameter variation on energy absorption characteristic of thermoplastic honeycomb sandwich structure. *Arab. J. Sci. Eng.* **46**, 12487–12507 (2021). <https://doi.org/10.1007/s13369-021-05987-9>
15. Garmabi, H., Tabari, S.E.A., Javadi, A., Behrouzi, H., Hosseini, G.: An investigation on morphology and mechanical properties of HDPE/nanoclay/nanoCaCO₃ ternary nanocomposites. In: *AIP Conference Proceedings*, vol. 1713, No. 1, p. 090005 (2016)
16. Sahu, S.K., Badgayan, N.D., Sreekanth, P.R.: Understanding the influence of contact pressure on the wear performance of HDPE/multi-dimensional carbon filler based hybrid polymer nanocomposites. *Wear* 438–439 (2019). <https://doi.org/10.1016/j.wear.2019.01.125>
17. Badgayan, N.D., Sahu, S.K., Samanta, S., Sreekanth, P.S.R.: Evaluation of dynamic mechanical and thermal behavior of HDPE reinforced with MWCNT/h-BNNP: an attempt to find possible substitute for a metallic knee in transfemoral prosthesis. *Int. J. Thermophys.* **40**(10), 1–20 (2019)
18. Dabees, S., Tirth, V., Mohamed, A., Kamel, B.M.: Wear performance and mechanical properties of MWCNT/HDPE nanocomposites for gearing applications. *J. Market. Res.* **12**, 2476–2488 (2020)
19. Sahu, S.K., Badgayan, N.D., Samanta, S., Sreekanth, P.S.R.: Experimental investigation on multidimensional carbon nanofiller reinforcement in HDPE: an evaluation of mechanical performance. *Mater. Today Proc.* **24**, 415–421 (2020)
20. Dimple, D., Shruti, M., Badgayan, N.D., Sahu, S.K.: Finite element analysis of hdpe-based hybrid nanocomposite for potential use as liner material for total hip prosthesis. *Adv. Eng. Design Select Proc. FLAME* **2020**, 305 (2021)
21. Sharanraj, V., Ramesha, C.M., Kumar, V., Sadashiva, M.: Finite element analysis of Zirconia ceramic biomaterials used in medical dental implants. *Interceram-Int. Ceram. Rev.* **68**(3), 24–31 (2019)
22. Fernandes, C.P., Glantz, P.O.J., Svensson, S.A., Bergmark, A.: A novel sensor for bite force determinations. *Dent. Mater.* **19**(2), 118–126 (2003)

Process Simulation of Electrical Discharge Machining: A Review



Diksha Jaurker  and M. K. Pradhan 

Abstract Electrical discharge machining (EDM) is a metal removal machining process that is characterized by erosion caused by a rapidly occurring discharge between the tool and the workpiece. In the modern world, EDM faces numerous challenges when it comes to machining hard materials and complex shapes of structures. The thermal stress that develops just after the end of the spark and the residual stress that continues to develop after corresponding cooling, as well as the impacts of process parameters such as pulse on time, pulse off time, peak current, and output parameters such as metal removal rate, surface roughness, tool or electrode wear ratio, have been heavily researched and investigated in the past. The focus of this research is to examine prior findings about the used a suitable optimization technique for the EDM process and its variants as well as create a path to future scientific investigation.

Keywords Electrical discharge machining (EDM) · Finite element method (FEM) · Thermal stress · Residual stress · Simulation · Modelling

1 Introduction

Machining processes have been developing long along with the development of the human race, from the formation of wheel to computerized non-conventional machining. Now today's world demands high quality, precision machining processes for obtaining the standards, economical products in minimum time to achieve the industrial goal with higher efficiency. One of the most significant emerging machining processes to achieve the required goal in the world is Electrical Discharge Machining (EDM), which is a desirable non-conventional machining process getting attention for zero force, a contact-less process which enables machining of hard materials and complex geometries, with high precision, good surface finish which is not achieved

D. Jaurker (✉) · M. K. Pradhan

Department of Mechanical Engineering, Maulana Azad National Institute of Technology, Bhopal
462003, Madhya Pradesh, India

e-mail: dikshajaurker17@gmail.com

by conventional machining processes and its capability to regulate the process parameters to accomplish the requisite surface finish and dimensional accuracy. EDM has a wide-ranging application in industries such as die industries, aerospace, automotive, electronics industry, mould making, medical, micromechanics, etc.

Electrical Discharge Machining is a metal removing process, which removes metal by the means of electric spark thermal erosion with a constant electric field in a dielectric medium. The electrically conductive workpiece and tool are connected to the positive and negative terminal of the generator respectively, so they have a huge amount of free electrons to flow. When a potential difference is generated between tool and work-piece, the electric field will be developed, free electrons will be plucked in large numbers due to electrostatic force and get accelerated towards work-piece. Energized electrons will ionize the dielectric molecules generating more ions and electrons which will again undergo collision, leading to a huge increment in the concentration of ions and electrons between tool and workpiece, plasma channel will be established between tool and work-piece. Electrons will follow the least resistivity path, will move toward the work-piece in huge amount, hence spark will be generated and the work-piece will be impinged by electrons having high kinetic energy which will be converted into high-density thermal energy which results in localized melting workpiece causing material removal. This thermal erosion produces a recast layer on the machined surface with microcracks. Here due to localize non-uniform heating and rapid cooling of material generates a multi-layered Heat Affected Zone in the subsurface of the workpiece and consequently produces thermal stresses. If these stresses have magnitude more than the material's yield stress, they will persist in the workpiece as residual stress during subsequent cooling, which contributes to fatigue crack growth, crack closure, and fracture [1].

To study the complex process of EDM, we need to study the establishment of plasma channel between workpiece and tool, thermodynamics of the spark causing thermal erosion, microstructural and metallurgical changes of material. For this study, a heat transmission thermal problem needs to be constructed to model the EDM mechanism, where the electric spark generated in EDM is the heat input, and by solving this heat transmission thermal problem for the workpiece will give us the temperature distribution in it. And to solve this numerical model finite element method is used and the impact of various process parameters on the output parameters, temperature distribution, thermal stresses and residual stresses can be investigated.

1.1 Variants of EDM

Die-sinking EDM is a variant of EDM where the final desired shape of the workpiece is complemented by the tool shape when an electric field is set up between them and thermal erosion takes place.

Powder mixed EDM is a variant of EDM process where suitable electrically conductive abrasive powder particles are added into the dielectric fluid resulting in decreases

its insulation strength as these powder particles get ionized upon setting an electrical field and show accelerated zigzag motion between electrodes, leading to an increase in the inter-electrode gap, as result of which EDM performance improves and heighten surface finish is obtained in comparison to the conventional EDM.

Wire EDM is another variant of EDM where discharge occurs between metallic thin wire and workpiece, the metallic thin wire is used to cut shapes. Main cuts and trim cuts are performed on the work material using WEDM, the main cut is preferred when material removal rate (MRR) or cutting speed is a primary need and when high surface finish is more desired than the trim cut of performed at lower power setting after the main cut. [2]

2 Technique Used for the Study

- 2.1 **Finite element method (FEM)** is a computational technique for solving differential equations developed for mathematical modelling to investigate engineering problems in the fields of heat transfer, structural analysis, fluid dynamics, and also coupled problems like thermo-structural, electromagnetic, thermochemical, etc. In FEM the domain of the problem is discretized into small elements with the help of nodes and the differential equation is solved within the boundary of the element and by combining these discrete solutions, a global solution is obtained [3]. The chances of having error in the solution are minimized by increasing the number of elements hence reducing the element size.
- 2.2 **X-Ray Diffraction (XRD)** method is governed by the Bragg's law, when a specific wavelength (λ) beam of X-ray falls on the workpiece's surface, the scattered radiation undergoes interference. Bragg's law is stated by the below equation:

$$n\lambda = 2d \sin \theta$$

where,

- n Order of diffraction
- θ Diffraction angle
- d Distance between crystallographic planes

Firstly, the strain generating the shift in crystallographic planes is evaluated assuming linear elastic distortion of the crystal lattice and then the value of stress is evaluated using Hooke's law [4]

- 2.3 **Taguchi Method** is a statistical methodology to enhance the quality of the product to be manufactured, by the optimization of process parameters. The main intention is to improve the quality of a product and design robust systems that are more reliable under uncontrollable conditions [5].

- 2.4 **Scanning electron microscopy** is a technique used for the visualization and investigation of surfaces, where a fine electron beam is scanned through the fracture surface to produce a picture and the rate at which the image is scanned tells the issues. The pictures can later be advanced employing frame integration and averaging [6]. An electrically conductive workpiece is required for this method, at least the surface should be conductive, and, the workpiece should be electrically grounded to avoid the accumulation of an electrostatic charge at the surface.
- 2.5 **Focussed Ion Beam (FIB) milling—Digital Image Correlation (DIC)**. FIB is used to mill standard geometries and the relaxation causing the surface displacements is captured by the scanning electron microscope (SEM), than images are created using DIC software, these are then used with finite element modelling for calculation of the residual stresses in the workpiece [7].

3 Previous Works

Mohanty et al. [8] uses Field Emission SEM for two cases WS_2 combined with de-ionized water and MoS_2 powders mixed in deionized water and discovered that WS_2 coated samples have a heightened density of surface crack and residual stresses develop on the recast surface than that of MoS_2 powder coated samples. Yue et al. [9] performed experimental analysis using SEM, the influencing effect of thermal stress on material removal during EDM of the C_f -SiC composite and the stress distribution on the C_f -SiC composite's discharge surface was investigated. Thermal stress was generated that exceeded the tensile strengths. Srinivasa Rao et al. [10] investigated the impact of wire EDM parameters upon the residual stresses in aluminium 2014 T6 alloy with a L8 orthogonal array Taguchi method confirms that increasing the pulse on time and peak current, increases surface roughness and cutting speed. The spark gap voltage, pulse on time, peak current, and cutting speed all had a substantial impact on residual stresses.

Some researchers have conducted an experimental analysis employing the X-Ray Diffraction method and also performed computation analysis using FEM for the validation of results. Aghdeab et al. [11] using the X-ray diffraction method and FEM the residual stress arises during EDM was determined, and discovered that the residual stress boosted with raising the current, pulse on time, and pulse off time. Sundriyal et al. [12] investigated the powder mixed near-dry (PMND-EDM) process, and it was discovered that raising the concentration of metallic powder in the dielectric was assisting in broadening the plasma channel owing to an enhanced conduction all through machining and increasing the inter-electrode gap. Das and Joshi [4] used FEM model, calculated the wire safety index. The stresses arised on the wire were found to be greater than the molybdenum's yield stress. Tlili and Ghanem [13] developed a thermomechanical model based on hydrodynamic Gruneisen-type conduct for the hydrostatic component of the stress, paired with Johnson–Cook plasticity model

which reports for strain-rate-dependent stress in the scope of a shockwave condition and observed traction type residual stresses on the surface which is balanced by sublayer's compressive stresses. Saxena [14] estimate the thermal stresses and discovered that the initial compressive stresses encircling the formed crater, after heating change its nature to tensile, and as the crater reaches greater depth, the stresses transits into compressive residual stresses which bring the system into equilibrium. Zhanga et al. [15] Examined the thermal deformation of a thin-walled sample and concluded that the force at the bottom must equate the residual stress at the top of the thin-walled sheet. Where Salvati and Korsunsky [2] assesses micro- to nano-scale residual stress, used FIB-DIC method for modeling, which was validated by FEM analysis, and discovered that peak current and pulse on time, are critical for the intensity of induced residual stresses and crack emergence.

Bhattacharya et al. [16] applied FEM to simulate generated residual stresses during WEDM cutting and the volumetric strain change caused by phase transformation with the temperature introducing a user-defined subroutine. Thermal expansion is considered in the FEM analysis to account for metallurgical phase changes. Kumara and Jilte [17], discovered that the equivalent stress appears in the tool's and workpiece's core spark zone. The current density has a significant impact on the response output parameters. Mohapatra et al. [18] simulated for the wire using ANSYS Fluent and estimated the temperature and equivalent stress. The temperature of the wire was observed to vary up to 5500 K. At the centre of the wire length, equivalent stress was observed with a maximum effective stress of 397 MPa. Assarzadeh and Ghoreishi [19] performed an electrothermal simulation and discovered that progressive increases in discharge current create steadily deeper crater voids, implying the creation of more re-solidified materials atop the crater. Liu and Guo [20] accounted for massive random discharges to examine the residual stress arises in die-sinking EDM and investigated characteristics of sub surface's local and average residual stress. Singh and Kumar [21] calculated the radial, tangential and axial stresses in the electrode in the static structure module and observed that the magnitude of stress hikes with hike in current values. Pradhan [1], Biswas and Pradhan [22], Pradhan [23], Pradhan and Biswas [24] investigated the correlation between parameters and the highest temperature acquired at the end of the heating cycle and the residual stress arising, by FEA modelling, and it was discovered that compressive thermal stresses formed underneath the crater and tensile stresses existed farther from the axis of symmetry and observed that by intensifying the pulse energy the thermal stresses get affected to a greater depth. Kansal et al. [25] build the FEM model for powder mixed EDM and calculated the distribution of temperature and MRR from the temperature profiles and observed that along the radius and depth of the workpiece many different process parameters affect the temperature distributions. Allen and Chen [26] simulated for micro-EDM, analysed the residual stress and investigated the effects of vital EDM parameters on tool wear ratio and the dimension of the formed crater. Yadava et al. [27] presented for EDDG, a model has been created using FEM to assess thermal stresses. The developed algorithm first determines the temperature, and then using this temperature field, estimates the thermal stress field. Computations were performed in-plane strain conditions for various grinding wheel down feeds.

Das et al. [28] simulated with DEFORM to study the transient temperature and crater portrayal, the heat-affected zone and residual stresses in the workpiece.

Only that research is highlighted in Table 1, which used a suitable optimization technique such as the Finite Element Method (FEM), X-Ray diffraction method, FIB-DIC, SEM, and others for the EDM process and its variants such as WEDM, micro-EDM, powder-mixed EDM, powder-mixed near dry EDM, etc.

Along with the time, researchers are considering various aspects of the simulation, such as using a gaseous dielectric medium, evaluating different tool electrodes, analysing surface wettability, and micro-hardness, developing a customised mixing chamber for creating a heterogeneous dielectric mixture, and imposing the model with an infinite-element boundary to dodge shockwave reflection on the free surface, to ensure convergence towards the equilibrium condition. For the wire-EDM procedure, the wire safety index is analysed, microcracks on the wire surface are being analysed, and the authors are attempting to describe the shape and dimension of the spark.

4 Conclusion

In this review paper, a remark on various research works carried out in the field of EDM is presented.

The observed points are follows:

- It has been observed that thermal modelling of EDM mechanism followed by simulation is the key to investigate and predict the output parameters, temperature distribution and stresses, and these results have been validated by conducting experimental work.
- Experimental analysis carried out by researchers used X-ray diffraction method, Taguchi method, Scanning electron microscopy method, Focussed Ion Beam (FIB) milling—Digital Image Correlation (DIC) method.
- The experimental research shows that with increment in current pulse off time and pulse on time, increment in residual stress was observed.
- With the increment in current and voltage level, there is an increment in the maximum temperature and the maximum residual stresses.
- The depth at which the peak value of residual stresses will attain, increases proportionally with the pulse energy.
- The residual stresses comes very close or exceeds to the value of yield strength of the material at vicinity of spark location.

Table 1 Chronological ordered list of research work published related to simulation of Electric Discharge Machining from 2003 onwards

Year	Author(s)	Objective	Process version	Workpiece material	Technique used	Remarks
2021	Aghdeab, et al. [11]	To Investigate the residual stress developed in the workpiece during EDM process	EDM	3-D Tool steel AISI L2	X-ray diffraction and FEM	<ul style="list-style-type: none"> The experimental research shows that with increment in current pulse off time and pulse on time, increment in residual stress was observed Comparison of residual stress was made here for two specimens Residual stresses for the case of WS_2 coated samples were found to be more than MoS_2 coated samples More number of cracks were seen on the surface coated with WS_2
2021	Mohanty, et al. [8]	Analysis of the micro-hardness, indentation depths, wettability, residual stress, surface crack density and surface roughness	μ EDM	3-D Ti6Al4V sample with tungsten disulfide and molybdenum disulfide coatings	Field Emission Scanning Electron Microscope(FESEM)	

(continued)

Table 1 (continued)

Year	Author(s)	Objective	Process version	Workpiece material	Technique used	Remarks
2020	Salvati and Korsunsky [2]	Determination of micro-stress with in white layer, in two specimens having Main cut and Trim cut followed by main cut	EDM	AA6082-T6 Al alloy	FIB-DIC method and FEM	<ul style="list-style-type: none"> Consistency was found in compressive residual stress along with the thickness of the white layer for both specimens The compressive layer was thinner for the trim cut specimen than for that of the main cut specimen
2020	Sundriyal, et al. [12]	To investigate the impact of pulse-on time and concentration level of powder on MRR and residual stress respectively	Powder mixed near-dry EDM	EN-31 steel	X-ray diffraction and FEM	<ul style="list-style-type: none"> Gaseous dielectric is used An increment in MRR was observed with a decrease in pulse-on time MRR increase slightly and then reduces upon increasing in powder concentration level

(continued)

Table 1 (continued)

Year	Author(s)	Objective	Process version	Workpiece material	Technique used	Remarks
2020	Das and Joshi [4]	To determine the wire safety index	WEDM cutting 3-D	Molybdenum wire	X-ray diffraction (XRD) and FEM	<ul style="list-style-type: none"> The wire safety index is a ratio of the maximum residual stress developed and the yield stress of the wire With the increment in current and voltage level, there is an increment in the maximum temperature and the maximum residual stresses With the increment in pulse on-time, thermally affected region increases and peak temperature decreases
2020	Yue et al. [9]	To analyse the stress distribution on the Carbon-fiber-reinforced silicon carbide (Cf_SiC) composite during EDM	EDM 2-D	Cf_SiC composite with SiC coating	Scanning Electron Microscopy(SEM)	<ul style="list-style-type: none"> Experimental and simulation comparison is done here Higher cutting speed leads to the generation of thermal stress

(continued)

Table 1 (continued)

Year	Author(s)	Objective	Process version	Workpiece material	Technique used	Remarks
2019	Bhattacharya et al. [16]	Thermal analysis of the temperature profile and residual stress	WEDM cutting 2-D	P91 steel	FEM	<ul style="list-style-type: none"> The Residual stresses were observed to be of tensile nature When cutting is done at higher energy, higher the value of residual stresses were observed
2019	Zhanga et al. [15]	Investigate the surface integrity of thin-walled components during the WEDM process due to complex thermal deformation behaviour	WEDM cutting 2-D	Inconel 718	FEM	<ul style="list-style-type: none"> With an increase in discharge energy, thermal and residual stresses increases, but a after particular increase in pulse-on time the discharge energy becomes sufficient to vaporize the metal, which leads to low residual stresses

(continued)

Table 1 (continued)

Year	Author(s)	Objective	Process version	Workpiece material	Technique used	Remarks
2018	Kumara and Jilte [17]	Investigation of the impact of input parameters on equivalent stress	EDM	XW-42 steel	FEM	<ul style="list-style-type: none"> An increment in current and pulse on time value, increases the stress values Stresses are higher for a higher fraction of the total heat input that is absorbed by the workpiece Material flushing efficiency is supposed to be 100%
2018	Mohapatra et al. [18]	Investigation of temperature and equivalent stress for tool electrode	WEDM cutting	AISI 304 stainless steel	FEM	<ul style="list-style-type: none"> Equivalent stress was found with maximum effective stress of 397 MPa at the middle of the wire
2018	Tilili and Ghanem [13]	To investigate the mechanical behaviour of the workpiece layer during an electrical discharge and numerical prediction of the residual stresses and work hardening	EDM	AISI 316L	X-ray diffraction (XRD) and FEM	<ul style="list-style-type: none"> At the initial stage of solid-liquid boundary, in the sublayer, residual stresses are at their peak value

(continued)

Table 1 (continued)

Year	Author(s)	Objective	Process version	Workpiece material	Technique used	Remarks
2017	Assarzadeh and Ghoreishi [19]	Comparisons between experimental and simulated results of influence of input parameters on MRR	EDM	AISI 304 stainless steel	FEM	<ul style="list-style-type: none"> • With the increase in discharge time the temperature of workpiece decreases and the volume of vaporized material increases
2016	Srinivasa Rao et al. [10]	An analysis of influence of wire EDM parameters on residual stresses	WEDM	Aluminium 2014 T6 alloy	Taguchi method	<ul style="list-style-type: none"> • Tensile residual stresses were observed • As cutting speed increases, surface roughness and residual stresses also increases • The interaction of pulse on time, peak current and spark gap voltage, spark gap voltage, the interaction between pulse-on time and peak current, pulse-on time and peak current is the increasing order of parameters and their interactions' effect on residual stresses

(continued)

Table 1 (continued)

Year	Author(s)	Objective	Process version	Workpiece material	Technique used	Remarks
2016	Liu and Guo [20]	Investigation of the effect of massive random discharges on the residual stress	EDM	ASP 23 tool steel	FEM	<ul style="list-style-type: none"> • Instead of the workpiece's top surface, the maximum average residual stress was located in the subsurface • High surface roughness was the result of low residual stress on the workpiece surface • For low residual stress, low discharge energy is favourable • Compressive residual thermal stresses were present
2016	Saxena [14]	To investigate of residual stresses and comparing it with experimental results	EDM	AISI 4340	X-ray diffraction (XRD) and FEM	
2015	Singh and Kumar [21]	To investigate the thermal stresses occurring in electrode during EDM machining	EDM	Copper and graphite electrode	FEM	<ul style="list-style-type: none"> • The stress increases with increment in the pulse-on time and current • The temperature of the graphite electrode was found to be more than that of the copper electrode for the identical input parameters

(continued)

Table 1 (continued)

Year	Author(s)	Objective	Process version	Workpiece material	Technique used	Remarks
2014	Choudhary and Pradhan [29]	To investigate the effect of parameters leading to development of residual stresses beneath the crater	EDM	Molybdenum	FEM	<ul style="list-style-type: none"> The residual stresses were developed near the crater periphery in all the direction Residual stresses were found to be tensile as well as compressive in nature Point of failure due to residual stresses was also predicted
2012	Pradhan [1]	To Investigate the temperature distribution, thermal stresses and residual stresses	EDM	AISI D2 steel	FEM	<ul style="list-style-type: none"> The intensity of the peak stresses was unaffected by the magnitude of the spark energy produced No influence of pulse energy was found on the magnitudes of the maximum tensile and compressive residual stresses Increment in the depth where the residual stresses develop was observed with increase in the pulse energy

(continued)

Table 1 (continued)

Year	Author(s)	Objective	Process version	Workpiece material	Technique used	Remarks
2012	Biswas and Pradhan [22]	Investigation of the impact of machining parameters on the residual stresses	EDM	AISI D2 tool steel	FEM	<ul style="list-style-type: none"> For all combination of machining parameters, all component of the residual stresses gets dominated by radial component
2010	Pradhan [23]	To predict the nature of thermal stresses developed during EDM process	EDM	AISI D2 steel	FEM	<ul style="list-style-type: none"> The thermal tensile stresses were observed far from the axis of symmetry and the compressive thermal stresses were observed underneath the crater Thermal stresses develop to a greater depth when pulse energy increases

(continued)

Table 1 (continued)

Year	Author(s)	Objective	Process version	Workpiece material	Technique used	Remarks
2008	Pradhan and Biswas [24]	To investigation of residual stresses and thermal stresses due to non-uniform temperature fields	EDM	AISI 4140 steel	FEM	<ul style="list-style-type: none"> The values of residual stresses are high close to the surface and decreases sharply radially and axially away from the crater The largest value of Residual stress in the radial direction is 34 MPa in compression and 300 MPa in tension. Whereas in axial direction 16 MPa in compression and 63 MPa in tension
2008	Kansal et al. [25]	To investigate the thermal behaviour and the mechanism of material removal	PMEDM	AISID2 die steel	FEM	<ul style="list-style-type: none"> Both theoretical and experimental observation says that the MRR for PMEDM is higher than for the conventional EDM Radially elongation is more than that for depth for the craters formed in PMEDM

(continued)

Table 1 (continued)

Year	Author(s)	Objective	Process version	Workpiece material	Technique used	Remarks
2007	Allen and Chen [26]	To analyse the residual stress on molybdenum	Micro-EDM	Molybdenum	FEM	<ul style="list-style-type: none"> • After a single heat-flux numerically small residual stresses tensile in nature were remaining in the workpiece • Surface damage may cause over many spark cycles due to residual stresses build-up
2004	Yadava et al. [27]	To investigate the thermal stresses when the current is switched-off during Electrical discharge diamond grinding(EDDG)	EDDG	HSS	FEM	<ul style="list-style-type: none"> • Initially during grinding, at the vicinity of the top surface higher thermal stresses were found but afterwards, it shifts towards the bottom • The value of thermal stresses did not overcome the yield strength value

(continued)

Table 1 (continued)

Year	Author(s)	Objective	Process version	Workpiece material	Technique used	Remarks
2003	Das et al. [28]	To analyse the impact of multi-sparks discharge on transient temperature distribution, material alteration and developed residual stresses in the specimen due to single-pulse discharge	EDM	Copper and graphite	FEM	<ul style="list-style-type: none"> There was a significant increase in the residual stress at the vicinity of the surface but with increment in the depth, the stress vanishes rapidly At the vicinity of spark location, the value of residual stress gets close to the material's tensile strength

References

1. Pradhan, M.K.: Process Simulation, modelling and estimation of temperature and residual stresses electrical discharge machining of AISI D2 steel. *Isci* **2012**, 1–9 (2012)
2. Salvati, E., Korsunsky, A.M.: Micro-scale measurement & FEM modelling of residual stresses in AA6082-T6 Al alloy generated by wire EDM cutting. *J. Mater. Process. Technol.* **275**, 116373 (2020). <https://doi.org/10.1016/j.jmatprotec.2019.116373>
3. Baker, J.: Finite element method. In: *Handbook of Fluid Dynamics*, 2nd edn., pp. 36.1–36.63 (2016). doi: <https://doi.org/10.1016/B978-1-4557-3141-1.50032-0>
4. Das, S., Joshi, S.N.: Estimation of wire strength based on residual stresses induced during wire electric discharge machining. *Journal of Manufacturing Processes* **53**(October 2019), 406–419 (2020). doi: <https://doi.org/10.1016/j.jmapro.2020.03.015>
5. Modi, V.K., Desai, D.A.: Review of Taguchi method, design of experiment (Doe) & analysis of variance (Anova) for quality improvements through optimization in foundry. *Journal of Emerging Technologies and Innovative Research (JETIR)* **5**(1), 184–194 (2018)
6. Greenhalgh, E.: Methodology and tools for failure analysis of polymer composites. In: *Failure Analysis and Fractography of Polymer Composites*, pp. 23–106 (2009). doi: <https://doi.org/10.1533/9781845696818.23>
7. Solomon, M.: The national physical laboratory. *Nature* **69**(1795), 491–492 (1904). <https://doi.org/10.1038/069491a0>
8. Mohanty, et al.: *Surface Integrity and Residual Stress Analysis of μ EDM Coated Ti-alloy Miniature Components*. Taylor & Francis, London (2020)
9. Yue, X., Li, Q., Yang, X.: Influence of thermal stress on material removal of Cf_SiC composite in EDM. *Ceram. Int.* **46**(6), 7998–8009 (2020). <https://doi.org/10.1016/j.ceramint.2019.12.022>
10. Srinivasa Rao, P., Ramji, K., Satyanarayana, B.: Effect of wire EDM conditions on generation of residual stresses in machining of aluminum 2014 T6 alloy. *Alex. Eng. J.* **55**(2), 1077–1084 (2016). <https://doi.org/10.1016/j.aej.2016.03.014>
11. Aghdeab, S.H., Shwaish, R.R., Salman, T.M.: Determination and analysis of residual stress for AISI L2 tool steel in electric discharge machine (EDM). *IOP Conf. Ser.: Mater. Sci. Eng.* **1094**(1), 012074 (2021). doi: <https://doi.org/10.1088/1757-899x/1094/1/012074>
12. Sundriyal, S., Yadav, J., Walia, R.S., Vipin, Kumar, R.: Thermophysical-based modeling of material removal in powder mixed near-dry electric discharge machining. *J. Mater. Eng. Perform.* **29**(10), 6550–6569 (2020). doi: <https://doi.org/10.1007/s11665-020-05110-3>
13. Tlili, A., Ghanem, F.: A numerical investigation on the local mechanical behavior of a 316-L part during and after an EDM basic electrical discharge. *Int. J. Adv. Manuf. Technol.* **99**(9–12), 2755–2776 (2018). <https://doi.org/10.1007/s00170-018-2618-1>
14. Saxena, S.: Thermal Stresses due to electrical discharge machining on AISI4340, vol. 7, no. 5, pp. 165–173 (2016)
15. Zhang, Y., et al.: Simulation and experimental investigations of complex thermal deformation behavior of wire electrical discharge machining of the thin-walled component of Inconel 718. *J. Mater. Process. Technol.* **270**, 306–322 (2019). <https://doi.org/10.1016/j.jmatprotec.2019.02.020>
16. Bhattacharya, S., et al.: Simulation of residual stress using thermomechanical analysis on wire EDM cut surface. *Materials Today: Proceedings* **19**(xxxx), 462–467 (2019). doi: <https://doi.org/10.1016/j.matpr.2019.07.636>
17. Kumar, R., Jilte, R.: Thermal stress analysis of XW-42 steel workpiece using finite element modeling. *Materials Today: Proceedings* **5**(14), 28470–28479 (2018). <https://doi.org/10.1016/j.matpr.2018.10.134>
18. Mohapatra, K.D., Shaibu, V.B., Sahoo, S.K.: Modeling and analysis of wire EDM in a gear cutting process for a 2D model. *Materials Today: Proceedings* **5**(2), 4793–4802 (2018). <https://doi.org/10.1016/j.matpr.2017.12.053>
19. Assarzadeh, S., Ghoreishi, M.: Electro-thermal-based finite element simulation and experimental validation of material removal in static gap singlespark die-sinking electro-discharge

- machining process. *Proceedings of the Institution of Mechanical Engineers, Part B: Journal of Engineering Manufacture* **231**(1), 28–47 (2017). <https://doi.org/10.1177/0954405415572661>
20. Liu, J.F., Guo, Y.B.: Residual stress modeling in electric discharge machining (EDM) by incorporating massive random discharges. *Procedia CIRP* **45**, 299–302 (2016). <https://doi.org/10.1016/j.procir.2016.02.060>
 21. Singh, B., Kumar, S.: Finite element modeling and thermal stress analysis of copper and graphite electrode in EDM machining. *International Journal for Scientific Research and Development* **3**(04), 1921–1927 (2015)
 22. Biswas, C.K., Pradhan, M.K.: FEM of residual stress of EDMed surfaces. *Advanced Materials Research* **383–390**, 872–876 (2012). <https://doi.org/10.4028/www.scientific.net/AMR.383-390.872>
 23. Pradhan, M.K.: Modeling and simulation of thermal stress in electrical discharge machining process. In: 4th International Conference on Advances in Mechanical Engineering, S.V.N.I.T, Surat, India, September 2010, pp. 360–364 (2010)
 24. Pradhan, M.K., Biswas, C.K.: Modeling of residual stresses of Edmed Aisi 4140 steel, pp. 49–55 (2008)
 25. Kansal, H.K., Singh, S., Kumar, P.: Numerical simulation of powder mixed electric discharge machining (PMEDM) using finite element method. *Mathematical and Computer Modelling* (2008). Available: <http://www.sciencedirect.com/science/article/B6V0V-4PR3G9B-2/2/6ffd68a8e85a20b4c6173ac626f62372>
 26. Allen, P., Chen, X.: Process simulation of micro electro-discharge machining on molybdenum. *J. Mater. Process. Technol.* **186**(1–3), 346–355 (2007)
 27. Yadava, V., Jain, V.K., Dixit, P.M.: Theoretical analysis of thermal stresses in electro-discharge diamond grinding. *Mach. Sci. Technol.* **8**(1), 119–140 (2004). <https://doi.org/10.1081/MST-120034250>
 28. Das, S., Klotz, M., Klocke, F.: EDM simulation: finite element-based calculation of deformation, microstructure and residual stresses. *J. Mater. Process. Technol.* **142**(2), 434–451 (2003). [https://doi.org/10.1016/S0924-0136\(03\)00624-1](https://doi.org/10.1016/S0924-0136(03)00624-1)
 29. Choudhary, A., Pradhan, M.K.: Finite element analysis of electro discharge machining using ansys. In: 1st International Conference on Mechanical Engineering: Emerging Trends for Sustainability, February, pp. 18–26 (2014)

A Finite Element Study on the Effect of Bulk Material on the Auxetic Behavior of Additively Manufactured Three-Dimensional Reentrant Honeycomb



Aravind Rajan Ayagara , Chaitanya Vinayak Varma ,
and Rohan Gooty 

Abstract This study investigates the behavior of three dimensional reentrant auxetic honeycomb made of different bulk materials. The energy absorption capacity of auxetic structure depend on both geometrical properties of the unit cell as well as mechanical properties of the bulk material. Auxetic structures are classified as auxetic foams, 2D auxetic structures, and 3D auxetic structures. Based on the literature survey, 3D reentrant auxetic honeycomb (3DRAH) with a relative density of 0.16 were considered for this investigation. The important aspect of this study is to analyze the effect of bulk material and their properties on the performance of 3DRAH. A total of four commonly used plastic materials in additive manufacturing technology were selected as bulk material, they are Polylactic Acid (PLA), Acrylonitrile Butadiene Styrene (ABS), Nylon and High-Impact Poly Styrene (HIPS). All four auxetic models were subjected to quasistatic uniaxial compression using LS Dyna explicit solver. Our numerical simulations showed that at quasistatic loading conditions, the deformation mechanism of 3DRAH is a combination of in-plane bending, out-of-plane bending, and lateral distortion. Moreover, the stress–strain response and the Specific Energy Absorbed (SEA) of the 3DRAH sample are most influenced by the mechanical properties of the bulk material. It is proved through our simulations that as Young’s modulus of the bulk material increases, structural properties like Elastic modulus, Yield stress, Plateau stress and the SEA of the structure increase. No specific correlation was observed between mechanical properties of the material and the densification strain of the structure. We suppose that the densification strain of the structure is rather controlled by the aforementioned deformation mechanism.

A. R. Ayagara (✉) · R. Gooty

Department of Aeronautical Engineering, Institute of Aeronautical Engineering, Dundigal,
Hyderabad 500043, Telangana, India
e-mail: a.rajana@iare.ac.in

C. V. Varma

School of Mechanical Engineering, CBCMT, Vellore Institute of Technology, Vellore,
Tamil Nadu, India

Keywords 3D reentrant auxetic honeycombs · Fusion deposit modeling · Finite element analysis · LS Dyna · Specific energy absorption

1 Introduction

Auxetic materials or structures are the ones that possess a Negative Poisson's Ratio (NPR) i.e., they retract along the lateral directions when subjected to compression along the longitudinal direction and vice versa. They in fact show superior performances in mechanical, thermal, acoustic as well as impact energy absorption. The reason behind this improved performance is due to the arrangement of the structure. There are auxetics in foams, two-dimensions and three-dimensions as well. Numerous studies have been carried out on the behavior of aforementioned auxetic categories. One recent review on auxetics and auxetics subjected to large deformation [1], gives a detailed description on the effects of deformation rate, bulk material and the geometry on the behavior of different auxetic structures.

Out of the auxetic structures tested, the Reentrant Auxetic Honeycomb (RAH) is the best for impact and shows good energy absorption capacities [2]. One of the recent studies on three dimensional reentrant auxetic honeycombs (3DRAH), [3] had successfully implemented it for protection of face against impact. Despite the fact that 3DRAH has been successfully studied and implemented in practical applications, we do not see more publications that speak about neither the deformation mechanism nor the effect of bulk material. For example, [1] had presented a wide review but not many articles give an insight on 3DRAH. In contrast, they do conclude that the auxetic structure's behavior is controlled by the bulk material, relative density, unit cell dimensions [4], manufacturing technique used [4], and even the rate of loading. The negative Poisson's ratio along the two lateral directions is controlled by number of repetitions along all three directions.

Quite a few research articles address the use Finite Element Simulations for prediction of auxetic behavior in the literature. For example, [5] and [6] had carried out FE simulations of 2DRAH. Whereas, [3] present FE simulations concerning 3DRAH. Yet again, there are minimal number of articles on FE simulations of 3DRAH.

In this study, we present the effects of the bulk material on the behavior of 3DRAH under quasi-static compression through Finite Element simulations. All numerical simulations were carried out with LS Dyna Academic Explicit Solver. The FE model, results and discussions are presented in the sections below.

2 Materials and Method

2.1 Unit Cell Geometry

The unit cell configurations of a three-dimensional reentrant auxetic honeycomb (3DRAH) were adapted from [3]. According to them, the relative density (ρ_{eq}) of a 3DRAH can be controlled by three different parameters i.e., the reentrant angle (ϑ), the unit cell length (a) and the thickness of the strut (t). The latter two parameters are consolidated into one through a non-dimensional number (ξ), which gives us the ratio of thickness over unit cell length ($\xi = t/a$)

$$\xi = \frac{\cos\vartheta - \sin\vartheta}{2(1 - \sin\vartheta)} \tag{1}$$

$$\frac{\rho_{eq}}{\rho_s} = \frac{2\xi^2}{\cos\vartheta} [4 + \cos\vartheta \pm \sin\vartheta - 2\xi(3 \pm \sin\vartheta)] \tag{2}$$

That being said, the parameter ρ_s in the above equation is the mass density of the solid bulk material that is used in the process of additive manufacturing of the auxetic sample. You might notice that the relative density equation consists \pm symbol. This is to represent a change in relative density for both 3DRAH and the three-dimensional auxetic honeycomb (3DAH). The above equation for the case of 3DRAH, narrows down to the form below

$$\frac{\rho_{eq}}{\rho_s} = \frac{2\xi^2}{\cos\vartheta} [4 + \cos\vartheta + \sin\vartheta - 2\xi(3 + \sin\vartheta)] \tag{3}$$

The relative density equation corresponding to 3DRAH, when expanded, takes the form a cubic polynomial in terms of ξ as below.

$$a_3\xi^3 + a_2\xi^2 + a_1\xi + a_0 = 0 \tag{4}$$

Where the coefficients are

$$a_3 = \frac{4(3 + \sin\vartheta)}{\cos\vartheta}; a_2 = \frac{2(8 + \sin\vartheta + \cos\vartheta)}{\cos\vartheta}; a_1 = 0 \text{ and } a_0 = \frac{\rho_{eq}}{\rho_s}$$

The coefficient a_0 is the number that corresponds to a desired relative density value, which is a constant. In this study, the relative density was also kept constant at 0.16. Solving for the above set of equations, we can now establish the values corresponding to our relative density.

In this study, the relative density was also kept constant at 0.16. Solving for the set of equations published in [3], we can now establish the values corresponding to our relative density. The unit cell geometry considered in this study has $\vartheta = 30^\circ$, $a = 10$ mm, and $t = 1.2412$ mm.

2.2 Finite Element Model

The finite element simulations were carried out on the LS-Dyna explicit solver, which offers numerous contact algorithms between deformable and rigid bodies. The geometries designed in CATIA V5 were imported to ANSYS workbench in the LS Dyna environment to mesh and create the keyword file. The model aims in recreating the uniaxial compression at a constant displacement rate. The model is an assembly of a top plate, 3DRAH structure, and a bottom plate. The top and bottom plates were assumed to be rigid structures whereas the 3DRAH is a deformable one (see Fig. 1). The following paragraphs present the details on the FE model.

The top and bottom rigid plates were considered of $60 \text{ mm} \times 60 \text{ mm} \times 3 \text{ mm}$ and were meshed with 8 node hexahedral elements with one Gaussian integration point (ELFORM = 1). The element size chosen for rigid plates was 1 mm to avoid the formation of three-dimensional stress wave in a rigid or elastic [7]. On the other hand, the 3DRAH structure was meshed using tetrahedron elements (ELFORM = 13), which are similar to tetrahedron elements with one integration points but with an additional average of pressure. This additional averaging of nodal pressure, decreases the volumetric locking observed in numerical simulations involving incompressible or ductile materials. The element size chosen for auxetic sample was $t/2$ i.e., 0.621mm to avoid the formation of volumetric locking as well as negative volume that arises due to large element size in tetrahedral elements.

Constitutive Law

Constitutive law is one of the most important factors of a FE model. If not chosen wisely, it shall lead to divergence of the numerical simulation. Quite a few authors in our literature survey have stated that the behavior of the bulk material of an auxetic structure will affect the behavior of the structure. Put in simpler words, the ductility or brittleness of the bulk material will have an influence on the auxetic behavior. The

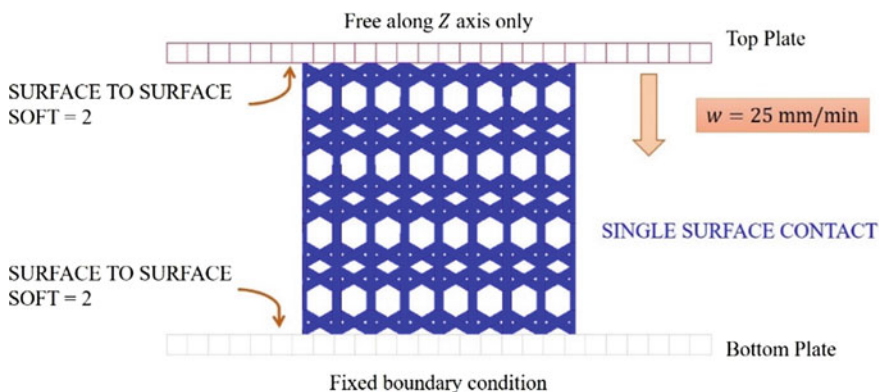


Fig. 1 The finite element model of the rigid plates and 3DRAH structure assembly with other details

loading plates were assumed to be rigid in nature, thus, the material model *MAT-009 RIGID of LS Dyna material library was used to define them, using density 7800 kg m⁻³, Young’s Modulus of 210 GPa and Poisson’s Ratio 0.3.

In this study, we have investigated four different materials as bulk material for auxetic structure: Poly Lactic Acid (PLA), Acrylonitrile Butadiene Styrene (ABS), Nylon and High-Impact Poly Styrene (HIPS). All four materials were modelled using a Piecewise Elastic Plastic constitutive law (*MAT-024) in the LS Dyna material library. The MAT-024 constitutive law in LS Dyna, provides the user with the option of giving either the basic data for the plastic behavior or a set of eight data points in terms of plastic strain and plastic stress. The first method was chosen in this work.

The constitutive law assumes an isotropic hardening behavior by default. The yield function (ϕ) post elastic domain is

$$\phi = \frac{1}{2} S_{ij} S_{ij} - \frac{\sigma_P^2}{3} \leq 0 \tag{5}$$

The parameters S_{ij} and σ_y are deviatoric stress components and plastic stress respectively. This material model does offer the consideration of strain rate effects on the plastic domain. The strain rate sensitive plastic stress is given in Eq. 6, that is considered through Cowper-Symmonds Law. In addition to that, σ_{y0} is the material yield strength, E_P is the plastic modulus and ϵ_{eff}^P is the effective plastic strain.

$$\sigma_P = \left[1 + \left(\frac{\dot{\epsilon}}{C} \right)^{\frac{1}{p}} \right] \{ \sigma_{y0} + E_P (\epsilon_{eff}^P) \} \tag{6}$$

$$E_P = \frac{E_{TAN} \cdot E}{E_{TAN} + E} \tag{7}$$

Here, E is the Young’s Modulus of the material and E_{TAN} is the tangent modulus of the plastic phase of the material. For example, the presents the stress strain curves from literature (round markers) and the interpolated model using basic data from LS Dyna (dashed black line). A summary of the MAT-024 inputs given form all materials is presented in Table 1 (Fig. 2).

Table 1 Material properties required to define the *MAT-024 constitutive law in LS Dyna

Bulk material	Density ρ (kg/m ³)	Young’s modulus E (GPa)	Poisson’s ratio ν	Yield strength σ_y (MPa)	Tangent modulus E_T (GPa)	Source
PLA	1240	0.973	0.36	15.7	0.513	[8]
ABS	1010	1.05	0.3	34	0.491	[2]
Nylon	984	0.493	0.39	36.1	0.295	[2]
HIPS	1080	2.05	0.35	19.3	0.534	[9]

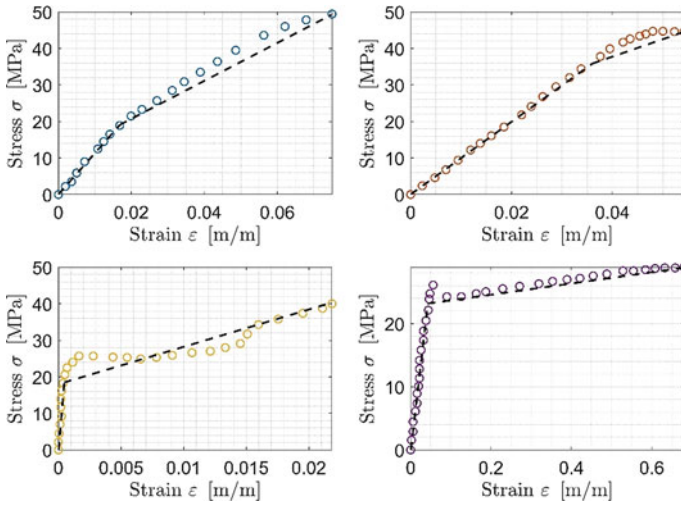


Fig. 2 Constitutive law adaptation by *MAT-024 for PLA (top left), ABS (top right), nylon (bottom left) and HiPS (bottom right) using material properties in Table 1

Boundary Conditions and Contact

Boundary conditions are also one of the important aspects for a good and reliable FE model. The experimental test is uniaxial; therefore the bottom plate is fixed whereas the top plate is given a displacement boundary condition along z axis at a rate of 25 mm min^{-1} . The auxetic sample was free to move along all three directions.

Another important aspect of the numerical simulation is the transfer of forces from the rigid plate to auxetic sample. This is possible by defining an appropriate contact algorithm between the rigid plates and auxetic sample. Even though the rigid plate moves at a constant speed, in turn applying load on the auxetic structure, the energy transmission between each constituent of the assembly as well as the transmission of forces between two continuums cannot be done just by giving different properties. There must be a physical contact that shall help the solver to recognize different continuums of the system. For this purpose, a total of three contacts were defined between each constituent of the assembly. An automatic surface to surface contact based on the pinball segment penalty formulation was defined between the auxetic and the rigid plates (*CONTACT_AUTOMATIC_SURFACE_TO_SURFACE with SOFT = 2 option of LS Dyna). The pinball segment-based penalty formulation i.e., SOFT = 2 was chosen due to the difference in the order of magnitudes of the material properties of plate and auxetic structure. To avoid the interpenetration of elements of the auxetic structure along the compression process, a single surface contact was defined between the elements of auxetic structure (*CONTACT_AUTOMATIC_SINGLE_SURFACE of LS Dyna). It is to be duly noted that all contacts were assumed to be friction less. A pictorial representation of

the FE mesh alongside boundary conditions and contact indications is presented in Fig. 1.

3 Results and Discussions

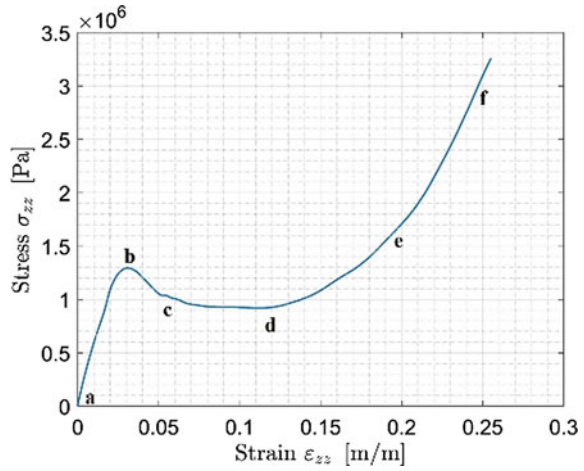
The contact algorithm used in this study, gives us the contact force between two contact surfaces i.e., top plate and auxetic as well as auxetic and bottom plate. Taking the contact force between top plate and the auxetic structure, we can easily determine the corresponding stress values in the auxetic. Moreover, the numerical model will also provide us with the displacement of the sample along X , Y , and Z axes with respect to time. These displacements shall lead us to the corresponding nominal strain values with respect to time. The initial lengths of auxetic along all three directions are 40×10^{-3} m respectively and the initial area A_0 is 0.0016m^2 in the transversal plane i.e., the XY plane. These give us the nominal stress and nominal strains along the loading and transversal directions.

3.1 Stress Versus Strain Response of 3DRAH Samples

The stress strain response of all auxetics showed three stages, initial elastic phase till yield, reduction of rigidity and plateau stage, and the densification stages. During the initial elastic stage, the struts show elastic deformation. If the applied load is removed before the structure starts to yield, the structure will come back to its original position. Post the yield point (i.e., point b) the struts start to buckle or bend, therefore, projecting loss of rigidity of the structure. If we continue the loading, the stress levels start to stabilize at a constant value for increased deformation. This indicates that the struts are undergoing buckling process till the onset of densification or one part of the auxetic structure is buckling whereas the other part is still intact. Post this point, the struts are totally distorted so that even small increase in strain will induce large stress concentrations and hence contributing to exponential increase of stress.

The physical states of the PLA-3DRAH corresponding to the key points in the stress strain curve (see Fig. 3) are presented in Fig. 5. The stress strain curve can be linked to the physical state of the sample. For example, let us see the state **b**, which corresponds to yield of the structure. At this point, we see the first lateral distortion (in XY plane) of the sample (twisting like a Rubric cube), which is due to the bending of struts. An increase in stress will lead to more distortion and thus loss of rigidity till the point **c**. Further increase in load, will make the sample to twist as well as buckle along the longitudinal (YZ plane) and transversal plane (XZ plane). At certain point, the layers start to collapse, this marks the onset of densification stage (point **d**). Continuation of increase in stress, will add up to collapse of other layer till ultimate failure of the sample.

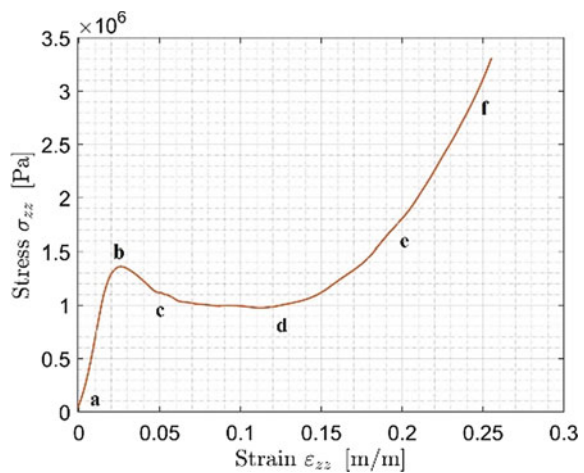
Fig. 3 Stress–strain response of PLA-3DRAH under uniaxial compression



The stress strain response of ABS-3DRAH (Fig. 4) also resembles the PLA-3DRAH, with minor changes as the values of stress and strain at the key points is almost the same for both PLA and ABS. This is because both ABS and PLA belong to the basic polymer family used in additive manufacturing. A keen observation to the Fig. 6 reveals that the struts buckle more with respect to those in Fig. 5 at yield point. In other words, the struts with ABS have the capacity of taking more loads before point **b**. Moreover, they also show evidences of more lateral distortion as well as out-of-plane and in-plane bending of the structure. Once the structure reaches densification stage, we can notice same response as that of PLA.

Similarly, the stress strain response and the physical states of the Nylon-3DRAH are presented in Figs. 7 and 9 alongside the HiPS-3DRAH counterparts in Figs. 8

Fig. 4 Stress–strain response of ABS-3DRAH under uniaxial compression



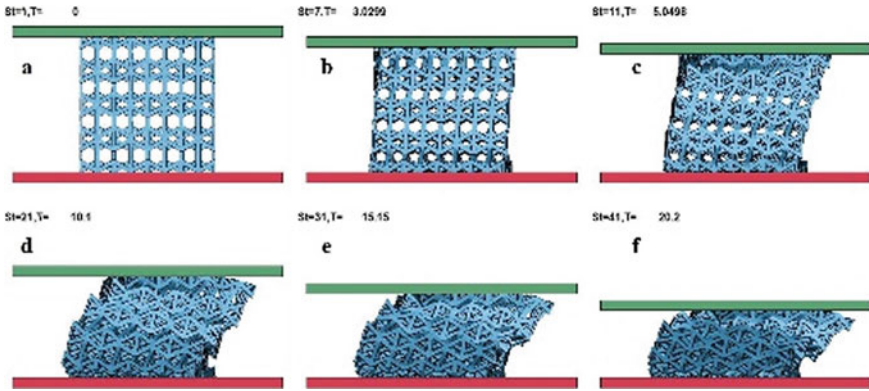


Fig. 5 Deformation states of PLA-3DRAH for corresponding key points

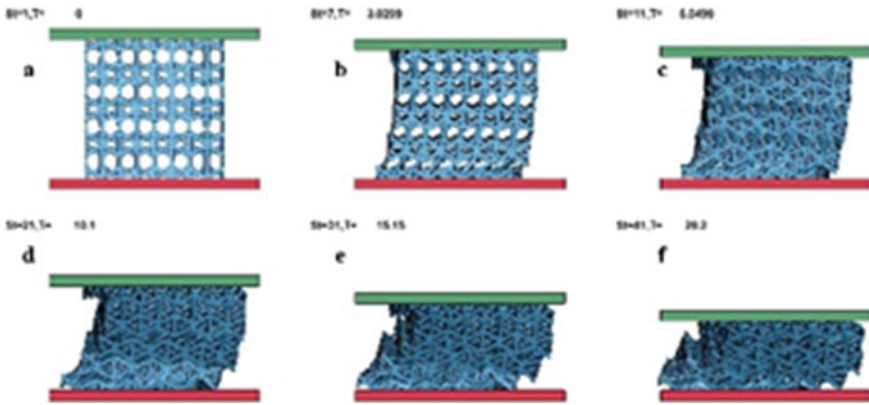
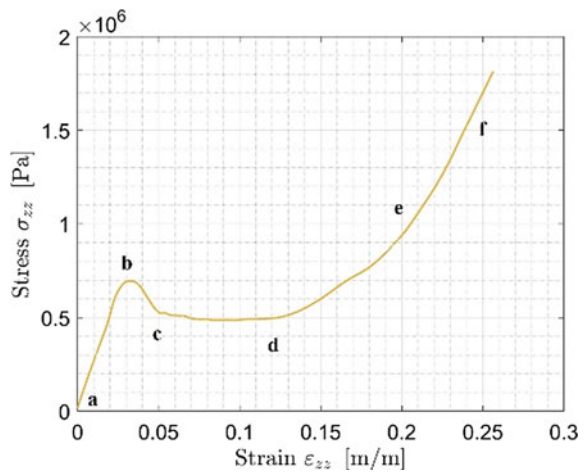


Fig. 6 Deformation states of ABS-3DRAH for corresponding key points

Fig. 7 Stress strain response of nylon-3DRAH under uniaxial compression



and 10. Similar to PLA and ABS, Nylon and HiPS show lateral distortion and in-plane/out-of-plane bending of the sample. Despite the fact that Nylon and HiPS belonging to the same family of polymers, they show very less similarities in the stress strain values. Simply stating, the stresses for HiPS are twice that observed in Nylon as in contrast to the PLA-ABS family. The stress strain responses yet prove the effect of bulk material on the behavior of 3DRAH structure (Table 2).

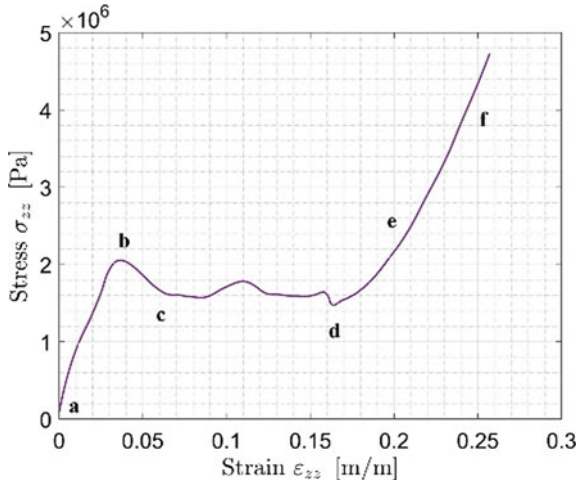


Fig. 8 Stress strain response of HiPS-3DRAH under uniaxial compression

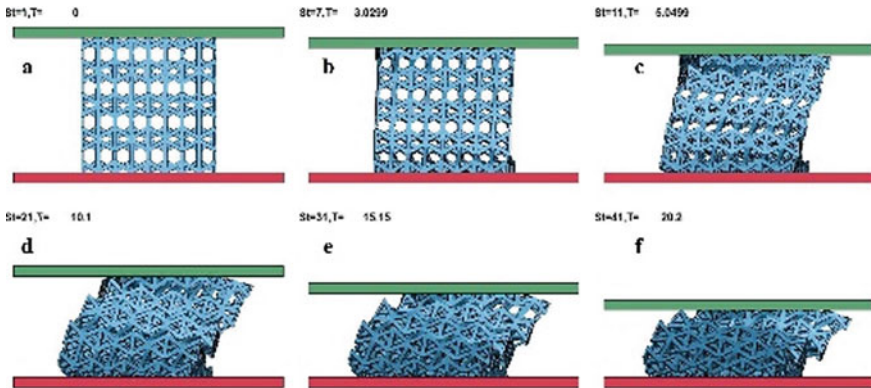


Fig. 9 Deformation states of the nylon-3DRAH for corresponding strain values

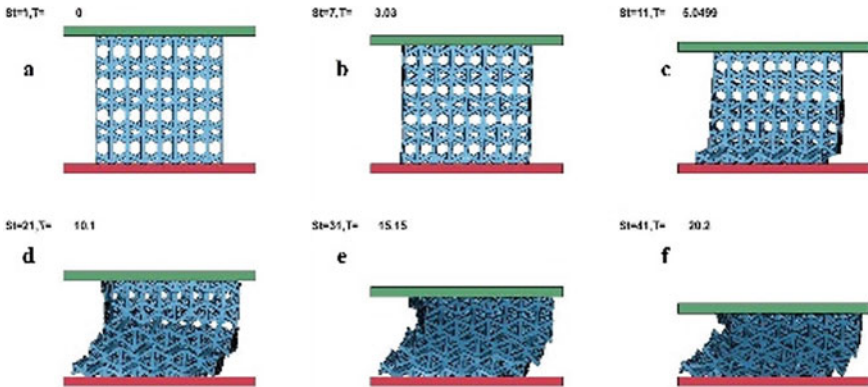


Fig. 10 Deformation states of the HiPS-3DRAH for corresponding strain values

Table 2 Summary of key points of the 3DRAH structure

Bulk material	Elastic modulus (MPa)	Yield strength (MPa)	Plateau stress (MPa)	Densification strain (m/m)	Densification modulus (MPa)
PLA	45.90	1.312	0.990	0.124	20.230
ABS	51.32	1.375	1.047	0.125	18.472
Nylon	22.17	0.696	0.518	0.123	10.528
HiPS	53.86	2.040	1.639	0.163	37.906

3.2 Poisson’s Ratio of 3DRAH Samples

Auxetic materials are different from conventional materials as they possess a negative Poisson’s ratio. The Poisson’s ratio ν_{xz} and ν_{yz} were calculated from strains specified above. The longitudinal direction in this study is Z and the lateral directions are X and Y. A comparison of the Poisson’s ratio for all bulk materials along both lateral planes (ν_{xz} , ν_{yz}) are presented below. The variation of Poisson’s ratio with the longitudinal strain ϵ_{zz} are represented by solid lines and the corresponding value at densification strain (ϵ_d) are represented by star markers.

Since the auxetic structure is no longer reliable after the densification point as there will be damage and failure of struts, we consider only the variation of Poisson’s ratio only till the densification point (point **d**). The Poisson’s ratio for PLA, ABS, and Nylon shows an initial increase, followed by a decrease in Poisson’s ratio before the densification point (see Fig. 11). Whereas, HiPS in contrast shows a monotonic increase. This conclusion is valid for both ν_{xz} and ν_{yz} in Fig. 12. A quantitative comparison of the Poisson’s ratio for all bulk materials is presented in Table 3

Seeing these numbers, it is evident that the 3DRAH structure shows relatively good Poisson’s ratio performance along the XZ plane when compared to YZ plane.

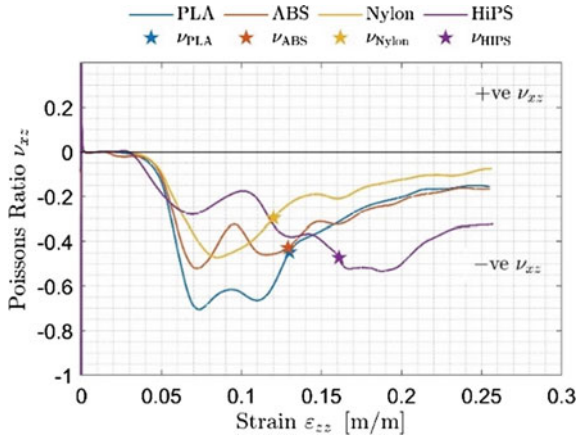


Fig. 11 Poisson's ratio ν_{xz} for all bulk materials

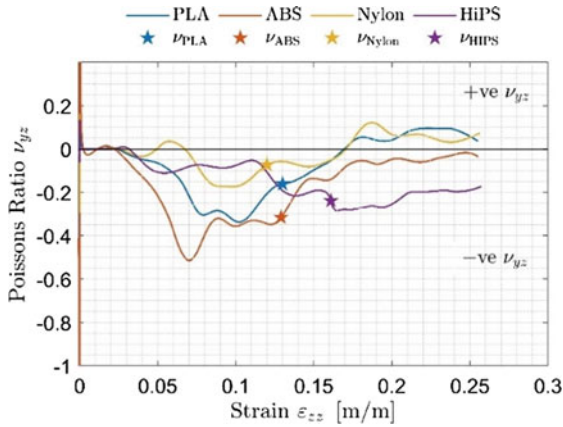


Fig. 12 Poisson's ratio ν_{yz} for all bulk materials

Table 3 Poisson's ratio for all bulk materials at densification point (star markers)

Bulk material	Poisson's ratio ν_{xz}	Poisson's ratio ν_{yz}
PLA	- 0.47	- 0.16
ABS	- 0.44	- 0.32
Nylon	- 0.27	- 0.06
HiPS	- 0.52	- 0.28

3.3 Energy Absorption of 3DRAH Samples

The interest of auxetic structures is to have high energy absorption capacity for a given loading condition. The energy absorbed by an auxetic structure is the area under the stress strain curve till the point of densification. In simpler terms, it is the strain energy that we are talking about. Similar to the Poisson’s ratio, the energy absorbed should be considered only till the point of densification. There are several indices that are used to evaluate the energy absorption capacity of an auxetic material. The common parameter is the Specific Energy Absorption (SEA), which is energy absorbed per unit mass of the sample. This is the index that we follow here. A quick look to Fig. 13 reveals that the HiPS-3DRAH is the one with high energy absorption whilst the Nylon-3DRAH is the one that has the least.

As mentioned in Sect. 2.1, all geometries have a volume of 640000mm³. The difference in SEA arises from the deformation mechanism of the sample and the density of the bulk material. Table 4 shows the quantitative comparison of all four bulk materials.

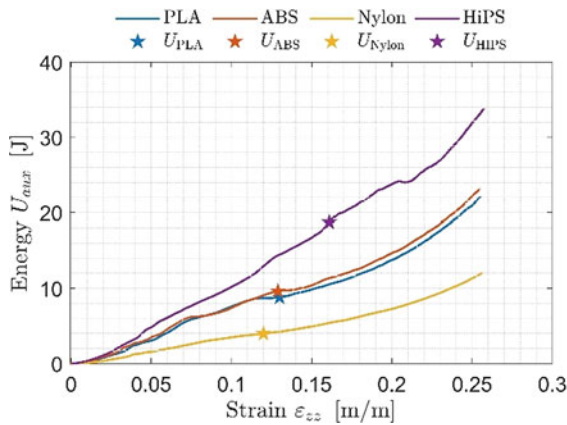


Fig. 13 Energy absorbed by different samples and their corresponding energies at densification

Table 4 Strain energy absorbed and SEA index at densification for all samples

Bulk material	Strain energy, U (J)	Density, ρ (kg m ⁻³)	Mass (kg)	SEA (J kg ⁻¹)
PLA	8.731	1240	0.0794	110
ABS	9.580	1010	0.0646	148.3
Nylon	4.053	984	0.0630	64.33
HiPS	19.67	1080	0.0691	284.68

4 Conclusions

Finite element simulations of 3DRAH structures under quasistatic uniaxial compression were carried out. A total of four different bulk material properties were tested for the structure. All sample showed dominant shear, lateral distortion due to a mixed stress state of tension, compression, bending and shear among the struts of the structure. Change in bulk material affects the quantities which control stress–strain response and energy absorption. Auxetic samples made from High-impact Poly-Styrene is the one that showed better performance in stress–strain behavior as well energy absorbed during the compression period till densification. As Young’s modulus of the bulk material increases, structural properties like Elastic modulus, Yield stress, Plateau stress and the SEA of the structure increase. No specific correlation was observed between mechanical properties of the material and the densification strain of the structure. The samples in fact undergo large deformation, this means that damage accumulation in the bulk material shall further affect the performance of the structure. A study consider the adverse effects of damage is in progress, which will shed more light in understanding the exact behavior of 3D Reentrant Auxetic Honeycomb under quasistatic as well as dynamic loading.

References

1. Zhang, J., Lu, G., You, Z.: Large deformation and energy absorption of additively manufactured auxetic materials and structures: a review. *Composites Part B* **201**, 108340 (2020)
2. Alex, R., Dulara, K., Tuan, N., Priyan, M., Gursel, A., Andrew, W.: Development and performance evaluation of large-scale auxetic protective systems for localized impulsive loads. *International Journal of Protective Structures* **10**, 390–417 (2019)
3. Faraci, D., Driemeier, L., Comi, C.: Bending-dominated auxetic materials for wearable protective devices against impact. *J. Dynamic Behavior Mater.* 2199–7454 (2020)
4. Yang, L., Harrysson, O., West, H., Cormier, D.: Mechanical properties of 3D re-entrant honeycomb auxetic structures realized via additive manufacturing. *Int. J. Solids Struct.* **69–70**, 475–490 (2015)
5. Ou, Y., Yan, S., Wen, P.: In-plane impact dynamics analysis of re-entrant honeycomb with variable cross-section. *Computer Modeling in Engineering Sciences* (2020)
6. Hu, L.L., Zhou, M.Z., Deng, H.: Dynamic crushing response of auxetic honeycombs under large deformation: theoretical analysis and numerical simulation. *Thin Walled Struct.* **131**, 373–384 (2018)
7. Ayagara, A.R., Langlet, A., Hambli, R.: On dynamic behavior of bone: experimental and numerical study of porcine ribs subjected to impact loads in dynamic three-point bending tests. *Journal of Mechanical Behavior of Biomedical Materials* **98**, 336–347 (2019)
8. Alhabri, M., Kong, I., Patel, V.I.: Simulation of uniaxial stress-strain response of 3D-printed polylactic acid by nonlinear finite element analysis. *Applied Adhesive Science* **8**, 2895 (2020)
9. Dagli, G., Argon, A.S., Cohen, R.E.: Particle-size effect in craze plasticity of high-impact polystyrene. *Polymer* **36**, 2173–2180 (1995)

Path-Planning of Robot End-Effector for Hairline Crack Sealing Using Intelligent Techniques



Santosh Kumar and B. Sandeep Reddy

Abstract Recent years have seen robotics expand to the development of various inspection and repair technologies. Robotic solutions are being explored for the development of technologies to repair cracks and leakages in industrial pipelines. Literature review indicates that a lot of cracks in industrial pipes are in the form of straight lines or a hairline, at the initial stage and gradually increase with time. However, if repaired at the initial stage, these cracks can be prevented from propagating. Crack repair requires an appropriate tool placed at the end-effector of a robot, and further requires that the end-effector is able to trace the path formed by the crack. In such a manner, if the end-effector holds the sealing device, it can be applied over the crack to seal it effectively. In this paper, the path planning of the end-effector of a 3-DOF manipulator is presented using intelligent techniques, to ensure that the end-effector can trace the path over the crack. ANFIS (Adaptive Neuro-Fuzzy Inference System) is used to address the inverse kinematics problem. The Gaussian (gauss) membership function is utilized in the ANFIS architecture during the training process.

Keywords Inverse kinematics · Repair robot · Workspace · ANFIS

1 Introduction

Robotics is the fastest growing industry nowadays. The challenges faced in robotics range from inspection to repair to path planning to control strategies and positional accuracy. Robots are generally used to save a human being from laborious and dangerous work. Recent advances in robotics indicate a growing trend to apply the principles of robotics for developing maintenance, inspection and repair technologies

S. Kumar (✉)
IIT Guwahati, Guwahati, India
e-mail: santosh_kumar@iitg.ac.in

B. S. Reddy
Mechanical Engineering, IIT Guwahati, Guwahati, India
e-mail: bsandeepr@iitg.ac.in

© The Author(s), under exclusive license to Springer Nature Singapore Pte Ltd. 2022
K. C. Popat et al. (eds.), *Advances in Mechanical Engineering and Material Science*,
Lecture Notes in Mechanical Engineering,
https://doi.org/10.1007/978-981-19-0676-3_22

271

for industrial pipelines. Great dangers are posed to the health of workers involved in cleaning and repairing operations in industrial pipelines [1]. There are many types of toxic gases produced especially in sewer pipelines. The primary component of sewer gas includes hydrogen sulfide, methane, ammonia, and carbon dioxide, which if inhaled, may lead to death. Further problems exist in the actual conducting of inspection, maintenance and repairs in real pipelines due to poor accessibility to various parts of the pipelines, inaccurate fault/leak detection methods, the requirement of continual condition monitoring and so on. One of the major problems in the use of robotics technology in the development of robotic repair technologies is that repair requires the use of a manipulator system with an end-effector (holding the tool for repair), to navigate in closed pipelines. Given the restricted diameter of pipelines and pipeline bends, manipulation of the end-effector becomes problematic. In mathematical terms, manipulation requires the inverse kinematics solutions to exist [2].

This paper deals with the case of cracks in industrial pipelines. Sewer pipelines, for example, are made up of concrete and stoneware for smaller dimensions and brickwork and reinforced concrete for larger dimensions. The crack in a sewer pipe is generally hairline in nature at the initial stage and gradually increases with time. The leading cause of cracks in sewer pipelines is improper construction, improper maintenance, and high traffic load [3]. When it comes to the development of robotic technologies for repairing cracks, then certain questions arise as to the choice of the robotic system and its design, the type of end-effector to be used, path planning and control of the end-effector and so on. One of the most important problems in such a case is one of path planning as it is necessary to accurately describe the desired end-effector motion within the physical constraints imposed by the pipeline. In this paper, a 3-DOF serial robot manipulator is considered which has to navigate an industrial pipeline bend (shown in Fig. 1) to repair a crack. Figure 1a, b show a schematic of the problem considered in this paper comprising repair of cracks in a pipeline using a 3-DOF planar robot. The robot, although wheeled, is presumed to remain stationary

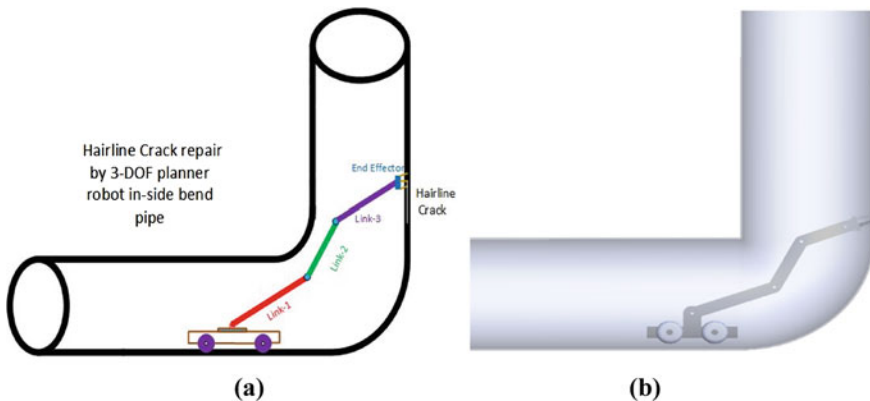


Fig. 1 a Line diagram and b cad model, of sewer pipeline with inspection robot

at the time of repair and only the links (arms) will rotate to guide the end-effector to carry out the repair.

The guiding of the end-effector for repair requires the computation of inverse kinematics of the 3-DOF robot. The study of forward kinematics of serial robots is a simple task, but computing inverse kinematics is more challenging as the relation between joint space and Cartesian space contain nonlinear term which involves transcendental equation having more than one solution. Although the 3-DOF serial robot inverse kinematics has been analytically computed in literature [2], more efficient computational methods are needed when dealing with real-life robots (especially when DOF is higher than three). Furthermore, to the best of our knowledge, 3-DOF robotic systems and their use in the repair of cracks has not been investigated. Efficient methods for the computation of inverse kinematics, has in recent years lead to the use of intelligent techniques. The two most popular soft computing techniques are artificial neural network and Adaptive Neuro-Fuzzy Inference System [3–6]. These techniques generate faster input–output relations than analytical methods. In these techniques, the network is trained by the large data of forward kinematics and the solution for inverse kinematics is accordingly computed.

The paper is organized as follows. In Sect. 2, the 3-DOF planar robot is described. In Sect. 3, the ANFIS technique which will use for inverse kinematics computation is described. In Sect. 4, ANFIS technique is applied for generation of inverse kinematics of the 3-DOF serial robot. Section 5 compares the ANFIS technique to the analytically computed inverse kinematics solution developed in literature. Section 6 presents the conclusion and future work in related areas.

2 Description of 3-DOF Serial Robot

In this work, we have considered a 3-DOF serial robot. The length of the links a , b , and c are 125 cm, 85 cm, and 65 cm, respectively and all the joints of the manipulator are rotary. The first link of a robot is fixed on a cart and the last link is connected to a three-finger gripper as the end effector. The forward and inverse kinematic solutions have been found analytically in literature [2]. Figure 2 illustrates the line diagram of the three-arm serial robot.

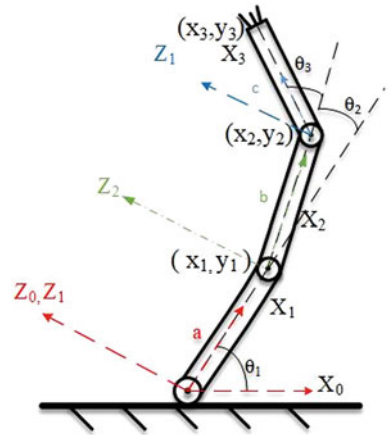
The forward kinematics, providing the end-effector positions for a given set of joint angles, can be described as

$$x_3 = a \times \cos \theta_1 + b \times \cos(\theta_1 + \theta_2) + c \times \cos(\theta_1 + \theta_2 + \theta_3) \quad (1)$$

$$y_3 = a \times \sin \theta_1 + b \times \sin(\theta_1 + \theta_2) + c \times \sin(\theta_1 + \theta_2 + \theta_3) \quad (2)$$

The inverse kinematics relations, describing the joint angles for a given set of end-effector positions, are as below.

Fig. 2 Schematic of 3 DOF serial robotic arm



$$\varphi = \tan^{-1}\left(\frac{y_3}{x_3}\right) \tag{3}$$

$$x_2 = x_3 - c \times \cos \varphi, \quad y_2 = y_3 - c \times \sin \varphi$$

$$\theta_2 = -\cos^{-1}\left(\frac{x_2^2 + y_2^2 - a^2 - b^2}{2 \times a \times b}\right) \tag{4}$$

$$\theta_1 = \tan^{-1}\left(\frac{y_2}{x_2}\right) - \tan^{-1}\left(\frac{b \times \sin \theta_2}{a + b \times \cos \theta_2}\right) \tag{5}$$

$$\theta_3 = \varphi - \theta_1 - \theta_2 \tag{6}$$

The (x_1, y_1) , (x_2, y_2) , and (x_3, y_3) are the end coordinate of link 1, link 2, and link 3. And θ_1, θ_2 , and θ_3 are the angle of the respective link. This can be found in Eqs. (1–6). The above Eqs. (1) and (2) represent the positions, and Eq. (6) illustrates the orientation of the last link (end-effector) [2].

3 The Intelligent Technique (ANFIS) for Path Planning

ANFIS technique is based on the principle of neural networks and fuzzy logic. The adaptive neuro-fuzzy inference system was been proposed by Jang and Sun [4]. Both neural networks and fuzzy logic are model-free estimators and share the common ability to deal with uncertainties. Details on ANFIS can be found in the reference [5], which applies ANFIS for control of robotic manipulators. However, for the sake of completeness, ANFIS is described in brief as below. ANFIS network has five different layers, namely, nodes layer, membership layer, rule layer, defuzzification,

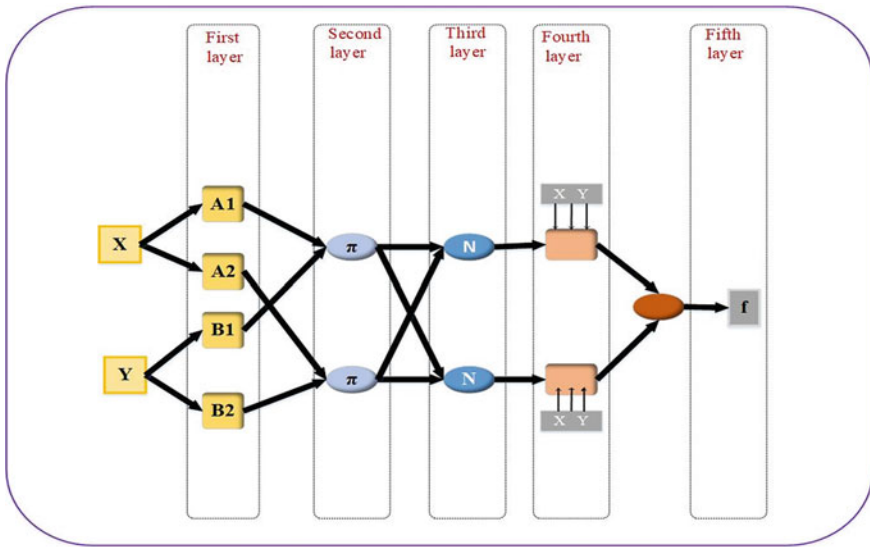


Fig. 3 Architecture of ANFIS technique

and output layer for solving the problem. The structure of the ANFIS network is shown in Fig. 3. The various layers can be described as follows.

Layer 1: Fuzzification layer

In this layer input, x and y are fuzzified by the adaptive node of this layer. For each crisp input, x and y have fuzzy sets, and attached corresponding membership functions that give a degree of membership variable with respect to fuzzy sets. These will be the output of the node. The fuzzy set for crisp inputs x and y are represented by $A_j (j = 1, 2)$ and $B_j (j = 1, 2)$. Moreover, membership functions are represented by $\mu_{A_j}(x)$ and $\mu_{B_j}(y)$. The Membership functions are so many types for this layer like triangular, trapezoidal, Gaussian, bell shaped, and sigmoid. In this paper, Gaussian member function [6] is used whose membership value is

$$\mu(x; \sigma, a) = e^{-\frac{(x-a)^2}{2\sigma^2}}$$

where parameter σ denotes the width of the curve and a shows the distance from the origin.

Layer 2: Rule layer or product (T-norm operation) layer

In this layer, the node will connect the antecedent part of the rules by using the algebraic product. The output of this layer will be the product of all incoming input.

$$w_j = \mu_{A_j}(x) \cdot \mu_{B_j}(y)$$

Layer 3: Normalization layer

Each node of this layer receives input from all the nodes of the previous layer and calculates the firing strength of a given rule. The normalized firing strength of the j th point can be calculated by the j th nodes firing strength to the sum of all rules of firing strength.

$$\bar{w}_j = \frac{w_j}{w_1 + w_2}$$

where \bar{w}_j shows the normalized firing strength of given rule.

Layer 4: Defuzzification layer

In this layer, nodes are connected to the corresponding normalization node, and receives the initial signal x and y . The defuzzification node determines the weighted consequent value of a given rule which may be represented as follows

$$\bar{w}_i \cdot f_i(x, y) = \bar{w}(p_i x + q_i y + r_i)$$

where \bar{w}_i represents the normalized weight of rule i , $f_i(x, y)$ is the output function, p_i , q_i and r_i are linear consequent parameters represent the total number of rules in the rule base.

Layer 5: Summation layer

In this layer, we calculate the overall output of the ANFIS network, by summing all defuzzification signals from the previous layer.

$$\text{Final output} = \sum_{i=1}^2 \bar{w}_i \cdot f_i(x, y) = \frac{\sum_{i=1}^2 w_i \cdot f_i(x, y)}{\sum_{i=1}^2 w_i}$$

In all of these layers, two types of the node are used first: a square node for adaption of the parameters, and a circular node which behaves like a fixed node with no parameter [7–12].

4 Implementation of ANFIS for Computation of Inverse Kinematics of the 3-DOF Serial Robotic Arm

In this section, the use of the ANFIS approach to find the inverse kinematics of a 3-DOF system is presented. ANFIS works on the principle of training and testing of the input–output dataset. In the training dataset, the joint variable (θ) is regarded as an input dataset and the Cartesian coordinates of the robot's end-effector (x and y) are considered output datasets. The array of output datasets (x and y) is generated by

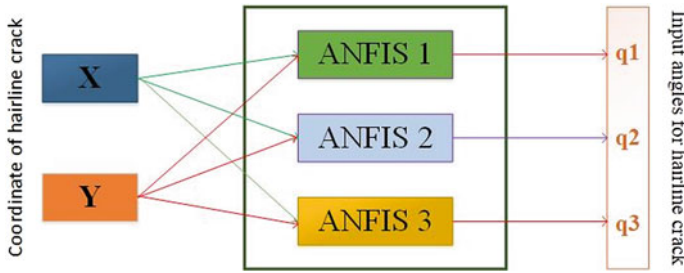


Fig. 4 ANFIS network for computing inverse kinematic solution of a hairline crack

feeding joint angles θ_1 , θ_2 , and θ_3 into forward kinematic formulations. The range of joint angles to form the input–output training dataset is as follows.

$$\theta_1 = \pi/6 : 0.04 : \pi/4, \theta_2 = -\pi/2 : 0.04 : \pi/3, \theta_3 = -\pi : 0.04 : \pi/6.$$

After forming the training dataset, for the given data set (θ_1 , θ_2 , and θ_3), three ANFIS models are generated (ANFIS 1, ANFIS 2, and ANFIS 3) using *genfis* command in MATLAB. Further, in the testing phase, the ANFIS predicted inverse kinematic solutions (q_1, q_2, q_3) are computed for the desired trajectory using *evalfis* command. The relationship between crack trajectory and ANFIS-estimated joint angles is shown in Fig. 4, as follows [13].

The three training datasets are constituted as (x, y, θ_1) , (x, y, θ_2) , and (x, y, θ_3) where total 16 rules are formed considering four MFs for each input parameter. These rules are responsible for establishing the information base. A total of 10 epochs are considered after running the training network several times with different number of epochs. The training process is stopped when specified tolerance level is achieved. By default, a neuro-fuzzy model uses two network learning methods; backpropagation- and hybrid-based. The first one uses a gradient descent algorithm [14], while the second one utilizes the least square method [15] and gradient descent algorithm to calculate the error. The second one, i.e., hybrid one, is used in this work to train ANFIS architecture.

5 Results and Discussions

In this section, the numerical simulation results of the application of ANFIS for computing inverse kinematics solutions is presented. Figure 5 shows the plots of the various configurations of the manipulator based on inverse kinematics solutions computed (both analytically and using ANFIS). MATLAB has been used for computational purposes.

In Fig. 5a, the workspace of the end-effector for which the ANFIS network is trained is shown. In this, we have restricted ourselves to a specified range of θ_1 ,

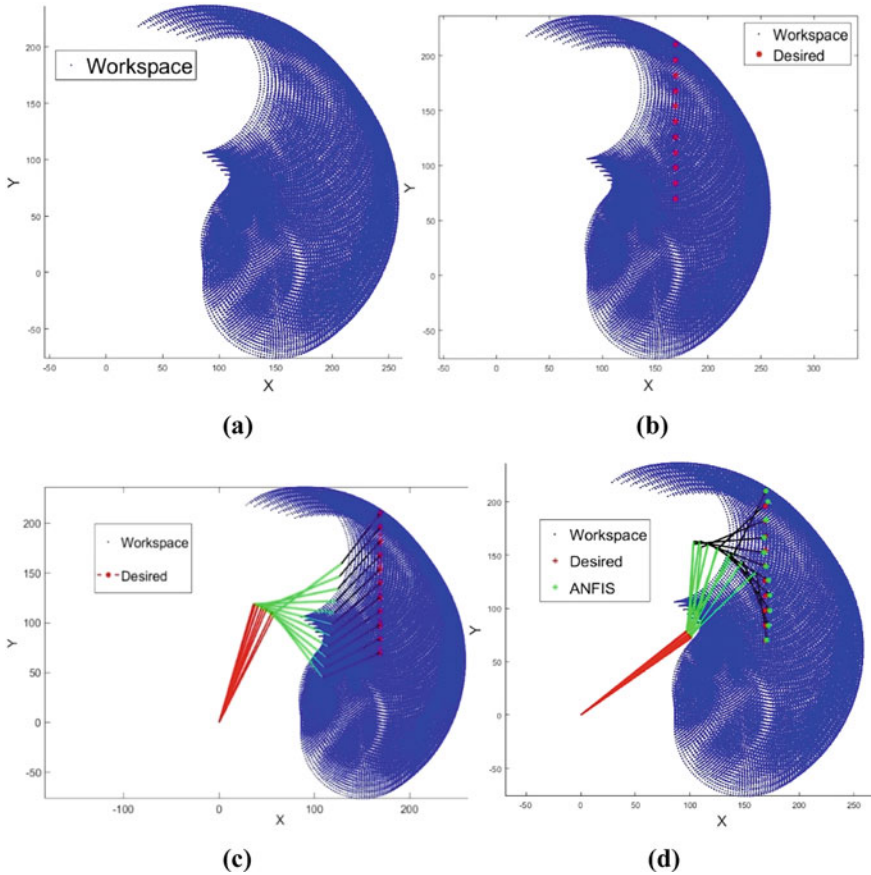


Fig. 5 a Workspace of end-effector, b the desired coordinate points along the hairline crack, c analytical inverse kinematics solutions by via points, d desired, and ANFIS coordinate point along hairline crack

θ_2 , and θ_3 as mentioned in section IV. Because, under training and overtraining both deviate from the result. Figure 5c shows the desired path along the hairline crack (i.e. the analytically obtained inverse kinematics solutions). Figure 5d shows a comparison between the manipulator configurations based on inverse kinematics solutions obtained analytically when compared to those obtained using ANFIS. The crack path is assumed as a straight line. And the equation of this straight path is $x = 169$ units, and y varies from 210 to 70 units.

The error of each point has been shown in Table 1. It is found that the deviation of the end effector, in this case, is the range of micrometer, which is tolerable for hairline crack (Table 2).

From Tables 3 and 4, it is found that there is little difference in solutions obtained analytically and via ANFIS, for joint 1. But at joint 2 and joint 3, the difference

Table 1 Error in coordinate (X, Y) on a hairline crack

S. No.	Erx (error in X coordinate) in mm scale	Ery (error in Y coordinate) in mm scale
1	0.0745571300084237	-0.00481438686590536
2	0.241960653390669	0.397849419493977
3	0.0778327574824544	0.115311398387598
4	-0.127632931576937	-0.172405936520187
5	-0.153713787794354	-0.187429139625587
6	0.0222301887538322	-0.0697010733479402
7	0.261517945983374	0.0207083503058215
8	0.414466695796608	0.0331909035000137
9	0.404964936853568	0.00138729688327004
10	0.271482987895453	-0.00414613918066209
11	0.138677114371686	0.0304737618740475

Table 2 Input angles for hairline crack repair by analytical and ANFIS method

S. No.	θ_{1A} Desired input	q_1 ANFIS input	θ_{2A} Desired input	q_2 ANFIS input	θ_{3A} Desired input	q_3 ANFIS input
1	1.0806	0.6836	-0.4650	0.3459	0.2776	0.0781
2	1.1813	0.6266	-0.8063	0.6682	0.4842	-0.5322
3	1.2335	0.6212	-1.0392	0.8496	0.6281	-1.0623
4	1.2623	0.6480	-1.2261	0.8837	0.7462	-1.4408
5	1.2747	0.6749	-1.3849	0.8280	0.8491	-1.6695
6	1.2738	0.6840	-1.5234	0.7466	0.9414	-1.8063
7	1.2610	0.6753	-1.6458	0.6685	1.0254	-1.9080
8	1.2372	0.6578	-1.7543	0.5895	1.1023	-2.0052
9	1.2029	0.6420	-1.8500	0.4875	1.1726	-2.1016
10	1.1587	0.6354	-1.9336	0.3402	1.2362	-2.1772
11	1.1053	0.6380	-2.0052	0.1475	1.2926	-2.2038

is large in comparison to joint 1. The same thing can also be observed in Fig. 6d. However, one major observation at joint 2 and 3 are the deviation of ANFIS angle from analytical are opposite in nature, i.e. the error is clockwise in the former and anti-clockwise in the latter. In other words, joint 2 is having a negative error then joint 3 is having a positive error. Actually in this case, the effect of joint 2 is compensated by joint 3. Therefore, the resultant effect on the end effector is very negligible.

For every position of the end effector of the 3-DOF robot, there will be two configurations: one is elbow up, and the other is elbow down solution. Most of the time, it has been observed that one of the desired solutions goes outside the pipe. In

Table 3 Minimum and maximum error at respective joint (analytical elbow up)

Joint	Error at joint 1	Error at joint 2	Error at joint 3
1	0.396983699061118	-0.810950179446667	0.199490637913691
2	0.554784578996670	-1.47456901099477	1.01644464429932
3	0.612256700725698	-1.88878363824177	1.69037518341620
4	0.614312184311730	-2.10975417391159	2.18702873949296
5	0.599810755512012	-2.21281401356801	2.51864819730823
6	0.589810316223132	-2.27000109735052	2.74774470457943
7	0.585690231910501	-2.31425074258355	2.93342931086449
8	0.579389373339927	-2.34370781161512	3.10752267331058
9	0.560917890200388	-2.33750503793550	3.27415638337131
10	0.523312710551048	-2.27385696963490	3.41335580534757
11	0.467385502596472	-2.15269124541966	3.49634496759702

Table 4 Error at the respective joint when elbow down position

Joint	Error at joint 1	Error at joint 2	Error at joint 3
1	0.0221148674188520	0.119075845312667	-0.35566655203377
2	-0.089420238726995	0.138106342079596	0.0479741089486149
3	-0.209852045701527	0.189533659322347	0.434166632279309
4	-0.345353877058462	0.342354897212324	0.694585729739234
5	-0.471660765967208	0.556889981546427	0.820415723673008
6	-0.574200129305971	0.776807747828878	0.864946304929136
7	-0.655079620217825	0.977328199610135	0.882620220799133
8	-0.724497817869547	1.16480348693352	0.902898565971418
9	-0.793945662925160	1.36252737460883	0.928987523952533
10	-0.871627896903169	1.59340845237608	0.941030990790800
11	-0.957937135146601	1.85776840685764	0.911207953062787

this case, the elbow-down solution is going outside the sewer pipe. The error at joint angles 1, 2, and 3 are shown in Table 4 when the elbow is in down configuration.

6 Conclusion and Future Work

In this work, the inverse kinematics of a 3-DOF robot has been determined by ANFIS technique. The technique has applications in the development of robotic technologies for hairline crack sealing. ANFIS supports potential conformity and involves computational cost. The main advantage of ANFIS is to solve non-linear, transcendental, and non-closed form solutions for higher DOFs manipulators without analytically

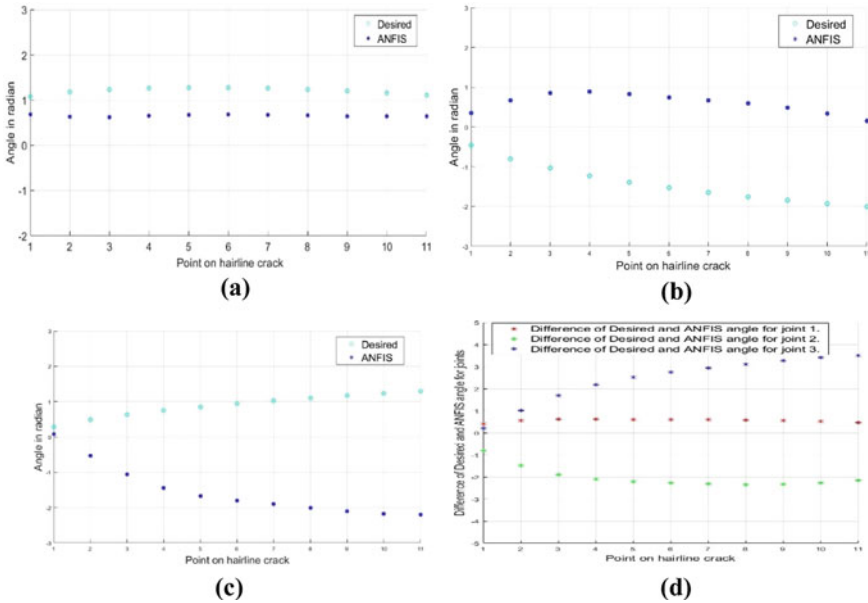


Fig. 6 **a** The input of the Desired and ANFIS angle for the first joint, **b** the input of the Desired and ANFIS angle for the second joint, **c** the input of the Desired and ANFIS angle for third joint, **d** the error of joint angles at respective point

finding the inverse kinematic solutions. Once the network is trained for a given workspace then the chances of error for a given workspace are less in this method. The above-mentioned intelligent method is currently being investigated for the case where obstacles exist in the path of crack and even in the path of the robot. Furthermore, the intelligent technique is also being investigated in the case of collaborative robots whose end-effectors can simultaneously follow the path of the crack in a synchronized manner. Thus, these results may be helpful in 3D space path planning.

References

1. Millar, A.: How robotics are ushering in a new era of pipeline repair technology (2020). <https://www.nsenerybusiness.com/features/pipelinerepair-technology-robotics/>
2. Ghosal, A.: Robotics: fundamental concepts and analysis (2006). Oxford University Press
3. Kampfer, W., Bartzke, R., Ziehl, W.: Flexible mobile robot system for smart optical pipe inspection. *Ndestruct. Eval. Util. Pipelines II* **3398**(March 1998), 75–83 (1998). <https://doi.org/10.1117/12.302534>
4. Jang, J.R.: ANFIS: adaptive-network-based fuzzy inference system. **23**(3) (1993)
5. Adhyaru, D.M., Patel, J., Gianchandani, R.: Adaptive neuro-fuzzy inference system based control of robotic manipulators. In: *ICMET 2010—2010 International Conference on Mechanical and Electrical Technology, Proceedings* **1**(1), 353–358 (2010). <https://doi.org/10.1109/ICMET.2010.5598379>

6. Adil, O., Ali, A., Ali, M., Ali, A.Y., Sumait, B.S.: Comparison between the effects of different types of membership functions on fuzzy logic controller performance. *Int. J. Emerg. Eng. Res. Technol.* **3**(April), 76 (2015). Available: <https://www.researchgate.net/publication/282506091>
7. Kundu, S., Parhi, D.R.: Navigational analysis for under water mobile robot based on multiple ANFIS approach. *J. Adv. Mech. Eng. Sci.* **1**(1), 46–56 (2015). <https://doi.org/10.18831/james.in/2015011005>
8. Chen, Y.H., Der Chang, C.: An intelligent ANFIS controller design for a mobile robot. In: *Proceedings 4th IEEE International Conference on Applied System Innovation 2018, ICASI 2018*, no. 1, pp. 445–448 (2018). <https://doi.org/10.1109/ICASI.2018.8394280>
9. Narayan, J., Jhunjhunwala, S., Gupta, M., Dwivedy, S.K.: Backpropagation neural network based design of a novel sit-to-stand exoskeleton at seat-off position for paraplegic children. In: *2020 6th International Conference on Control, Automation and Robotics ICCAR 2020*, pp. 546–552 (2020). <https://doi.org/10.1109/ICCAR49639.2020.9108021>
10. Imen, M., Mansouri, M., Shoorehdeli, M.A.: Tracking control of mobile robot using ANFIS. In: *2011 IEEE International Conference Mechatronics Automation ICMA 2011*, pp. 422–427 (2011). <https://doi.org/10.1109/ICMA.2011.5985695>
11. Narayan, J., Dwivedy, S.K.: Robust LQR-based neural-fuzzy tracking control for a lower limb exoskeleton system with parametric uncertainties and external disturbances. *Appl. Bionics Biomech.* **2021**, 1–20 (2021). <https://doi.org/10.1155/2021/5573041>
12. Algabri, M., Mathkour, H., Ramdane, H.: Mobile robot navigation and obstacle-avoidance using ANFIS in unknown environment. *Int. J. Comput. Appl.* **91**(14), 36–41 (2014). <https://doi.org/10.5120/15952-5400>
13. Duka, A.-V.: Neural network based inverse kinematics solution for trajectory tracking of a robotic arm. *Procedia Technol.* **12**, 20–27 (2014). <https://doi.org/10.1016/j.protcy.2013.12.451>
14. Mandic, D.P.: Descent algorithm. *Signal Process.* **11**(2), 115–118 (2004)
15. Axelsson, O.: A generalized conjugate gradient, least square method. *Numer. Math.* **51**(2), 209–227 (1987). <https://doi.org/10.1007/BF01396750>

Author Index

A

Aashish, R., 11
Abhay Gupta, 1
Abhinav Singh, 11
Akshaykumar Khatane, 217
Amit Malgol, 87
Aravind Rajan Ayagara, 257
Arpitha, G. R., 171
Ashesh Saha, 11, 23, 87

B

Baskar, P., 217

C

Chaitanya Vinayak Varma, 257

D

Debabrata Chakraborty, 159
Deepansh Gill, 181
Devaki Devi, K., 127
Diksha Jaurker, 237
Duc-Nam Nguyen, 139

G

Gopi Krishna, C., 47

H

Hamza Afser Delvi, 115
Harikrishnan, S., 37

I

Ich-Hung Dam, 139

J

Jitender Singh, 149
Jithin Velayudhan, 23

K

Karthik, J., 207
Kaveti Upender, 103
Kesav Chandran, 217
Kishore Babu, N., 47

M

Mahesh Kumar, T., 47
Manas Kumar Pal, 207
Manda Sreeja, 127
Manish, M., 37
Manoj D. Yadav, 199
MashtaqAhamed Attar, M., 115
Mayank Dey, 229
Mohammed Faheem, 115
Mohit, H., 171

N

Naga Phani Shastry, M., 127
Narayanan, M. D., 23
Nitesh Dhar Badgayan, 229

P

Phani Prabhakar, P., 47

Prabir Sarkar, [149](#)
Pradhan, M. K., [181](#), [237](#)

R

Rahul Vamsi Katabathuni, [229](#)
Rajdeep Ghosh, [159](#)
Rajidi Shashidhar Reddy, [1](#)
Ravi Kumar, B. V. R., [103](#)
Ridwan, [115](#)
Rohan Gooty, [257](#)
Ruban, R., [171](#)
Rudolf Ragis, [217](#)

S

Sandeep Reddy, B., [271](#)
Santosh Kumar, [271](#)
Santosh Kumar Sahu, [229](#)

Sarath Kumar, G. V., [47](#)
Sarth Shah, [63](#)
Satyajit Panda, [1](#)
Sher Afghan Khan, [115](#)
Sinchana, T. C., [199](#)
Souptick Chanda, [159](#)
Srinivasa Rao, M. S., [103](#)
Subhash, S. R., [199](#)
Suheel, J. I., [115](#)
Surbhi Razdan, [63](#)
Sushmitha, S., [199](#)

V

Van-Huong Vu, [139](#)
Van-Tuan Nguyen, [139](#)
Venkata Ramana, M., [103](#)
Vinothkumar, A., [171](#)
Vishwas Mahesh, [199](#)

Subject Index

A

Active control, 64, 78
Active magnetic bearing, 11–15, 18
Additive manufacturing, 257, 259, 264
Aesthetics, 149, 150, 152
Aluminium alloy, 182, 188, 190
Aluminum alloying, 103, 107, 209, 219, 221
Analysis of Variance (ANOVA), 127, 128, 132, 133, 135, 161, 166, 167, 186, 194
Angle of impact, 217, 219, 223, 226
ANSYS, 41, 44, 163, 186, 189, 190, 194, 195, 217, 218, 221, 232, 241, 260
Area ratio, 115, 122

B

Bifurcation, 23–25, 29–34
Bio-implant material, 229
Bone growth, 159–161, 164–166, 168, 169
Brake caliper, 24, 207–209, 212–215
Brake rotor, 207–212, 214, 215

C

Carbon Nano Tubes (CNT), 172, 229–233, 235
Chaos, 23, 24, 29, 30, 32, 34
Combustion, 116
Computational fluid dynamics, 38, 41, 72, 80
Conceptual design, 199, 201, 205
Continuous system, 25, 87, 100
Crash test, 217–219

D

Dental implant, 160, 229–231, 233, 235
Diesel, 175
DP steel, 48, 49, 51, 58
3D Reentrant Auxetic Honeycombs, 257, 270

E

Electrical Discharge Machining (EDM), 107, 237–245, 247–254
Electromechanical sensors, 146
Electrospinning, 139, 141, 144, 146
Emission, 48, 172, 240, 243
Ensemble learning, 103–105
Equivalent Von-Mises stress, 229, 232–235
Eye-tracker, 149, 152, 153

F

Fiber orientation, 139, 140, 142, 143
Finite element analysis, 181, 183, 190, 192, 229, 230, 232, 241
Flow control, 63–65, 76, 77, 81, 115, 120, 121, 123, 124
Formability, 49, 51, 58–60
Friction-induced oscillator, 23, 25, 34
Frictions Stir Welding (FSW), 103–107, 113, 187
Frontal structure, 217, 226

G

Gyroscopic effect, 87, 88, 90, 92, 94, 95, 100

H

Harmonic balance method, 1, 2, 4, 8
 Health care, 37, 38
 High Density Polyethylene, 229

I

Implant, macro-textures, 160–162
 Indoor air conditioning, 37, 38
 Inverse kinematics, 271–273, 276–278,
 280, 281
 IS:65032 aluminum alloy, 103, 108

J

Jeffcott rotor, 11, 12, 15–19, 21

K

Kelvin-Voigt model, 1, 2, 4, 6–8

L

Laser welding, 47–50, 54, 59
 LS Dyna, 257, 258, 260–262

M

Machine learning, 63–68, 70, 72, 75, 76,
 78–81, 103, 104, 106, 159, 160, 169
 Mechanical properties, 47–49, 59, 108,
 128, 182, 187, 209, 230, 257, 270
 Metal Removal Rate (MRR), 127, 128, 130,
 131, 133, 136, 239, 241, 244, 248,
 252
 Microjets, 115–117, 124
 Modal analysis, 23, 27, 28, 34, 87, 89, 90,
 100, 211
 Modelling, 5, 15, 64, 65, 71, 74, 75, 81,
 159, 161, 162, 183, 189–192, 195,
 218–220, 229, 232, 239–242
 Model predictive control, 11, 12, 14–19
 Multi Walled Carbon Nano Tubes
 (MWCNT), 171, 177, 178, 230

N

Nano additive, 171, 176, 178
 Nanocomposite, 229–231, 233, 235
 Nanofibers, 139, 141–144, 146
 Neural networks, 64, 66, 68, 70, 72, 73, 75,
 76, 79, 106, 127, 129, 131, 159–162,
 165–169, 195, 273, 274

P

Performance, 12, 14, 17, 24, 43, 64, 65, 69,
 73, 77, 80, 103, 104, 127, 131, 132,
 134, 135, 140, 141, 144, 146, 149,
 165, 166, 171, 172, 208, 209, 226,
 230, 239, 257, 258, 267, 270
 Piezoelectric fibers, 140
 Product design, 149, 150, 152

Q

Quasiperiodic route, 23, 29, 30, 32, 34

R

Reduced-order finite element model, 1, 2,
 5, 6, 8
 Repair robot, 271–273
 Residual stress, 185, 191, 193, 237, 238,
 240–254
 Respiratory droplets, 37, 38, 42–44
 Rotary inertia, 87, 88, 90, 92, 95, 100

S

Simulation, 12, 16, 17, 29, 38–40, 63, 64,
 72, 74–77, 80, 92, 165, 189,
 218–220, 223, 231–235, 237, 241,
 242, 245, 257, 258, 260, 262, 270,
 277
 Simulink, 11, 12, 15–17, 19–21
 Specific energy absorption, 269
 Stainless Steel (SS), 163, 167, 181–183,
 186, 189, 190, 194, 247, 248
 Stopping distance, 207–209
 Sudden expansion, 115, 116

T

Tailor Welded Blanks, 48
 Tensile properties, 50, 106
 Thermal stress, 237, 238, 240, 241, 245,
 249–253
 Tribological functions, 171
 TRIP steel, 48, 49, 51, 52, 58
 Turbulence modeling, 63, 72, 73

V

Ventilation, 37–39, 41, 43, 144, 145
 Vibration, 1–3, 11, 12, 15, 17–19, 24–26,
 29, 87–89, 91–94, 100, 139
 Viscoelastic sandwich beam, 1–3, 8

W

Wall pressure, [116](#), [119](#), [120](#), [124](#)

Waste segregator, [199](#), [201–205](#)

Workspace, [277](#), [278](#), [281](#)